



HAL
open science

Controlled synthesis of Ru nanoparticle covalent assemblies and their catalytic application

Yuanyuan Min

► **To cite this version:**

Yuanyuan Min. Controlled synthesis of Ru nanoparticle covalent assemblies and their catalytic application. Coordination chemistry. Institut National Polytechnique de Toulouse - INPT, 2020. English. NNT : 2020INPT0021 . tel-04163415

HAL Id: tel-04163415

<https://theses.hal.science/tel-04163415>

Submitted on 17 Jul 2023

HAL is a multi-disciplinary open access archive for the deposit and dissemination of scientific research documents, whether they are published or not. The documents may come from teaching and research institutions in France or abroad, or from public or private research centers.

L'archive ouverte pluridisciplinaire **HAL**, est destinée au dépôt et à la diffusion de documents scientifiques de niveau recherche, publiés ou non, émanant des établissements d'enseignement et de recherche français ou étrangers, des laboratoires publics ou privés.



Université
de Toulouse

THÈSE

En vue de l'obtention du

DOCTORAT DE L'UNIVERSITÉ DE TOULOUSE

Délivré par :

Institut National Polytechnique de Toulouse (Toulouse INP)

Discipline ou spécialité :

Chimie Organométallique et de Coordination

Présentée et soutenue par :

Mme YUANYUAN MIN
le vendredi 14 février 2020

Titre :

Controlled synthesis of Ru nanoparticle covalent assemblies and their catalytic application

Ecole doctorale :

Sciences de la Matière (SDM)

Unité de recherche :

Laboratoire de Chimie de Coordination (LCC)

Directeur(s) de Thèse :

M. PHILIPPE SERP
MME MARIA ROSA AXET MARTI

Rapporteurs :

M. GIULIANO GIAMBASTIANI, CONSIGLIO NAZIONALE DE RICERCA
Mme PATRICIA LARA MUNOZ, UNIVERSITE DE SEVILLE

Membre(s) du jury :

M. ROMUALD POTEAU, INSA TOULOUSE, Président
M. ANTONIO LEYVA PEREZ, UNIVERSITAT POLITECNICA DE VALENCE, Membre
M. IANN C. GERBER, INSA TOULOUSE, Invité
M. JEAN-CYRILLE HIERSO, UNIVERSITE DE BOURGOGNE, Invité
Mme MARIA ROSA AXET MARTI, CNRS TOULOUSE, Membre
M. PHILIPPE SERP, TOULOUSE INP, Membre

Acknowledgement

Firstly, I would like to express my sincere gratitude to my supervisors, Prof. Philippe Serp and Dr. M. Rosa Axet. Thanks to them accepting me to do this interesting project, and guide me to become a doctor. I learned a lot from them experimentally and theoretically, most importantly, how to be a chemist.

Many thanks to Prof. Giuliano Giambastiani, Prof. Patricia Lara Muñoz, who are the reviewers of my thesis, proved my defense and provided me lots of valuable suggestions. And I am also very grateful to Prof. Romuald Poteau, Prof. Antonio Leyva Pérez, Prof. Jean-Cyrill Hierso and Dr. Iann Gerber for your enlightening questions and suggestions throughout my PhD defense.

In the framework of my project, I appreciated very much all the supports from our collaborators. Dr. Iann Gerber and Dr. Iker del Rosal in Laboratoire de Physique et Chimie des Nano-objets (INSA, Toulouse) supported me with excellent DFT calculation. The ligands were provided by Prof. Jean-Cyrille Hierso, Dr. Houssein Nasrallah and Dr. Didier Poinot in ICMUB group in Université de Bourgogne, Dijon and Prof. Silverio Coco in Universidad de Valladolid (Spain).

During my two months' internship in Complutense University of Madrid, I am very grateful to Prof. Nazario Martin and Prof. Beatriz María Illescas Martínez, as their kind guidance and the experiences in their group improved me a lot in organic chemistry. The hospitality of the entire team in Madrid made my stay warm and delightful, which I appreciated very much.

Many researchers from different laboratories supported me in various characterization. I could not finish my thesis without their assistance. Hereby, I am grateful for Vincent Colliere who did pretty high resolution TEM images for me, Pierre Roblin providing SAXS analysis, Pierre Lecante supporting me with the WAXS analysis and Dr. Andrea Falqui who performed the interesting electron tomography analysis in the thesis. Many thanks to Dr Yannick Coppel for SS-NMR characterization, Sonia Mallet-Ladeira for

the XRD analysis, Marine Tasse for AFM test, Yann Tison for the XPS analysis, Mr. Alain Moreau and Ms. Isabelle Borget for ICP and elemental analysis.

I also would like to thank my colleges and all present or former members of the Catalysis Fine Chemical groups. Our technicians, Laurent Ropiquet, Idaline Chanteperdrix and Nora Imlyhen are always kind and willing to help me in the Lab. And the nice discussions with the researchers in our lab always benefit me a lot, thanks to Dr. Jerome Volkman, Prof. Martine Urrutigoity, Prof. Maryse Gouygou, Prof. Philippe Kalck, Dr. Odile Dechy-Cabaret, Dr. Jérôme Durand, Dr. Carole Le Berre

I am very thankful to Dr. Nicolas Gimeno, Camila Rivera Carcamo, Dr. Zhishan Luo, Dr. Jian Ye, Amel Ghogia, Jeremy Audevard and Canio Scarfiello for their accompany and friendship for the past three years.

Finally, my special thanks to my husband, Haosheng Liang, he is beside me and supporting and encouraging me always on the way to be a doctor. At last, many thanks to my family for their love.

Yuanyuan MIN

Résumé

Ce travail de recherche porte sur la préparation d'assemblages covalents de nanoparticules (NP) de Ru stabilisés par différentes molécules fonctionnelles, ainsi que sur l'étude des relations structure/activité de ces assemblages pour des réactions d'hydrogénation catalytique. Le **chapitre 1** passe en revue la bibliographie relative aux assemblages covalents de NP métalliques en fonction des stratégies de synthèse utilisées et de leur application en catalyse. Le **chapitre 2** décrit la préparation d'assemblages covalents tridimensionnels (3D) de NP de Ru caractérisés par: a) des NP de Ru de taille nanométrique bien définie, stabilisées par des ligands adamantane, bis-adamantane et diamantane fonctionnalisés, et ii) une distance interparticulaire ajustable. La chimie de coordination avec des ligands amine et acides carboxyliques a été étudiée. Dans le cas de ligands d'acide carboxylique, il a été montré que les espèces de Ru formées lors de l'assemblage de NP sont capables de décarbonyler partiellement les ligands d'acide carboxylique à température ambiante. Le mécanisme de cette réaction a été élucidé par DFT. Le **chapitre 3** détaille l'utilisation d'autres briques moléculaires élémentaires pour la formation d'assemblages de NP de Ru. Nous avons montré que l'utilisation d'un ligand tricarboxylique-hexyloxy triphénylène conduisait à la formation d'assemblages bidimensionnels (2D) de NP de Ru présentant une distance interparticulaire et une taille de NP homogènes. De plus, des assemblages 3D de NP de Ru ont été préparés avec de l'anthracène 9,10-dicarboxylique et un fullerène C₆₀ fonctionnalisé par un hexa-adduit. Dans le **chapitre 4**, nous avons étudié les performances catalytiques de ces nouveaux réseaux covalents de NP de Ru dans diverses réactions. Tous ces matériaux constituent un ensemble intéressant pour étudier les effets structuraux et électroniques du catalyseur en catalyse hétérogène. Les assemblages sont actifs et atteignent une bonne sélectivité en styrène dans l'hydrogénation sélective du phénylacétylène. En particulier, nous avons démontré que des effets de confinement et des effets électroniques se produisaient et que la distance interparticulaire des NP de Ru affectait l'activité du catalyseur, tandis que les effets

électroniques liés aux ligands régissaient principalement la sélectivité du catalyseur. Nous discutons enfin la stabilité des assemblages de NP de Ru.

Mots-clés: ruthénium; nanoparticule; acides carboxyliques; amines; polymantane; triphénylène; hydrogénation; phénylacétylène

Abstract

This research work focuses on the preparation of Ru nanoparticle (NP) covalent assemblies stabilized by different functional molecules, and the study of structure/activity relationships for catalytic hydrogenation reactions. **Chapter 1** reviews the metal NP covalent assemblies according to the synthesis strategies and their application in catalysis. **Chapter 2** described the preparation of three-dimension (3D) Ru NP covalent assemblies characterized by: i) well-defined nanometric-sized Ru NP stabilized by functionalized adamantane, bis-adamantane and diamantane ligands, and ii) a tunable inter-particle distance. The coordination chemistry with amine and carboxylic acid ligands towards the Ru NP surface was investigated. In the case of carboxylic acid ligands, it was shown that Ru species formed during the NP assembly are able to partially decarbonylate carboxylic acid ligands at room temperature. The mechanism of this reaction was elucidated by DFT. **Chapter 3** detailed the use of other molecular building blocks for Ru NP assembly formation. We showed that the use of tricarboxylic-hexyloxy triphenylene ligand leads to the formation of two-dimensional (2D) Ru NP assemblies with homogeneous inter-particle distance and NP size. Additionally, 3D Ru NP assemblies were prepared with 9, 10-dicarboxylic anthracene and a hexa-adduct functionalized C₆₀ fullerene. In **Chapter 4** we studied the catalytic performances of the Ru NP networks in various reactions. All these materials constitute an interesting set to investigate the structural and electronic effects in heterogeneous catalysis. In the selective hydrogenation of phenyl acetylene, the assemblies are active, reaching good selectivity towards styrene. Especially, we demonstrated that confinement and electronic effects are occurring and that Ru NP inter-particle distance affects the catalyst activity, whereas electronic effects mainly govern the catalyst selectivity. The stability of the Ru NP assembly is finally discussed.

Keywords: ruthenium; nanoparticle; carboxylic acids; amines; polymantane; triphenylene; hydrogenation; phenylacetylene

Table of contents

Acknowledgement.....	i
Résumé	I
Abstract	III
General introduction and objectives.....	VII
List of abbreviations.....	XIV
Chapter 1 Covalent assembly of metal nanoparticles – strategies for synthesis and catalytic applications	1
1.1 Introduction.....	3
1.2 Direct cross-linking synthesis methods	3
1.2.1 Layer-by-layer method	6
1.2.2 Two-phase method.....	10
1.2.3 One-phase method.....	16
1.2.4 Langmuir-Blodgett (LB) method	20
1.2.5 Light triggered self-assemblies	20
1.2.6 Single step wet chemical synthesis	21
1.2.7 Novel strategies producing NP assemblies.....	22
1.3 Indirect cross-linking synthesis methods	24
1.3.1 Click chemistry.....	24
1.3.2 Covalent coupling reactions	27
1.3.3 Biomolecular coupling	31
1.3.4 Metal ion-induced nanoparticle assembly.....	34
1.3.5 Light-induced self-assembly of irreversible nanoparticle networks	37
1.4 Stimuli-responsive reversible covalent networks of nanoparticles.....	40
1.4.1 Dynamic covalent chemistry	40
1.4.2 Metal ions as chemical stimuli	42
1.4.3 Dynamic covalent chemistry assisted by light as physical stimulus	45
1.5 Metal nanoparticle assemblies as catalysts	47
1.5.1 Reduction reactions	48

1.5.2 Oxidation reactions.....	54
1.5.3 Miscellaneous reactions	57
1.6 Conclusion	62
1.7 References.....	64
Chapter 2 Controlled synthesis of 3D ruthenium nanoparticle covalent assemblies from polymantane ligands	83
2.1 Introduction.....	85
2.2 Results and discussion	86
2.2.1 Structure of Ru nanoparticles and Ru nanoparticle assemblies	87
2.2.2 Coordination of carboxylate and amine ligands on Ru nanoparticle surface	96
2.3 Conclusion	117
2.4 Experimental section.....	118
2.5 References.....	137
Chapter 3 3D and 2D self-assemblies of Ru nanoparticles via multitopic ligands	144
3.1 Introduction.....	146
3.2 Results and discussion	150
3.2.1 3D Ru NP assemblies with hexa-substituted fullerene.....	150
3.2.2 Synthesis and characterization of Ru NP assemblies through tricarboxylic-hexyloxy triphenylene	157
3.2.3 Synthesis and characterization of Ru NP assemblies through 9,10- dicarboxylic acid anthracene	174
3.3 Conclusion	177
3.4 Experimental section.....	179
3.5 References.....	189
Chapter 4 Catalytic applications of Ru NP covalent assemblies.....	195
4.1 Introduction.....	197
4.2 Results and discussion	198
4.2.1 C-H activation - bromination	198
4.2.2 Hydrogenation of quinoline.....	200

4.2.3 Hydrogenation of phenylacetylene.....	203
4.3 Conclusion	226
4.4 Experimental section.....	227
4.5 References.....	231
General conclusions and perspectives	236
Chapitre 5 Résumé	243
5.1 Introduction.....	245
5.2 Assemblage covalent de nanoparticules métalliques - stratégies de synthèse et applications catalytiques	247
5.3 Synthèse contrôlée d'assemblages covalents de nanoparticules de ruthénium 3D à partir de ligands polymantanes.....	248
5.4 Auto-assemblages 3D et 2D de nanoparticules de Ru produits à partir des ligands multitopiques	254
5.5 Applications catalytiques des assemblages covalents de NP de Ru.....	258
5.6 Perspectives à ces travaux de thèse.....	263
5.7 Références.....	264

General introduction and objectives

It has been almost two-hundred years since the conception of the first industrial catalysts,¹ and one hundred years since the first important catalytic processes (such as the Haber-Bosch process). Since then, the progresses in catalysis and catalyst development have greatly changed human lifestyle,² and catalysis is essential for the development of a sustainable world. The main task of scientific research in catalysis is to find how to control chemical reactions in the desired direction, achieving high activity and selectivity under mild conditions, while reaching maximum catalyst stability and low production costs.³ Recent researches are trying to depict an accurate portrait on crucial steps in chemical reactions therefore proposing theories that can guide in the catalyst design, which includes a large variety of methods and materials.⁴

10

Because of the demand to develop sustainable and green chemistry, heterogeneous catalysts such as supported catalysts are considered to outweigh homogeneous ones, especially in industrial production, because of their recyclability and easy separation.¹¹ However, supported catalysts suffer from some drawbacks, such as ill-defined active centers and metal/support interactions, broad metal particle size distribution, and no control of inter-particle distance (Figure 1a). On the other side, homogeneous catalysts are attractive due to the well-defined nature of the active sites, which is possible to finely tune to reach tremendous activity/selectivity. Colloidal nanoparticles (NP) are nanomaterials combining the features of homogenous and heterogeneous catalysts, in which coordination chemistry play a vital role.¹² Techniques to prepare colloidal NP can provide exquisite control over size, shape and composition such that the heterogeneity of catalytic materials can be drastically decreased, even to the level of atomically-precise materials (Figure 1b).¹³ However, their separation from the reaction mixture is difficult, if not impossible on a large scale.

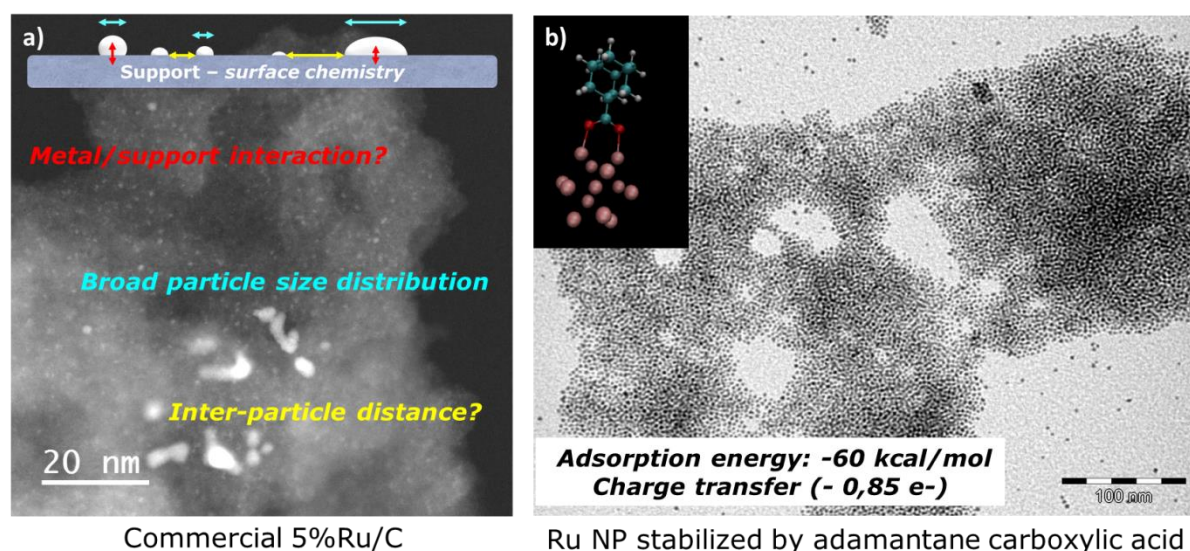


Figure 1 a) STEM-HAADF micrograph of a commercial Ru/C catalyst; and b) TEM micrograph of Ru NP stabilized by adamantane carboxylic acid prepared in this work.

To circumvent this issue, colloidal NP can be deposited on a support, for example, supported on polymer, carbon material or inorganic substrates,¹⁴⁻¹⁶ or stabilized in a specific phase, such as ionic-liquid.^{17,18} However, in that case also it is difficult to control the inter-particle distance, which is an important parameter in catalysis,¹⁹⁻²¹ and the fact to deposit the NP on the support change significantly the electronic properties of the original, ligand stabilized NP.

Therefore, it could be interesting to utilize the covalent assembly of metal NP in catalysis considering the confined space and possible robust network, which are desirable for applications in catalysis. Nevertheless, the covalent assembly of metal NP has received relatively little attention for applications in catalysis. The objective of the thesis is to design innovative nanomaterials containing metallic ruthenium NP and di- or multi-topic ligands insuring covalent bonding between NP. In such NP networks, we expect to have: i) a good control of NP size and electronic interactions with the ligand/support, ii) a good control of inter-particle distance thanks to the choice of the ligand/spacer, and iii) a facile catalyst separation due to the macroscopic shape of the final material. Given that the catalyst structure can be designed and well-defined,

reaching a molecular understanding, it will be feasible to understand the structure-performance relationship and to develop predictable heterogeneous catalysis, which is most of the time very challenging.

Thus, a series of original and self-assembled hybrid nanostructures containing Ru NP and various ligands bearing carboxylic or amine groups were produced and characterized. The organic backbone, which can be considered also as the support, consists in sp^2 (anthracene, fullerene, triphenylene) or sp^3 (polymantanes) carbon containing molecules of different sizes. Different Ru NP assemblies either tri- or bi-dimensional were synthesized and fully characterized. Theoretical calculations were performed to support the experimental results concerning the stability of the assemblies and the nature of the coordination chemistry at NP surface. Finally, we have evaluated the catalytic performances of these nanostructures for various reactions. Particular attention has been devoted to the selective hydrogenation of phenylacetylene to styrene, which is an important industrial production. The intrinsic properties of the assemblies, confinement and electronic effect, is demonstrated to have associated influences on the catalytic activity and selectivity.

This PhD thesis is composed of four chapters:

The first chapter is devoted to an exhaustive bibliographic study on covalent assemblies of metal nanoparticles, focusing particularly on the various strategies for synthesis and on the rare examples of catalytic applications. As far as the synthesis of covalent assemblies of metal NP is concerned, while the first assemblies were produced with simple methods, efficient and more complex systems have been engineered and applied recently, such as the formation of reversible covalent networks of metal NP. If the metal-ligand interaction is strong enough, the principal advantages of covalent metal NP assemblies in catalysis are their stability and robustness, which led in some cases to a better recycling, when compared to unassembled metal NPs. Furthermore, in some cases assembled metal NPs displayed better catalytic performances than isolated metal NPs.

The second deals with the use of bi-functional polymantanes (i.e. rigid sp^3 -hybridized diamondoids) as linker compounds to build up, *via* a straightforward and up-scalable method, Ru NP networks presenting uniform particle size and inter-particle distance, as well as a well-defined chemical environment. Two series of functionalized adamantanes, bis-adamantanes and diamantanes bearing carboxylic acid or amine functional groups have been used as building blocks to produce networks of ruthenium NP. Both the nature of the ligand and the Ru/ligand ratio affect the inter-particle distance in the assemblies. The first finding of this work is that during the synthesis of these NP covalent assemblies from polymantane carboxylic ligands, intermediate species are able to decarbonylate the carboxylic acid at room temperature and under 3 bar of hydrogen. This is an important discovery considering that this reaction for producing biofuel is usually conducted under extremely harsh conditions (150-250 °C, 10-60 bar H_2). DFT calculations have allowed us to propose a mechanism for this unexpected reaction.

In the third chapter, Ru NP assemblies have been successfully produced using carboxylic functionalized fullerene, triphenylene, and anthracene ligands. These ligands allow tuning the assembly structure (3D with the fullerene ligand and 2D with the triphenylene or anthracene ligands) and inter-particle distance. Coordination *via* the carboxylate group on the surface of Ru NP was confirmed by several analytical techniques. As for polymantanes ligands studied in chapter 2, carbon monoxide was generated during the synthesis by ligand decarbonylation and/or solvent decomposition, which remains adsorbed on NP surface.

In the last chapter of this PhD thesis, we have investigated the catalytic properties of Ru NP assemblies in three different reactions: C-H activation (bromination), hydrogenation of quinoline and phenylacetylene. It is shown that the Ru NP carboxylate covalent assemblies are disassembled into isolated NP both in bromination and quinoline hydrogenation reactions even though showing good activity. For application in phenylacetylene hydrogenation, the short-range ordered assemblies keep their integrity and present a correlation between activity, selectivity and inter-particle

distance and electronic properties of the Ru NP. However, we also demonstrated that the stability of the assemblies is still a problem for phenylacetylene hydrogenation since the structure cannot stand recycling tests.

Finally, the perspectives for the continuation of this work in catalysis and also some propositions to obtain covalent networks of NP with better stability are suggested.

References

1. Robertson, A., The Early History of Catalysis. *Platinum Met. Rev.* **1975**, *19*, 64-69.
2. Hagen, J., *Industrial Catalysis: A Practical Approach*. John Wiley & Sons: **2015**.
3. Derouane, E. G., Catalysis in the 21st Century, Lessons from the Past, Challenges for the Future. *Cattech* **2001**, *5*, 214-225.
4. Fujdala, K. L.; Tilley, T. D., Design and Synthesis of Heterogeneous Catalysts: the Thermolytic Molecular Precursor Approach. *J. Catal.* **2003**, *216*, 265-275.
5. Zhang, Y.; Yang, X.; Zhou, H.-C., Synthesis of MOFs for Heterogeneous Catalysis via Linker Design. *Polyhedron* **2018**, *154*, 189-201.
6. Dufaud, V.; Davis, M. E., Design of Heterogeneous Catalysts via Multiple Active Site Positioning in Organic-inorganic Hybrid Materials. *J. Am. Chem. Soc.* **2003**, *125* (31), 9403-9413.
7. Vojvodic, A.; Nørskov, J. K., New Design Paradigm for Heterogeneous Catalysts. *Natl. Sci. Rev.* **2015**, *2*, 140-143.
8. Greeley, J., Theoretical Heterogeneous Catalysis: Scaling Relationships and Computational Catalyst Design. *Annu. Rev. Chem. Biomol. Eng.* **2016**, *7*, 605-635.
9. Hutchings, G. J., Heterogeneous Catalysts—Discovery and Design. *J. Mater. Chem.* **2009**, *19*, 1222-1235.
10. Gao, C.; Wang, J.; Xu, H.; Xiong, Y., Coordination Chemistry in the Design of Heterogeneous Photocatalysts. *Chem. Soc. Rev.* **2017**, *46*, 2799-2823.
11. Sun, L. B.; Liu, X. Q.; Zhou, H. C., Design and Fabrication of Mesoporous Heterogeneous Basic Catalysts. *Chem. Soc. Rev.* **2015**, *44*, 5092-5147.
12. Yan, N.; Yuan, Y.; Dyson, P. J., Nanometallic Chemistry: Deciphering Nanoparticle Catalysis from the Perspective of Organometallic Chemistry and Homogeneous Catalysis. *Dalton Trans* **2013**, *42*, 13294-13304.
13. Jiang, Y.; Gao, Q., Heterogeneous Hydrogenation Catalyses over Recyclable Pd(0) Nanoparticle Catalysts Stabilized by PAMAM-SBA-15 Organic-Inorganic Hybrid Composites. *J. Am. Chem. Soc.* **2006**, *128*, 716-717.
14. Losch, P.; Huang, W.; Goodman, E. D.; Wrasman, C. J.; Holm, A.; Riscoe, A. R.;

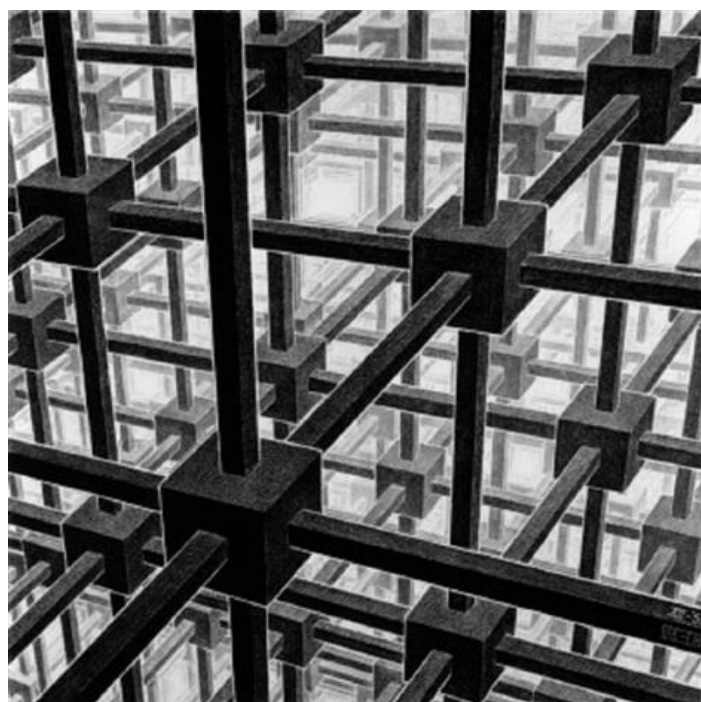
- Schwalbe, J. A.; Cargnello, M., Colloidal Nanocrystals for Heterogeneous Catalysis. *Nano. Today* **2019**, *24*, 15-47.
15. Luechinger, N. A.; Loher, S.; Athanassiou, E. K.; Grass, R. N.; Stark, W. J., Highly Sensitive Optical Detection of Humidity on Polymer/Metal Nanoparticle Hybrid Films. *Langmuir* **2007**, *23* (6), 3473-3477.
16. Teddy, J.; Falqui, A.; Corrias, A.; Carta, D.; Lecante, P.; Gerber, I.; Serp, P., Influence of Particles Alloying on the Performances of Pt–Ru/CNT Catalysts for Selective Hydrogenation. *J. Catal.* **2011**, *278*, 59-70.
17. Karakulina, A.; Gopakumar, A.; Akcok, I.; Roulier, B. L.; LaGrange, T.; Katsyuba, S. A.; Das, S.; Dyson, P. J., A Rhodium Nanoparticle-Lewis Acidic Ionic Liquid Catalyst for the Chemoselective Reduction of Heteroarenes. *Angew. Chem. Int. Ed. Engl.* **2016**, *55*, 292-296.
18. Scholten, J. D.; Leal, B. C.; Dupont, J., Transition Metal Nanoparticle Catalysis in Ionic Liquids. *ACS Catal.* **2012**, *2*, 184-200.
19. Antolini, E., Structural Parameters of Supported Fuel Cell Catalysts: The Effect of Particle Size, Inter-particle Distance and Metal Loading on Catalytic Activity and Fuel Cell Performance. *Appl. Catal. B* **2016**, *181*, 298-313.
20. Prieto, G.; Zečević, J.; Friedrich, H.; de Jong, K. P.; de Jongh, P. E., Towards Stable Catalysts by Controlling Collective Properties of Supported Metal Nanoparticles. *Nat. Mater.* **2013**, *12*, 34-39.
21. Mistry, H.; Behafarid, F.; Reske, R.; Varela, A. S.; Strasser, P.; Roldan Cuenya, B., Tuning Catalytic Selectivity at the Mesoscale via Interparticle Interactions. *ACS Catal.* **2016**, *6*, 1075-1080.

List of abbreviations

1-THQ	1,2,3,4- tetrahydroquinoline
2D	Two dimensional
3D	Three dimensional
5-THQ	5,6,7,8-tetrahydroquinoline
Ad	Adamantane
AnDC	9,10-dicarboxylic acid anthracene
AFM	Atomic force microscopy analyses
ATR-IR	Attenuated total reflection infrared
BAd	Bis-adamantane
BE	Binding energy
C ₆₀	Fullerene
C ₆₆ (COOH) ₁₂	Fullerenehexamalononic acid
CNT	Carbon nanotube
CP MAS	Cross-Polarization magic-angle spinning
DAd	Diamantane
DBU	1,8-diazabicyclo[5.4.0]undec-7-ene
DFT	Density functional theory
DHQ	Decahydroquinoline
DMA	Dimethylacetamide
Eads	Adsorption energy
ET	Electron tomography
FFT	Fast Fourier Transform
FWHM	Full width at half maximum
GC	Gas chromatography
GC-MS	Gas chromatography–mass spectrometry
HAADF	High-angle annular dark-field imaging
HF	Hexa-adducts functionalized fullerene

HRTEM	High-resolution transmission electron microscopy
ICP	Inductively coupled plasma
I	Intensity
MeOH	Methanol
MS	Mass spectra
NBS	Bromosuccinimide
NP	Nanoparticles
Q	Quinoline
RDF	Radial distribution function
[Ru(COD)(COT)]	(1,5-cyclooctadiene)(1,3,5-cyclooctatriene)ruthenium
SAXS	Small-angle X-ray scattering
SS-NMR	Solid State Nuclear Magnetic Resonance Spectroscopy
STEM	Scanning Transmission Electron Microscopy
TBATB	Tetrabutylammonium tribromide
TEM	Transmission Electron Microscopy
TGA	Thermogravimetric analysis
THF	Tetrahydrofuran
TOF	Turnover frequency
TPD	Temperature-programmed desorption
TPhC	Triphenylene carboxylic acid
TPhTC	Triphenylene tricarboxylic acid
WAXS	Wide-angle X-ray scattering
XPS	X-ray photoelectron spectroscopy
XRD	X-Ray Diffraction

Chapter 1 Covalent assembly of metal nanoparticles – strategies for synthesis and catalytic applications



Cubic Space Division par Maurits Cornelis Escher (1953)

1. Covalent assembly of metal nanoparticles – strategies for synthesis and catalytic applications

1.1 Introduction

1.2 Direct cross-linking synthesis methods

1.2.1 Layer-by-layer method

1.2.1 Two-phase method

1.2.3 One-phase method

1.2.4 Langmuir-Blodgett (LB) method

1.2.5 Light triggered self-assemblies

1.2.6 Single step wet chemical synthesis

1.3 Indirect cross-linking synthesis methods

1.3.1 Click chemistry

1.3.2 Covalent coupling reactions

1.3.3 Biomolecular coupling

1.3.4 Metal ion-induced nanoparticle assembly

1.3.5 Light-induced self-assembly of irreversible nanoparticle networks

1.4 Stimuli-responsive reversible covalent networks of nanoparticles

1.4.1 Dynamic covalent chemistry

1.4.2 Metal ions as chemical stimuli

1.4.3 Dynamic covalent chemistry assisted by light as physical stimulus

1.5 Metal nanoparticle assemblies as catalysts

1.5.1 Reduction reactions

1.5.2 Oxidation reactions

1.5.3 Miscellaneous reactions

1.6 Conclusion

1.7 References

1.1 Introduction

Metal nanoparticles (NP) have attracted the interest of the catalysis community, as it has been shown that their inherent properties, such as size, shape, crystallographic structure, in addition to surface modifiers (ligands and/or supports) have a remarkable impact on their catalytic properties.¹⁻⁴ In this sense, a considerable effort has been devoted to understand and tune these characteristics. On the other hand, supramolecular catalysis allows creating unique catalyst-substrate interactions, that can be tailored to direct substrates along particular reaction paths and selectivities.⁵⁻⁷ The assembly of metal NP could also permit to direct substrates, or to create confined spaces in order to produce more efficient catalysts. Nevertheless, the assembly of metal NP has received relatively little attention for applications in catalysis. Several approaches have been described for the directed self-assembly of metallic NP⁸ that involves manipulation of: i) molecular interaction forces *i.e.*, Van der Waals (VdW),⁹ electrostatic interactions,¹⁰ zwitterion type electrostatic interactions,¹¹⁻¹⁴ hydrogen bonding,¹⁵⁻¹⁹ host-guest interactions,²⁰ DNA-assisted assemblies,²¹ ii) covalent interactions *i.e.*, coordination bonds, bifunctional linkage, or iii) external fields²² *i.e.*, capillary forces, magnetic²³ and electric field. This bibliography survey will focus on the creation of covalent interactions between NP, since they may provide robust NP networks, which are desirable for applications in catalysis. Covalent assemblies of metal NP have been obtained following several methodologies: direct cross-linking methods, indirect cross-linking methods, and stimuli-responsive reversible covalent networks of NP, which are described in the next sections. The applications in catalysis of metal NP assemblies are also discussed.

1.2 Direct cross-linking synthesis methods

This section provides an overview of metal NP covalent assemblies through directed linkage, *i.e.* ligand molecules bearing two or more anchoring groups (dithiol, dicarboxylic, etc.) bound on the surface of adjacent metal NP to establish various dimensional networks (1-D, 2-D, 3-D). The covalent metal NP assemblies have been investigated for more than thirty years. For a large portion of the research reported, the synthesis process involved a ligand exchange procedure. Thus, a ditopic ligand achieving cross-linking would replace the mono-functional ligand stabilizing the isolated metal NP (monolayer-protected NP). Different methods can be used to build

covalent NP networks such as the layer-by-layer method (LBL), the two-phase method, the one-phase method, Langmuir-Blodgett (LB) method, and some others. Among them, the first three methods (Figure 1.1) are the most frequently employed ones.

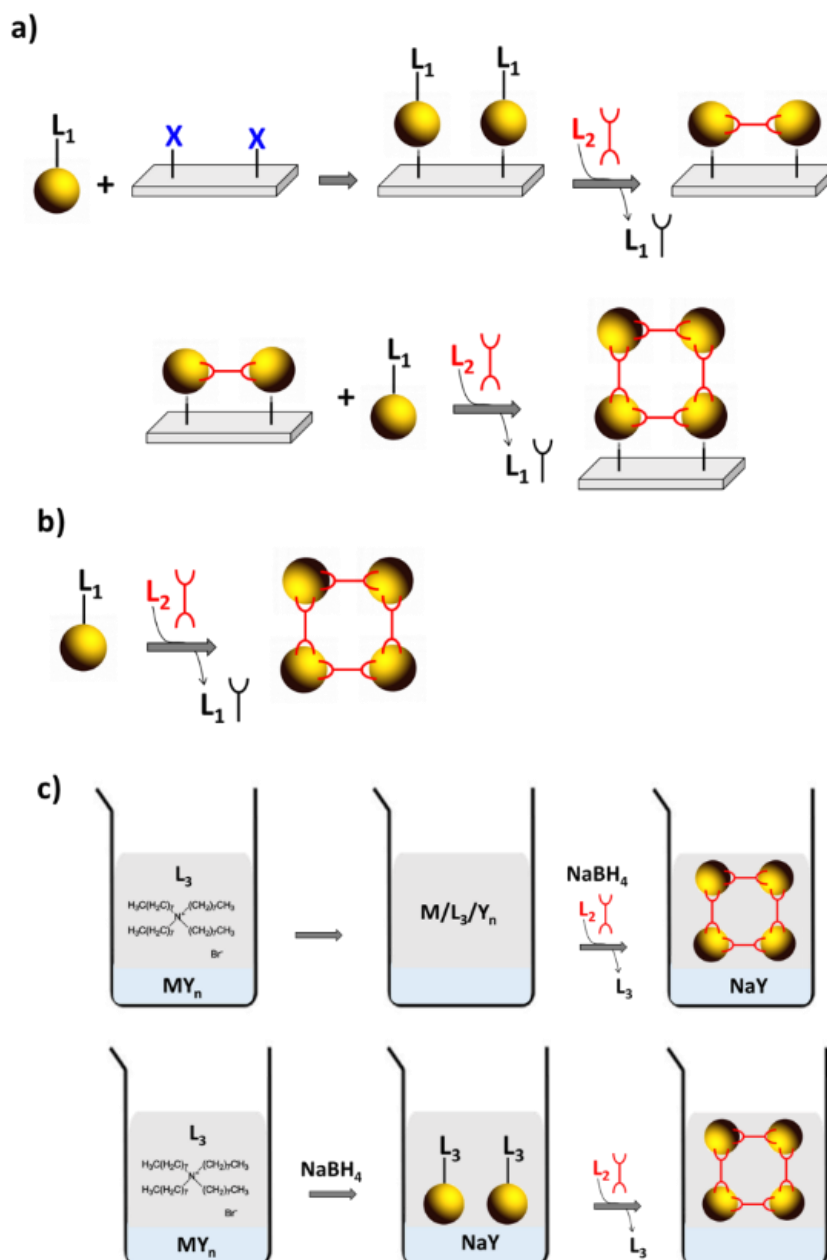


Figure 1.1 Methods involving ligand exchange for the preparation of metal NP networks: a) layer-by-layer; b) one-phase; and c) two-phase methods.

The review of the metal nanostructures will be classified and presented according to the synthesis method. Table 1.1 shows representative examples of metal NP networks produced by direct cross-linking methods.

Table 1.1 Representative examples of metal NP networks produced by the direct cross-linking methods.

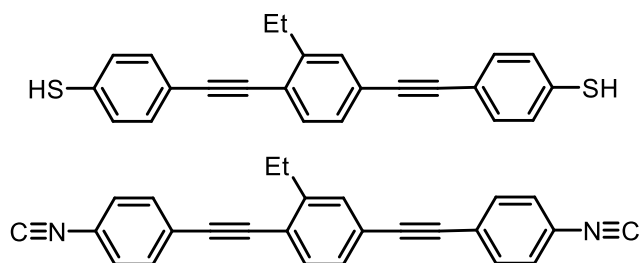
Metal	Ligand	Method	NP size (nm)	Inter-NP distance (nm) ^a	Ref.
Au	1,4-di(4-thiophenylethynyl)-2-ethylbenzene	LBL	3.7	1.7	24
Au	DMAAB/DMAAcH/PBDT/cHBDT (Table 1.2)	LBL	~4	~1	25
Au	octanedithiols/ biphenyldithiols	Two-phase	1~5	~1	26
Au	MeSi(CH ₂ SMe) ₃ /Si(CH ₂ SMe) ₄	Two-phase	6.4 ± 0.8	~2	27
Au	RAFT Oligomers	Two-phase	4.6 ± 1.5	0.6	28
Au	C ₆₀ thiol polymer	Two-phase	10.8 ± 1.5	3.3 ± 0.8	29
Au	V, Y, and X shaped methylthio aryl ethynyls	Two-phase	5.1 ± 0.9	1.1~1.7	30
Au	X-MTA	Two-phase	5~6	1.5	31
Au	X'-MTA	Two-phase	5~6	1.3	31
Ag	Dithiol with Pt (Figure 1.8)	Two-phase	4.31 ± 0.28	2.1 ± 0.2	32
Au	fluorenyl dithiol	Two-phase	3~7	1.2~3.0	33
Au	α,ω-dithiol	One-phase	2/ 5	1.5	34
Pd	1,4-phenylene diisocyanide, 4,4'-Bis(diphenylphosphino)biphenyl, 1,3,5-Tris([2,2':6',2''-terpyridin]-4'- ylethynyl)benzene	One-phase	~2.4	~2	35
Au	1,8-octanedithiol	One-phase	5	0.59~1.4	36
Au	HSC ₆ H ₄ SC ₆ H ₄ SH	LB	5.1	1.6	37
AuAg	9,9-didodecyl-2,7-bis-thiofluorene	Two-phase	3~5	1.5	38
Pd	Tetrakis(terpyridine)	One-phase	2.7	1.2	39
Au	Two pyridine-N-oxide	One-phase	5.2 ± 0.3	5.7/6.0 (center-center)	40
Au	One pyridine-N-oxide and one ArF-I group	One-phase	5.2 ± 0.3	7.26 (center-center)	40
Ru	Ru@C ₆₆ (COOH) ₁₂	Single step wet chemical synthesis	1.5	2.85 (center-center)	41

^a Except for ref ⁴⁰ and ⁴¹, the distance between NP is the edge to edge distance.

1.2.1 Layer-by-layer method

Along the development of metal NP assemblies, LBL self-assembly of building blocks has played a significant role, as it allows controllable growth over a substrate turning into a nanocomposite demonstrating specific optical and electrical properties.^{42,43} The LBL technique is a versatile approach to create ultrathin surface coatings on a wide range of surfaces. It involves a ligand/linker exchange process during the assembly cycle, by immersion of substrates into solution of NP and a linker molecule.

In 1996, R. P. Andres *et al.*²⁴ reported the preparation of the 2-D self-assembly of Au NP connected by ditopic ligands, in which a solid substrate acted as a template to obtain the 2-D growth. In this process, isolated metal NP were first produced in the gas-phase, and protected by alkylthiols in solution. After that, the NP were coated on a substrate placed into aryl dithiol or di-isonitrile ligand solution (Scheme 1.1), the NP were linked into an assembly by means of a ligand exchange. The authors demonstrated that by modifying the NP size or composition, the length and chemical structure of the linker, and the nature of the substrate, a wide range of electronic properties could be modulated. For instance, the electrical conductance of NP assemblies (78 nS) was lower than the one measured for unlinked NP (133 nS).



Scheme 1.1 Ditopic ligands used for the synthesis of NP assemblies.

C. Zhong *et al.* described a novel strategy toward the assembly of bimetallic AuAg NP *via* carboxylate- Ag^+ binding at selective sites on the NP surface, giving an assembly of composition $\text{Au}_{23}\text{Ag}_{77}$ (Figure 1.2).⁴⁴ The possibility to modify the composition of the AuAg NP as well as the chain length of the dicarboxylic acids allows modulating the optical and electronic properties. The AuAg but also Au NP assemblies⁴⁵ with different inter-particle distances, adjusted by varying the $\text{X}-(\text{CH}_2)_n-\text{X}$ length, were applied for vapor sensing, revealing a correlation between sensitivity (electric conductivity) and inter-particle spacing.⁴⁶

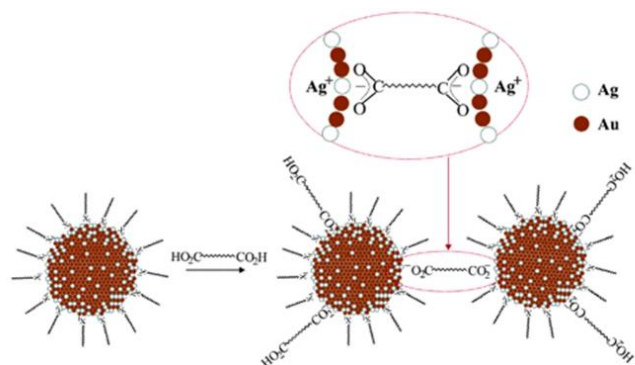


Figure 1.2 Schematic representation of the surface binding sites and the selective linkage for the assembly of AuAg NP mediated by dicarboxylic acid ligands. Reproduced with permission from ref.⁴⁴

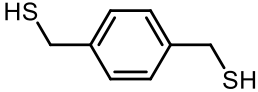
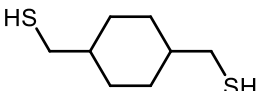
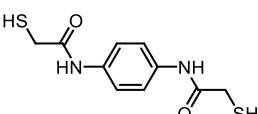
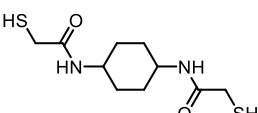
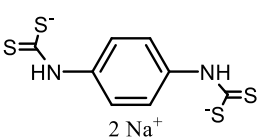
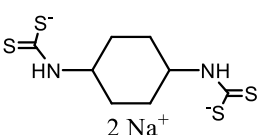
Another alloyed AuAg NP assembly was produced from the 4-aminothiophenol (PATP) linker on substrate, and investigated by Raman scattering.⁴⁷ The LBL assembly was produced first by using the protonated pyridine groups of a polyvinylpyridine functionalized glass as anchoring sites for negatively charged Au NP. PATP ligands were then adsorbed on Au NP through the formation of Au-S bonds. The PATP molecule, which possesses two resonance structures (benzenoid and quinonoid), can interact with Ag NP through the quinonoid form. It was concluded from the Raman study that the *b2* vibrational mode of PATP is enhanced by charge transfer from the Ag to Au NP due to PATP acting as tunnel in between.

Alkanedithiols with different carbon chain length (C₆, C₉, C₁₂, C₁₆), which are typical linkers for Au NP assemblies, were investigated for applications in sensing.⁴⁸ X-ray photoelectron spectroscopy (XPS) analyses of a 2-D film composed of Au NP assembly confirmed that dodecylamine ligands on Au NP were quantitatively exchanged by alkanedithiol, of which 60% of the alkanedithiol are bound to NP by both groups, while 40% are bound with only one thiol-group. All films showed ohmic I-V characteristics and Arrhenius-type activation of charge transport. Interlinked NP assemblies help to enhance the conductivity of the films compared to free NP. Indeed, the electron-tunneling decay constant β_N , was much lower for non-covalently linked NP film. A fast and fully reversible increase of film resistance was measured upon exposure to vapors of toluene or tetrachloroethylene. The resistance increases exponentially with increasing alkanedithiol chain length at a given concentration. This type of film was forecasted as a promising material for sensing applications, which was studied later extending the ligand to alkanedithiol-C₁₂, 4,4'-terphenyldithiol and [4]-staffane-3,3'''-dithiol to make chemiresistors. This study revealed that the flexibility and resistivity of the interlinkage has a

profound impact on the response characteristics of the sensors.⁴⁹ Thus, the use of the flexible 1,12-dodecanedithiol as linker induces the interlinked film to respond with an increase in resistance. Oppositely, with a rigid linker with a staffane backbone the interlinked film responded with a decrease in resistance.

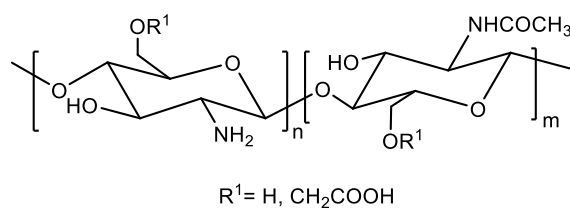
In a similar attempt of investigating the influence of dithiol ligands, J. M. Wessels *et al.* synthesized Au NP assembly films from six different dithiols, which were classified into three groups according to the nature of the group in the middle and at the end (Table 1.2).²⁵ The optical and electrical properties of the films were highly influenced by the nature of the ligand. Especially, the conductivity increased by one order of magnitude for linkers that contain a cyclohexane ring instead of a benzene ring. As the molecule consists in non-conjugated and conjugated parts, according to the electron tunneling decay constant (β_{N-CON}), the conductivity can be tuned from the insulating to the metallic limit, regardless of the inter-particle spacing (4 ± 0.8 nm, $d_{NP} \sim 1$ nm).

Table 1.2 An overview of the DT linker molecules and the distances between S atoms and S⁻ atoms.²⁵

Ligand	Abbreviations	Length (Å)	Δ (EHOMO-LUMO)	
	BDMT	7.7	4.0	Bis-mercaptopmethylenes
	cHDMT	8.2	5.0	
	DMAAB	14.8	3.5	Bis-acetamidothiols
	DMAAcH	14.9	4.7	
	PBDT	10.7	2.7	Bis-dithiocarbamates
	cHBDT	9.6	3.2	

Y. Daskal *et al.* followed the Au NP assembly deposition using a quartz crystal microbalance. This is a suitable method as it can sense material deposition in the nanogram range.⁵⁰ The assembly efficiency is higher for shorter alkyldithiols, and ligands with more strongly interacting functional groups such as alkyldithiocarbamates, which outperformed alkyldiamines. Comparing plasmon resonance, a typical and well-studied feature of Au NP, the spectrum of the bisdithiocarbamate composite exhibits a distinct blue shift, which was attributed to more delocalized electron charge at the NP, because the linker possesses bulkier groups allowing a longer structure.

The number of the deposition cycles performed to produce multilayer films on substrate counts importantly for properties and applications. Thus, enhanced localized surface plasmon resonance sensing was obtained with multilayer structures fabricated with 1,10-decanedithiol as linker from four NP deposition cycles.⁵¹ This was reflected by a ~4 -fold improvement of the sensitivity to the changes of the environmental refractive index compared to the submonolayer structure. J. Dhar *et al.* produced Au and Ag NP composite thin films with a carboxyl-functionalized chitosan polymer bearing COO⁻ and -NH₂ groups (Scheme 1.2), which were deposited on flat quartz substrates.⁵² The process of assembly allows producing up to more than 40 layers, the growth of which was monitored by UV-visible spectroscopy, atomic force microscopy (AFM), and scanning electron microscopy (SEM). The catalytic activity of these composite films was investigated for an organic electron transfer reaction. The kinetic data obtained suggest that the reaction rates are directly related to the NP size and porosity of the membrane. The reaction rates were five and six times higher, respectively, with films of 10 and 40 layers of Au NP (5 nm). Mainly NP located on the film surface are the ones that take part in the reaction, since the accessibility of the embedded NP decreases as a function of number of layers.



Scheme 1.2 A carboxyl functionalized chitosan polymer.

1.2.2 Two-phase method

In the method of Brust (two-phase synthesis),^{53,54} the linker is added to a solution of the metal precursor with phase transfer molecules, and reduction afforded NP self-assemblies.²⁶ This two-phase method is called mediator-template strategy,²⁷ as the transfer molecule capped with hydrophobic chain works like a template between NP, and as linker to mediate the assembly. Thus, spherical Au NP assemblies (~ 20 -300 nm diameter) were produced taking advantage of linker molecules with tri- and quart-ending groups, $\text{Si}(\text{CH}_2\text{SMe})_3$ or $\text{Si}(\text{CH}_2\text{SMe})_4$ (Figure 1.3).^{27,55,56} In these works, multidentate thioether ligands were used as molecular mediators and tetraalkylammonium-capped Au NP (5 nm) as templates. The assemblies can be disassembled by adding decanethiolate, as reflected by the optical response, because the binding of thiolates is stronger than that of thioethers, which may pave the way to drug delivery applications because of the reversible process.

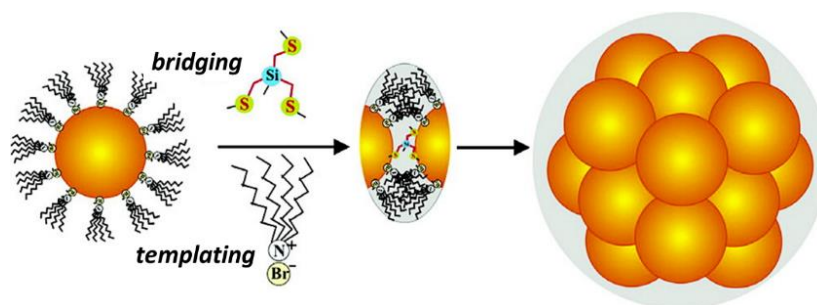


Figure 1.3 Schematic illustration of Au NP assembly formation *via* mediator-template strategy. Reproduced with permission from ref.²⁷

When deposited on a support, the spheres can spread onto the hydrophobic surface, indicating the soft nature of the outmost layer of the assembly. In a subsequent work,⁵⁷ the self-assembly process was assessed from the kinetic and thermodynamic point of view. It was concluded that the process is enthalpy-driven. The enthalpy change ($-1.3 \text{ kcal.mol}^{-1}$) was close to the magnitude of the VdW interaction energy for alkyl chains, and the condensation energy of hydrocarbons.

Gold NP network formation mediated by multifunctional synthetic polymers is also a versatile strategy.⁵⁸ M P. Stemmler *et al.* describe a protocol to produce a Au NP assembly after introducing polyphenylene-dendrimers bearing 16 lipoic acid end groups (Figure 1.4).⁵⁹ The

loosely coordinated network rearranged rapidly within hours, showing strong optical coupling between Au NP and a corresponding spectral shift detected by UV-vis-NIR spectroscopy.

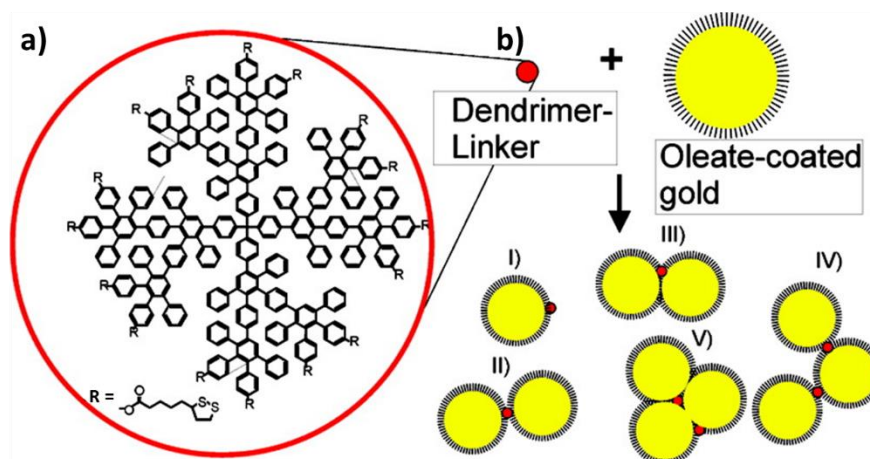


Figure 1.4 a) Dendrimer used as linker; and b) schematic representation of the formation of aggregates from dendrimers (red spheres) and Au NP. Reproduced with permission from ref.⁵⁹

Another example of using polymers is described by C. Rossner *et al.*, who produced spherical shape Au NP network with multifunctional polymers of styrene bearing multiple trithiocarbonate groups as linkers to interconnect Au NP (Figure 1.5).^{28,60,61} The authors demonstrated that the formation of assemblies relies more on the polymer length than the anchoring group number. The distance between NP can be tuned in a wide range when regulating the length of the polymer chain. The internal structures of the 3-D networks were characterized by small-angle X-ray scattering (SAXS), dynamic light scattering (DLS), and UV-vis extinction spectroscopy. These analyses have revealed that a large fraction of Au NP network can only be obtained when the number of styrene units between two anchoring sites in RAFT (reversible addition-fragmentation chain transfer) oligomers is below a crucial threshold, which is probably due to the formation of loops that may sterically impede cross-linking with different NP. Their work provided useful information to build self-assembled NP networks with respect to the degree of polymerization of polymers. It was also shown in the case of hyperbranched polymer-Au NP assemblies that the degree of branching of the linker polymer, in addition to the concentration and number of anchoring groups, has a strong influence on the self-assembly process.⁶²

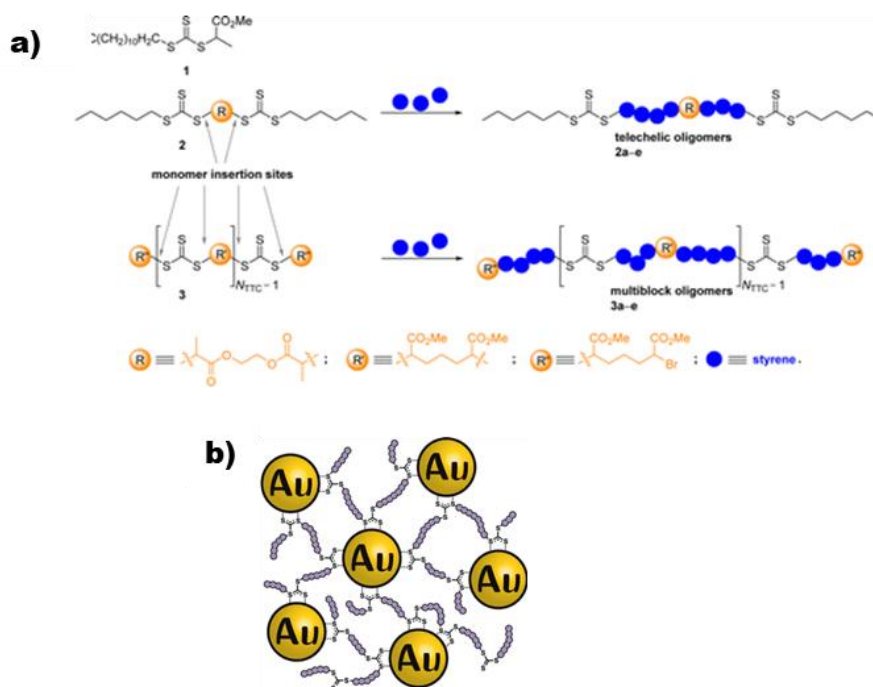


Figure 1.5 a) Synthetic scheme of the RAFT polymer. Reproduced with permission from ref.²⁸ b) The structures of the Au NP assembly cross-linked by di- and multifunctional RAFT oligomers. Reproduced with permission from ref.⁶⁰

Disulfide functionalized C_{60} polymers produced by reacting bis-2-aminoethyl disulfide with C_{60} constitute another example of the use of a polymer to produce Au NP 2-D self-assemblies through Au-S bond on a substrate (Figure 1.6).²⁹ In that case, part of the S-S bonds in the polymeric chain are broken, forming Au-S bonds. The 2-D films obtained on electrodes were used to fabricate single electron devices, which exhibited Coulomb blockade type current-voltage characteristics.

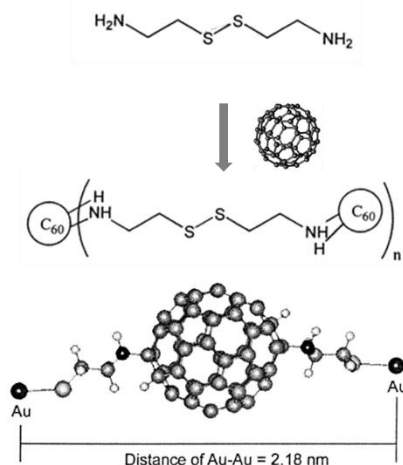


Figure 1.6 C₆₀ polymer structure and the correlation between two Au NP. Reproduced with permission from ref.²⁹

The influence of the number of ending groups in linker ligands on tuning inter-particle interactions and structures was investigated by Zhong *et al.*³⁰ Four different rigid aryl ethynyl molecules with V, Y, and X shapes attached to 2,3,4 methylthio- end-groups were used as linkers for Au NP (Figure 1.7), showing an influence on the optical and spectroscopic properties. The measured average edge-to-edge inter-particle distance ranged between 1.1 and 1.7 nm according to the nature of the ligand, which are in good agreement with molecular modeling results for the inter-particle orientations. It was shown that sequential addition of ligands can induce an initial partial disassembly. Thus, if a network is built from a weakly coordinating ligand, the addition of a ligand that binds strongly causes an initial disassembly due to exchange of ligands, before the second ligand mediated the formation of mixed ligand assemblies. For X-shaped arylethynes, it was also shown that their molecular rigidity, π -conjugation, and importantly the tunability in terms of size, shape, and binding strength affect the size, kinetics, optical, and spectroscopic properties of the assembly.³¹

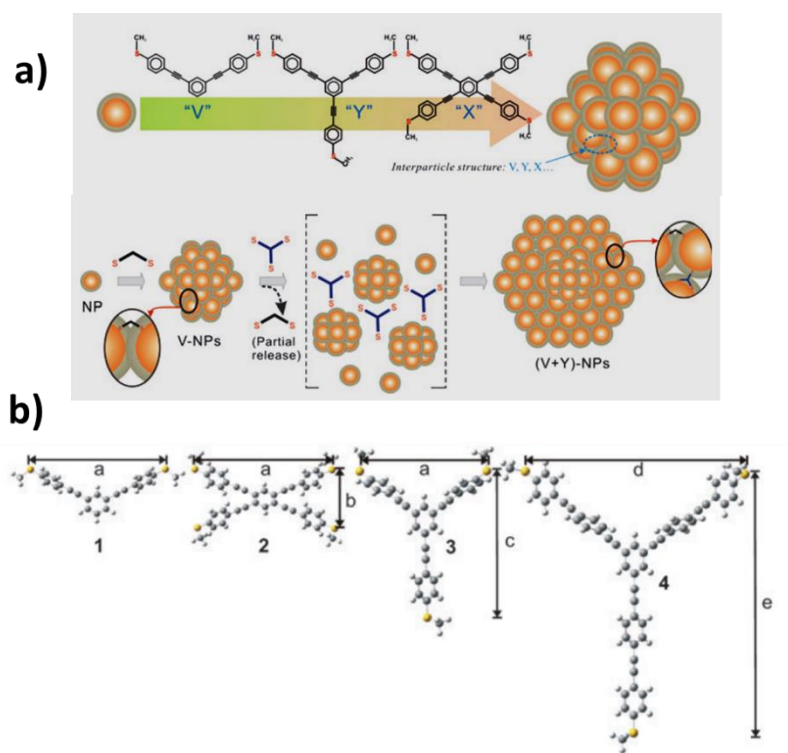


Figure 1.7 a) Schematic illustration of the NP assembly by two mediators (*e.g.*, V and Y) in a sequential addition process; and b) structures of V, X, and Y-shaped methylthio arylethyne. Reproduced with permission from ref.³⁰

The group of I. Fratoddi has shown that Ag NP networks can be produced by means of the organometallic compound *trans, trans*-[CH₃CO-S-Pt(PBu₃)₂(C≡C-C₆H₄-C₆H₄-C≡C)-Pt(PBu₃)₂-S-COCH₃].³² The organometallic bifunctional thiol-containing Pt(II) centers bridge the Ag NP (Figure 1.8). The 2-D networks were obtained through -SH derivatives covalently bound to Ag NP surface without Pt-S bond cleavage. Employing an accurate synchrotron radiation-induced XPS experiment, a semi-quantitative analysis of the chemical interactions between Ag and the complex was performed. The percentage of completely and partially covalent thiols was 54.6% (direct covalent bond) and 45.4% (one terminal grafting involving noncovalent interactions between NP), respectively. A subsequent work was performed to characterize the material by X-ray absorption fine structure spectroscopy (XAFS) and XPS techniques, providing deeper insight at the atomic level into the physicochemical properties of the material.⁶³

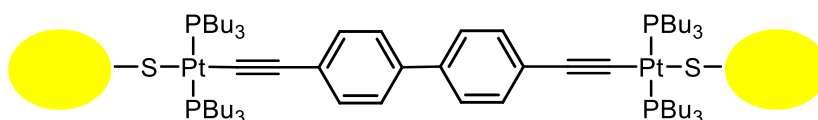


Figure 1.8 Silver NP linked by a Pt-containing organometallic dithiol bridge.

Dithiol organic molecules with different chain lengths and various middle groups have been used to tune the structure and the optical and electric properties of Au NP networks. For instance, Au NP networks were produced from 9,9-didodecyl-2,7-bis(acetylthio)fluorene (Au NP-1) and 9,9-didodecyl-2,7-bis(acetylthiophenylethynyl)fluorene (Au NP-2) playing the role of linkers.³³ A red shift of the emission band for Au NP-1 in emission spectroscopy was observed compared to the free thioester, suggesting an electron density flow to the gold center through the S-bridge, whereas the effect was quenched in Au NP-2, probably due to the increased distance of the fluorenyl chromophore from the gold core. The same type of molecule (π - π

conjugated 9,9-didodecyl-2,7-bis-thiofluorene, FL) was reported to give a structural reorganization of the Au NP assembly after thermal treatments (Figure 1.9).³⁸

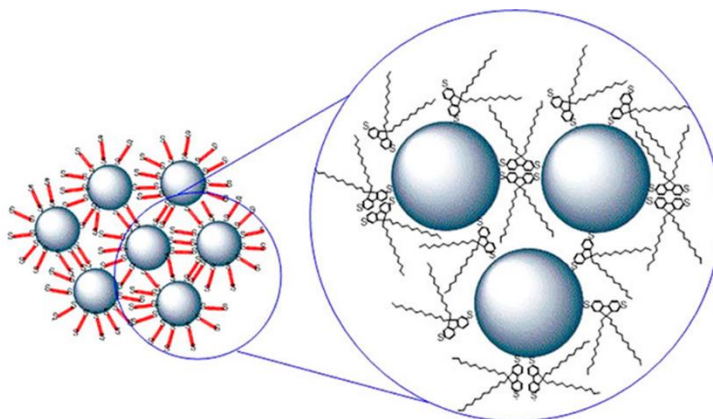


Figure 1.9 Schematic representation of Ag NP assembly mediated by FL molecule. Reproduced with permission from ref.⁶⁴

With the help of grazing incidence X-ray diffraction technique, it was proposed that a partial transition from a hexagonal-like to a cubic-like packing of Au NP occurred during the thermal annealing (up to 100 °C with a rate of 10 °C/min). The electric properties of the Au NP assemblies and deposited films were also probed.⁶⁴ Current-voltage (I/V) response curve follows a non-ohmic relation for Au NP few layer thin films, with a conduction mechanism that strongly depends on polarons and bipolarons along π bridges of the carbon chain of the fluorene bridge. For multilayer thick films, the properties followed approximately an ohmic law. In contrast, Au NP few layer thin films possess a resistance two orders of magnitude smaller. The overall resistance decreases upon illumination thanks to the organic linkers in the network, and optoelectronic properties appeared.

Another example of studying the influence of the dithiol ligands involves the use of (4,4'-dithiol-biphenyl (BI), 4,4'-dithiolterphenyl (TR) and 4,4'-dithiol-trans-stilbene (ST)).⁶⁵ XPS analyses showed that both physisorbed and chemisorbed thiols are present on the NP surface. Ag NP showed a lower quantity of physisorbed thiol and a higher tendency to form interconnected networks. Furthermore, the Au NP-BI and Au NP-TR possess high stability both in solution and under thermal stressing conditions (500 °C).⁶⁶

Besides Au and Ag NP networks, Pt NP networks have been also produced by means of the two-phase method. E. Morsbach *et al.* reported Pt NP porous three-dimensional network built with bifunctional amines from “unprotected” NP through a two-phase method.⁶⁷⁻⁶⁹ The accessibility of the metal sites in the assembly was characterized by cyclic voltammetry for determining the electrochemical surface area (ECSA), showing that 50% of the metal surface atoms are ligand-free. This showed that more potential catalytically active sites are present than in NP produced using mono-amine ligands with more ligands coordinated on the surface. IR characterizations demonstrated that Pt NP are coordinated by the amine. The presence of adsorbed CO originated from the solvent (ethanol decomposition) indicates that ligand-free adsorption sites are present for all ligand-linked NP network. On the other hand, the absence of CO in capped NP indicates the formation of a full monolayer of hexadecylamine on Pt NP.⁶⁸

1.2.3 One-phase method

This method is similar to the two-phase solution method but carried out with the ligand exchange or linkage in one pot in order to simplify the procedure. In the work published by F. L. Leibowitz *et al.* the one-phase method was also called one-step exchange-cross-linking-precipitation route.³⁴ The materials synthesized had comparable electrical properties to those prepared by the LBL method. The ligand exchange process took place in 1,9-nonanedithiol solution with 2 and 5 nm decanethiol capped Au NP, followed by loading on a support, which resulted in covalently linked thin films. The surface plasmon resonance displayed by the assemblies having inter-NP distances shorter than the NP size, shifted at longer wavelength. The electrochemical properties are different, as the redox current of 2-nm NP was more suppressed than 5-nm ones reflecting partial blockage electron transfer barrier, gold-sulfur binding were suspected to be influenced with the facets, corners, or edges of nanocrystals. The modifiable feature was important for further catalytic application.⁷⁰ Following the same preparation route, Au-Pt alloyed NP assembly cross-linked by 1,9-nonanedithiol were produced and applied for methanol electrooxidation.⁷¹ If controlling assembly in 2-D or 3-D has been achieved with success, the 1-D assembly is still a challenge. Nonetheless, the use of nonanedithiol produced size-controlled 1-D linear assemblies.⁷² The length and branches of these gold nanochains were tuned by varying the ratio of dithiols to Au NP, resulting in dimers, oligomers and branched linear shapes.

The use of aromatic compounds bearing bidentate or tridentate coordination sites as cross-linkers (1,4-phenylene diisocyanide, 4,4'-bis(diphenylphosphino)biphenyl, 1,3,5-tris([2,2':6',2''-terpyridin]-4'-ylethynyl)benzene) allows producing Pd NP networks.³⁵ The

resulting assemblies have shown better hydrogen storage capacities than isolated Pd NP. Also, the tetrakis(terpyridine) linker (Figure 1.10a) was used to interconnect Pd NP to well-organized self-assemblies as a result of the rigid tetrahedral core.³⁹

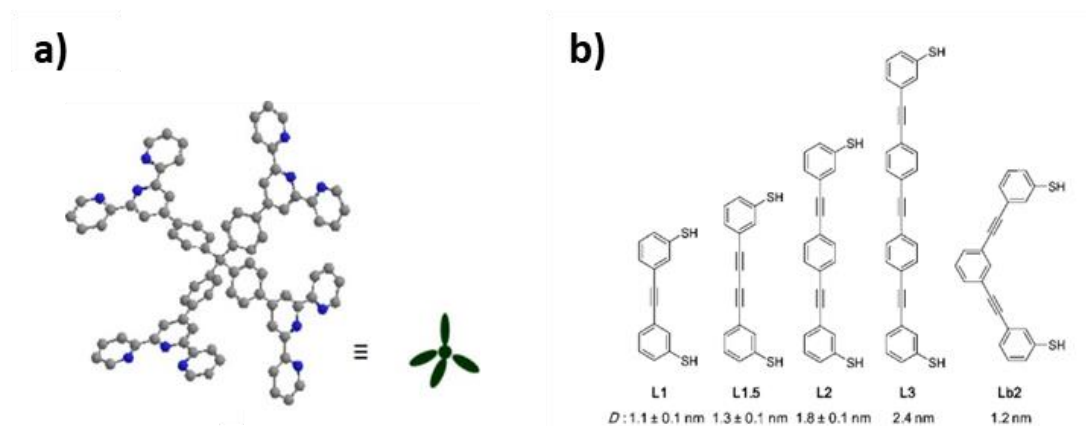


Figure 1.10 a) Structure of the tetra(terpyridine) linker used for Pd NP network synthesis. Reproduced with permission from ref.³⁹ b) Chemical structures of L_n ($n = 1, 1.5, 2, 3$) and L_{b2} . Reproduced with permission from ref.⁷⁴

Supra-spheres (80~320 nm) containing large amounts of metal NP, and involving more than two different kinds of metals (nearly monodisperse (5.5 nm) Au, Ag, Pd, or Pt NP stabilized by dodecylamine and didodecyldimethylammonium bromide) were produced from 1,8-octanedithiol.⁷³ These supra-spheres can be converted into a new material (*nanoporous metals*) by removing the organic ligands, extending the potential of metal NP assembly for material design.

M. Neouze *et al.* presented a new approach to build networks of Pt NP using both a carboxylic acid functional thiol ligand (mercaptopropionic acid) and an alcohol functional thiol ligand (mercaptoethanol) before introducing them into a TiO_2 matrix.⁷⁵ Pt NP stabilized by the two different ligands (Au-S coordination) were cross-linked. FTIR analyses have shown that the -COOH groups did not react with the -OH groups, and that the pending -COOH groups interact as $-COO^-$ groups with neighboring Pt NP. Furthermore, there were residual pending carboxylic acids of the Pt-Pt network that can further coordinate to the titanium centers of the TiO_2 matrix, ensuring stability to the coating film.

A work of M. Boterashvili *et al.* reports the use of different building blocks, single-crystalline and multiple-twinned Au NP and cross-linkers possessing two binding sites (pyridine-N-oxide

and/or tetrafluoro-iodoaromatics, ArF-I) (Figure 1.11) to control the aggregation of Au NP via halogen bonding.⁴⁰ The authors demonstrated that N-oxide moieties contribute more to the formation of organized Au NP networks, whereas the ArF-I moieties differ in bonding reactivity with different facets. The observed reactivity of the single-crystalline and multiple-twinned Au NP to assembly illustrates the importance of NP crystallinity to control the self-assembly degree, providing aspects to consider for designing material in future work.

Even though the assembly of Au NP with dithiol molecules has been investigated in detail, the production of ordered super-lattices is still a significant challenge. S. Nayak *et al.* found that using the one-phase route to produce self-assemblies, short-ranged *fcc* (face-centered cubic) crystals can be formed from the cross-linked network for specific dithiol linker-length and NP size.⁷⁵ The stability of the lattices was evaluated based on geometrical considerations and numerical simulations as a function of ligand length and number of connected nearest-neighbors, and a phase diagram of super-lattice formation was provided by the authors. The methods employed provide perspective in further exploration for well-crystallized lattices.

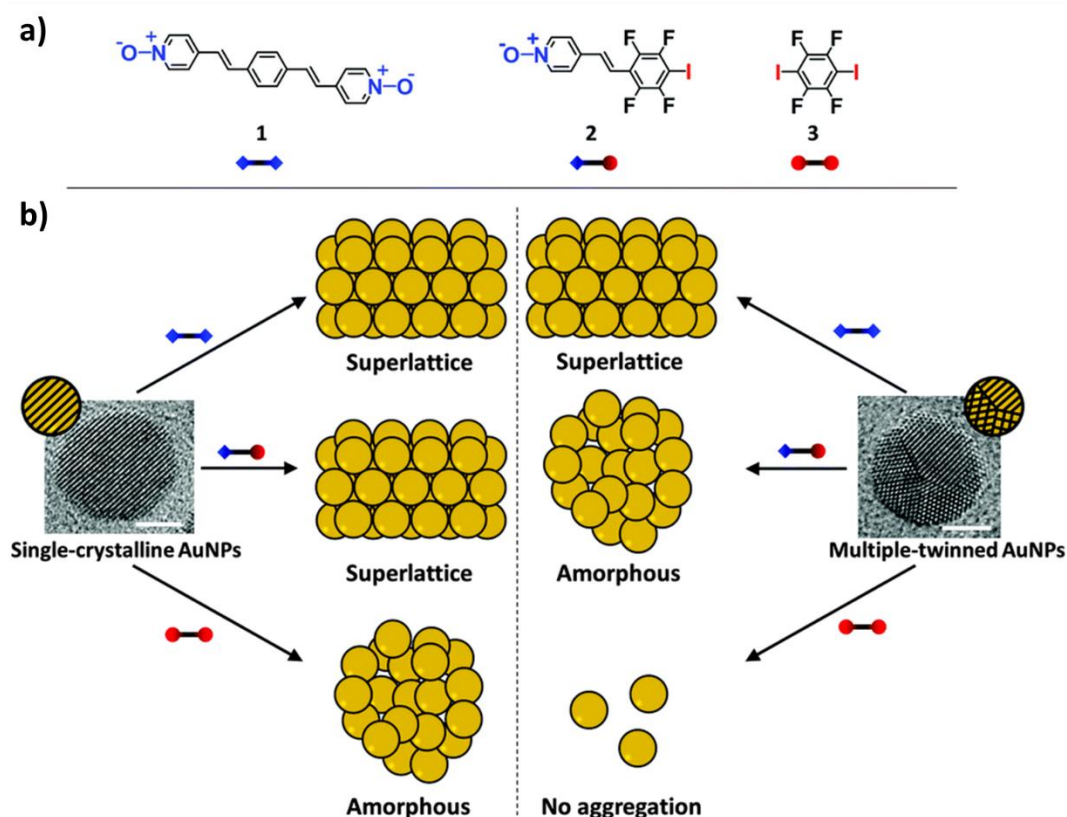


Figure 1.11 a) Molecular structures of cross-linkers **1-3**; and b) schematic representation of the reactions between Au NP and the cross-linkers (**1-3**). Reproduced with permission from ref.⁴⁰

Further management of Au NP assemblies was investigated, and an interesting electric device was constructed, consisting of an electric platform of nano-electrode-molecule-NP bridge, showing a significant improvement of reproducibility of electrical measurements (Figure 1.12).³⁶ The Au NP (5 nm) situated between the nano-electrode (19 nm) were connected with 1,8-octanedithiol where the outer thiol groups are protected by triphenylmethyl (ω -trityl), which lead to reproducible and stable metal-molecule bonds replacing the physisorbed metal-molecule junction. Correspondingly, the conductivity increased and the spread of the resistance histogram reduced by one order of magnitude, which demonstrated that the platform can be a potential method for characterization of Au NP networks and furthermore molecule levels current transport application.

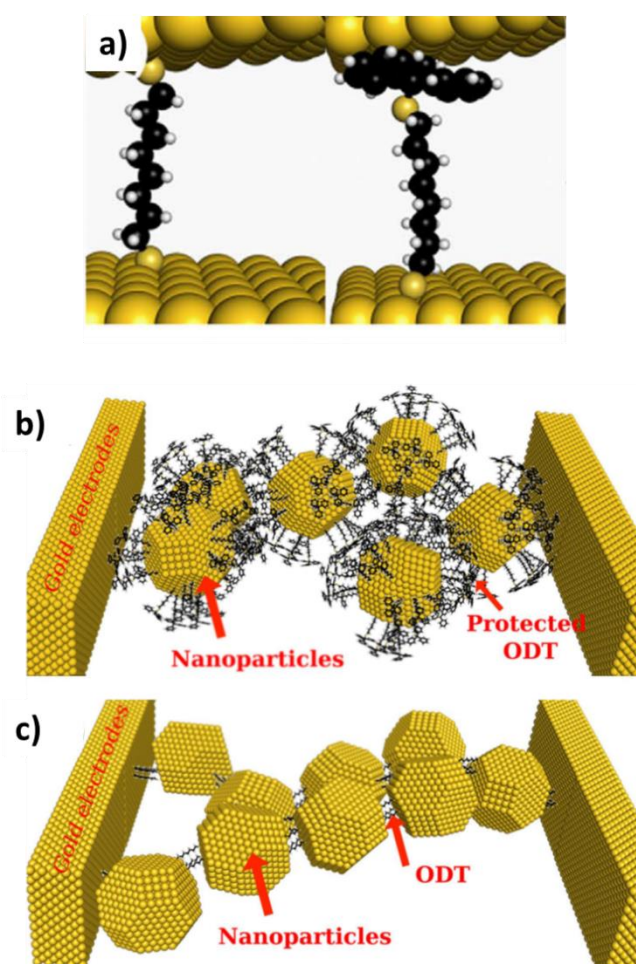


Figure 1.12 Schematic representation of a) 1,8-octanedithiol chemisorbed at two nearby gold surfaces and triphenylmethyl protected 1,8-octanedithiol chemisorbed at one end and physisorbed at other end; b) trapped ω -trityl protected 1,8-octanedithiolcoated (ODT) Au NP; and c) the junction after removal of

the trityl protective resulting in formation of chemisorbed junctions at both ends of 1,8-octanedithiol. Reproduced with permission from ref.³⁶

1.2.4 Langmuir-Blodgett (LB) method

The LB method makes use of the surface-pressure to initiate the NP cross-linking onto a substrate. One example reported by S. Chen uses 4,4'-thiobisbenzenethiol as bifunctional linker that facilitated cross-linking of mono-layer-protected Au NP.³⁷ 2-D NP networks were prepared by using the LB method, where neighboring NP were chemically bridged by the bifunctional linker at the air/water interface. The fluctuations of surface pressure were studied during the formation of the assembly, showing that high surface pressures help to activate crosslinking, which resulted in long-range ordered and robust NP networks. The typical surface plasmon band of Au NP redshifted by 30 nm, which was attributed to the electronic coupling interactions between neighboring NP. Ordered arrays of quantum dots can be produced by photo-oxidation to remove the organic part in the network.⁷⁶

1.2.5 Light triggered self-assemblies

Photoactive ligands have been used to create NP structures, which confers to the NP networks unique properties derived from the ligands in response to light stimulus. A light adjustable Au NP network was produced by using azobenzene thiol derivatives as inter-particle linkers. It was shown that the spacing between NP can be reversibly controlled by *trans-cis* isomerization of the azobenzene moiety induced by UV and visible light (Figure 1.13).⁷⁷ Analogously, another photoactive *trans*-ligand 4,4'-bis(11-mercaptoundecanoxy)azobenzene (ADT) containing a photo-switchable azobenzene unit, was used to assemble metal NP into assembly triggered by UV irradiation modified by light of different wavelengths.^{78,79} In that case, the self-assembly was irreversible for high ligand surface concentrations, resulting in NP organized into permanently cross-linked structures by dithiols.

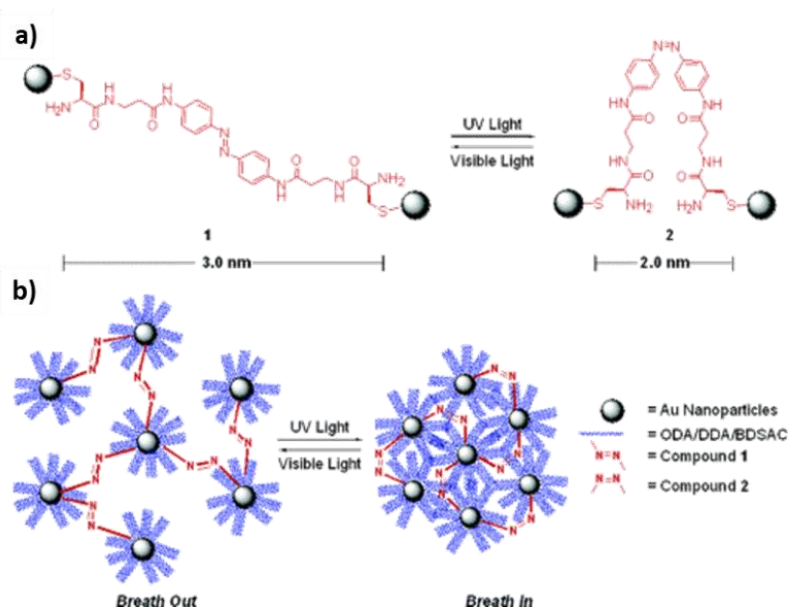


Figure 1.13 a) Scheme of photoactive linker molecule; and b) reversible tunable Au NP assembly. Reproduced with permission from ref.⁷⁷

1.2.6 Single step wet chemical synthesis

Besides the ligand exchange strategy, we can also mention a directed covalent assembly produced in one-step, in which the self-assembly process by linker ligand is constructed when the metal NP are growing without any other mono-capped ligand/stabilizer. As described by Serp *et al.*, C₆₆(COOH)₁₂ hexa-adduct can be used as a building block to construct 3-D networks *via* carboxylate bridges with very homogeneous and well crystallized sub-1.8 nm Ru NP, displaying a Ru NP-NP distance of 2.85 nm (Figure 1.14).⁴¹ Furthermore, IR, SSNMR and XPS point out that the substituted fullerene coordinates to the Ru NP *via* carboxylate groups, which was corroborated by Density Functional Theory(DFT) calculations.

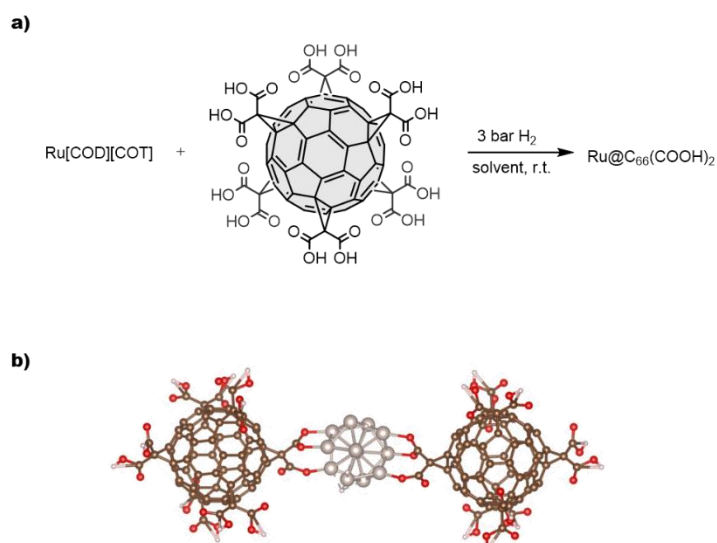


Figure 1.14 a) Synthesis of $C_{66}(\text{COOH})_{12}$ -mediated covalent assembly of Ru NP; and b) optimized structure of the $C_{66}(\text{COOH})_{12}$ -Ru₁₃- $C_{66}(\text{COOH})_{12}$ species by DFT. Reproduced with permission from ref.⁴¹

E V. Solovyeva *et al.* prepared Ag NP assemblies in a controllable way with diaminostilbene as linker for Surface Enhanced Raman Scattering (SERS) detection, with the intention that the well interlinked NP can form hot spots providing intensive SERS spectra.⁸⁰ Indeed, only interconnected Ag NP at sub- or monolayer surface coverage formed hot spots. The Ag aggregates obtained demonstrate a high SERS activity, suggesting that such substrates could be used for SERS detection of analytes at a single-molecule level.

In this single step method, the effect of the multidentate rigid ligands on the size of Au NP was also investigated with different length of aryl ethynyls dithiol molecules.⁷⁴ It was revealed that the size of the Au NP and the final structure as NP or assemblies are synergistically regulated by ligand length, ratio of ligand to metal and ligand coordination mode on the NP surface.

1.2.7 Novel strategies producing NP assemblies

Covalent organic frameworks (COFs) are porous materials with well-defined 2- or 3-dimensional structures using organic molecules as building blocks. COFs have been used as supports for metal NP with rather evenly distribution.⁸¹⁻⁸⁴ S. Lu *et al.* have produced Pt NP@COF hybrid material with well dispersed average NP using thioether-containing COF (Figure 1.15).⁸⁵ The strong anchoring groups inside the pores facilitate the binding of metal NP and COF, as supported to some extent by XPS characterization, which provide a potential pathway to get well-organized covalent NP assemblies by designing anchoring groups on COF.

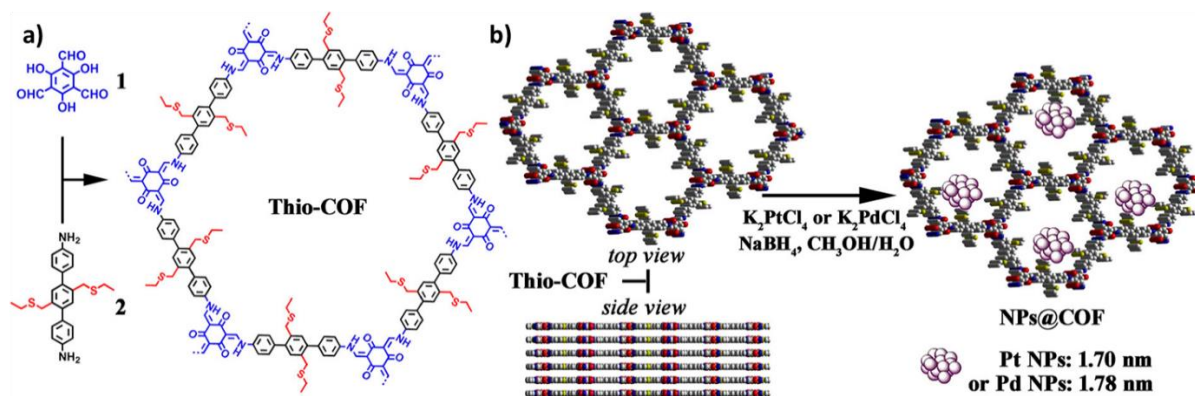


Figure 1.15 a) Synthesis of Thio-COF; and b) schematic representation of the synthesis of Thio-COF supported Pt NP@COF and Pd NP@COF. Reproduced with permission from ref.⁸⁵

The use of several length DNA sequences allowed also to produce assemblies of Au NP. Au NP stabilized by alkanethiol-capped oligonucleotides were linked into short-range and long-range ordered networks by complementary linker oligonucleotide (DNA) strands (Figure 1.16), in which the optical properties are affected by aggregate size as well as inter-particle distance.^{86,87}

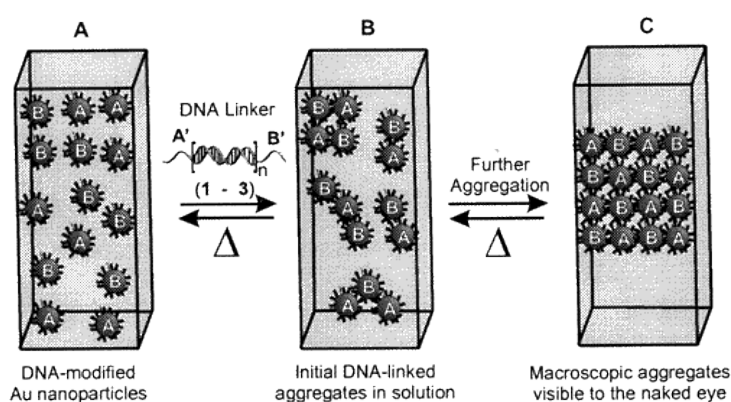


Figure 1.16 Scheme showing the DNA-based nanoparticle assembly strategy. Reproduced with permission from ref.⁸⁷

An interesting strategy to interconnect Pd clusters was proposed by U. Simon *et al.*⁸⁸ The 3-D network was built by insertion of the bifunctional linker molecules 4,4'-diamino-1,2-diphenylethane into Pd₅₆₁phen₃₆ clusters coordinated by the NH₂ groups. The three-dimensional arrangement of Pd₅₆₁phen₃₆O₂₀₀ clusters was deoxygenated by H₂ to Pd₅₆₁phen₃₆ clusters in a water–pyridine solution at room temperature with the formation of H₂O₂. The resulting material showed an increase of the charging energy from 0.02 eV to 0.05 eV and a decrease of the electrical capacitance between the clusters compared to dense aggregates before insertion of the linkers. This showed the control of the physical properties of cluster arrangements in chemical way is possible, and contributed to understanding of the structure–property relationship in the nanomaterials.

From this analysis of the literature dealing with direct cross-linking methods, it is clear that the direct covalent bonding of metal NP into assemblies is highly impacted by the choice of the

multidentate ligand. The chain length, the binding group and middle backbone tune the properties of the final material at different levels. Deep insight into the self-assembly process were obtained at both the nano and atomic levels by a vast panel of characterization techniques, as well as theoretical calculations. A large proportion of work involved Au and Ag, particularly because of their potential applications in optics, sensors and electronics. Less work has been devoted to other noble metals of interest for catalysis, such as Pt, Pd, or Ru, meaning that additional efforts are needed to develop reliable methods to produce covalent networks of NP with these metals.

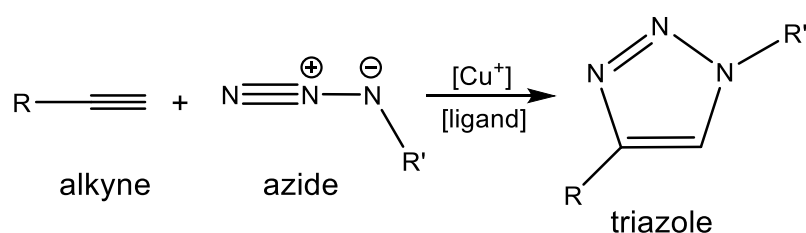
1.3 Indirect cross-linking synthesis methods

Besides the direct cross-linking methods that often involved the use of ditopic ligands to directly link metal NP, several indirect methods have also been reported. These methods use the reaction between NP stabilized by specific ligands, which allow a coupling reaction between them to create the metal NP network. Various reactions have been described so far to connect ligand-capped NP (click chemistry, Diels Alder reaction, nucleophilic substitution, among others) either under thermal- or photo-activation. Table 1.3 shows representative examples obtained with these methods.

1.3.1 Click chemistry

Click chemistry, a group of chemical reactions with favorable reaction rate and orthogonality, is an efficient way for NP modification,⁸⁹ including their assembly. Trials with NP have been reported based on click chemistry, including copper-catalyzed cycloaddition, strain-promoted azide-alkyne cycloaddition,⁹⁰ and inverse-demand Diels-Alder reaction.⁹¹

Metallic NP can be modified by azide- and/or alkyne-functional groups, and then assembled into organized arrays through the basic Cu(I)-catalyzed azide/alkyne-‘click’ chemistry approach (Scheme 1.3).



Scheme 1.3 Azide–alkyne 1,3-dipolar cycloaddition reaction.

Table 1.3 Representative examples of metal NP networks produced by the indirect cross-linking methods.

Metal	Ligand/reactants	Method	Size (nm)	Inter-NP distance (nm) ^a	Ref.
Au	1-Azide-1-undecane thiol Dialkyne derivative/CuSO ₄	Click chemistry	2	2	92
Au	Octadentate thioethers	Acetylene oxidative coupling	1.1	0.8 to 2.5	93
Au	Norbornenethiols Ru catalyst	Ring-opening metathesis polymerization	4.3	7	94
Au	Terminal amines on polyethylene glycol (NP) Thiolated amine (nanorods) Traut's reagent	Dithiol coupling	2.5 and 1.8 (NP) 50x5 (nanorods)	0.9 and 1.6	95
CdSe	2-aminoethanethiol Glutaraldehyde	Condensation	2.7	3.2 to 7.6	96
Ag	Polyvinyl alcohol Dicarboxylic acids	Esterification	10.4	0.93 (oxalic acid) 1.74 (sebacic acid) 0.98 (hydroquinone)	97
Pt	Aluminum-organic-stabilizer Bifunctional alcohols	Protonolytic cross-linking reaction	1.2	1.23 (4,4'-dihydroxybiphenyl)	98

^a The distance between NP is the edge-edge distance if not otherwise noted.

Two procedures have been followed, either the use of a mixture of NP (one population being azide-functionalized and the other one alkyne-functionalized), or the reaction of azide- or alkyne-functionalized NP with a dialkyne or a diazide (tri- and tetra-azides have also been used), respectively. The Huisgen 1,3-cycloaddition reaction between azide and ethynyl groups has been employed to obtain assemblies (nanochains) of Au nanorods.⁹⁹ Using a 1:1 mixture of the nanorods stabilized by azidoalkane- and alkyne-thiols allows the formation of chainlike assemblies. The preferred end-to-end assembly of the Au nanorods could be attributed to the preferential ligand displacement at the (111) faces at the end of the nanorods. In the case of Au NP (2 nm), Au NP networks with an inter-particle distance of 2 nm (which fits with the molecular length of 1.8 nm for the rigid azobenzene unit) were obtained by click reactions of azide-functionalized Au NP and dialkyne-terminated functional molecules (Figure 1.17a-c).⁹²

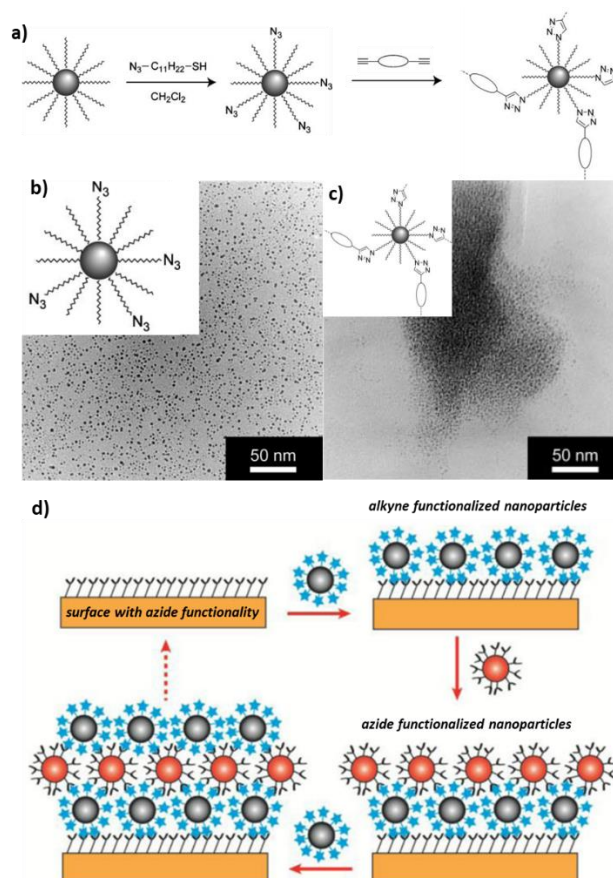


Figure 1.17 a) Typical procedure to obtain Au NP network using click chemistry; b) TEM micrograph of azide-functionalized Au NP; and c) TEM micrograph of the Au NP network

prepared by the click reaction. Reproduced with permission from ref.⁹² d) Basic scheme of NP multilayers deposition. Reproduced with permission from ref.¹⁰⁶

A similar procedure (use of azide-tagged Au NP and a dialkyne cross-linker) was also followed with Au NP of *ca.* 18 nm diameter.¹⁰⁰ The aggregation rate was found to depend on Cu concentration, but in all cases, aggregation was clearly visible within 20 min from the beginning of the reaction. The reaction of gold NP (1.3 nm) stabilized by a single dendritic thioether ligand comprising an alkyne function with di-, tri- and tetra-azide linker molecules has also been reported.¹⁰¹ In that case, dimers, trimers and tetramers could be selectively produced after the click reaction with the corresponding linker. All measured inter-NP distances were significantly shorter than the calculated maximum possible spacing. This behavior was due to the fact that the NP rearrange in a more folded geometry. Mixtures of gold NP that have azide- and alkyne-terminated groups have also been used to produce covalent networks.¹⁰²⁻¹⁰⁴ This click reaction was also used for the covalent bonding of functionalized Au NP onto surfaces,¹⁰⁵ or to produce multi-layers of covalently bonded Au NP onto surfaces (Figure 17d).^{106,107} Interestingly, it was possible to use the click cycloaddition to prepare assemblies of Au nanorods and Ag NP.¹⁰⁸ For this reaction, new disulfides with azide (for Ag NP) or alkyne (for Au nanorods) terminations were used.

Covalent assemblies of other metals than gold have also been prepared by click chemistry, such as Fe NP,¹⁰⁹ or core-shell CdSe/ZnS quantum dots.¹¹⁰ The case of iron NP is particularly interesting since it highlights the limit of the method in the case of NP that can suffer oxidation. The authors stated that the solutions for avoiding oxidation when assembling such NP are: i) extremely efficient click reactions to avoid surface oxidation; ii) the solvents excluding of substantial source of oxygen; and iii) thermal or photochemical methods requiring no catalysts without addition of water-based solvents. Finally, it is worth mentioning that 1,3-dipolar cycloaddition reactions, such as those forming 1,2,3-triazoles can be reversed, but the necessary conditions make the potential use of the reverse reactions rather unrealistic at this point.¹¹¹

1.3.2 Covalent coupling reactions

In addition to click reactions, diverse organic transformations have been used to connect metal NP into 1-D, 2-D or 3-D assemblies. For instance, an amide-coupling reaction was used to organize Au NP into linear chains.¹¹² The originality of this work lies in

the functionalization of the polar singularities that must form when a curved NP surface is coated with ordered monolayers, such as a phase-separated mixture of ligands (1-nonanethiol and 4-methylbenzenethiol) coated leading to point defects, that is, sites at which the ligands assume a nonequilibrium tilt angle and are more prone to be replaced in place-exchange reactions. This approach made the NP able to bind along specific directions as the same the atoms and molecules do. Gold NP coated with a binary mixture of 1-nonanethiol and 4-methylbenzenethiol were first produced, and their reaction with 1,6-diaminohexane produces linear chains of Au NP. These important results suggest that polar singularities react faster than other defects in the ligand shell.

Fiałkowski *et al.* used a naphthalene dianhydride derivative as cross-linking agent that forms amide bonds with the aminothiolate ligand that stabilized Au NP (5.6 nm) under biphasic conditions.¹¹³ In this system, the thiol group is coordinated to Au NP surface, and the unbound amino group has the capability of binding protons in a reversible way so that an equilibrium between the protonated and non-protonated amino groups is established depending on the pH. To carry out the cross-linking reaction, the Au NP have to be brought close enough the ones to the others. To do so, the authors transferred the Au NP from the bulk aqueous phase to the oil-water interface that takes place only at specific (basic) pH levels. This technique allows the formation of freestanding monolayer of covalently bonded Au NP at the water/oil interface.

Azo (-N=N-) or amido (CONH) linkages were also used to covalently attach Au and CdS NP (Figure 1.18 a).¹¹⁴ These reactions were carried out under very dilute conditions to control the assembly and avoid the polymerization. Indeed, at high ligand concentrations, the NP formed a network of chains for both amido and azo functionalized NP. Gold NP (1.2 nm)-CdSe-ZnS quantum dots (5.6, 6.8, and 7.8 nm) assemblies were formed *via* covalent coupling of carboxy-functionalized Au NP, which were activated with N-hydroxysuccinimide, with amine-functionalized quantum dots.¹¹⁵ Esterification reactions were used for the covalent binding of OH-terminated (polyvinylalcohol, PVA) Ag NP (10.4 nm) by means of dicarboxylic acid compounds (oxalic, 1-(+)-tartaric, *d*-glucaric acid and sebacic acid) with a defined molecular length.⁹⁷ PVA plays a key role in this reaction because it acts as the reducing agent of Ag^I, the surface stabilizer of the resulting NP, and as a mild Lewis acid that can exhibit oxophilic character towards the carbonyl group, which forms the basis for the catalysis

of the esterification reaction. As expected, the increase in the molecular length of the diacids results in larger inter-NP spacing (Figure 1.19).

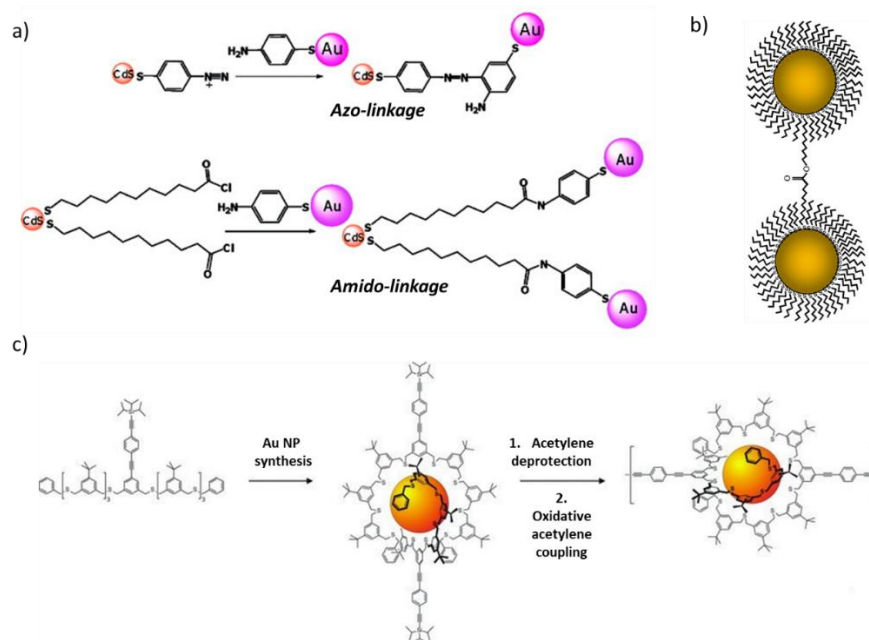


Figure 1.18 a) Azo and amido linkage. Reproduced with permission from ref.¹¹⁴ b) Ester coupling. Reproduced with permission from ref.¹¹⁶ c) Oxidative acetylene coupling for the assembly of Au NP. Reproduced with permission from ref.⁹³

Ester coupling (Figure 1.18b) of monolayer-protected Au NP (11-mercaptopundecanoic acid exchanged and 11-mercaptopundecanol exchanged) was performed with ester coupling reagents such as 1,3-dicyclohexylcarbodiimide and 4-(dimethylamino)pyridine.¹¹⁶ Bifunctionalized Au NP (1.1 nm) with two octadentate thioether ligands were covalently interlinked.⁹³ Since two ligands are required to cover the NP surface, exactly two triisopropylsilyl-protected acetylenes are present as functional groups on the periphery of the NP, allowing their interlinking by wet chemistry. The method involved: i) deprotection of the acetylene by fluoride ions, and ii) rapid (15 min.) oxidative acetylene coupling (Figure 1.18c). In these assemblies, the inter-particle distance (0.8-2.5 nm) that depends on the length of the oligo(phenyleneethynyl) rod is generally shorter than the linker length (1.4-2.7 nm), which may indicate a tangential arrangement of the rigid-rod structure at the Au NP's surface. Dithiol coupling was reported as an efficient method to covalently link Au NP and Au nanorods (length = 50

nm, width 5 nm).⁹⁵ In this work, the control of the position, spacing and quantity of Au NP per nanorod is achieved through anisotropic surface functionalization of the nanorod with aminoalkylthiols of increasing size. The dithiol coupling was performed by converting the terminal amines on polyethylene glycol stabilized Au NP into thiols through an excess of a cyclic thioimidate (Traut's reagent, 2-iminothiolane HCl). Au NP (4.3 nm) functionalized with norbornenethiol were cross-linked by ring-opening metathesis polymerization (ROMP) with the use of a water-soluble pyridine-substituted ruthenium benzylidene catalyst.⁹⁴ The ROMP of the Au NP can be achieved across a large area, stitching the NP crystalline domains together.

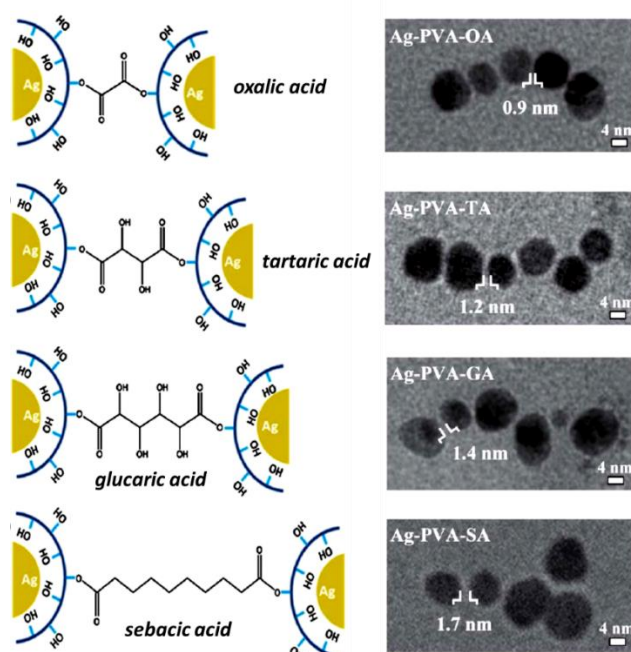


Figure 1.19 Assembly of Ag NP mediated by different dicarboxylic acid compounds, and the resulting TEM images, where the average inter-particle distances are indicated. Reproduced with permission from ref.⁹⁷

The amination reaction of fullerene C_{60} with amine-functionalized Au NP¹¹⁷ was used to produce C_{60} -linked Au NP.¹¹⁸ For the assembly, the C_{60} were reacted with 4-aminothiophenoxide/hexanethiolate-protected Au NP. Although resulting from a non-covalent bond, the affinity of streptavidin for biotin results in the strongest biological interaction known, and it was used for the end-to-end linkages of gold nanorods.¹¹⁹ A protonolytic cross-linking reaction of aluminum-organic-stabilized Pt NP with bifunctional alcohols (ethylene glycol, hydroquinone, 4,4'-dihydroxybiphenyl and

1,10-decanediol) was reported by Bönemann *et al.* to build 3-D Pt NP networks.⁹⁸ The key feature of this synthesis is the formation of an organometallic colloidal protecting shell around the Pt NP. When reacting with bifunctional ligands, a cross-linking of the NP occurs that leads to the formation of a 3-D NP network (Figure 1.20). The control of the inter-particle distance can be achieved by varying the length of the spacer molecules (Table 1.3).

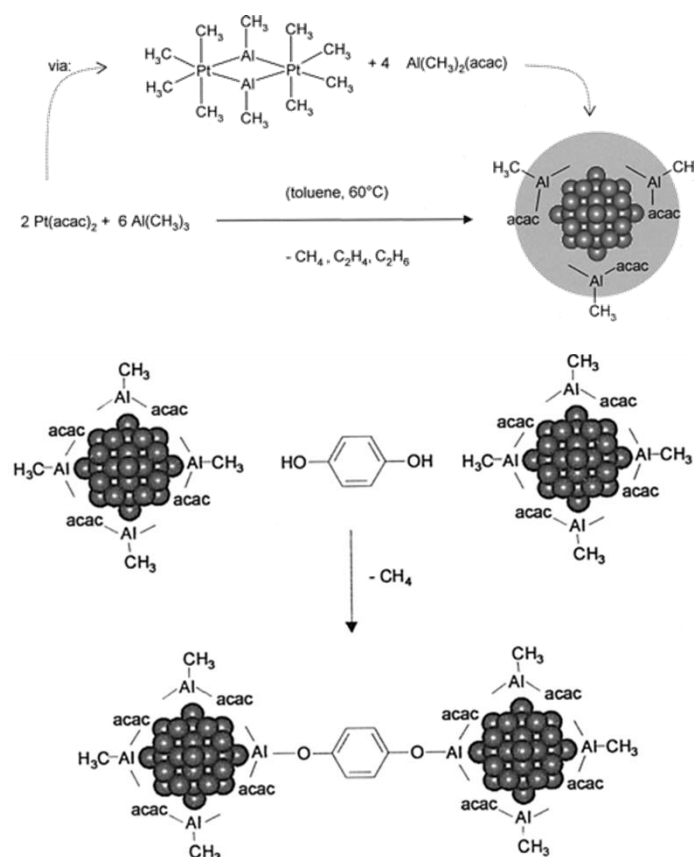


Figure 1.20 Assembly of Pt NP by a protonolytic cross-linking reaction. Reproduced with permission from ref.⁹⁸

Finally, CdSe NP (2.7 nm) modified with 2-aminoethanethiol were cross-linked with the homobifunctional amine-reactive crosslinker glutaraldehyde.⁹⁶

1.3.3 Biomolecular coupling

Compared to linking using small organic ligands, linking with biomolecules including DNA, supramolecular protein,¹²⁰ and viruses offers several advantages. First, these biomolecules can be tailored to specific lengths by varying the number of base pairs. Additionally, the double-helix structure of DNA is rigid, enabling the precise control

of the spacing. Thus, NP network engineering with DNA gives independent control of three important design parameters (NP size, lattice parameters, and crystallographic symmetry) by separating the identity of the particle from the variables that control its assembly.¹²¹ One- two- and three-dimensional assemblies of metal NP have been obtained with DNA. There is a very rich literature^{21,129-131} on that subject and we will discuss in this section only some basic principles of NP assembly with DNA. This kind of superstructures have found applications in (electro)catalysis.¹²²⁻¹²⁸ In some studies, the DNA has been removed through calcination to generate robust porous NP superlattices.¹²²

Although many modifications are available for functionalizing DNA to bind to metals,¹³² it can be used as a ligand by itself.¹³³ The coordination chemistry of DNA nucleosides (2'-deoxyadenosine (dA), 2'-deoxycytidine (dC), 2'-deoxyguanosine (dG) and 2'-deoxythymidine (dT)) on Au NP was probed by surface-enhanced Raman spectroscopy, and is shown in Figure 1.21.¹³⁴ The coordination of the dA, dC, and dG is stronger to Au NP than that of dT. The dA mainly binds to Au NP *via* an N atom of the imidazole ring, and the NH₂ group participates in the coordination process. The dC binds to the Au surface *via* an N atom of the pyrimidine ring with a partial contribution from the oxygen of C=O group. The coordination of dG implicates both the N atom and the oxygen of the C=O group of the pyrimidine ring. Only dT binds to the Au surfaces *via* the oxygen of C=O group of the pyrimidine ring.

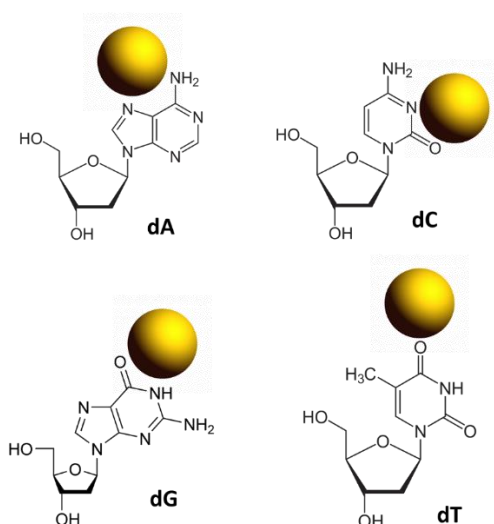
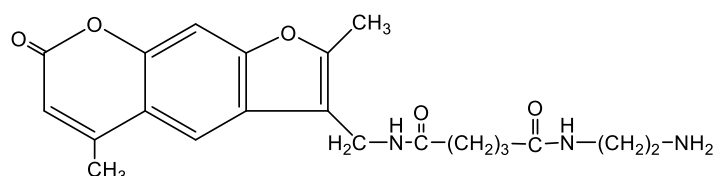


Figure 1.21 Proposed structures of DNA nucleosides bound to the gold NP. Reproduced with permission from ref.¹³⁴

1-D DNA@Au NP wires were generated by a method involving the incorporation of functionalized Au NP (psoralen-modified NP, 3 nm, Scheme 1.4) into double-stranded DNA, followed by the photochemical cross-linking (12 Watt UV lamp, $\lambda > 360$ nm) of the ligand to the DNA matrix.¹³⁵ Under these conditions, psoralen undergoes a photoinduced $2\pi+2\pi$ cycloaddition with the thymine residues, a process that leads to the covalent attachment of the ligand to the DNA.



Scheme 1.4 Molecule of psoralen.

Labean *et al.* used a combination of self-assembly, molecular recognition, and templating, which rely on an oligonucleotide covalently bounded to a high-affinity gold-binding peptide. After integration of the peptide-coupled DNA into a self-assembling superstructure, the templated peptides recognize and bind the Au NP.¹³⁶ Gold NP, 1.4 nm in diameter, were assembled in 2-D arrays with inter-particle spacing of 4 and 64 nm. The NP formed precisely integrated components, which are covalently bonded to the DNA scaffolding. For the self-assembly of NP into 3-D lattices, the use of DNA origami frames (rigid and with well-defined geometries) has emerged as a promising solution.¹³⁷ Thus, the 3-D organization of Au NP (7, 10 and 15 nm) spatially arranged in pre-determined positions was reported using DNA origami octahedron as frame.¹³⁸ The octahedra can serve as programmable inter-particle linkers. 2-D organization of Au NP has also been reported by wrapping them in flower-shaped DNA origami structures.¹³⁹

1.3.4 Metal ion-induced nanoparticle assembly

Modification of NP with metal coordination compounds^{140,141} offers the possibility of their assembly on surfaces,¹⁴² but also to create metal NP networks with coordination bonds connecting the NP. This strategy has been mainly employed for the development of plasmon-based colorimetric sensors for ultrasensitive molecular diagnostics.¹⁴³ The technic is based on controlled aggregation of NP in the presence of metal ions. Aggregation of metal NP in the presence of analyte ions changes the color of the NP solution. Covalent assemblies have been built with various families of ligands such as carboxylates, amino acids (Figure 1.22a), amine ligands, or crown ethers (Figure 1.22b). While most of the reports rely on irreversible metal NP assemblies, attempts to use metal ions as chemical stimuli for reversible assembly has also been reported (see section 2.3.2). Table 1.4 shows representative examples obtained with various ligands and cations for gold, Ni₂P and CdTe NP.

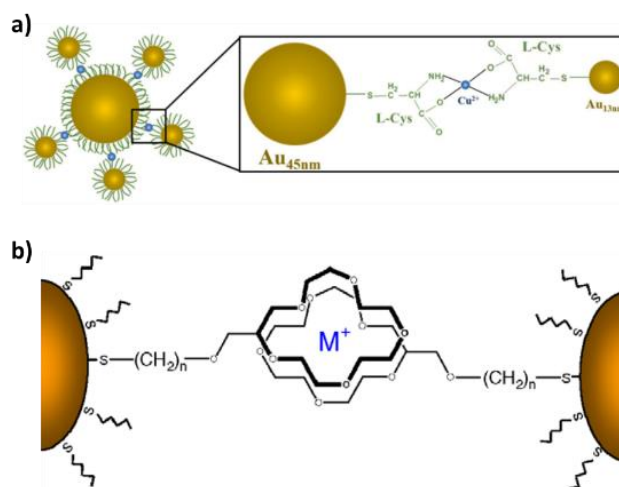
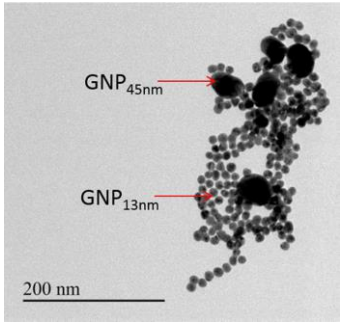
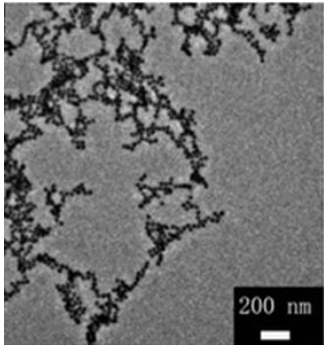
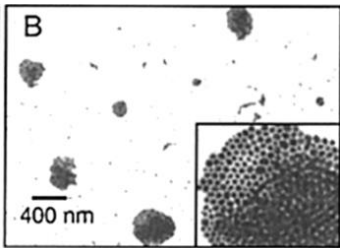
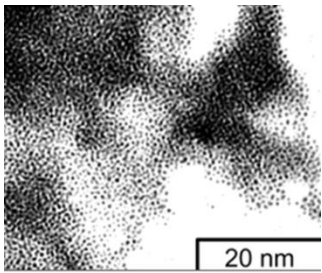
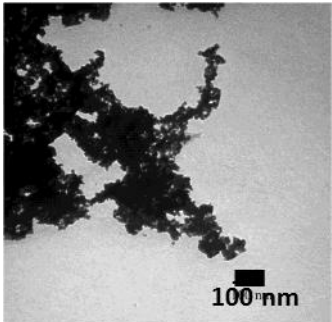
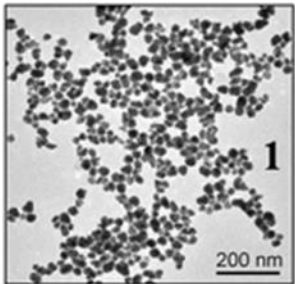
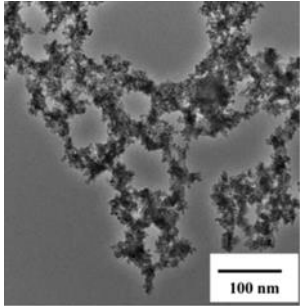


Figure 1.22 a) Illustration of Cu²⁺ mediated assembly of Au NP after self-assembly. Reproduced with permission from ref.¹⁴⁴ b) Crown ether-metal ion-crown ether “sandwich” inter-particle bridge. Reproduced with permission from ref.¹⁴⁵

Table 1.4 Representative examples of NP networks obtained with various ligands and cations for gold, Ni₂P and CdTe NP.

Metal	Ligand	Metal ion	NP diameter	TEM	Ref.
-------	--------	-----------	-------------	-----	------

Au ^{a)}	Amino acid (L-cysteine)	Cu ^{II}	13 and 15 nm		144
Au	Amino acid (L-cysteine)	Hg ²⁺ , Cd ²⁺ , Fe ³⁺ , Pb ²⁺ , Al ³⁺ , Cu ²⁺ , and Cr ³⁺	30 nm	-	146
Au ^{b)}	Amino acid (histidine)	Fe ³⁺	18 nm		147
Au	Crown ether	K ⁺ , Na ⁺ , and Ag ⁺	Au ₁₄₀ , Au ₂₂₀ , and Au ₃₀₉	-	145
Au	Crown ether	K ⁺ and Na ⁺	18 nm	-	148
Au ^{c)}	Crown ether	K ⁺	18 nm		149
Au	Pyridine	Cu ²⁺	2 nm	-	150
Au ^{d)}	Terpyridine	Fe ²⁺ , Zn ²⁺ , Cu ⁺ , Ag ⁺	2 nm		151
Au	Phenanthroline	Os ³⁺	90 nm	-	152

Au ^{e)}	1,10-Phenanthroline	Li ⁺	4 and 32 nm		153
Au	Carboxylate (citrate)	Na ⁺ , Ca ²⁺ , Mg ²⁺ , Cu ²⁺ , Zn ²⁺ , and Al ³⁺	18 nm	-	154
Au ^{e)}	Carboxylate (valine)	Pb ²⁺	22 to 75 nm		155
Au	Carboxylate	Pb ²⁺ , Hg ²⁺ , and Cd ²⁺	14 nm	-	156
Au	Bishydroxamate	Zr ⁴⁺	6 nm	-	157
Ni ₂ P ^{f)}	Carboxylate	Ni ²⁺	8-9 nm		158
CdTe	Mercaptomethyltetrazole	Cd ²⁺	3 nm	-	159

a) Figure reproduced with permission from ref. ¹⁴⁴. b) Figure reproduced with permission from ref. ¹⁴⁷. c) Figure reproduced with permission from ref. ¹⁴⁹. d) Figure reproduced with permission from ref. ¹⁵¹. e) Figure reproduced with permission from ref. ¹⁵³. f) Figure reproduced with permission from ref. ¹⁵⁵.
 Figure reproduced with permission from ref. ¹⁴⁸.

1.3.5 Light-induced self-assembly of irreversible nanoparticle networks

The use of externally manipulated light offers excellent spatial and temporal control for the signal molecule's activation, degradation, or creation/disruption of a self-assembled system.¹⁶⁰ Light-induced self-assembly (LISA) of metal NP have thus found applications into the biomedical field. Although most of the work deals with non-covalent interactions (mainly NP aggregation due to changes in electrostatic stabilization), some works have reported the irreversible and photo-chemically activated formation of NP networks (Figure 1.23).

Zhao and co-workers reported that UV light irradiation triggers Au NP that are respectively functionalized with *o*-nitrobenzyl alcohol and benzylamine to proceed with a covalent ligation reaction.¹⁶¹ Indeed, *o*-nitrobenzyl alcohol and benzylamine can undergo an aldehyde-amine ligation-like coupling reaction under UV irradiation. This reaction leads to the assembly of Au NP into anisotropic 1-D arrays in aqueous solution *via* indazolone linkages (Figure 1.23 a). The formation of anisotropic 1-D Au NP arrays was attributed to the anisotropic electrostatic repulsions during the self-assembling of the charged NP.

The self-assembly of Au NP or nanorods into chains and networks was also achieved by a UV light in the presence of silver ions; taking advantage of the easy photoreduction property of silver nitrate.¹⁶⁴

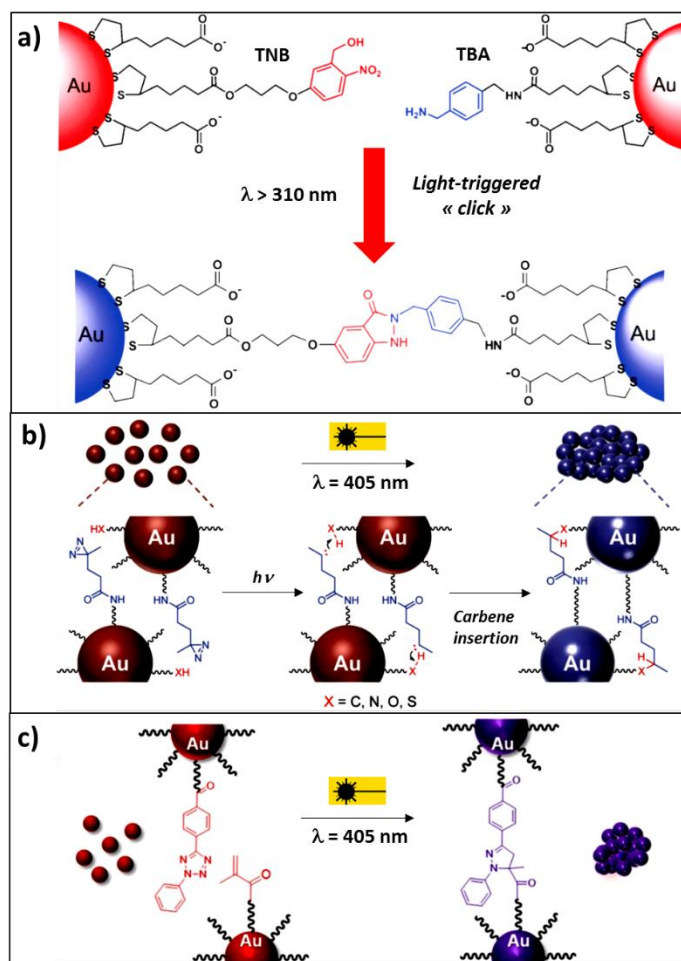
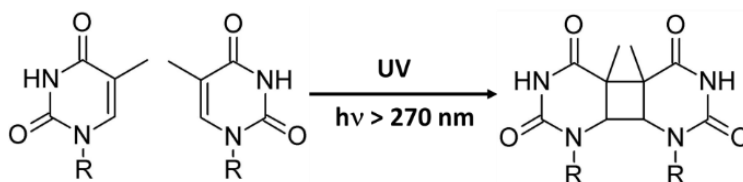


Figure 1.23 Some examples of light-induced self-assembly of irreversible NP networks: a) UV light irradiation promotes the irreversible assembly of Au NP functionalized with o-nitrobenzyl alcohol and benzylamine. Reproduced with permission from ref.¹⁶¹ b) Photolabile Au NP covalently cross-linkable with a 405 nm laser irradiation *via* a diazirine terminal group of PEG5000 ligands. Reproduced with permission from ref.¹⁶² c) Photolabile Au NP covalently cross-linkable with a 405 nm laser irradiation between 2,5-diphenyltetrazole and methacrylic groups attached PEG5000 ligands. Reproduced with permission from ref.¹⁶³

The authors used cetyl trimethylammonium bromide (CTAB) (or citrate)-capped gold NP or nanorods that were mixed with the required concentrations of silver salt (the assembly was strongly dependent on the AgNO_3 content), and then exposed to a 365 nm UV lamp. From High-Resolution Transmission Electron Microscopy (HRTEM) and XPS analyses the authors proposed the formation of a core-shell Ag@Au structure (near identical lattice constants of Au (0.408 Å) and Ag (0.409 Å)) on both NP and nanorods. The group of Shi studied the light-triggered covalent coupling of gold

NP.^{162,163} They have shown that Au NP (20 nm) stabilized with photolabile diazirine terminal group of PEG5000 (polyethyleneglycol, Mn = 5000) can be covalently crosslinked upon 405 nm laser irradiation (Figure 1.23b).¹⁶² The surface diazirine group is first transformed into a carbene species upon laser excitation at 405 nm. Then, the resulting reactive carbene moieties formed covalent bonds with ligands of adjacent Au NP through C-C, C-H, O-H, and X-H (X = heteroatom) insertions, leading to the formation of covalently cross-linked Au NP aggregates. It is worth mentioning that the water susceptibility of the diazirine group will suppress the photo-crosslinking efficiency. Another strategy reported by the same group involves the use of photolabile Au NP that can effectively form cross-linked aggregates upon 405 nm laser irradiation, between 2,5-diphenyltetrazole and methacrylic groups attached to PEG5000 on the surfaces of 23 nm Au NP (Figure 1.23c).¹⁶³ The tetrazole groups on the NP surface firstly undergo a facile cyclo-reversion reaction upon laser excitation at 405 nm to release N₂ and to generate nitrile imine dipoles that cyclize spontaneously with the alkene moieties of methacrylic acid on the adjacent Au NP to afford pyrazoline cycloadducts, leading to the formation of covalently cross-linked NP networks. The degree of connection of the Au NP was strongly dependent on the exposure time. Finally, the photochemical assembly of 3.2 nm Au NP was also realized by using the photodimerization of thymine (Scheme 1.5).¹⁶⁵ In that work, mixtures of 11,11'-dithiobis(undecanoic acid 2-(thymine-1-yl)ethyl ester) and 1-dodecanethiol were used as stabilizers to suppress intramolecular photoreaction of the thymine units on the Au NP surface.



Scheme 1.5 Photodimerization of thymine units.

The diameter of the obtained NP aggregates became larger with increasing photo-irradiation time: 0.15, 0.25, and 1 μm were observed after 6, 22, and 72 h, respectively. In a study dealing with 2 and 7 nm Au NP, Ralston *et al.* have shown that the photo-

dimerization of thymine, which is a [2+2] cycloaddition reaction, was mainly influenced by particle size, surface charge, and solvent type.^{166,167}

1.4 Stimuli-responsive reversible covalent networks of nanoparticles

Stimuli-responsive nanomaterials have been particularly studied for biomedical applications, such as drug delivery.¹⁶⁸ In the field of catalysis with metal NP, artificial switchable catalysts usually rely on non-covalent interactions between NP that induce aggregation.¹⁶⁹⁻¹⁷¹ Higher activity is achieved when the NP are homogeneously distributed in the reaction medium, while it is lowered after aggregation. Association of metallic NP with stimuli-responsive gels/polymers is another strategy, for which catalytic performances can be modified by organizing and confining metal NP.^{172,173} Diverse stimuli have successfully been used to direct reversible NP covalent networks.¹⁷⁴ They can be classified as chemical stimuli (dynamic covalent chemistry,¹⁷⁵ metal ions) and physical (mainly light).

1.4.1 Dynamic covalent chemistry

Dynamic covalent chemistry usually relates to chemical reactions carried out reversibly under conditions of equilibrium control, which are employed by chemists to make complex supramolecular assemblies from discrete molecular building blocks.¹⁷⁶

Borsley and Kay have demonstrated that gold NP can be covalently and reversibly assembled using boronate ester chemistry (Figure 1.24) to form covalent bonds with 1,2-dihydroxybenzenes (catechols).¹⁷⁷ After the addition of different ditopic catechols in the presence of N-methylmorpholine, the aggregation of NP occurs and leads to an insoluble material. Indeed, boronic acids react with various dihydroxy compounds to yield boronate esters in the presence of Lewis bases. Treating the resulting precipitate with a monofunctional catechol, makes it possible to break the covalent bonds between NP and form free NP in solution. This phenomenon is nevertheless slow (5 days for aggregation and 42 days for disaggregation). Qu *et al.* also took advantage of the reversibility of boron chemistry to produce Au NP networks that are composed of covalent and readily reversible spiroborate diester linkages.¹⁷⁸ Au NP stabilized with thioctic amides terminated by D-lactose (D-Lac) were cross-linked with borate ions by forming dynamic-covalent spiroborates between the *cis*-vicinal diol sites of D-Lac under alkaline conditions. In the presence of external chemical stimulus, such as *cis*-

vicinal diols that compete for bonding with the borate, the spiroborate linkages between the Au NP can be broken. TEM micrographs of the initial D-Lac stabilized Au NP and of their assembly and disassembly are shown on Figure 1.24 c-e.

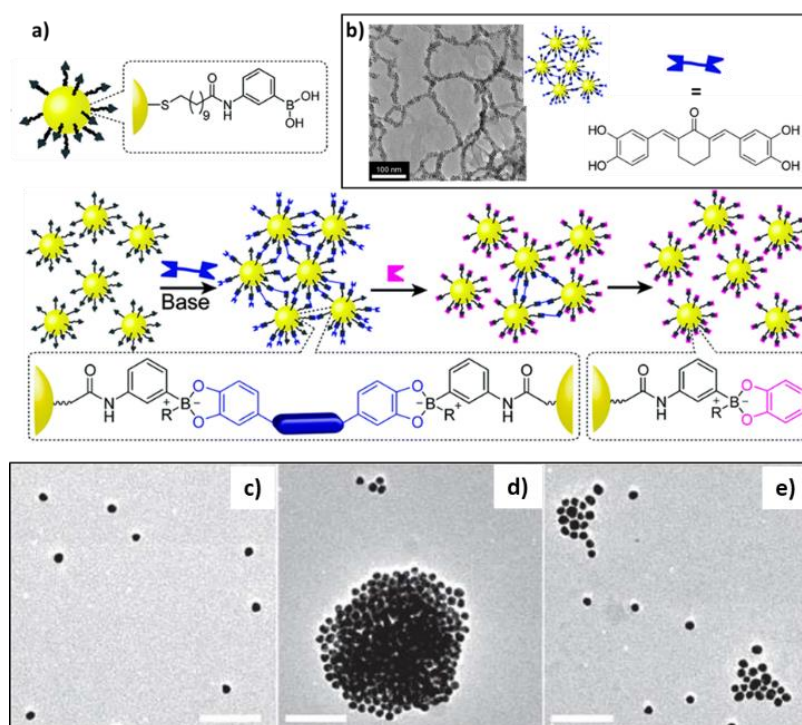


Figure 1.24. a) Schematic representation of boronate ester-driven dynamic covalent Au NP assembly and disassembly on sequential addition of a bifunctional linker and a monofunctional capping unit ($R = N$ -methylmorpholinium); and b) Chemical structures of a bifunctional catechol linker and representative TEM image of the assemblies formed on treating Au NP with the linker. Reproduced with permission from ref.¹⁷⁷ c) TEM image of D-Lac-Au NP; d) TEM images of the assembly of D-Lac-Au NP; and e) TEM images of the disassembly of D-Lac-Au NP. Scale bar: 100 nm. Reproduced with permission from ref.¹⁷⁸

The thermally reversible Diels-Alder reaction between furan and maleimides has been also investigated to connect and disconnect Au NP (Figure 1.25a).⁹¹ Maleimide-modified monolayer-protected Au NP (2-Au) were produced from protected furan-maleimide NP (1-Au) *via* a thermally reversible Diels-Alder reaction. These maleimide-NP served as a general platform for a Diels-Alder reaction with furan modified Au NP (3-Au) to prepare 3D networks reversibly. A similar strategy was followed by Xia *et al.*, but in that case the reaction occurred through mild Diels-Alder

cross-linking between maleimide bearing oligo(p-phenylenevinylene)- OPV- and 2 nm furan functionalized Au NP (Au-f) as depicted in Figure 1.25b.¹⁷⁹

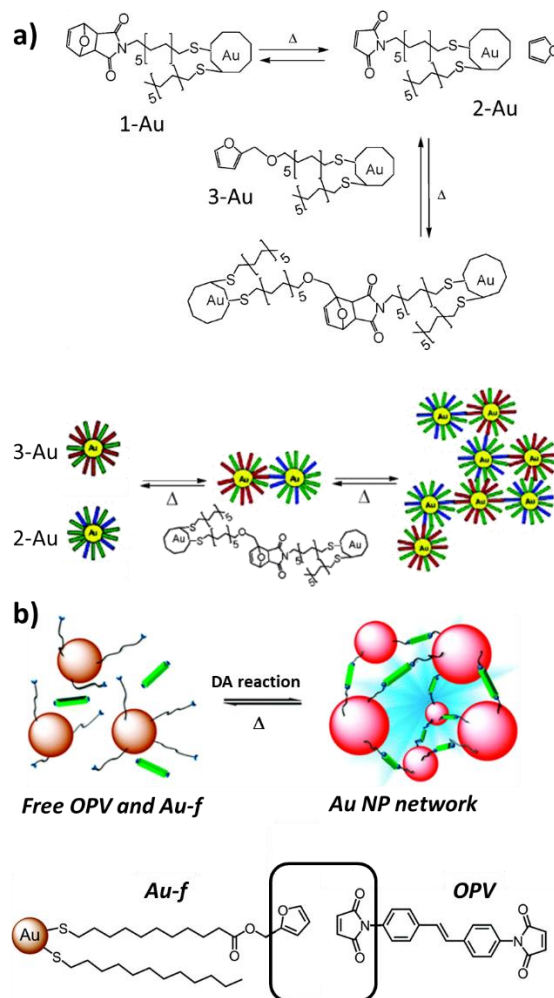


Figure 1.25 a) Forward and retro Diels-Alder reactions between maleimide-modified Au NP (2-Au) and furan-modified Au NP (3-Au). Reproduced with permission from ref.⁹¹ b) Representative illustration for the thermos-reversible Diels-Alder reaction leading to ordered Au NP self-assemblies. Reproduced with permission from ref.¹⁷⁹

1.4.2 Metal ions as chemical stimuli

The interest of assembling (plasmonic) NP using metal ions comes initially from the development of sensors to detect these often-toxic ions. The self-assembly, disassembly, and reassembly of Au nanorods mediated by $[(\text{disulfide-terminated tpy})_2\text{-M}^{\text{II}}]$ complexes ($\text{M} = \text{Fe}, \text{Cd}$) was investigated by Newcome *et al.*¹⁸⁰ The side faces of the Au nanorods are protected more strongly by the CTAB than their tips, where the ligand

exchange reaction occurs preferentially with the M^{II} -based cross-linker. Facile disassembly occurred upon NaOH addition for the Fe^{II} linker, and $Cd(NO_3)_2 \cdot 4H_2O$ addition for the Cd^{II} linker. The process was not reversible in the case of iron since subsequent Fe^{II} addition results in the chelation of Fe^{II} by two terpyridine units on the same nanorod. Reversibility was achieved using Cd^{II} , since cadmium complexes with terpyridine ligands are weaker and more labile.

Metal-ion-induced reversible self-assembly of carboxylated peptide-functionalized gold NP was reported by Mandal *et al.*¹⁸¹ The extent of assembly (2-D and 3-D structures) is dependent on the amount of metal ions (Pb^{II} , Cd^{II} , Cu^{II} , and Zn^{II}) present in aqueous solution. The process is completely reversible by addition of alkaline ethylenediaminetetraacetic acid (EDTA) solution (Figure 1.26).

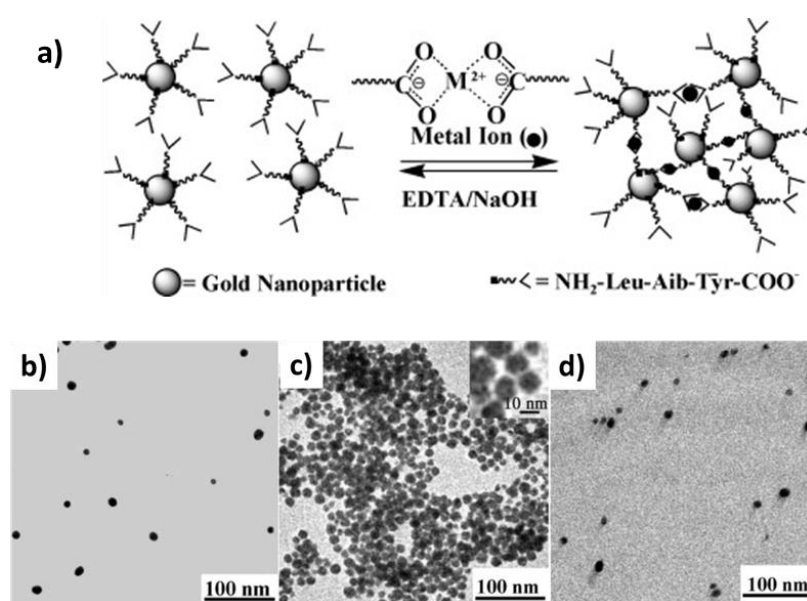


Figure 1.26 a) Metal-ion-induced reversible self-assembly of carboxylated peptide-functionalized Au NP; and TEM images of a NP suspension b) before addition of metal ions, c) 10 min after addition of Pb^{II} ions, and d) 5 min after addition of alkaline EDTA solution to the solution of Au NP containing Pb^{II} ions. Reproduced with permission from ref.¹⁸¹

In order to achieve the formation of stable NP aggregation, which is difficult to control by binding divalent metal ions with carboxylate ligands because of charge neutralization on the NP, Pillai *et al.* studied how the colloidal stability is affected by the incorporation of different amounts of thiols terminated with NMe_3^+ groups within

monolayers of COO⁻-terminated ligands (Figure 1.27).¹⁸² After addition of Pb^{II}, NP containing 80% of a COO⁻- and 20% of NMe₃⁺-terminated thiol formed aggregates. Including the NMe₃⁺ species within the protective coating was essential for reversing the self-assembly. The subsequently added NaOH sequestered Pb^{II} from NP aggregates, resulting in the disassembly. Without NMe₃⁺ species, Pb^{II} ions were bound too strongly and could not be removed using NaOH.

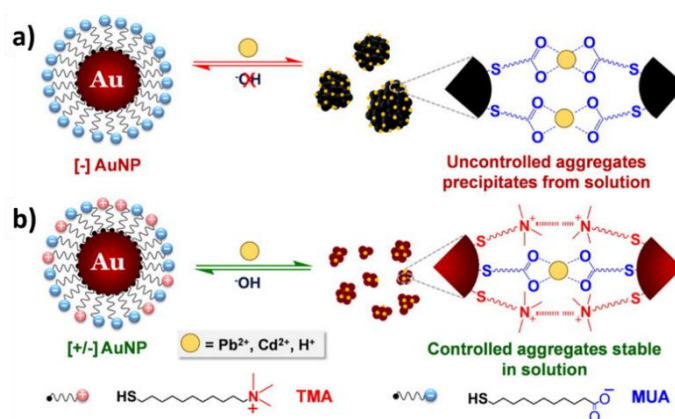
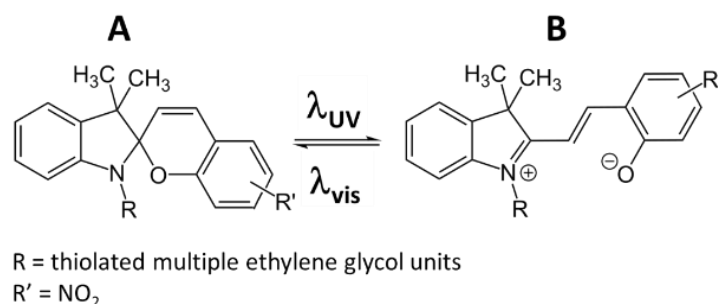


Figure 1.27 Concept of regulating inter-particle forces to achieve controlled aggregation in charged NP. The interactions of a) [-] and b) [+/-] AuNP with triggering ions resulting in the formation of unstable and stable AuNP-ion aggregates, respectively. The colloidal stability of [+/-] AuNP is retained in the aggregates due to the electrostatic repulsions experienced from the like charged head groups on adjacent NP. Reproduced with permission from ref.¹⁸²

The use of Au NP capped with a zwitterionic peptide (AuNP-(EK)₃) has allowed Surareungchai *et al.* to trap Ni^{II} ions.¹⁸³ Zwitterionic polypeptide-capped Au NP contain alternate carboxylic/amine groups. The zwitterionic peptide can function dually by being able to trap metal ions and maintain colloidal stability. The authors have demonstrated that the aggregation mechanism is due to the interactions between the -NH₂ group of the peptide and Ni^{II}, and the aggregation process is reversible because the pH controls the protonation/deprotonation of the -COOH/-NH₂ groups, and therefore the ligand affinity. Spiropyran-terminated alkanethiols were used to stabilize gold NP.¹⁸⁴ Under visible light, the spiropyran (photoswitchable organic molecules) exists in their nonplanar and closed form (A), which isomerized to the planar and open form (merocyanine, B) with UV light irradiation heterocyclic ring cleavage (Scheme

1.6). The open form has a phenolate group that can bind with Cu^{II} metal ions, and the chelated metal ions can be released by visible light irradiation.



Scheme 1.6 Spiropyran (A) to merocyanine (B).

Finally, other chemical stimuli can be investigated. Thus, in the case of covalent cross-linking of gold NP with dithiol molecules, which is normally considered to be an irreversible self-assembly process, it was recently shown that the process may be reversible by oxidizing the dithiolate linkers with ozone.¹⁸⁵ Ozone quantitatively oxidizes the dithiolate groups to weakly bound sulfonates, thereby damaging the cross-linking and freeing the NP to redisperse as charge-stabilized colloids. The process is repeatable by adding additional dithiol to reinitiate the assembly.

1.4.3 Dynamic covalent chemistry assisted by light as physical stimulus

The use of light-induced reactions as external stimuli offers rapid and precise spatial control in closed systems.¹⁸⁶ A simple way to render NP photoresponsive is to functionalize their surfaces with ligands terminated by light-switchable moieties, which can lead to light-induced reversible self-assembly (LIRSA). Photoreversible [2+2] photocycloaddition^{186,187} or reversible Diels-Alder reaction employing a diarylethene as the diene and a maleimide as the dienophile¹⁸⁸ have been used for exerting photocontrol over the connection and disconnection of dynamic covalent bonds.

The successful LIRSA of gold NP stabilized with coumarin ligands was reported by Zhan *et al.*¹⁸⁹ Due to the thiolated coumarin derivative, Au NP can be self-assembled by light irradiation at 365 nm *via* a [2+2] photocycloaddition, and the resulting purple NP network can be disassembled back to the initial deep red disperse state by a relatively short exposure to UV light, as shown in Figure 1.28 a. This LIRSA cycle was

repeated four times (Figure 1.28 b). A similar procedure was used by Lin *et al.* with amphiphilic star-like poly(acrylic acid)-block-poly(7-methylacryloyloxy-4-methylcoumarin) diblock copolymers.¹⁹⁰

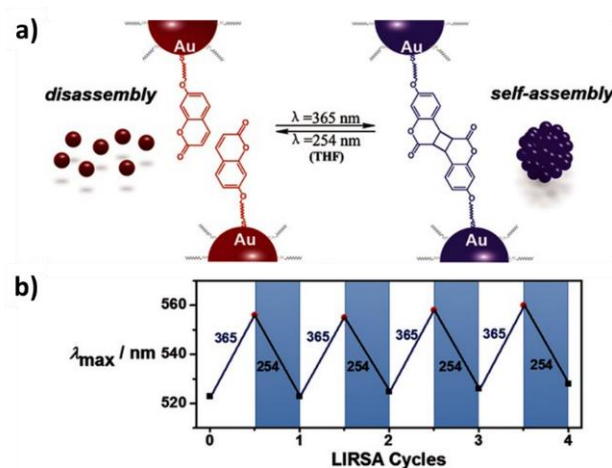


Figure 1.28 a) The LIRSA behavior of Au NP; and b) reversible change in the wavelength maximum during assembly of Au NP with illumination at $\lambda = 365 \text{ nm}$ (72 h) and disassembly at $\lambda = 254 \text{ nm}$ (60 min). Reproduced with permission from ref.¹⁸⁹

The use of 3-cyanovinylcarbazole as a photochemical switch to reversibly ligate gold NP assemblies using light was reported by Kanaras *et al.*¹⁹¹ In this work gold NP stabilized with oligonucleotides are hybridized under the appropriate conditions to form NP networks. The sequences used in this work are reported in Table 1.3. Each DNA sequence has a thiol-modification, a spacer part of 15 thymine bases and a complementarity region of 15 bases with carbazole modification. The oligonucleotide-coated NP contains a 3-cyanovinylcarbazole modification, which can react upon irradiation at $\lambda = 365 \text{ nm}$ with an adjacent thymine in the complementary strand *via* a [2+2] photocycloaddition, causing the formation of a cyclobutane (Figure 1.29). This photochemical process can be reversed upon irradiation with light at $\lambda = 312 \text{ nm}$.

All the indirect cross-linking methods we have seen up to now rely on the use of organic ligands to direct the NP assembly that act as inter-particle spacers. Thus, the NP interactions are mediated by these ligands, and their presence can be detrimental to electrical transport, inter-particle coupling, and thermal stability, properties of

importance for catalysis. Therefore, the synthesis of self-supported NP networks with direct inter-particle linkages (metallic and not covalent bonding) has also been investigated. Mono- and bimetallic NP were self-assembled using destabilizer *via* oxidation of the ligand leading to non-supported metal nanostructure.¹⁹²⁻¹⁹⁴

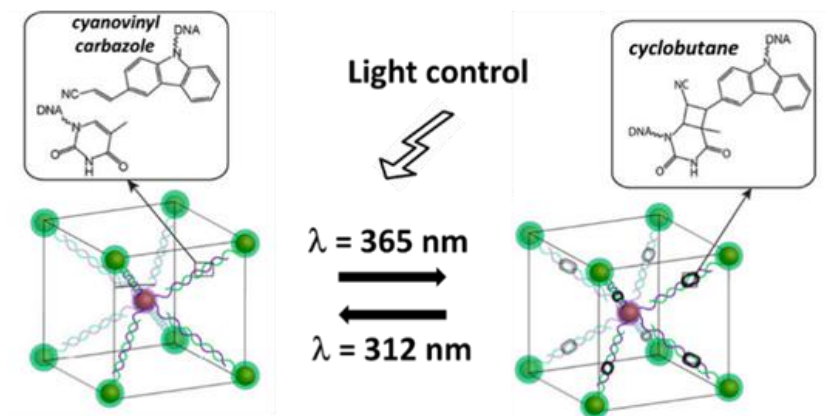


Figure 1.29 Reversible photochemical ligation of Au nanoparticle networks. Reproduced with permission from ref.¹⁹¹

1.5 Metal nanoparticle assemblies as catalysts

It has been shown that assemblies of metal NP can be beneficial for catalytic applications. For instance, FePt NP assembled on graphene were more active and robust than the same NP or commercial Pt NP deposited on a commercial carbon support for the oxygen reduction reaction.¹⁹⁵ Also, Ru nanochains produced by self-assembling of Ru NP (3.5 nm) were more efficient as CO oxidation catalyst than the respective isolated NP (3.5 nm) or 6 nm Ru NP.¹⁹⁶ The self-assembly of the Ru NP was accomplished by reacting the Ru NP seeds with cetyltrimethylammonium bromide in water, which allowed the authors to obtain interconnected networks of Ru NP, the length of which varies from a few tens of nanometers to the micron scale. Photoresponsive Au NP (6 nm), Fe₃O₄ NP (11 nm) and SiO₂ NP (17 nm) led to a reversible self-assembly by using the azobenzene anchored to their surface and light.¹⁹⁷ In this particular example, the cavity in between the NP was exploited to trap selectively some molecules, including enantiomeric compounds, and also to perform reactions more efficiently in the confined space. The acid-catalysed hydrolysis of an acetal or the anthracene dimerization reaction proceeded more efficiently compared to unconfined reactions (without the assemblies in the reaction media). The dimensions of the

confined space could be modulated by the NP size as well as by the lengths of the surface ligands. Even though those examples do not concern specifically covalently bound metal NP, they show that assemblies of metal NP can find applications as catalyst and that their assembly affects in a positive way their activity, robustness, or both. Covalent assemblies of metal NP have also been used as catalysts; however, a limited work on the field has been described up to now, and in many cases, the effect of the assemblies compared to non-aggregated NP has not been discussed. Nevertheless, some works have evidenced that the covalent assemblies of metal NP have a positive effect in the catalytic performances with respect to other catalytic systems.^{198,199} Also, the possibility to use dynamic (switchable) assemblies triggered by different stimuli (pH, light, temperature) has been exploited,^{169,170,173} which, in some cases are reversible, thus allowing one to turn on/off the catalytic reaction at will.¹⁹⁸

As stated in the previous sections, a large volume of scientific contributions in the field of covalent assemblies of metal NP is devoted to Au and at certain extent to Ag, mainly because of their possible applications in several fields such as optics, sensors and electronics.^{200,201} Au assembled NP have also found applications as catalysts, mainly in reduction^{52,126,198,202,203} and oxidation reactions.^{45,70,71,107,122,204} Even if predominately metal NP assemblies pivot around Au NP, other metals have been discussed and investigated. Metals such as Pd, Pt and Ru that possess excellent catalytic properties, have also been studied for the production of NP assemblies, which in turn can be used as catalysts.^{201,205} Some examples of the use of metal NP assemblies as catalyst in reduction, oxidation, water splitting as well as in other reactions are summarized in Tables 1.5, 1.6, and 1.7, respectively, and representative systems are discussed below.

1.5.1 Reduction reactions

Thin films of Au NP prepared by means of the LBL method using O-carboxymethyl chitosan as stabilizer, were used as catalysts for the reduction 4-nitrophenol by NaBH₄.⁵² The catalyst layers deposited on glass plates (10, 20 or 40 layers), and the size of the Au NP (5 nm or 10-20 nm) were crucial for the measured catalytic activity. The reaction rate was higher with catalysts with less layers (10 layers) and smaller NP size (5 nm), hence proportional to the available catalytic metal surface, related to the porosity and NP size. SEM analyses were performed after catalysis, showing that the most active catalyst was the less stable, but no leaching tests were reported.

Au NP inside DNA hydrogel were synthesised by reduction of HAuCl_4 adsorbed in the DNA hydrogel by NaBH_4 (Figure 1.30).¹²⁶ The material displayed a weak absorbance band at $\lambda = 550$ nm, with an average NP size of 2.8 ± 1.0 nm. Reduction of 4-nitrophenol to 4-aminophenol by NaBH_4 was monitored spectroscopically. The calculated rate constant was $1.5 \times 10^{-3} \text{ s}^{-1}$, which according to the authors was faster than the rates of analogous systems. However, no recycling test or characterization of the catalysts after catalysis was given to evaluate the robustness of this Au nanocomposite.

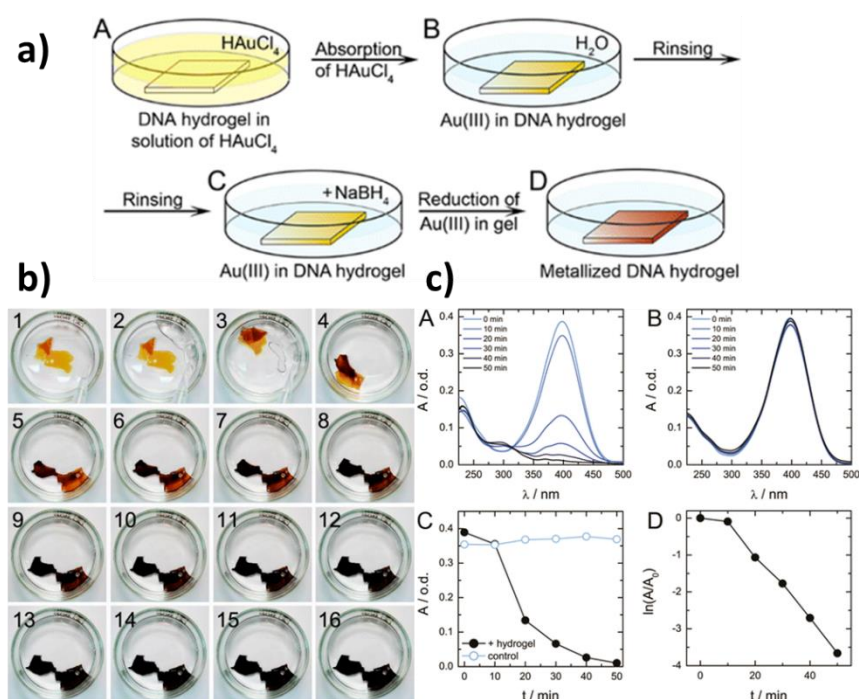


Figure 1.30 a) Protocol for preparation of hybrid hydrogel; b) reduction of HAuCl_4 in the DNA hydrogel. Photographic images of the DNA hydrogel film containing HAuCl_4 after addition of 5 mL of a solution of 10 mM NaBH_4 . The time interval between snapshots is 1.5 s; and c) (A and B) Time dependent changes in UV-vis absorbance spectra of 4-nitrophenol solution (0.2 mM) with (A) and without (B) added hybrid hydrogel (0.1 g) after addition of NaBH_4 (1 mM) in 1 mL of water solution, (C) time dependence of nitrophenol absorbance at $\lambda = 400$ nm in solution with (filled circles) and without (open circles) hybrid hydrogel, and (D) time dependence of the normalized nitrophenol absorbance at $\lambda = 400$ nm built in logarithmic coordinates. Reproduced with permission from ref.¹²⁸

Two-dimensional self-assembled AuCu NP were synthesised from CuCl_2 and HAuCl_4 in the presence of hexadecylamine by reduction with glucose, to give well-organized

assemblies into highly flexible ribbon-like structures.²⁰² The morphology and the self-assembly was highly dependent on the synthetic procedure. These assemblies were active in the photocatalytic degradation of 4-nitrophenol by NaBH₄, which was carried out with a 515 nm continuous laser.

1-D or 3-D assemblies of Au NP were synthesised in a controlled manner by adjusting the pH in the reduction of HAuCl₄ by α -cyclodextrin. While alkaline solutions promoted the synthesis of isolated Au NP, higher pH produced Au NP assemblies. 1-D assemblies could also be obtained by the host-guest interaction between α -cyclodextrin capped Au NP and toluene.²⁰⁶ The Au NP were tested as catalyst in the reduction of 4-nitrophenol by NaBH₄. An effect of the size on the catalytic performances was evidenced, which was mainly attributed to the fact that smaller NP have a larger catalytically active metallic surface, but the effect of the assembly was not studied. The α -cyclodextrin was also used to create Au/Fe₃O₄ assemblies, which were used as reduction catalyst of methylene blue with NaBH₄.²⁰³ The assemblies were synthesised by mixing oleic acid-decorated Fe₃O₄ NP with α -cyclodextrin-decorated Au NP thanks to the host-guest binding of oleic acid and α -cyclodextrin. The synthesised bimetallic structures spontaneously assembled into spherical architectures in water by controlling several parameters: a high ratio and small size of α -cyclodextrin-decorated Au NP allowed to produce the assembly. The nanocomposite was catalytically active for the reduction of methylene blue, and due to the presence of Fe₃O₄ NP, it was easily recovered and reused up to seven times.

Stimuli - responsive NP assemblies of Au and surface modified TiO₂ display a reversible dynamic self-assembly, by the reversible covalent bond due to Schiff base formation, responding to an acid/base stimulus.¹⁹⁸ Water-soluble, ammonium-modified TiO₂ NP (TiO₂-NH₂ NP) and aldehyde-modified Au NP (Au-CHO NP) did not form the corresponding Schiff base as the amine groups are protonated in water. The increase of the pH to 11 led to the deprotonation of the ammonium groups on the TiO₂ and in consequence, to the efficient formation of the Schiff base and the assembly of both NP, TiO₂-NH₂ and Au-CHO NP. Under basic conditions the catalyst that was effectively connected was more efficient for the photocatalytic degradation of methylene blue than the unassembled system under neutral conditions. Furthermore, the addition of the macrocycle cucurbit[6]uril (CB[6]) under acid conditions, led to a noncovalent self-assembly of TiO₂-NH₂ and Au-CHO NP, which in turn behaved differently in the

photocatalytic degradation reaction. Due to the high aggregation of the NP in this case, the catalyst was almost inactive (Figure 1.31). The control of the pH leads to an artificial switchable photocatalyst, where the three described different states of the catalyst had remarkably different photocatalytic performances. The authors pointed out that these differences are the result of the control of the electron-transfer efficiency between Au and TiO₂ NP (controlled by the covalent dynamic assembly), and the accessibility of the catalytic active surface (noncovalent self-assembly).

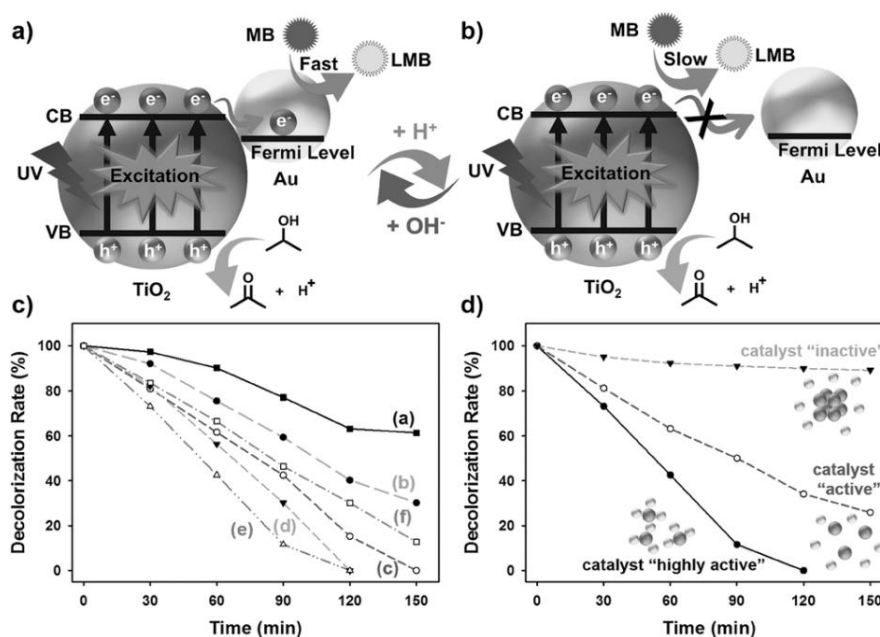


Figure 1.31 a, b) The pH-switching photocatalytic mechanism of the dynamic covalent heteroassembly of Au-CHO and TiO₂-NH₂ NP; c) photocatalytic decolorization of methylene blue (MB) curves of the Au-TiO₂ complexed in basic conditions with different amounts of Au) curNP: a) 0; b) 20; c) 40; d) 100; e) 160; f) 220 μL; d) photocatalytic decolorization of the tri-stable system under different pH conditions. Reproduced with permission from ref.¹⁹⁸

Ru NP assemblies displaying a short range order were obtained with the use of a hexakis fullerene C₆₀ adduct.⁴¹ The C₆₆(COOH)₁₂ multitopic ligand bearing -COOH anchoring groups, robustly coordinated to the Ru NP surfaces, the high symmetry of which giving the possibility to create a 3-D assembly. Ru@C₆₆(COOH)₁₂ assemblies were active in the hydrogenation of nitrobenzene, and TEM analysis performed after catalysis have shown that the 3-D assembly is maintained. However, the lack of porosity of the

assembly induces a lower catalytic activity, when compared to other Ru based systems, which is due to the poor accessibility to the Ru NP surface.

Pd NP embedded in a COF structure were successfully used as catalyst for the reduction of 4-nitrophenol with NaBH_4 .⁸⁴ Pd NP encapsulated in a sacrificial MOF, were used to create a COF in a second step reaction, which coated the Pd/MOF species. The subsequent selective etching of the MOF allowed encapsulation of multiple Pd NP inside the cavities of the COF. The reduction of 4-nitrophenol was monitored by UV-vis absorption spectroscopy, the constant rate calculated to be 0.41 min^{-1} . The catalytic performance of this catalyst was compared to other Pd NP systems, which evidenced the superior catalytic activity of the encapsulated Pd NP, and an effect of the shell thickness of the COF. The catalyst was characterised by microscopy after catalysis, which revealed no change in the Pd NP systems. Filtration and recycling tests (up to 4 cycles), together with the characterisation after catalysis suggested that Pd NP are effectively protected from aggregation and leaching by the COF shell. The successful synthesis of a thiol-modified COF allowed the synthesis of Pd or Pt NP within the pores.⁸⁵ K_2PtCl_4 or K_2PdCl_4 were first embedded in the thiol-modified COF and successively, the metallic salts were reduced with NaBH_4 . Using this straightforward procedure ultra-small NP (<2 nm) of both metals were confined in the COF structure. Pt NP were successfully used as catalyst in the reduction of 4-nitrophenol by NaBH_4 . The catalyst was reused six times, displaying up to 90% of conversion in each cycle. TEM image shows that the recycled catalyst does not undergo aggregation. Similarly, Pd NP within the thiol-modified COF were used as catalyst in the Suzuki-Miyaura coupling reaction. Excellent catalytic activities were also observed. The catalytic performances were compared with Pd NP and with the $[\text{PdCl}_2(\text{PPh}_3)_2]$ complex, evidencing the positive effect of the encapsulation, as lower activities were obtained with these latter systems. The catalyst exhibited excellent stability and recyclability under the catalytic reaction conditions, as evidenced by TEM analyses and recycling tests (up to five cycles).

In another example, chain-like aggregates of NiWO_4 were used as catalyst in the reduction of ferricyanide to ferrocyanide in the presence of $\text{Na}_2\text{S}_2\text{O}_3$ under light.¹²⁷

Table 1.5 Reduction reactions catalysed by NP assemblies

Metal	Ligand	Method	Reaction	Ref.
Au	O-Carboxymethyl Chitosan	LBL	Reduction of 4-nitrophenol by NaBH ₄	52
Au	DNA cross-linked hydrogel	DNA-assisted	Reduction of 4-nitrophenol by NaBH ₄	126
AuCu	Hexadecyl amine	One-phase	Photocatalytic reduction of 4-nitrophenol by NaBH ₄	202
Au	α -cyclodextrin	Indirect cross-linking	Reduction of 4-nitrophenol by NaBH ₄	206
Au/Fe ₃ O ₄	Oleic acid and α -cyclodextrin	Indirect cross-linking	Reduction of methylene blue by NaBH ₄	203
Au/TiO ₂	Amine and aldehyde compounds	Dynamic self-assembly	Photocatalytic reduction of methylene blue	198
Ru	C ₆₆ (COOH) ₁₂	One-phase	Hydrogenation of nitrobenzene by H ₂	41
Pd	COF	Two-phase	Reduction of 4-nitrophenol by NaBH ₄	84
Pt	Thio-COF	One-phase	Reduction of 4-nitrophenol by NaBH ₄	85
Pt	DNA	One-phase	Reduction of nitroarenes by NaBH ₄	124
NiWO ₄	DNA	One-phase	K ₃ [Fe(CN) ₆] to K ₄ [Fe(CN) ₆] in the presence of Na ₂ S ₂ O ₃ under UV-light	127
AuPt	Peptide-SWCNT	One-phase	Electrocatalytic oxygen reduction	123
Au	Thiol	LBL	Electrocatalytic oxygen reduction	45

The electrocatalytic oxygen reduction was used to confirm the controlled arrangement of AuPt NP assemblies.¹²³ Peptide coated single-walled carbon nanotubes (SWCNT) were prepared, to further accommodate AuPt NP, synthesised by reduction of HAuCl_4 and PtCl_6 with NaBH_4 in the presence of several peptide coated-SWCNT supports. The peptide coated SWCNT supports connect efficiently the conducting SWCNT with the electrocatalytically active NP. Engineering the peptide allowed the efficient control of the distance between the bimetallic NP, creating controlled assemblies. The electrochemical performances were governed by the size and inter-particle distance, which was further endorsed by theoretical calculations.

1.5.2 Oxidation reactions

A three-step process was used to synthesize catalytically active superlattices of Au NP, which consisted of: i) adsorption of citrate-capped Au NP on thiol-DNA, followed by the formation of body-centred cubic (*bcc*) superlattices by addition of different DNA linker strands, ii) silica embedding of the Au NP DNA superlattices, and iii) calcination in air for 2h at 350 °C (Figure 1.32).¹²² This procedure gave rise to the production of robust porous structures containing arranged Au NP, which maintained the *bcc* superlattice structures. The Au NP were active in the aerobic oxidation of 4-hydroxybenzyl alcohol, while DNA-functionalized Au NP (unsupported) as well as the uncalcined superlattice Au NP were inactive, pointing out the importance of the ligand and porosity. Nevertheless, the recycling test showed almost not catalytic activity, which was attributed by the authors to the poisoning of the catalyst by the products of the catalytic reaction.

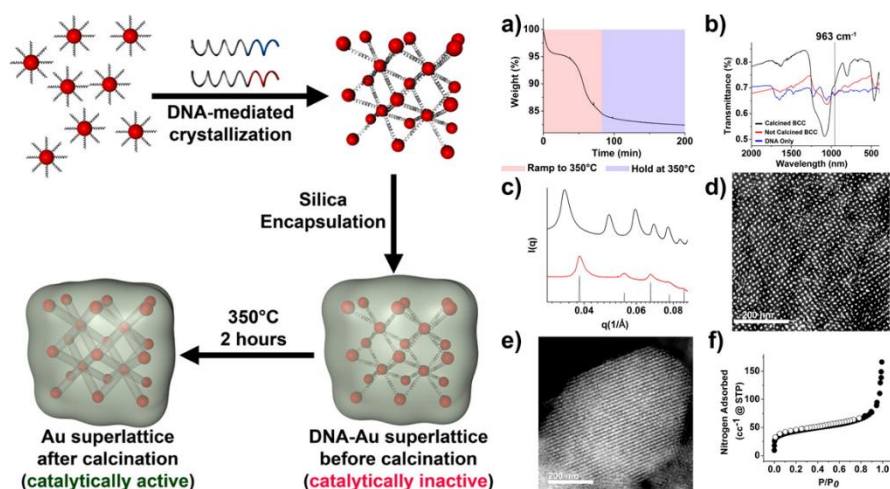


Figure 1.32 Left) Schematic representation of the synthesis of DNA-AuNP superlattices; and right) a) TGA trace of silica-embedded DNA-AuNP superlattices; b) FTIR spectrum of pure DNA only (blue), superlattices before calcination (red), and superlattices after calcination (black); c) SAXS data of the as-synthesized solution-phase *bcc* superlattices (black) compared to the silica-embedded lattices after calcinations (red). Theoretical scattering from a perfect *bcc* lattice is shown in gray; d,e) TEM images of silica-encapsulated superlattices after calcination at 350 °C for 2 h; f) Nitrogen adsorption (filled circles)/desorption (hollow circles) isotherms of calcined nanoparticle superlattices. Reproduced with permission from ref.¹²²

ZnWO₄ NP chain-like assemblies¹²⁸ were synthesised similarly to the chain-like aggregates of NiWO₄¹²⁷ described by the same group. ZnWO₄ NP assemblies were prepared by reaction of Zn(NO₃)₂·6H₂O salt with Na₂WO₄·2H₂O in DNA by microwave heating. NP size and chain lengths were controlled by tuning the reaction parameters. ZnWO₄ NP assemblies were active in benzyl alcohol oxidation using H₂O₂ as oxidizing agent. The catalyst was recycled 5 times with a slight decrease of the activity.

Thiolate-encapsulated gold NP assembled as thin-films on electrodes were efficient catalysts for the electrooxidation of CO.⁷⁰ Decanethiolate was used to produce 2 and 5 nm Au NP on glassy carbon electrodes by cross-linking with 1,9-nonanedithiol. The 2 nm Au NP are more active for CO oxidation than the 5 nm Au NP. The same authors further studied the 2 nm Au assembled NP, by investigating the effect of the number of layers deposited (up to 20) on different supports (glassy carbon and carbon black), in the electrooxidation of CO, MeOH and, electroreduction of oxygen.⁴⁵ Similarly, AuPt NP were used as electrocatalyst for MeOH oxidation.⁷¹

Azide- and alkyne-terminated groups have been used to produce covalent networks by click chemistry and LBL, allowing the production of assemblies of Au NP onto several surfaces (Figure 1.33).¹⁰⁷ Alkyne-functionalized substrates (titania, silica, tin oxide, glass, stainless steel substrates) were immersed in a 3.5 wt% solution of azide-functionalized NP in THF for 12 h, and then immersed in an aqueous solution of copper sulphate and ascorbic acid for another 6 h to catalyse the click reaction. To produce multilayers, the Au NP assembly was subsequently soaked in an alkyne-functionalized NP suspension as many times as required. The authors point out that the growth rate of the monolayer was inversely proportional to the size of the NP and the density of the

particles depended on the solvent, as well as on the substrate, being higher on TiO₂. Cyclic voltammetry profiles (up to 150 cycles) performed during methanol electro-oxidation with the Au NP monolayers on silica, titania, ITO and stainless steel substrates in electrolyte solution (0.1 M NaOH + 2.5 M MeOH) have confirmed the high stability of the catalytic systems. The same catalytic systems have been also tested in water splitting and photocatalytic degradation of Rhodamine B dye.

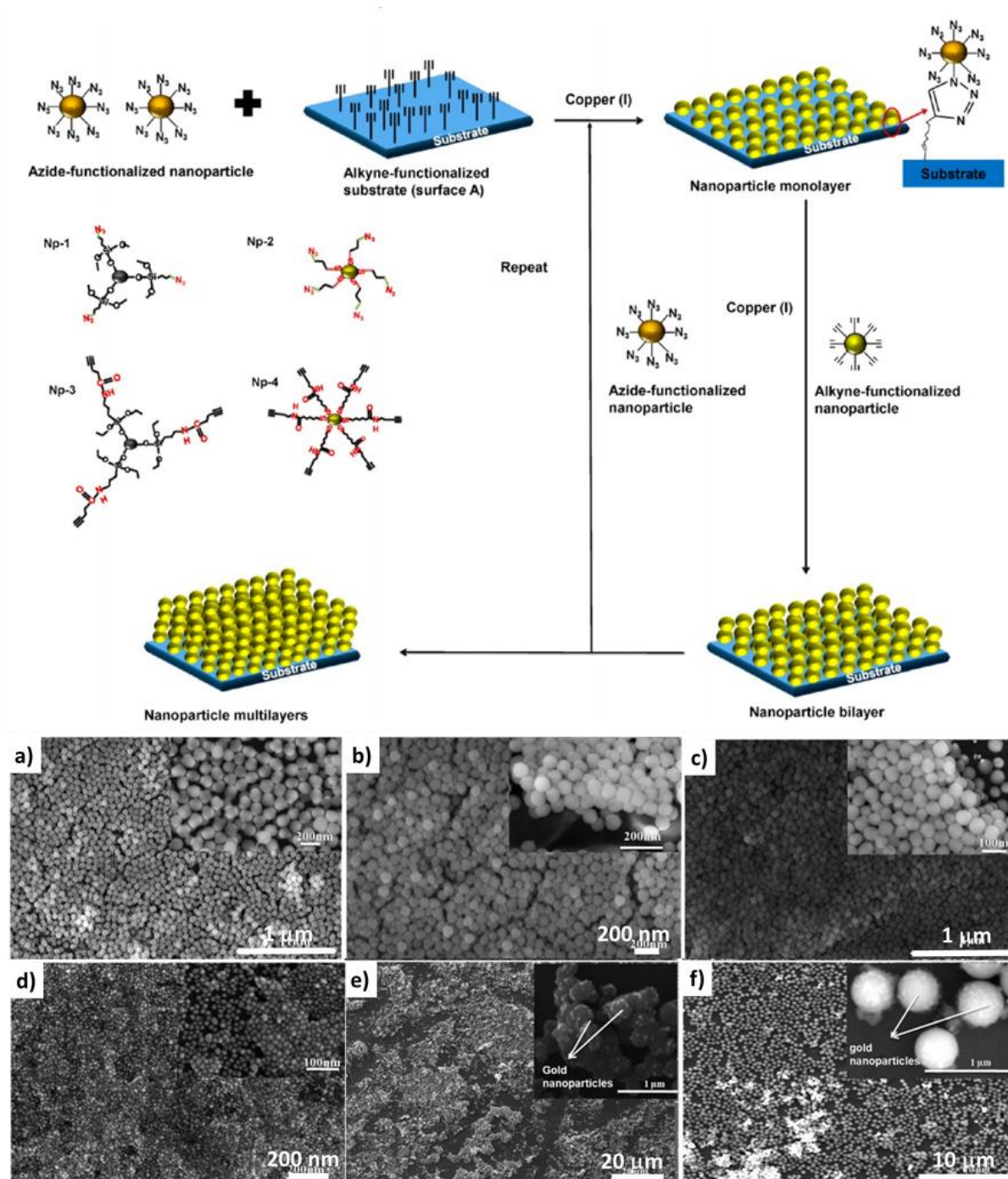


Figure 1.33 Up) Schematic representation of the synthesis of an azide-functionalized NP assembly on alkyne-functionalized substrates via click chemistry; and bottom) SEM images of a) two (scale bar 1 μm , inset 200 nm), b) three (scale bar 200 nm, inset 200 nm), and c) four layers of silica nanoparticles (scale bar 1 μm , inset 100 nm); and d) bilayer of gold nanoparticles (scale bar 200 nm, inset 100 nm), e) Au@TiO₂@silicon (scale bar 20 μm , inset 1 μm), and (f) Au@SiO₂@silicon (scale bar 10 μm , inset 1 μm). Reproduced with permission from ref.¹⁰⁷

Table 1.6 Oxidation reactions catalysed by NP assemblies

Metal	Ligand	Method	Reaction	Ref.
Au	DNA	DNA-assisted	Aerobic 4-hydroxybenzyl alcohol oxidation	122
ZnWO ₄	DNA	DNA-assisted	Benzyl alcohol oxidation by H ₂ O ₂	128
Au	Thiol	Two-phase	Electrooxidation of CO	70
Au	Thiol	LBL	Electrooxidation of CO and MeOH	45
AuPt	Thiol	Two-phase	Electrooxidation of MeOH	71
Au	Azide + alkyne	Click-chemistry	Electrooxidation of MeOH	107

1.5.3 Miscellaneous reactions

Au NP deposited onto several surfaces discussed above (Figure 1.33) were active catalysts for the electrochemical water splitting.¹⁰⁷ The onset potential at approximately 0.7 V (*vs* SCE) for all four monolayer Au NP assemblies on silicon, titania, ITO, and stainless steel substrates shows the oxygen-evolution current at approximately 0.6, 11, 2.3, and 45 mA/cm², respectively, which is higher than that of the bare substrates. The authors claim that the overall current density is dependent on the NP density, the electrocatalytic activity of the substrate, and the metal-NP support interactions (Figure 1.34). The comparison of these systems to other Au NP based catalysts pointed out a positive effect of the assemblies in terms of stability.

Photocatalytic water splitting was also investigated by using CdSe NP assemblies as catalyst.¹⁹⁹ Capped oleylamine/thiol Au, Pd, Pt, CdSe NP can form NP assemblies by the photo-oxidation of the capping thiol ligands. The assemblies consisted of vesicles, the size of which could be tuned by the size of the NP, and the thickness (number of NP layers) by the solvents used. Indeed, the type and the polarity of the solvent is crucial in the formation of the vesicles by light. Concerning the catalytic properties, the

photocatalytic rate using the prepared CdSe nanovesicles was 1.5 times of that using individual CdSe NP, due to the enhanced light absorption of the assembly. Also, the catalytic activity remained unchanged after 10 h of visible light irradiation. This is clearly in contrast with the activity of isolated CdSe NP, the activity of which decreased to less than 40% of the initiate value. The authors attributed this robustness to the mechanical strength in aqueous solution of the vesicles.

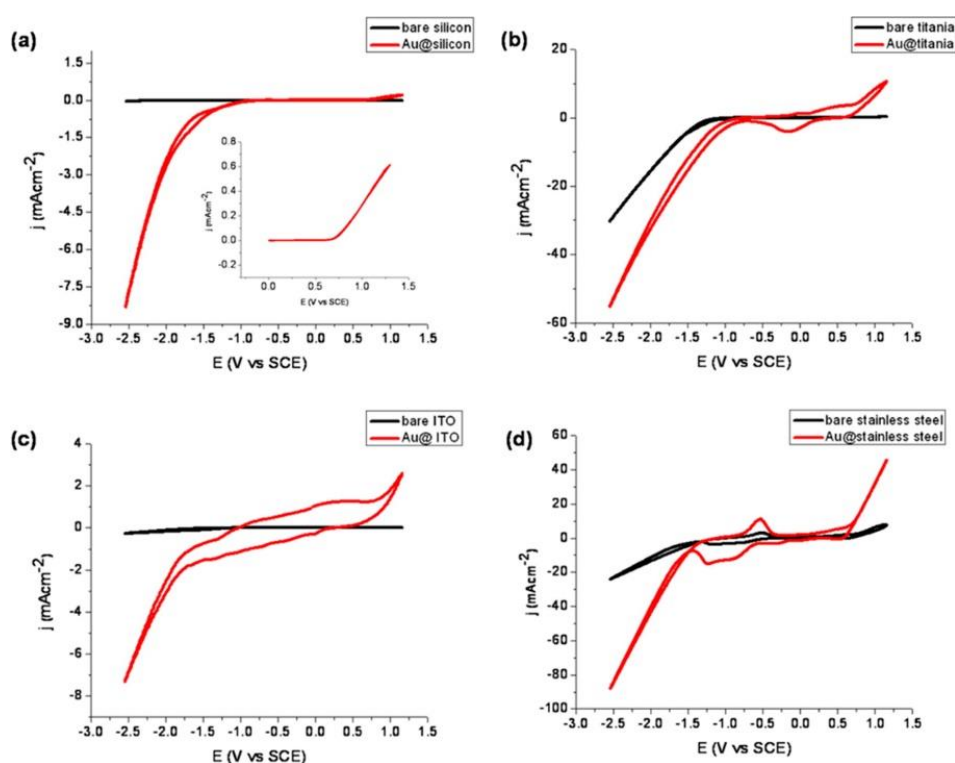


Figure 1.34 Cyclic voltammetric results for water splitting on (a) Au@silicon, (b) Au@titania, (c) Au@ITO, and (d) Au@stainless steel substrates. Reproduced with permission from ref.¹⁰⁷

Unprotected Pt NP were assembled by the addition of several amino compounds (mono and diamines), using a two-phase method.⁶⁷⁻⁶⁹ The chemical structure of the ligands plays a crucial role in the performance of the Pt based catalyst in the catalytic H₂ gas sensing. Monoamine assemblies were less stable and sintered, while diamine assemblies show better stability, which was related to the reduction of the ligand desorption rates and degradation. Ligand backbone also plays a role; aromatic

structures remained stable during H₂ oxidation, while alkyl fragments oxidized and decomposed.

Photo-switchable catalysis mediated by the assembly of Au NP has been reported (Figure 1.35). The formation of the assembly triggered by light is used in two different ways. In a first example the assembly of Au NP led to an inactive catalyst when the assembly is triggered by light;¹⁷¹ in the second example, the disassembly of the Au NP allows the Zn^{II}-coordinated β -cyclodextrin dimer to be free to coordinate to the substrates and the catalytic reaction proceeds.²⁰⁷

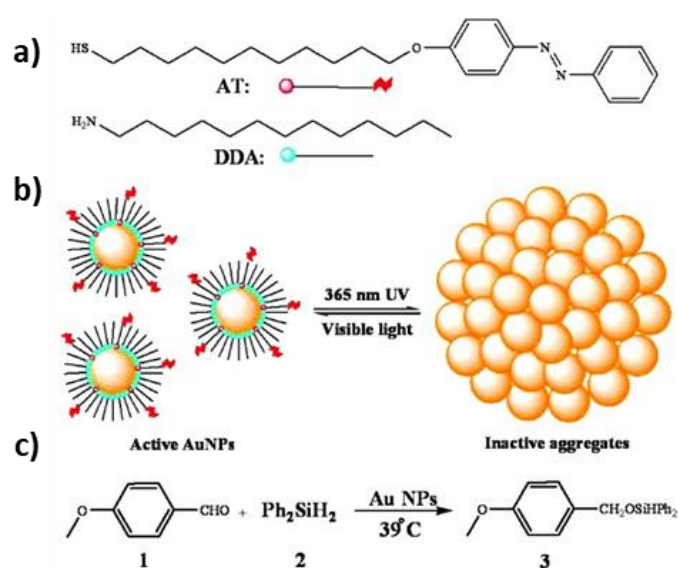


Figure 1.35 a) Molecular structures of the “background” DDA surfactant and of the photoresponsive azobenzene-thiol ligand, AT. b) Schematic representation of a photoswitchable Au NP system. Dispersed NP are catalytically active; aggregated NP are catalytically inactive. c) Hydrosilylation of 4-methoxybenzaldehyde catalyzed by Au NP in dry toluene at 39 °C and under argon. Reproduced with permission from ref.¹⁷¹

Au NP capped with a mixture of dodecylamine (DDA) and photo-switchable azobenzene-terminated alkane thiols remain unaggregated in the absence of light, therefore exposing a large catalytic active surface area (catalysis on). Upon UV light irradiation, Au NP assembled and were no longer able to catalyse the hydrosilylation reaction (catalysis off) (Figure 1.35). The reaction could be turned on and off several times over time as depicted in Figure 1.36. Even though three on-off cycles could be

efficiently performed, after that, the aggregation of Au NP was less efficient and as a consequence, the catalyst displayed some catalytic activity when off. The authors point out that the possible reason is the displacement of some surface ligands by coordination of reagents or products, which leads to the loss of the photo-responsive azobenzene-thiol ligand.

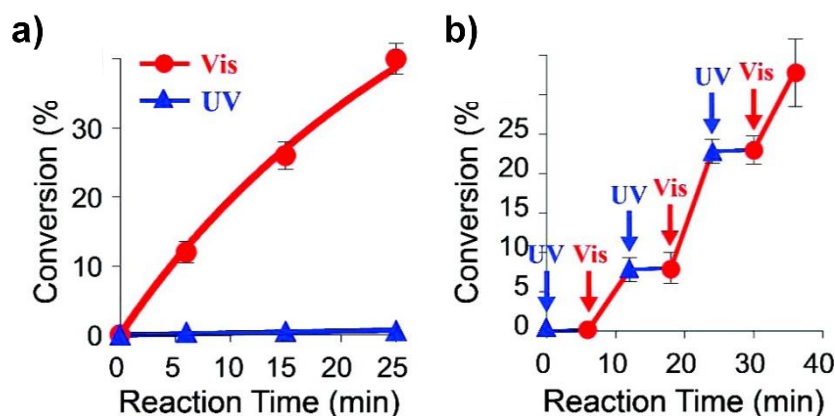


Figure 1.36 (A) Percent conversion for the Au NP-catalyzed hydrosilylation of 4-methoxybenzaldehyde as a function of time under irradiation with visible light (red markers) and under 365 nm UV irradiation (blue markers). Surface coverage of azobenzene ligands on the AuNP was $\chi = 0.3$. (B) Hydrosilylation of 4-methoxybenzaldehyde can be switched “on” by visible light (red portions of the curve) and “off” by UV (blue portions). For the experiments shown, $\chi = 0.31$. Error bars were calculated based on standard deviations from three NP batches, three samples per batch. Reproduced with permission from ref.¹⁷¹

The photoisomerization of the azobenzene unit from the *trans* to the *cis* form under UV-light irradiation was also exploited to generate another photo-switchable catalyst.²⁰⁷ In this case, the host-guest interaction of Au NP containing azobenzene units with a β -cyclodextrin dimer was controlled by light. Under UV-light irradiation, the *cis* form of the azobenzene weakened the binding with the β -cyclodextrin, allowing the host to encapsulate the substrates and catalyse the reaction. Under visible light *trans* azobenzene forms the inclusion complex with the β -cyclodextrin, turning off the catalytic reaction. Several catalytic cycles of the catalysed ester hydrolysis could be achieved with this system, and in addition, the reaction rate of this system was higher than that of other Au based catalysts.

Table 1.7 Miscellaneous reactions catalysed by NP assemblies

Metal	Ligand	Method	Reaction	Ref.
Au	Azide + alkyne	Click chemistry	Electrochemical water splitting	107
CdSe	Thiol	Light-triggered	Photocatalytic water splitting	199
Pt	Amine	Two-phase	Catalytic H ₂ gas sensing	67,68
Pt	Amine	Two-phase	Catalytic H ₂ gas sensing.	67,69
Pt	Thio-COF	One-phase	Suzuki–Miyaura coupling reaction	85
Au	Amines and azobenzene- thiols	Light-triggered	Hydrosilylation of 4-methoxy-benzaldehyde	171
Au	Thiol and azobenzene- thiols	Light-triggered	Ester hydrolysis	207

1.6 Conclusion

The covalent assembly of metal NP has been reviewed, focusing on the methodologies of synthesis and their applications in catalysis. As far as the synthesis is concerned, the direct cross-linking synthesis methods are simple, efficient and well-controlled. The properties of the metal NP and NP networks can be tuned through the nature of the linker molecule. The indirect cross-linking synthesis methods involved more complex systems that have been engineered and applied recently. Numerous works involved Au and Ag and limited studies have been devoted to other noble metals of interest for catalysis, such as Pt, Pd, or Ru,. Finally, the formation of reversible covalent networks of metal NP is now possible by application of diverse stimuli. This concept, which has been rarely employed in catalysis, deserves further studies. In our work, we will focus on the direct method to produce heterogeneous catalyst. Meanwhile, considering the impact of the ligand in NP networks we will investigate different type of linkers, based on polymantane, triphenylene and fullerene backbones.

If the metal-ligand interaction is strong enough, one advantage of covalent metal NP assemblies in catalysis should be the stability and robustness. Compared to colloidal NP, which suffer from a difficult separation (if not impossible for large-scale processes), NP networks should also allow simplifying the separation process. In catalysis and according to the reaction, the presence of ligands on NP surface can be either positive (selectivity/activity control, like in homogeneous catalysis) or negative (limited adsorption site, poisoning)

Finally, compared to a conventional heterogeneous catalyst, for which important characteristics such as NP size, inter-particle distance, and surface interactions with the support at the atomic level are not well controlled yet, the use of covalent metal NP assemblies produced from a bottom-up approach constitutes an interesting way for a better control of these key structural parameters. Table 1.8 present the advantages and drawbacks of these three types of catalysts. From this table, it seems that the use of

covalent metal NP assemblies in catalysis could be a good compromise between colloidal NP and conventional heterogeneous catalysts.

Table 1.8 Comparison of colloidal NP, covalent networks of NP and conventional heterogeneous supported catalysts in terms of parameters relevant to catalytic performances.

Catalyst	NP size	Inter-particle distance	Presence of ligand	Metal support interaction	Robustness	Separation
Colloid NP	+	-	-	-	-	X
Covalent network of NP	+	+	-	-	-	-
Heterogenous catalyst	X	X	+	X	+	+

1.7 References

1. Serp, P.; Philippot, K.; Editors: *Nanomaterials in Catalysis*; Wiley-VCH Verlag GmbH & Co. KGaA, 2013.
2. Jin, R.; Zeng, C.; Zhou, M.; Chen, Y., Atomically Precise Colloidal Metal Nanoclusters and Nanoparticles: Fundamentals and Opportunities. *Chem. Rev.* **2016**, *116*, 10346-10413.
3. Jin, R.; Pei, Y.; Tsukuda, T., Controlling Nanoparticles with Atomic Precision. *Acc. Chem. Res.* **2019**, *52*, 1.
4. Astruc, D.; Editor: *Nanoparticles and Catalysis*; WILEY INTERSCIENCE: New York, 2008.
5. Meeuwissen, J.; Reek, J. N. H., Supramolecular Catalysis Beyond Enzyme Mimics. *Nat. Chem.* **2010**, *2*, 615-621.
6. Liu, J.; Chen, L.; Cui, H.; Zhang, J.; Zhang, L.; Su, C.-Y., Applications of Metal-Organic Frameworks in Heterogeneous Supramolecular Catalysis. *Chem. Soc. Rev.* **2014**, *43*, 6011-6061.
7. Brown, C. J.; Toste, F. D.; Bergman, R. G.; Raymond, K. N., Supramolecular Catalysis in Metal-Ligand Cluster Hosts. *Chem. Rev.* **2015**, *115*, 3012-3035.
8. Grzelczak, M.; Vermant, J.; Furst, E. M.; Liz-Marzán, L. M., Directed Self-Assembly of Nanoparticles. *ACS Nano* **2010**, *4*, 3591-3605.
9. Wei, W.; Bai, F.; Fan, H., Surfactant-Assisted Cooperative Self-Assembly of Nanoparticles into Active Nanostructures. *iScience* **2019**, *11*, 272-293.
10. Sastry, M.; Rao, M.; Ganesh, K. N., Electrostatic Assembly of Nanoparticles and Biomacromolecules. *Acc. Chem. Res.* **2002**, *35*, 847-855.
11. Lim, I. I. S.; Ip, W.; Crew, E.; Njoki, P. N.; Mott, D.; Zhong, C.-J.; Pan, Y.; Zhou, S., Homocysteine-Mediated Reactivity and Assembly of Gold Nanoparticles. *Langmuir* **2007**, *23*, 826-833.
12. Lim, I. I. S.; Ouyang, J.; Luo, J.; Wang, L.; Zhou, S.; Zhong, C.-J., Multifunctional Fullerene-Mediated Assembly of Gold Nanoparticles. *Chem. Mater.* **2005**, *17*, 6528-6531.
13. Sutradhar, S.; Patnaik, A., Structure and Dynamics of a N-Methylfulleropyrrolidine-Mediated Gold Nanocomposite: A Spectroscopic Ruler. *ACS Appl. Mater. Interfaces* **2017**, *9*, 21921-21932.

14. Lim, I. I. S.; Pan, Y.; Mott, D.; Ouyang, J.; Njoki, P. N.; Luo, J.; Zhou, S.; Zhong, C.-J., Assembly of Gold Nanoparticles Mediated by Multifunctional Fullerenes. *Langmuir* **2007**, *23*, 10715-10724.
15. Tricard, S.; Said-Aizpuru, O.; Bouzouita, D.; Usmani, S.; Gillet, A.; Tassé, M.; Poteau, R.; Viau, G.; Demont, P.; Carrey, J.; Chaudret, B., Chemical tuning of Coulomb Blockade at Room-Temperature in Ultra-Small Platinum Nanoparticle Self-Assemblies. *Mater. Horiz.* **2017**, *4*, 487-492.
16. Nonappa; Haataja, J. S.; Timonen, J. V. I.; Malola, S.; Engelhardt, P.; Houbenov, N.; Lahtinen, M.; Häkkinen, H.; Ikkala, O., Reversible Supracolloidal Self-Assembly of Cobalt Nanoparticles to Hollow Capsids and Their Superstructures. *Angew. Chem. Int. Ed.* **2017**, *56*, 6473-6477.
17. Gomez, S.; Erades, L.; Philippot, K.; Chaudret, B.; Collière, V.; Balmes, O.; Bovin, J.-O., Platinum Colloids Stabilized by Bifunctional Ligands: Self-Organization and Connection to Gold. *Chem. Commun.* **2001**, 1474-1475.
18. Boal, A. K.; Ilhan, F.; DeRouchey, J. E.; Thurn-Albrecht, T.; Russell, T. P.; Rotello, V. M., Self-Assembly of Nanoparticles into Structured Spherical and Network Aggregates. *Nature* **2000**, *404*, 746-748.
19. Yucknovsky, A.; Mondal, S.; Burnstine-Townley, A.; Foqara, M.; Amdursky, N., Use of Photoacids and Photobases To Control Dynamic Self-Assembly of Gold Nanoparticles in Aqueous and Nonaqueous Solutions. *Nano Lett.* **2019**, *19*, 3804-3810.
20. Li, D.; Qi, L., Self-Assembly of Inorganic Nanoparticles Mediated by Host-Guest Interactions. *Curr. Opin. Colloid Interface Sci.* **2018**, *35*, 59-67.
21. Julin, S.; Nummelin, S.; Kostainen, M. A.; Linko, V., DNA Nanostructure-Directed Assembly of Metal Nanoparticle Superlattices. *J. Nanopart. Res.* **2018**, *20*, 119.
22. Watanabe, K.; Kuroda, K.; Nagao, D., External-Stimuli-Assisted Control over Assemblies of Plasmonic Metals. *Materials* **2018**, *11*, 794.
23. Singamaneni, S.; Bliznyuk, V. N.; Binek, C.; Tsymbal, E. Y., Magnetic Nanoparticles: Recent Advances in Synthesis, Self-Assembly and Applications. *J. Mater. Chem.* **2011**, *21*, 16819-16845.
24. Andres, R. P.; Bielefeld, J. D.; Henderson, J. I.; Janes, D. B.; Kolagunta, V. R.; Kubiak,

- C. P.; Mahoney, W. J.; Osifchin, R. G., Self-Assembly of a Two-Dimensional Superlattice of Molecularly Linked Metal Clusters. *Science* **1996**, *273*, 1690-1693.
25. Wessels, J. M.; Nothofer, H. G.; Ford, W. E.; von Wrochem, F.; Scholz, F.; Vossmeier, T.; Schroedter, A.; Weller, H.; Yasuda, A., Optical and Electrical Properties of Three-Dimensional Interlinked Gold Nanoparticle Assemblies. *J. Am. Chem. Soc.* **2004**, *126*, 3349-3356.
26. Lin, G.; Wang, Y.; Zhang, Q.; Zhang, X.; Ji, G.; Ba, L., Controllable Formation and TEM Spatial Visualization of Cross-Linked Gold Nanoparticle Spherical Aggregates. *Nanoscale* **2011**, *3*, 4567-4570.
27. Maye, M. M.; Lim, I. I. S.; Luo, J.; Rab, Z.; Rabinovich, D.; Liu, T.; Zhong, C.-J. Mediator-Template Assembly of Nanoparticles. *J. Am. Chem. Soc.* **2005**, *127*, 1519-1529.
28. Rossner, C.; Glatter, O.; Saldanha, O.; Köster, S.; Vana, P., The Structure of Gold-Nanoparticle Networks Cross-Linked by Di- and Multifunctional RAFT Oligomers. *Langmuir* **2015**, *31*, 10573-10582.
29. Shih, S.-M.; Su, W.-F.; Lin, Y.-J.; Wu, C.-S.; Chen, C.-D., Two-Dimensional Arrays of Self-Assembled Gold and Sulfur-Containing Fullerene Nanoparticles. *Langmuir* **2002**, *18*, 3332-3335.
30. Yan, H.; Lim, S. I.; Zhang, Y.-J.; Chen, Q.; Mott, D.; Wu, W.-T.; An, D.-L.; Zhou, S.; Zhong, C.-J., Molecularly-Mediated Assembly of Gold Nanoparticles with Interparticle Rigid, Conjugated and Shaped Aryl Ethynyl Structures. *Chem. Commun.* **2010**, *46*, 2218-2220.
31. Lim, I. I. S.; Vaiana, C.; Zhang, Z.-Y.; Zhang, Y.-J.; An, D.-L.; Zhong, C.-J., X-Shaped Rigid Arylethynes to Mediate the Assembly of Nanoparticles. *J. Am. Chem. Soc.* **2007**, *129*, 5368-5369.
32. Matassa, R.; Fratoddi, I.; Rossi, M.; Battocchio, C.; Caminiti, R.; Russo, M. V., Two-Dimensional Networks of Ag Nanoparticles Bridged by Organometallic Ligand. *J. Phys. Chem. C* **2012**, *116*, 15795-15800.
33. Quintiliani, M.; Bassetti, M.; Pasquini, C.; Battocchio, C.; Rossi, M.; Mura, F.; Matassa, R.; Fontana, L.; Russo, M. V.; Fratoddi, I., Network Assembly of Gold Nanoparticles Linked through Fluorenyl Dithiol Bridges. *J. Mater. Chem. C* **2014**, *2*, 2517-2527.
34. Leibowitz, F. L.; Zheng, W.; Maye, M. M.; Zhong, C.-J., Structures and Properties of

Nanoparticle Thin Films Formed via a One-Step Exchange–Cross-Linking–Precipitation Route. *Anal. Chem.* **1999**, *71*, 5076-5083.

35. Yamamoto, Y.; Miyachi, M.; Yamanoi, Y.; Minoda, A.; Maekawa, S.; Oshima, S.; Kobori, Y.; Nishihara, H., Synthesis and Hydrogen Storage Properties of Palladium Nanoparticle–Organic Frameworks. *J. Inorg. Organomet. Polym.* **2013**, *24*, 208-213.

36. Jafri, S. H.; Lofas, H.; Blom, T.; Wallner, A.; Grigoriev, A.; Ahuja, R.; Ottosson, H.; Leifer, K., Nano-Fabrication of Molecular Electronic Junctions by Targeted Modification of Metal-Molecule Bonds. *Sci. Rep.* **2015**, *5*, 14431.

37. Chen, S. W., Two-Dimensional Crosslinked Nanoparticle Networks. *Adv. Mater.* **2000**, *12*, 186-189.

38. Fontana, L.; Fratoddi, I.; Venditti, I.; Ksenzov, D.; Russo, M. V.; Grigorian, S., Structural Studies on Drop-Cast Film Based on Functionalized Gold Nanoparticles Network: The Effect of Thermal Treatment. *Appl. Surf. Sci.* **2016**, *369*, 115-119.

39. Yamanoi, Y.; Yamamoto, Y.; Miyachi, M.; Shimada, M.; Minoda, A.; Oshima, S.; Kobori, Y.; Nishihara, H., Nanoparticle Assemblies via Coordination with a Tetrakis(terpyridine) Linker Bearing a Rigid Tetrahedral Core. *Langmuir* **2013**, *29*, 8768-8772.

40. Boterashvili, M.; Shirman, T.; Popovitz-Biro, R.; Wen, Q.; Lahav, M.; van der Boom, M. E., Nanocrystallinity and Direct Cross-Linkage as Key-Factors for the Assembly of Gold Nanoparticle-Superlattices. *Chem. Commun.* **2016**, *52*, 8079-8082.

41. Leng, F.; Gerber, I. C.; Lecante, P.; Bentaleb, A.; Muñoz, A.; Illescas, B. M.; Martín, N.; Melinte, G.; Ersen, O.; Martinez, H.; Axet, M. R.; Serp, P., Hexakis [60]Fullerene Adduct-Mediated Covalent Assembly of Ruthenium Nanoparticles and Their Catalytic Properties. *Chem. Eur. J.* **2017**, *23*, 13379-13386.

42. Richardson, J. J.; Cui, J.; Björnmalm, M.; Braunger, J. A.; Ejima, H.; Caruso, F., Innovation in Layer-by-Layer Assembly. *Chem. Rev.* **2016**, *116*, 14828-14867.

43. Xiao, F.-X.; Pagliaro, M.; Xu, Y.-J.; Liu, B., Layer-by-Layer Assembly of Versatile Nanoarchitectures with Diverse Dimensionality: a New Perspective for Rational Construction of Multilayer Assemblies. *Chem. Soc. Rev.* **2016**, *45*, 3088-3121.

44. Kariuki, N. N.; Luo, J.; Hassan, S. A.; Lim, I. I. S.; Wang, L.; Zhong, C. J., Assembly of Bimetallic Gold–Silver Nanoparticles via Selective Interparticle Dicarboxylate–Silver

- Linkages. *Chem. Mater.* **2006**, *18*, 123-132.
45. Maye, M. M.; Luo, J.; Han, L.; Kariuki, N. N.; Zhong, C.-J., Synthesis, Processing, Assembly and Activation of Core-Shell Structured Gold Nanoparticle Catalysts. *Gold Bull.* **2003**, *36*, 75-82.
46. WangWang; Shi, X.; Kariuki, N. N.; Schadt, M.; Wang, G. R.; Rendeng, Q.; Choi, J.; Luo, J.; Lu, S.; Zhong, C.-J., Array of Molecularly Mediated Thin Film Assemblies of Nanoparticles: Correlation of Vapor Sensing with Interparticle Spatial Properties. *J. Am. Chem. Soc.* **2007**, *129*, 2161-2170.
47. Zhou, Q.; Li, X.; Fan, Q.; Zhang, X.; Zheng, J., Charge Transfer between Metal Nanoparticles Interconnected with a Functionalized Molecule Probed by Surface-Enhanced Raman Spectroscopy. *Angew. Chem. Int. Ed.* **2006**, *45*, 3970-3973.
48. Joseph, Y.; Besnard, I.; Rosenberger, M.; Guse, B.; Nothofer, H.-G.; Wessels, J. M.; Wild, U.; Knop-Gericke, A.; Su, D.; Schlögl, R.; Yasuda, A.; Vossmeier, T., Self-Assembled Gold Nanoparticle/Alkanedithiol Films: Preparation, Electron Microscopy, XPS-Analysis, Charge Transport, and Vapor-Sensing Properties. *J. Phys. Chem. B* **2003**, *107*, 7406-7413.
49. Joseph, Y.; Peic, A.; Chen, X.; Michl, J.; Vossmeier, T.; Yasuda, A., Vapor Sensitivity of Networked Gold Nanoparticle Chemiresistors: Importance of Flexibility and Resistivity of the Interlinkage. *J. Phys. Chem. C* **2007**, *111*, 12855-12859.
50. Daskal, Y.; Tauchnitz, T.; Guth, F.; Dittrich, R.; Joseph, Y., Assembly Behavior of Organically Interlinked Gold Nanoparticle Composite Films: A Quartz Crystal Microbalance Investigation. *Langmuir* **2017**, *33*, 11869-11877.
51. Ye, J.; Bonroy, K.; Nelis, D.; Frederix, F.; D'Haen, J.; Maes, G.; Borghs, G., Enhanced Localized Surface Plasmon Resonance Sensing on Three-Dimensional Gold Nanoparticles Assemblies. *Colloids Surf. A* **2008**, *321*, 313-317.
52. Dhar, J.; Patil, S., Self-Assembly and Catalytic Activity of Metal Nanoparticles Immobilized in Polymer Membrane Prepared via Layer-by-Layer Approach. *ACS Appl. Mater. Interfaces* **2012**, *4*, 1803-1812.
53. Vitale, F.; Fratoddi, I.; Battocchio, C.; Piscopiello, E.; Tapfer, L.; Russo, M. V.; Polzonetti, G.; Giannini, C., Mono- and Bi-Functional Arenethiols as Surfactants for Gold Nanoparticles: Synthesis and Characterization. *Nanoscale Res. Lett.* **2011**, *6*, 103.

54. Brust, M.; Schiffrin, D. J.; Bethell, D.; Kiely, C. J., Novel Gold-Dithiol Nano-Networks with Non-Metallic Electronic Properties. *Adv. Mater.* **1995**, *7*, 795-797.
55. Maye, M. M.; Chun, S. C.; Han, L.; Rabinovich, D.; Zhong, C.-J., Novel Spherical Assembly of Gold Nanoparticles Mediated by a Tetradentate Thioether. *J. Am. Chem. Soc.* **2002**, *124*, 4958-4959.
56. Lim, I.-I. S.; Zhong, C.-J., Molecularly-Mediated Assembly of Gold Nanoparticles. *Gold Bull.* **2007**, *40*, 59-66.
57. Lim, I. I. S.; Maye, M. M.; Luo, J.; Zhong, C.-J., Kinetic and Thermodynamic Assessments of the Mediator–Template Assembly of Nanoparticles. *J. Phys. Chem. B* **2005**, *109*, 2578-2583.
58. Shenhar, R.; Norsten, T. B.; Rotello, V. M., Polymer-Mediated Nanoparticle Assembly: Structural Control and Applications. *Adv. Mater.* **2005**, *17*, 657-669.
59. Stemmler, M. P.; Fogel, Y.; Müllen, K.; Kreiter, M., Bridging of Gold Nanoparticles by Functional Polyphenylene Dendrimers. *Langmuir* **2009**, *25*, 11917-11922.
60. Rossner, C.; Ebeling, B.; Vana, P., Spherical Gold-Nanoparticle Assemblies with Tunable Interparticle Distances Mediated by Multifunctional RAFT Polymers. *ACS Macro Lett.* **2013**, *2*, 1073-1076.
61. Rossner, C.; Ebeling, B.; Vana, P., Design Strategies for the Fabrication of Tailored Nanocomposites via RAFT Polymerization. *Controlled Radical Polymerization: Materials*; American Chemical Society, 2015, 1188, 293-307.
62. Dey, P.; Blakey, I.; Thurecht, K. J.; Fredericks, P. M., Hyperbranched Polymer–Gold Nanoparticle Assemblies: Role of Polymer Architecture in Hybrid Assembly Formation and SERS Activity. *Langmuir* **2014**, *30*, 2249-2258.
63. Battocchio, C.; Fratoddi, I.; Fontana, L.; Bodo, E.; Porcaro, F.; Meneghini, C.; Pis, I.; Nappini, S.; Mobilio, S.; Russo, M. V.; Polzonetti, G., Silver Nanoparticles Linked by a Pt-Containing Organometallic Dithiol Bridge: Study of Local Structure and Interface by XAFS and SR-XPS. *Phys. Chem. Chem. Phys.* **2014**, *16*, 11719-11728.
64. Fratoddi, I.; Matassa, R.; Fontana, L.; Venditti, I.; Familiari, G.; Battocchio, C.; Magnano, E.; Nappini, S.; Leahu, G.; Belardini, A.; Li Voti, R.; Sibilia, C., Electronic Properties of a Functionalized Noble Metal Nanoparticles Covalent Network. *J. Phys. Chem. C* **2017**, *121*,

18110-18119.

65. Fontana, L.; Bassetti, M.; Battocchio, C.; Venditti, I.; Fratoddi, I., Synthesis of Gold and Silver Nanoparticles Functionalized with Organic Dithiols. *Colloids Surf. A* **2017**, *532*, 282-289.
66. Bearzotti, A.; Papa, P.; Macagnano, A.; Zampetti, E.; Venditti, I.; Fioravanti, R.; Fontana, L.; Matassa, R.; Familiari, G.; Fratoddi, I., Environmental Hg Vapours Adsorption and Detection by using Functionalized Gold Nanoparticles Network. *J. Environ. Chem. Eng.* **2018**, *6*, 4706-4713.
67. Morsbach, E.; Kunz, S.; Bäumer, M., Novel Nanoparticle Catalysts for Catalytic Gas Sensing. *Catal. Sci. Technol.* **2016**, *6*, 339-348.
68. Morsbach, E.; Spéder, J.; Arenz, M.; Brauns, E.; Lang, W.; Kunz, S.; Bäumer, M., Stabilizing Catalytically Active Nanoparticles by Ligand Linking: Toward Three-Dimensional Networks with High Catalytic Surface Area. *Langmuir* **2014**, *30*, 5564-5573.
69. Morsbach, E.; Brauns, E.; Kowalik, T.; Lang, W.; Kunz, S.; Bäumer, M., Ligand-Stabilized Pt Nanoparticles (NPs) as Novel Materials for Catalytic Gas Sensing: Influence of the Ligand on Important Catalytic Properties. *Phys. Chem. Chem. Phys.* **2014**, *16*, 21243-21251.
70. Maye, M. M.; Lou, Y.; Zhong, C.-J., Core-Shell Gold Nanoparticle Assembly as Novel Electrocatalyst of CO Oxidation. *Langmuir* **2000**, *16*, 7520-7523.
71. Lou, Y.; Maye, M. M.; Han, L.; Luo, J.; Zhong, C.-J., Gold-Platinum Alloy Nanoparticle Assembly as Catalyst for Methanol Electrooxidation. *Chem. Commun.* **2001**, 473-474.
72. Hussain, I.; Brust, M.; Barauskas, J.; Cooper, A. I., Controlled Step Growth of Molecularly Linked Gold Nanoparticles: from Metallic Monomers to Dimers to Polymeric Nanoparticle Chains. *Langmuir* **2009**, *25*, 1934-9.
73. Klajn, R.; Gray, T. P.; Wesson, P. J.; Myers, B. D.; Dravid, V. P.; Smoukov, S. K.; Grzybowski, B. A., Bulk Synthesis and Surface Patterning of Nanoporous Metals and Alloys from Supra Spherical Nanoparticle Aggregates. *Adv. Funct. Mater.* **2008**, *18*, 2763-2769.
74. Sakamoto, M.; Tanaka, D.; Teranishi, T., Rigid Bidentate Ligands Focus the Size of Gold Nanoparticles. *Chem. Sci.* **2013**, *4*, 824-828.
75. Nayak, S.; Horst, N.; Zhang, H.; Wang, W.; Mallapragada, S.; Travesset, A.; Vaknin, D., Ordered Networks of Gold Nanoparticles Crosslinked by Dithiol-Oligomers. *Part. Part. Syst.*

- Charact.* **2018**, *35*, 1-7.
76. Chen, S., Langmuir–Blodgett Fabrication of Two-Dimensional Robust Cross-Linked Nanoparticle Assemblies. *Langmuir* **2001**, *17*, 2878-2884.
77. Sidhaye, D. S.; Kashyap, S.; Sastry, M.; Hotha, S.; Prasad, B. L. V., Gold Nanoparticle Networks with Photoresponsive Interparticle Spacings. *Langmuir* **2005**, *21*, 7979-7984.
78. Klajn, R.; Bishop, K. J. M.; Grzybowski, B. A., Light-Controlled Self-Assembly of Reversible and Irreversible Nanoparticle Suprastructures. *Proc. Natl. Acad. Sci.* **2007**, *104*, 10305-10309.
79. Klajn, R.; Bishop, K. J. M.; Fialkowski, M.; Paszewski, M.; Campbell, C. J.; Gray, T. P.; Grzybowski, B. A., Plastic and Moldable Metals by Self-Assembly of Sticky Nanoparticle Aggregates. *Science* **2007**, *316*, 261-264.
80. Solovyeva, E. V.; Ubyivovk, E. V.; Denisova, A. S., Effect of Diaminostilbene as a Molecular Linker on Ag Nanoparticles: SERS Study of Aggregation and Interparticle Hot Spots in Various Environments. *Colloids Surf. A* **2018**, *538*, 542-548.
81. Kalidindi, S. B.; Oh, H.; Hirscher, M.; Esken, D.; Wiktor, C.; Turner, S.; Van Tendeloo, G.; Fischer, R. A., Metal@COFs: Covalent Organic Frameworks as Templates for Pd Nanoparticles and Hydrogen Storage Properties of Pd@COF-102 Hybrid Material. *Chem. Eur. J.* **2012**, *18*, 10848-56.
82. Pachfule, P.; Panda, M. K.; Kandambeth, S.; Shivaprasad, S. M.; Diaz, D. D.; Banerjee, R., Multifunctional and Robust Covalent Organic Framework–Nanoparticle Hybrids. *J. Mater. Chem. A* **2014**, *2*, 7944-7952.
83. Pachfule, P.; Kandambeth, S.; Diaz Diaz, D.; Banerjee, R., Highly Stable Covalent Organic Framework–Au Nanoparticles Hybrids for Enhanced Activity for Nitrophenol Reduction. *Chem. Commun.* **2014**, *50*, 3169-3172.
84. Cui, K.; Zhong, W.; Li, L.; Zhuang, Z.; Li, L.; Bi, J.; Yu, Y., Well-Defined Metal Nanoparticles@Covalent Organic Framework Yolk-Shell Nanocages by ZIF-8 Template as Catalytic Nanoreactors. *Small* **2019**, *15*, 1804419.
85. Lu, S.; Hu, Y.; Wan, S.; McCaffrey, R.; Jin, Y.; Gu, H.; Zhang, W., Synthesis of Ultrafine and Highly Dispersed Metal Nanoparticles Confined in a Thioether-Containing Covalent Organic Framework and Their Catalytic Applications. *J. Am. Chem. Soc.* **2017**, *139*, 17082-

17088.

86. Mirkin, C. A.; Letsinger, R. L.; Mucic, R. C.; Storhoff, J. J., A DNA-Based Method for Rationally Assembling Nanoparticles into Macroscopic Materials. *Nature* **1996**, *382*, 607-609.
87. Storhoff, J. J.; Lazarides, A. A.; Mucic, R. C.; Mirkin, C. A.; Letsinger, R. L.; Schatz, G. C., What Controls the Optical Properties of DNA-Linked Gold Nanoparticle Assemblies? *J. Am. Chem. Soc.* **2000**, *122*, 4640-4650.
88. Simon, U.; Flesch, R.; Wiggers, H.; Schön, G.; Schmid, G., Chemical Tailoring of the Charging Energy in Metal Cluster Arrangements by Use of Bifunctional Spacer Molecules. *J. Mater. Chem.* **1998**, *8*, 517-518.
89. Li, N.; Binder, W. H., Click-Chemistry for Nanoparticle-Modification. *J. Mater. Chem.* **2011**, *21*, 16717-16734.
90. Escorihuela, J.; Marcelis, A. T. M.; Zuilhof, H., Metal-Free Click Chemistry Reactions on Surfaces. *Adv. Mater. Interfaces* **2015**, *2*, 1500135.
91. Zhu, J.; Kell, A. J.; Workentin, M. S., A Retro-Diels–Alder Reaction to Uncover Maleimide-Modified Surfaces on Monolayer-Protected Nanoparticles for Reversible Covalent Assembly. *Org. Lett.* **2006**, *8*, 4993-4996.
92. Kimoto, A.; Iwasaki, K.; Abe, J., Formation of Photoresponsive Gold Nanoparticle Networks via Click Chemistry. *Photochem. Photobiol. Sci.* **2010**, *9*, 152-156.
93. Hermes, J. P.; Sander, F.; Peterle, T.; Cioffi, C.; Ringler, P.; Pfohl, T.; Mayor, M., Direct Control of the Spatial Arrangement of Gold Nanoparticles in Organic-Inorganic Hybrid Superstructures. *Small* **2011**, *7*, 920-929.
94. Kosif, I.; Kratz, K.; You, S. S.; Bera, M. K.; Kim, K.; Leahy, B.; Emrick, T.; Lee, K. Y. C.; Lin, B.; Robust Gold Nanoparticle Sheets by Ligand Cross-Linking at the Air–Water Interface. *ACS Nano* **2017**, *11*, 1292-1300.
95. Nepal, D.; Drummy, L. F.; Biswas, S.; Park, K.; Vaia, R. A., Large Scale Solution Assembly of Quantum Dot–Gold Nanorod Architectures with Plasmon Enhanced Fluorescence. *ACS Nano* **2013**, *7*, 9064-9074.
96. Torimoto, T.; Tsumura, N.; Miyake, M.; Nishizawa, M.; Sakata, T.; Mori, H.; Yoneyama, H., Preparation and Photoelectrochemical Properties of Two-Dimensionally Organized CdS Nanoparticle Thin Films. *Langmuir* **1999**, *15*, 1853-1858.

97. Abargues, R.; Albert, S.; Valdés, J. L.; Abderrafi, K.; Martínez-Pastor, J. P., Molecular-Mediated Assembly of Silver Nanoparticles with Controlled Interparticle Spacing and Chain Length. *J. Mater. Chem.* **2012**, *22*, 22204-22211.
98. Bönnemann, H.; Waldöfner, N.; Haubold, H. G.; Vad, T., Preparation and Characterization of Three-Dimensional Pt Nanoparticle Networks. *Chem. Mater.* **2002**, *14*, 1115-1120.
99. Voggu, R.; Suguna, P.; Chandrasekaran, S.; Rao, C. N. R., Assembling Covalently Linked Nanocrystals and Nanotubes Through Click Chemistry. *Chem. Phys. Lett.* **2007**, *443*, 118-121.
100. Hua, C.; Zhang, W. H.; De Almeida, S. R. M.; Ciampi, S.; Gloria, D.; Liu, G.; Harper, J. B.; Gooding, J. J., A Novel Route to Copper(II) Detection using 'Click' Chemistry-Induced Aggregation of Gold Nanoparticles. *Analyst* **2012**, *137*, 82-86.
101. Sander, F.; Fluch, U.; Hermes, J. P.; Mayor, M.; Dumbbells, Trikes and Quads: Organic-Inorganic Hybrid Nanoarchitectures Based on "Clicked" Gold Nanoparticles. *Small* **2014**, *10*, 349-359.
102. Zhou, Y.; Wang, S.; Zhang, K.; Jiang, X., Visual Detection of Copper II by Azide- and Alkyne-Functionalized Gold Nanoparticles Using Click Chemistry. *Angew. Chem. Int. Ed.* **2008**, *47*, 7454-7456.
103. Xu, X.; Daniel, W. L.; Wei, W.; Mirkin, C. A., Colorimetric Cu²⁺ Detection using DNA-Modified Gold-Nanoparticle Aggregates as Probes and Click Chemistry. *Small* **2010**, *6*, 623-626.
104. Zhang, Y.; Li, B.; Xu, C., Visual Detection of Ascorbic Acid via Alkyne-Azide Click Reaction using Gold Nanoparticles as a Colorimetric Probe. *Analyst* **2010**, *135*, 1579-1584.
105. Rianasari, I.; de Jong, M. P.; Huskens, J.; van der Wiel, W. G., Covalent Coupling of Nanoparticles with Low-Density Functional Ligands to Surfaces via Click Chemistry. *Int. J. Mol. Sci.* **2013**, *14*, 3705-3717.
106. Liu, Y.; Williams, M. G.; Miller, T. J.; Teplyakov, A. V., Nanoparticle Layer Deposition for Highly Controlled Multilayer Formation Based on High-Coverage Monolayers of Nanoparticles. *Thin Solid Film* **2016**, *598*, 16-24.
107. Upadhyay, A. P.; Behara, D. K.; Sharma, G. P.; Bajpai, A.; Sharac, N.; Ragan, R.; Pala, R. G. S.; Sivakumar, S., Generic Process for Highly Stable Metallic Nanoparticle-

Semiconductor Heterostructures via Click Chemistry for Electro/Photocatalytic Applications. *ACS Appl. Mater. Interfaces* **2013**, *5*, 9554-9562.

108. Locatelli, E.; Ori, G.; Fournelle, M.; Lemor, R.; Montorsi, M.; Comes Franchini, M., Click Chemistry for the Assembly of Gold Nanorods and Silver Nanoparticles. *Chem. Eur. J.* **2011**, *17*, 9052-9056.

109. Liu, Y.; RamaRao, N.; Miller, T.; Hadjipanayis, G.; Teplyakov, A. V., Controlling Physical Properties of Iron Nanoparticles during Assembly by “Click Chemistry”. *J. Phys. Chem. C* **2013**, *117*, 19974-19983.

110. Jańczewski, D.; Tomczak, N.; Liu, S.; Han, M.-Y.; Vancso, G. J., Covalent Assembly of Functional Inorganic Nanoparticles by “Click” Chemistry in Water. *Chem. Commun.* **2010**, *46*, 3253-3255.

111. Bielski, R.; Witzak, Z., Strategies for Coupling Molecular Units if Subsequent Decoupling Is Required. *Chem. Rev.* **2013**, *113*, 2205-2243.

112. DeVries, G. A.; Brunnbauer, M.; Hu, Y.; Jackson, A. M.; Long, B.; Neltner, B. T.; Uzun, O.; Wunsch, B. H.; Stellacci, F., Divalent Metal Nanoparticles. *Science* **2007**, *315*, 358-361.

113. Andryszewski, T.; Iwan, M.; Hołdyński, M.; Fiałkowski, M., Synthesis of a Free-Standing Monolayer of Covalently Bonded Gold Nanoparticles. *Chem. Mater.* **2016**, *28*, 5304-5313.

114. Maneepprakorn, W.; Malik, M. A.; O’Brien, P., Developing Chemical Strategies for the Assembly of Nanoparticles into Mesoscopic Objects. *J. Am. Chem. Soc.* **2010**, *132*, 1780-1781.

115. Aldeek, F.; Ji, X.; Mattoussi, H., Quenching of Quantum Dot Emission by Fluorescent Gold Clusters: What It Does and Does Not Share with the Förster Formalism. *J. Phys. Chem. C* **2013**, *117*, 15429-15437.

116. Tognarelli, D. J.; Miller, R. B.; Pompano, R. R.; Loftus, A. F.; Sheibley, D. J.; Leopold, M. C., Covalently Networked Monolayer-Protected Nanoparticle Films. *Langmuir* **2005**, *21*, 11119-11127.

117. Shon, Y.-S.; Choo, H., [60]Fullerene-Linked Gold Nanoparticles: Synthesis and Layer-by-Layer Growth on a Solid Surface. *Chem. Commun.* **2002**, 2560-2561.

118. Dinh, T.; Shon, Y.-S., Direct Assembly of Photoresponsive C₆₀-Gold Nanoparticle Hybrid Films. *ACS Appl. Mater. Interfaces* **2009**, *1*, 2699-2702.

119. Caswell, K. K.; Wilson, J. N.; Bunz, U. H. F.; Murphy, C. J., Preferential End-to-End Assembly of Gold Nanorods by Biotin–Streptavidin Connectors. *J. Am. Chem. Soc.* **2003**, *125*, 13914-13915.
120. Pieters, B. J. G. E.; van Eldijk, M. B.; Nolte, R. J. M.; Mecinović, J., Natural Supramolecular Protein Assemblies. *Chem. Soc. Rev.* **2016**, *45*, 24-39.
121. Macfarlane, R. J.; Lee, B.; Jones, M. R.; Harris, N.; Schatz, G. C.; Mirkin, C. A., Nanoparticle Superlattice Engineering with DNA. *Science* **2011**, *334*, 204-208.
122. Auyeung, E.; Morris, W.; Mondloch, J. E.; Hupp, J. T.; Farha, O. K.; Mirkin, C. A., Controlling Structure and Porosity in Catalytic Nanoparticle Superlattices with DNA. *J. Am. Chem. Soc.* **2015**, *137*, 1658-1662.
123. Kang, E. S.; Kim, Y.-T.; Ko, Y.-S.; Kim, N. H.; Cho, G.; Huh, Y. H.; Kim, J.-H.; Nam, J.; Thach, T. T.; Youn, D.; Kim, Y. D.; Yun, W. S.; DeGrado, W. F.; Kim, S. Y.; Hammond, P. T.; Lee, J.; Kwon, Y.-U.; Ha, D.-H.; Kim, Y. H., Peptide-Programmable Nanoparticle Superstructures with Tailored Electrocatalytic Activity. *ACS Nano* **2018**, *12*, 6554-6562.
124. Sankar, S. S.; Sangeetha, K.; Karthick, K.; Anantharaj, S.; Ede, S. R.; Kundu, S., Pt Nanoparticle Tethered DNA Assemblies for Enhanced Catalysis and SERS Applications. *New J. Chem.* **2018**, *42*, 15784-15792.
125. Maeda, Y.; Akita, T.; Daté, M.; Takagi, A.; Matsumoto, T.; Fujitani, T.; Kohyama, M., Nanoparticle Arrangement by DNA-Programmed Self-Assembly for Catalyst Applications. *J. Appl. Phys.* **2010**, *108*, 094326.
126. Zinchenko, A.; Miwa, Y.; Lopatina, L. I.; Sergeyev, V. G.; Murata, S., DNA Hydrogel as a Template for Synthesis of Ultrasmall Gold Nanoparticles for Catalytic Applications. *ACS Appl. Mater. Interfaces* **2014**, *6*, 3226-3232.
127. Nithiyanantham, U.; Ede, S. R.; Anantharaj, S.; Kundu, S., Self-Assembled NiWO₄ Nanoparticles into Chain-like Aggregates on DNA Scaffold with Pronounced Catalytic and Supercapacitor Activities. *Cryst. Growth Des.* **2015**, *15*, 673-686.
128. Ede, S. R.; Ramadoss, A.; Nithiyanantham, U.; Anantharaj, S.; Kundu, S., Bio-molecule Assisted Aggregation of ZnWO₄ Nanoparticles (NPs) into Chain-like Assemblies: Material for High Performance Supercapacitor and as Catalyst for Benzyl Alcohol Oxidation. *Inorg. Chem.* **2015**, *54*, 3851-3863.

129. Tan, L. H.; Xing, H.; Lu, Y., DNA as a Powerful Tool for Morphology Control, Spatial Positioning, and Dynamic Assembly of Nanoparticles. *Acc. Chem. Res.* **2014**, *47*, 1881-1890.
130. Li, N.; Shang, Y.; Han, Z.; Wang, T.; Wang, Z.-G.; Ding, B., Fabrication of Metal Nanostructures on DNA Templates. *ACS Appl. Mater. Interfaces* **2019**, *11*, 13835-13852.
131. Niemeyer, C. M.; Simon, U., DNA-Based Assembly of Metal Nanoparticles. *Eur. J. Inorg. Chem.* **2005**, *2005*, 3641-3655.
132. Bandy, T. J.; Brewer, A.; Burns, J. R.; Marth, G.; Nguyen, T.; Stulz, E., DNA as Supramolecular Scaffold for Functional Molecules: Progress in DNA Nanotechnology. *Chem. Soc. Rev.* **2011**, *40*, 138-148.
133. Clever, G. H.; Kaul, C.; Carell, T., DNA–Metal Base Pairs. *Angew. Chem. Int. Ed.* **2007**, *46*, 6226-6236.
134. Jang, N.-H., The Coordination Chemistry of DNA Nucleosides on Gold Nanoparticles as a Probe by SERS. *Bull. Korean Chem. Soc.* *2002*, *Vol. 23, No. 12* **2002**, *23*, 1790-1800.
135. Patolsky, F.; Weizmann, Y.; Lioubashevski, O.; Willner, I., Au-Nanoparticle Nanowires Based on DNA and Polylysine Templates. *Angew. Chem. Int. Ed.* **2002**, *41*, 2323-2327.
136. Carter, J. D.; LaBean, T. H., Organization of Inorganic Nanomaterials via Programmable DNA Self-Assembly and Peptide Molecular Recognition. *ACS Nano* **2011**, *5*, 2200-2205.
137. Hong, F.; Zhang, F.; Liu, Y.; Yan, H., DNA Origami: Scaffolds for Creating Higher Order Structures. *Chem. Rev.* **2017**, *117*, 12584-12640.
138. Tian, Y.; Wang, T.; Liu, W.; Xin, H. L.; Li, H.; Ke, Y.; Shih, W. M.; Gang, O., Prescribed Nanoparticle Cluster Architectures and Low-Dimensional Arrays Built using Octahedral DNA Origami Frames. *Nature Nanotech.* **2015**, *10*, 637-644.
139. Schreiber, R.; Santiago, I.; Ardavan, A.; Turberfield, A. J., Ordering Gold Nanoparticles with DNA Origami Nanoflowers. *ACS Nano* **2016**, *10*, 7303-7306.
140. Mariana Rillo, S.; Patricia Bento da, S.; Rodrigo Alves de, S.; Karen Cristina dos, S.; Marlus, C., Recent Advances in Nanoparticle Carriers for Coordination Complexes. *Curr. Top. Med. Chem.* **2015**, *15*, 287-297.
141. Beloglazkina, E. K.; Majouga, A. G.; Romashkina, R. B.; Zyk, N. V.; Zefirov, N. S., Gold Nanoparticles Modified with Coordination Compounds of Metals: Synthesis and Application. *Russ. Chem. Rev.* **2012**, *81*, 65-90.

142. Rubinstein, I.; Vaskevich, A., Self-Assembly of Nanostructures on Surfaces Using Metal–Organic Coordination. *Isr. J. Chem.* **2010**, *50*, 333-346.
143. Tang, L.; Li, J., Plasmon-Based Colorimetric Nanosensors for Ultrasensitive Molecular Diagnostics. *ACS Sensors* **2017**, *2*, 857-875.
144. Weng, Z.; Wang, H.; Vongsvivut, J.; Li, R.; Glushenkov, A. M.; He, J.; Chen, Y.; Barrow, C. J.; Yang, W., Self-Assembly of Core-Satellite Gold Nanoparticles for Colorimetric Detection of Copper Ions. *Anal. Chim. Acta* **2013**, *803*, 128-134.
145. Pompano, R. R.; Wortley, P. G.; Moatz, L. M.; Tognarelli, D. J.; Kittredge, K. W.; Leopold, M. C., Crown ether-metal “sandwiches” as linking mechanisms in assembled nanoparticle films. *Thin Solid Films* **2006**, *510*, 311-319.
146. Sener, G.; Uzun, L.; Denizli, A., Colorimetric Sensor Array Based on Gold Nanoparticles and Amino Acids for Identification of Toxic Metal Ions in Water. *ACS Appl. Mater. Interfaces* **2014**, *6*, 18395-18400.
147. Guan, J.; Jiang, L.; Li, J.; Yang, W., pH-Dependent Aggregation of Histidine-Functionalized Au Nanoparticles Induced by Fe³⁺ Ions. *J. Phys. Chem. C* **2008**, *112*, 3267-3271.
148. Lin, S.-Y.; Chen, C.-h.; Lin, M.-C.; Hsu, H.-F., A Cooperative Effect of Bifunctionalized Nanoparticles on Recognition: Sensing Alkali Ions by Crown and Carboxylate Moieties in Aqueous Media. *Anal. Chem.* **2005**, *77*, 4821-4828.
149. Lin, S.-Y.; Liu, S.-W.; Lin, C.-M.; Chen, C.-h., Recognition of Potassium Ion in Water by 15-Crown-5 Functionalized Gold Nanoparticles. *Anal. Chem.* **2002**, *74*, 330-335.
150. Chen, S.; Pei, R.; Zhao, T.; Dyer, D. J., Gold Nanoparticle Assemblies by Metal Ion–Pyridine Complexation and Their Rectified Quantized Charging in Aqueous Solutions. *J. Phys. Chem. B* **2002**, *106*, 1903-1908.
151. Norsten, T. B.; Frankamp, B. L.; Rotello, V. M., Metal Directed Assembly of Terpyridine-Functionalized Gold Nanoparticles. *Nano Lett.* **2002**, *2*, 1345-1348.
152. Zeng, Q.; Marthi, R.; McNally, A.; Dickinson, C.; Keyes, T. E.; Forster, R. J., Host–Guest Directed Assembly of Gold Nanoparticle Arrays. *Langmuir* **2010**, *26*, 1325-1333.
153. Obare, S. O.; Hollowell, R. E.; Murphy, C. J., Sensing Strategy for Lithium Ion Based on Gold Nanoparticles. *Langmuir* **2002**, *18*, 10407-10410.

154. Miller, A.; Adams, S. Z.; Wang, L., Study of the Interaction of Citrate-Capped Hollow Gold Nanospheres with Metal Ions. *J. Nanomed. Nanotechnol.* **2016**, *7*, 1000371.
155. Priyadarshini, E.; Pradhan, N., Metal-Induced Aggregation of Valine Capped Gold Nanoparticles: An Efficient and Rapid Approach for Colorimetric Detection of Pb(2+) Ions. *Sci. Rep.* **2017**, *7*, 9278-9278.
156. Kim, Y.; Johnson, R. C.; Hupp, J. T., Gold Nanoparticle-Based Sensing of "Spectroscopically Silent" Heavy Metal Ions. *Nano Lett.* **2001**, *1*, 165-167.
157. Wanunu, M.; Popovitz-Biro, R.; Cohen, H.; Vaskevich, A.; Rubinstein, I., Coordination-Based Gold Nanoparticle Layers. *J. Am. Chem. Soc.* **2005**, *127*, 9207-9215.
158. Hitihami-Mudiyanselage, A.; Senevirathne, K.; Brock, S. L., Bottom-Up Assembly of Ni₂P Nanoparticles into Three-Dimensional Architectures: An Alternative Mechanism for Phosphide Gelation. *Chem. Mater.* **2014**, *26*, 6251-6256.
159. Lesnyak, V.; Voitekhovich, S. V.; Gaponik, P. N.; Gaponik, N.; Eychmüller, A., CdTe Nanocrystals Capped with a Tetrazolyl Analogue of Thioglycolic Acid: Aqueous Synthesis, Characterization, and Metal-Assisted Assembly. *ACS Nano* **2010**, *4*, 4090-4096.
160. Bao, C.; Zhu, L.; Lin, Q.; Tian, H., Building Biomedical Materials using Photochemical Bond Cleavage. *Adv. Mater.* **2015**, *27*, 1647-1662.
161. Lai, J.; Xu, Y.; Mu, X.; Wu, X.; Li, C.; Zheng, J.; Wu, C.; Chen, J.; Zhao, Y., Light-Triggered Covalent Assembly of Gold Nanoparticles in Aqueous Solution. *Chem. Commun.* **2011**, *47*, 3822-3824.
162. Cheng, X.; Sun, R.; Yin, L.; Chai, Z.; Shi, H.; Gao, M., Light-Triggered Assembly of Gold Nanoparticles for Photothermal Therapy and Photoacoustic Imaging of Tumors In Vivo. *Adv. Mater.* **2017**, *29*, 1604894.
163. Xia, H.; Gao, Y.; Yin, L.; Cheng, X.; Wang, A.; Zhao, M.; Ding, J.; Shi, H., Light-Triggered Covalent Coupling of Gold Nanoparticles for Photothermal Cancer Therapy. *ChemBioChem* **2019**, *20*, 667-671.
164. Zhen, S. J.; Zhang, Z. Y.; Li, N.; Zhang, Z. D.; Wang, J.; Li, C. M.; Zhan, L.; Zhuang, H. L.; Huang, C. Z., UV Light-Induced Self-Assembly of Gold Nanocrystals into Chains and Networks in a Solution of Silver Nitrate. *Nanotechnology* **2013**, *24*, 055601.
165. Itoh, H.; Tahara, A.; Naka, K.; Chujo, Y., Photochemical Assembly of Gold Nanoparticles

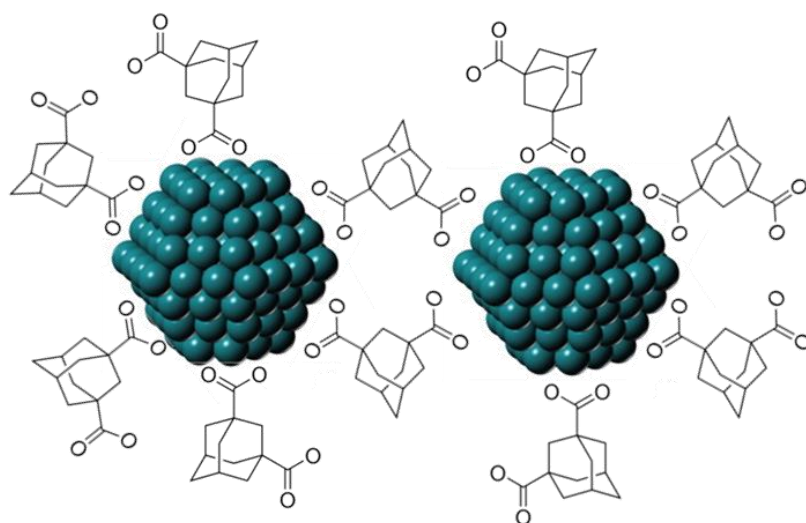
- Utilizing the Photodimerization of Thymine. *Langmuir* **2004**, *20*, 1972-1976.
166. Zhou, J.; Beattie, D. A.; Sedev, R.; Ralston, J., Synthesis and Surface Structure of Thymine-Functionalized, Self-Assembled Monolayer-Protected Gold Nanoparticles. *Langmuir* **2007**, *23*, 9170-9177.
167. Zhou, J.; Sedev, R.; Beattie, D.; Ralston, J., Light-Induced Aggregation of Colloidal Gold Nanoparticles Capped by Thymine Derivatives. *Langmuir* **2008**, *24*, 4506-4511.
168. Blum, A. P.; Kammeyer, J. K.; Rush, A. M.; Callmann, C. E.; Hahn, M. E.; Gianneschi, N. C., Stimuli-Responsive Nanomaterials for Biomedical Applications. *J. Am. Chem. Soc.* **2015**, *137*, 2140-2154.
169. Blanco, V.; Leigh, D. A.; Marcos, V., Artificial Switchable Catalysts. *Chem. Soc. Rev.* **2015**, *44*, 5341-5370.
170. Vassalini, I.; Alessandri, I., Switchable Stimuli-Responsive Heterogeneous Catalysis. *Catalysts* **2018**, *8*, 569.
171. Wei, Y.; Han, S.; Kim, J.; Soh, S.; Grzybowski, B. A., Photoswitchable Catalysis Mediated by Dynamic Aggregation of Nanoparticles. *J. Am. Chem. Soc.* **2010**, *132*, 11018-11020.
172. Díaz Díaz, D.; Kühbeck, D.; Koopmans, R. J., Stimuli-Responsive Gels as Reaction Vessels and Reusable Catalysts. *Chem. Soc. Rev.* **2011**, *40*, 427-448.
173. Zhang, J.; Zhang, M.; Tang, K.; Verpoort, F.; Sun, T., Polymer-Based Stimuli-Responsive Recyclable Catalytic Systems for Organic Synthesis. *Small* **2014**, *10*, 32-46.
174. Grzelczak, M.; Liz-Marzan, L. M.; Klajn, R., Stimuli-Responsive Self-Assembly of Nanoparticles. *Chem. Soc. Rev.* **2019**, *48*, 1342-1361.
175. Kay, E. R., Dynamic Covalent Nanoparticle Building Blocks. *Chem. Eur. J.* **2016**, *22*, 10706-10716.
176. Rowan, S. J.; Cantrill, S. J.; Cousins, G. R. L.; Sanders, J. K. M.; Stoddart, J. F., Dynamic Covalent Chemistry. *Angew. Chem. Int. Ed.* **2002**, *41*, 898-952.
177. Borsley, S.; Kay, E. R., Dynamic Covalent Assembly and Disassembly of Nanoparticle Aggregates. *Chem. Commun.* **2016**, *52*, 9117-9120.
178. Wei, W.; Wu, L.; Xu, C.; Ren, J.; Qu, X., A General Approach using Spiroborate Reversible Cross-Linked Au Nanoparticles for Visual High-Throughput Screening of Chiral

- Vicinal Diols. *Chem. Sci.* **2013**, *4*, 1156-1162.
179. Liu, X.; Liu, H.; Zhou, W.; Zheng, H.; Yin, X.; Li, Y.; Guo, Y.; Zhu, M.; Ouyang, C.; Zhu, D.; Xia, A., Thermoreversible Covalent Self-Assembly of Oligo(p-phenylenevinylene) Bridged Gold Nanoparticles. *Langmuir* **2010**, *26*, 3179-3185.
180. Chan, Y.-T.; Li, S.; Moorefield, C. N.; Wang, P.; Shreiner, C. D.; Newkome, G. R., Self-Assembly, Disassembly, and Reassembly of Gold Nanorods Mediated by Bis(terpyridine) – Metal Connectivity. *Chem. Eur. J.* **2010**, *16*, 4164-4168.
181. Si, S.; Raula, M.; Paira, T. K.; Mandal, T. K., Reversible Self-Assembly of Carboxylated Peptide-Functionalized Gold Nanoparticles Driven by Metal-Ion Coordination. *ChemPhysChem* **2008**, *9*, 1578-1584.
182. Rao, A.; Roy, S.; Unnikrishnan, M.; Bhosale, S. S.; Devatha, G.; Pillai, P. P., Regulation of Interparticle Forces Reveals Controlled Aggregation in Charged Nanoparticles. *Chem. Mater.* **2016**, *28*, 2348-2355.
183. Parnsubsakul, A.; Oaew, S.; Surareungchai, W., Zwitterionic Peptide-Capped Gold Nanoparticles for Colorimetric Detection of Ni²⁺ *Nanoscale* **2018**, *10*, 5466-5473.
184. Liu, D.; Chen, W.; Sun, K.; Deng, K.; Zhang, W.; Wang, Z.; Jiang, X., Resettable, Multi-Readout Logic Gates Based on Controllably Reversible Aggregation of Gold Nanoparticles. *Angew. Chem. Int. Ed.* **2011**, *50*, 4103-4107.
185. Luan, Z.; Salk, T.; Abelson, A.; Jean, S.; Law, M., Reversible Aggregation of Covalently Cross-Linked Gold Nanocrystals by Linker Oxidation. *J. Phys. Chem. C* **2019**, *123*, 23643–23654.
186. Frisch, H.; Marschner, D. E.; Goldmann, A. S.; Barner-Kowollik, C., Wavelength-Gated Dynamic Covalent Chemistry. *Angew. Chem. Int. Ed.* **2018**, *57*, 2036-2045.
187. Cardenas-Daw, C.; Kroeger, A.; Schaertl, W.; Froimowicz, P.; Landfester, K., Reversible Photocycloadditions, a Powerful Tool for Tailoring (Nano)Materials. *Macromolecular Chemistry and Physics* **2012**, *213*, 144-156.
188. Göstl, R.; Hecht, S., Controlling Covalent Connection and Disconnection with Light. *Angew. Chem. Int. Ed.* **2014**, *53*, 8784-8787.
189. He, H.; Feng, M.; Chen, Q.; Zhang, X.; Zhan, H., Light-Induced Reversible Self-Assembly of Gold Nanoparticles Surface-Immobilized with Coumarin Ligands. *Angew. Chem.*

- Int. Ed.* **2016**, *55*, 936-940.
190. Chen, Y.; Wang, Z.; He, Y.; Yoon, Y. J.; Jung, J.; Zhang, G.; Lin, Z., Light-Enabled Reversible Self-Assembly and Tunable Optical Properties of Stable Hairy Nanoparticles. *Proc. Natl. Acad. Sci.* **2018**, *115*, E1391-E1400.
191. De Fazio, A. F.; El-Sagheer, A. H.; Kahn, J. S.; Nandhakumar, I.; Burton, M. R.; Brown, T.; Muskens, O. L.; Gang, O.; Kanaras, A. G., Light-Induced Reversible DNA Ligation of Gold Nanoparticle Superlattices. *ACS Nano* **2019**, *13*, 5771-5777.
192. Bigall, N. C.; Herrmann, A.-K.; Vogel, M.; Rose, M.; Simon, P.; Carrillo-Cabrera, W.; Dorfs, D.; Kaskel, S.; Gaponik, N.; Eychmüller, A., Hydrogels and Aerogels from Noble Metal Nanoparticles. *Angew. Chem. Int. Ed.* **2009**, *48*, 9731-9734.
193. Arachchige, I. U.; Brock, S. L., Sol-Gel Methods for the Assembly of Metal Chalcogenide Quantum Dots. *Acc. Chem. Res.* **2007**, *40*, 801-809.
194. Gao, X.; Esteves, R. J. A.; Nahar, L.; Nowaczyk, J.; Arachchige, I. U., Direct Cross-Linking of Au/Ag Alloy Nanoparticles into Monolithic Aerogels for Application in Surface-Enhanced Raman Scattering. *ACS Appl. Mater. Interfaces* **2016**, *8*, 13076-13085.
195. Guo, S.; Sun, S., FePt Nanoparticles Assembled on Graphene as Enhanced Catalyst for Oxygen Reduction Reaction. *J. Am. Chem. Soc.* **2012**, *134*, 2492-2495.
196. Sreedhala, S.; Vinod, C. P., Surfactant Assisted Formation of Ruthenium Nanochains under Mild Conditions and their Catalytic CO Oxidation Activity. *Chem. Commun.* **2015**, *51*, 10178-10181.
197. Zhao, H.; Sen, S.; Udayabhaskararao, T.; Sawczyk, M.; Kucanda, K.; Manna, D.; Kundu, P. K.; Lee, J.-W.; Kral, P.; Klajn, R., Reversible Trapping and Reaction Acceleration within Dynamically Self-Assembling Nanoflasks. *Nat. Nanotechnol.* **2016**, *11*, 82-88.
198. Zhang, Q.; Wang, W.-Z.; Yu, J.-J.; Qu, D.-H.; Tian, H., Dynamic Self-Assembly Encodes A Tri-stable Au-TiO₂ Photocatalyst. *Adv. Mater.* **2017**, *29*, 1604948.
199. Bian, T.; Shang, L.; Yu, H.; Perez, M. T.; Wu, L.-Z.; Tung, C.-H.; Nie, Z.; Tang, Z.; Zhang, T., Spontaneous Organization of Inorganic Nanoparticles into Nanovesicles Triggered by UV Light. *Adv. Mater.* **2014**, *26*, 5613-5618.
200. Neouze, M.-A., Nanoparticle Assemblies: Main Synthesis Pathways and Brief Overview on Some Important Applications. *J. Mater. Sci.* **2013**, *48*, 7321-7349.

201. Bouju, X.; Duguet, É.; Gauffre, F.; Henry, C. R.; Kahn, M. L.; Mélinon, P.; Ravaine, S., Nonisotropic Self-Assembly of Nanoparticles: From Compact Packing to Functional Aggregates. *Adv Mater* **2018**, *30*, 1706558.
202. Bazán-Díaz, L.; Mendoza-Cruz, R.; Velázquez-Salazar, J. J.; Plascencia-Villa, G.; Ascencio-Aguirre, F. M.; Ojeda-Galván, H. J.; Herrera-Becerra, R.; Guisbiers, G.; José-Yacamán, M., Synthesis and Properties of the Self-Assembly of Gold–Copper Nanoparticles into Nanoribbons. *Langmuir* **2018**, *34*, 9394-9401.
203. Chen, Z.; Li, J.; Zhang, X.; Wu, Z.; Zhang, H.; Sun, H.; Yang, B. Construction of Nanoparticle Superstructures on the Basis of Host-Guest Interaction to Achieve Performance Integration and Modulation. *Phys. Chem. Chem. Phys.* **2012**, *14*, 6119-6125.
204. Zhong, C. J.; Maye, M. M., Core–Shell Assembled Nanoparticles as Catalysts. *Adv. Mater.* **2001**, *13*, 1507-1511.
205. Henry, C. R., 2D-Arrays of Nanoparticles as Model Catalysts. *Catal. Lett.* **2015**, *145*, 731–749.
206. Huang, T.; Meng, F.; Qi, L., Facile Synthesis and One-Dimensional Assembly of Cyclodextrin-Capped Gold Nanoparticles and their Applications in Catalysis and Surface-Enhanced Raman Scattering. *J. Phys. Chem. C* **2009**, *113*, 13636-13642.
207. Zhu, L.; Yan, H.; Ang, C. Y.; Nguyen, K. T.; Li, M.; Zhao, Y., Photoswitchable Supramolecular Catalysis by Interparticle Host-Guest Competitive Binding. *Chem. Eur. J.* **2012**, *18*, 13979-13983.

Chapter 2 Controlled synthesis of 3D ruthenium nanoparticle covalent assemblies from polymantane ligands



2. Controlled synthesis of 3D ruthenium nanoparticle covalent assemblies from polymantane ligands

2.1 Introduction

2.2 Results and discussion

2.2.1 Structure of Ru nanoparticles and Ru nanoparticle assemblies

2.2.1.1 Transmission electron microscopy analyses

2.2.1.2 Wide-angle X-ray scattering analyses

2.2.1.3 Small-angle X-ray scattering analyses

2.2.1.4 Electron tomography analysis

2.2.2 Coordination of carboxylate and amine ligands on Ru nanoparticle surface

2.2.2.1 Surface modeling from coordination complex analysis

2.2.2.2 Infrared of Ru nanoparticle and Ru nanoparticle assemblies

2.2.2.3 Solid-State NMR analyses

2.2.2.4 CO adsorption analyses

2.2.2.5 X-ray photoelectron spectroscopy analyses

2.2.2.6 Temperature programmed desorption analyses

2.2.2.7 Theoretical calculations

2.3 Conclusion

2.4 Experimental section

2.5 References

2.1 Introduction

As depicted before, the self-assembly of molecules, clusters or nanostructures is a promising avenue for the development of organized nanostructures with peculiar properties and broad spectrum of emerging applications.¹⁻⁴ In the case of metal nanoparticles (NP), a combination of self- and directed assembly processes involving inter-particle forces can be used to produce the desired materials.⁴ To obtain stable NP assemblies, molecular mediators that can induce a covalent bond between the NP have to be used. Such molecules enable inter-particle distance and interaction tuning in the assemblies, allowing studying not only the properties of the individual NP, but also the collective effects of the two-dimensional (2D) and three-dimensional (3D) networks of NP.⁵⁻⁷ Networks of ruthenium NP⁸ have already been described, assembled by means of polytopic ligands. In general, the inter-particle distance can be modulated by changing the length of the alkyl chain of the ligands, and in that context ligand rigidity should be considered. The use of multi-carboxylate ligands, such as the C₆₆(COOH)₁₂ hexa-adduct, allowed to produce 3D networks of Ru NP (1.6 nm) showing an inter-particle distance of 2.85 nm.⁸

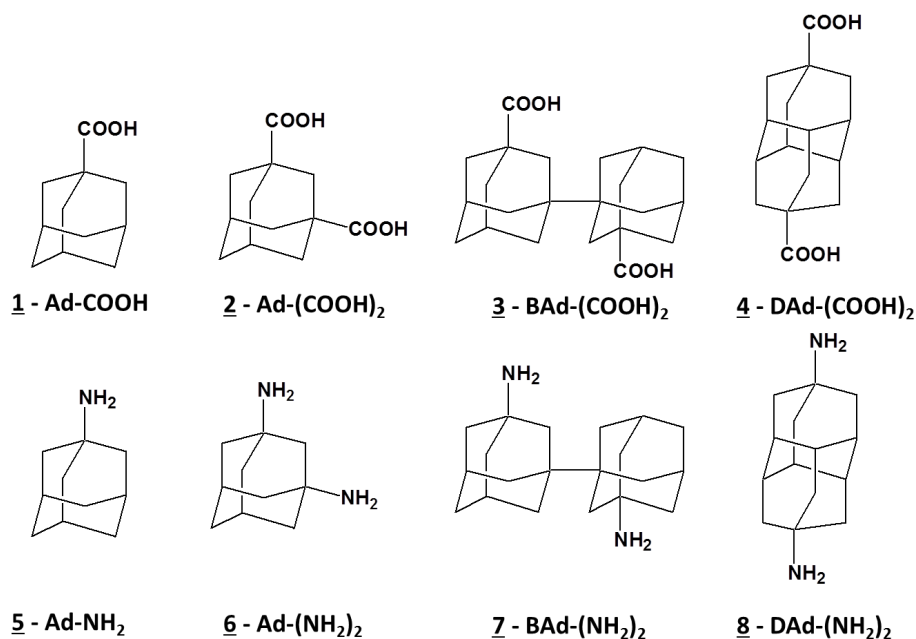
Nano diamonds are hydrocarbon cage molecules like adamantane and larger ones with repeated or superimposable diamond lattice (polymantane), which are of great rigidity, stability and potentiality for a large span of applications.⁹ The stable skeleton and carbon atoms in different but precise chemical environment make the accurate functionalization of these molecules feasible with flexible groups, extending the field of application, particularly for constructing new materials.¹⁰ Adamantane functionalized by tetrahedral amine worked as “bricks” in building 3D microporous covalent organic frameworks (COFs). Such materials were used as catalysts in the Knoevenagel reaction, they show high conversion (96 and 98%), very efficient size selectivity and nice recyclability.¹¹ Functionalized adamantane have been investigated as building blocks for nanostructure self-assembly.¹² The preparation of Pd nanolayers on self-assembled functional diamantane with hydroxyl and phosphine oxide groups was reported, leading to covalent Pd-O-PH-diamantane bonding species, and affording

sp^3 -hybrid nanocomposites for gas sensors.¹³⁻¹⁴

In this chapter, we describe the use of bi-functional polymantanes (*i.e.* rigid sp^3 -hybridized diamondoids) as ligands to build, *via* a straightforward and up-scalable method, Ru NP networks presenting uniform particle size and inter-particle distance, as well as a well-defined chemical environment. Adamantane, bis-adamantane and diamantane dicarboxylic and diamine ligands were used to produce a set of Ru NP networks with well-defined characteristics of interests for catalysis.

2.2 Results and discussion

We have used a set of different carboxylic and amine ligands bearing the sp^3 adamantane (Ad), bis-adamantane (BAd), and diamantane (DAd) backbone (Scheme 2.1). Most of these compounds were prepared by Houssein Nasrallah from the Institut de Chimie Moléculaire de l'Université de Bourgogne in the frame of research collaboration with Prof. J. C. Hierro (see section 2.4 for a detailed description of their synthesis).

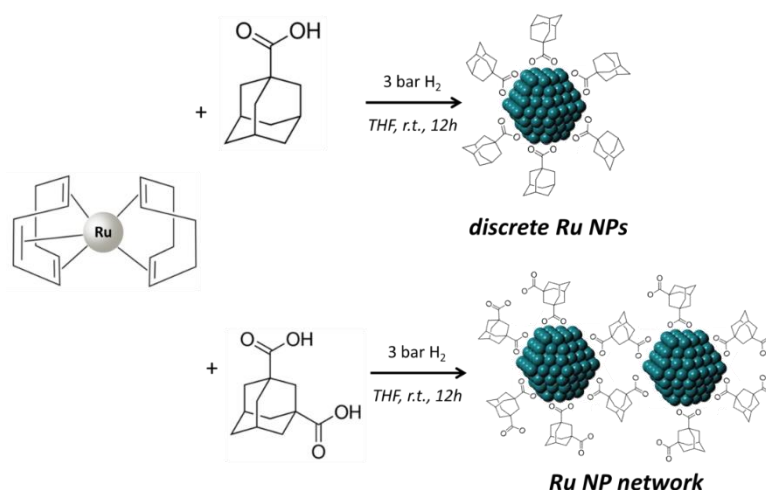


Scheme 2.1 Series of polymantane ligands, including adamantane, bis-adamantane, and diamantane backbone, used for the synthesis of discrete Ru NP and networks of Ru NP.

Compound 1,3-diaminoadamantane (**6**), Ad-(NH₂)₂, was prepared from 1,3-

dibromoadamantane in 28% yield following a reported method.¹⁵ The compound BAd-(NH₂)₂ **7** was obtained from bis-adamantane, which was prepared from 1-bromoadamantane homocoupling by metallic sodium.¹⁶⁻¹⁷ From commercial diamantane, the DAd-(NH₂)₂ **8** was obtained after selective dibromation on 4, 9 apical positions.¹⁸ Concerning the carboxylic polymantane derivatives: Ad-COOH **1** and Ad-(COOH)₂ **2** are commercially available, and DAd-(COOH)₂ **4** was prepared based on literature methods and isolated with 23% overall yield starting from 4,9-dihydroxy-diamantane.¹⁹⁻²⁰ We also tried to synthesize BAd-(COOH)₂ **3**, but the product is insoluble in all common organic solvents, which hamper its use.

The discrete NP and NP networks were conveniently obtained by reaction of (1,5-cyclooctadiene)(1,3,5-cyclooctatriene)ruthenium(0) ([Ru(COD)(COT)]) at room temperature in THF under 3 bar H₂ in the presence of the stabilizing ligand (see Scheme 2.2 for a representative example with ligands **1** and **2**). Different amounts of ligand were employed for the synthesis of some of the Ru NP, specifically 0.2, 0.1 and 0.05 molar equiv., with the aim to obtain different sizes and reactivity.



Scheme 2.2 Synthesis of Ru NP and NP networks using polymantane ligands as stabilizers.

2.2.1 Structure of Ru nanoparticles and Ru nanoparticle assemblies

The Ru NP and Ru NP assemblies were characterized by different techniques, including transmission electron microscopy (TEM), wide-angle X-ray scattering (WAXS), small-

angle X-ray scattering (SAXS), inductively coupled plasma (ICP) and electron tomography (ET). The most relevant structural parameters provided by these analyses are listed in Table 2.1. The experimental results are discussed in detail below.

Table 2.1 Mean size distributions, inter-particle distances and ruthenium content of the synthesized Ru NP and Ru NP networks.

Ligand	Ru/L (molar)	Ru loading (%)	Ru NP size (nm) ^{a)}	Ru NP size (nm) ^{b)}	NP network	Inter-particle distance (nm) ^{c)}
<u>1</u>	5/1	77.9	1.5 ± 0.6	1.5	no	-
	10/1	65.5	1.8 ± 0.5	2.2	no	-
	20/1	78.7	1.9 ± 0.6	2.5	no	-
<u>2</u>	5/1	50.2	1.7 ± 0.7	1.7	yes	2.2
	10/1	61.8	1.8 ± 0.8	2.0	yes	2.7
	20/1	70.1	1.9 ± 0.7	2.2	yes	2.7
<u>4</u>	10/1	67.7	1.8 ± 0.6	2.1	yes	2.9
<u>5</u>	10/1	82.5	1.6 ± 0.7	1.5	no	-
<u>6</u>	10/1	80.1	1.8 ± 0.7	1.9	yes	2.4
<u>7</u>	10/1	65.7	1.7 ± 0.6	1.2	yes	2.5
<u>8</u>	10/1	70.2	1.7 ± 0.7	2.1	yes	2.7

^{a)} From TEM. ^{b)} From WAXS. ^{c)} From SAXS.

2.2.1.1 Transmission electron microscopy analyses

We first verified that the mono-functionalized ligands **1** and **5**, can indeed stabilize Ru NP. Adamantane carboxylic acid **1** has already been used to stabilize FeCO₃ NP²¹ and CdSe quantum dots.²² To the best of our knowledge, the adamantane amine **5** has not been used before as ligand for surface stabilization in NP synthesis. The decomposition of [Ru(COD)(COT)] in the presence of **1** or **5** (Ru/ligand molar ratio = 10) leads to the formation of discrete Ru NP with size of 1.8 and 1.6 nm (TEM) respectively (Figure 2.1)

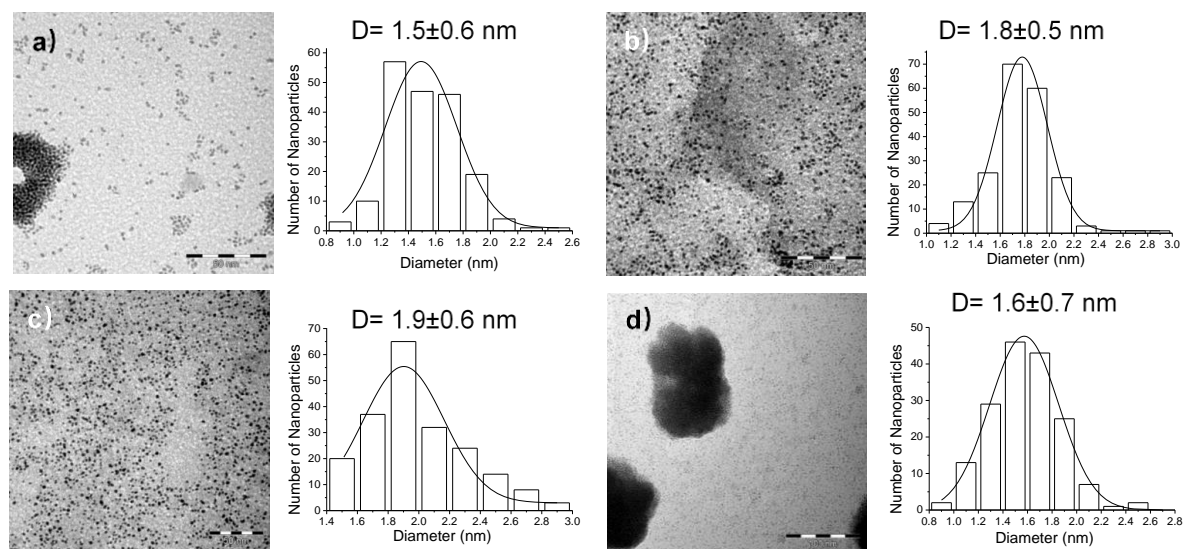


Figure 2.1 TEM micrographs and NP size histograms of Ru NP obtained with ligand **1** at a Ru/L molar ratio of: a) 5 (scale bar = 50 nm); b) 10 (scale bar = 50 nm); c) 20 (scale bar = 50 nm); and d) by ligand **5** with Ru/L molar ratio of 10 (scale bar = 100 nm).

The mean NP diameters were calculated from at least 200 NP in the TEM images. Similar NP sizes were reported for Ru NP prepared from $[\text{Ru}(\text{COD})(\text{COT})]$ and amines,²³ and carboxylic acid ligands.²⁴ The NP produced from the amine ligand **5** are more agglomerated than the ones produced from the carboxylic acid ligand **1**. This could result from the dynamic exchanges between free and coordinated species as amine ligands possess a facile reversible binding leading to Ru NP coalescence has been reported.²⁵

Pleasingly, the use of the bis-carboxylic acid (**2**, **4**) and bis-amino (**6-8**) bi-functional polymantanes induces the formation of networks of Ru NP (Figure 2.2). In these networks, the Ru NP size range between 1 and 2 nm, according to the Ru/L molar ratio, and to the nature of the ligand. Larger particles are obtained at higher Ru/L molar ratio: from 1.7 (Ru/L = 5) to 2.2 nm (Ru/L = 20) for ligand **2**.

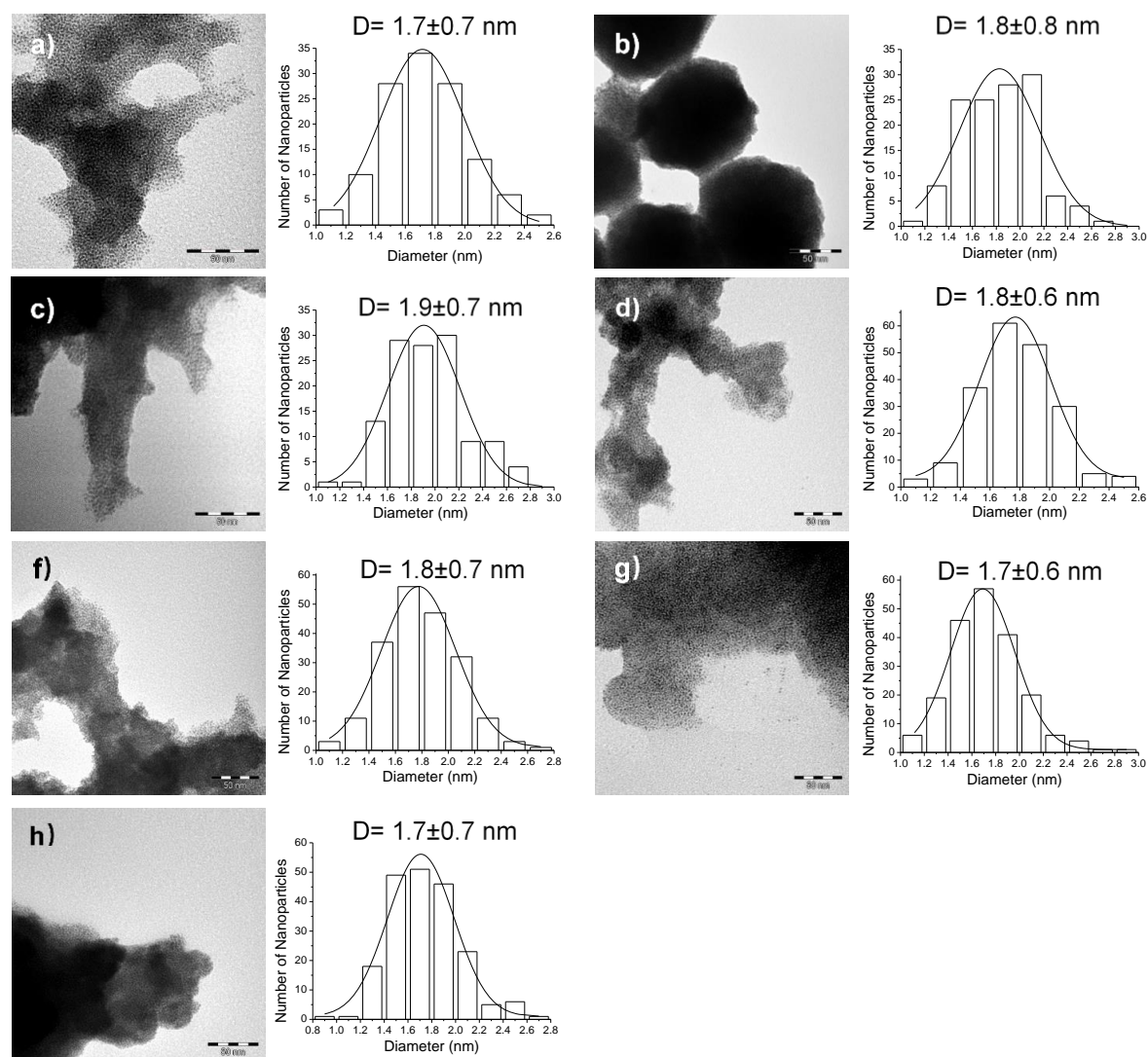


Figure 2.2 TEM micrographs and NP size histograms of Ru NP networks obtained by ligand **2** at a Ru/L molar ratio of: a) 5 (scale bar = 50 nm); b) 10 (scale bar = 50 nm); c) 20 (scale bar = 50 nm) and at a Ru/L molar ratio of 10 for ligands: e) **4** (scale bar = 50 nm); f) **6** (scale bar = 50 nm); g) **7** (scale bar = 50 nm); and h) **8** (scale bar = 50 nm).

This synthetic method allows the production of networks of metal NP with a relatively narrow particle size distribution, compared to conventional catalytic materials prepared on carbon supports.

2.2.1.2 Wide-angle X-ray scattering analyses

WAXS analyses have shown that **Ru@1** at 10/1 and 20/1 Ru/L molar ratio and **Ru@2**

at all ratio are well crystallized and highly consistent with the Ru *hcp* crystal structure. The coherence length (2.2 nm Ru NP produced from **1**) indicated by the radial distribution function (RDF) resultant from WAXS analyses (Figure 2.3) is larger than the mean diameters determined by TEM.

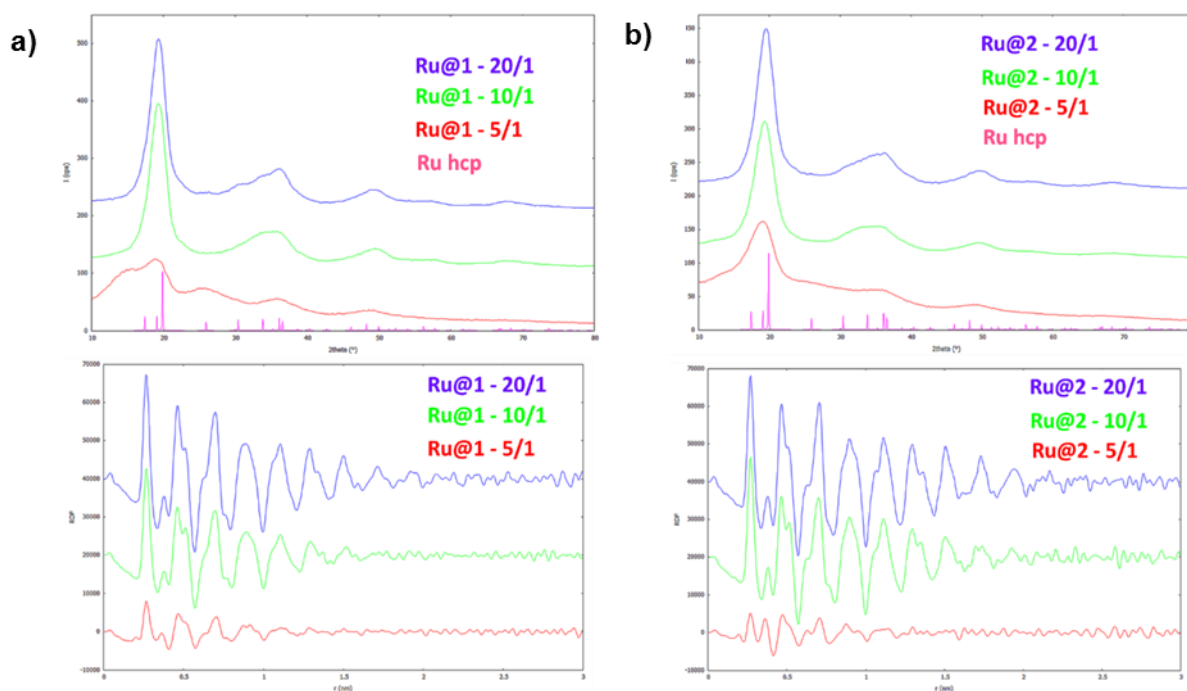


Figure 2.3 WAXS analyses for **Ru@1** and **Ru@2**: a) top, diffractograms of **Ru@1** at different Ru/ligand ratio with Ru *hcp* reference data; bottom, corresponding RDF; b) top, diffractograms of **Ru@2** at different Ru/ligand ratio with Ru *hcp* reference data; bottom corresponding RDF.

This feature, which was common to many of the samples prepared (see Table 2.1), was already reported for ligand stabilized metal NP.²⁶ The size of the NP embedded in the assembly produced by **2** is similar to isolated NP ranging from 1.7 ~ 2.2 nm. The increase of the Ru/L molar ratio (from 5/1 to 20/1 in the case of **1**) induces an increase of the Ru NP size (from 1.5 to 2.5 nm) and therefore provides an interesting control lever.

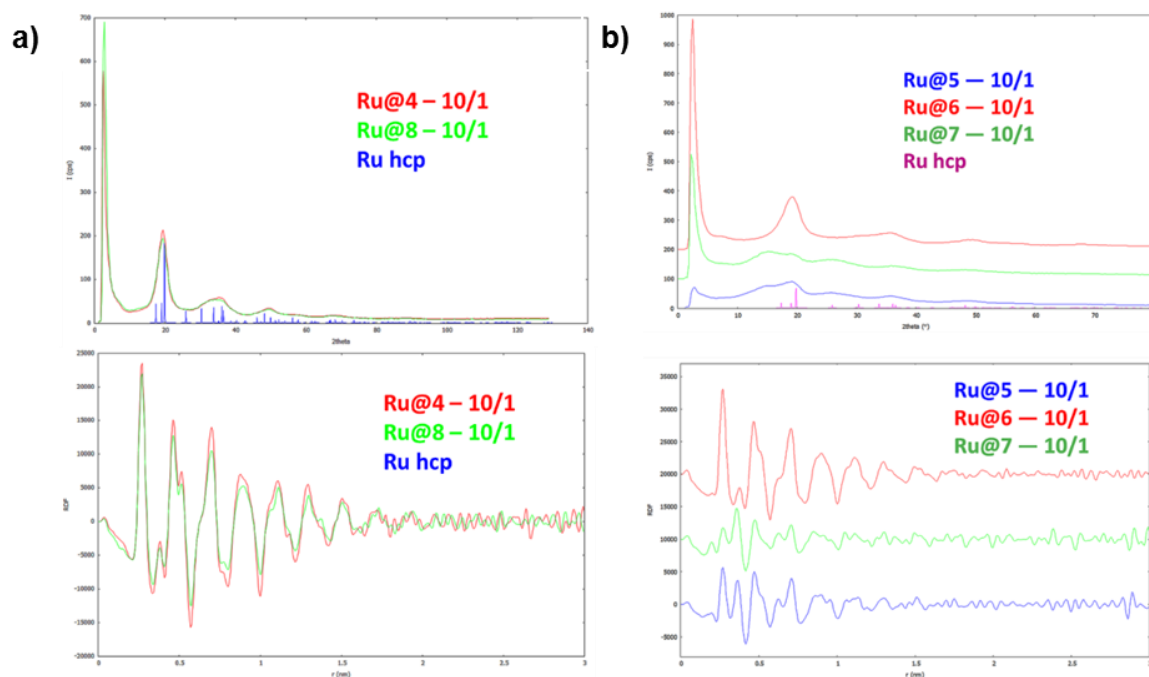


Figure 2.4 WAXS analyses for **Ru@4**, **Ru@5**, **Ru@6**, **Ru@7** and **Ru@8**: a) top, diffractograms of **Ru@4** and **Ru@8** at Ru/ligand ratio of 10 with Ru *hcp* reference data; bottom corresponding RDF; b) top, diffractograms of **Ru@5**, **Ru@6** and **Ru@7** at Ru/ligand ratio of 10 with Ru *hcp* reference data; bottom corresponding RDF.

Diffractograms and RDF clearly show that the Ru NP assemblies stabilized by ligands **4**, **6**, and **8** have a more crystalline structure than those stabilized by ligands **5** and **7**. The NP assemblies stabilized by amine groups show a mean NP size between 1.5 and 2.1 nm, except for **Ru@7**, which presents a smaller size perhaps due to the flexibility of the bis-adamantane.

2.2.1.3 Small-angle X-ray scattering analyses

SAXS analyses were performed to evaluate the inter-particle distances in the assemblies. The scattering intensity profiles (Figure 2.5) show a general increase of the scattering intensity towards small q values, which is coherent with a system constituted of Ru NP.⁸

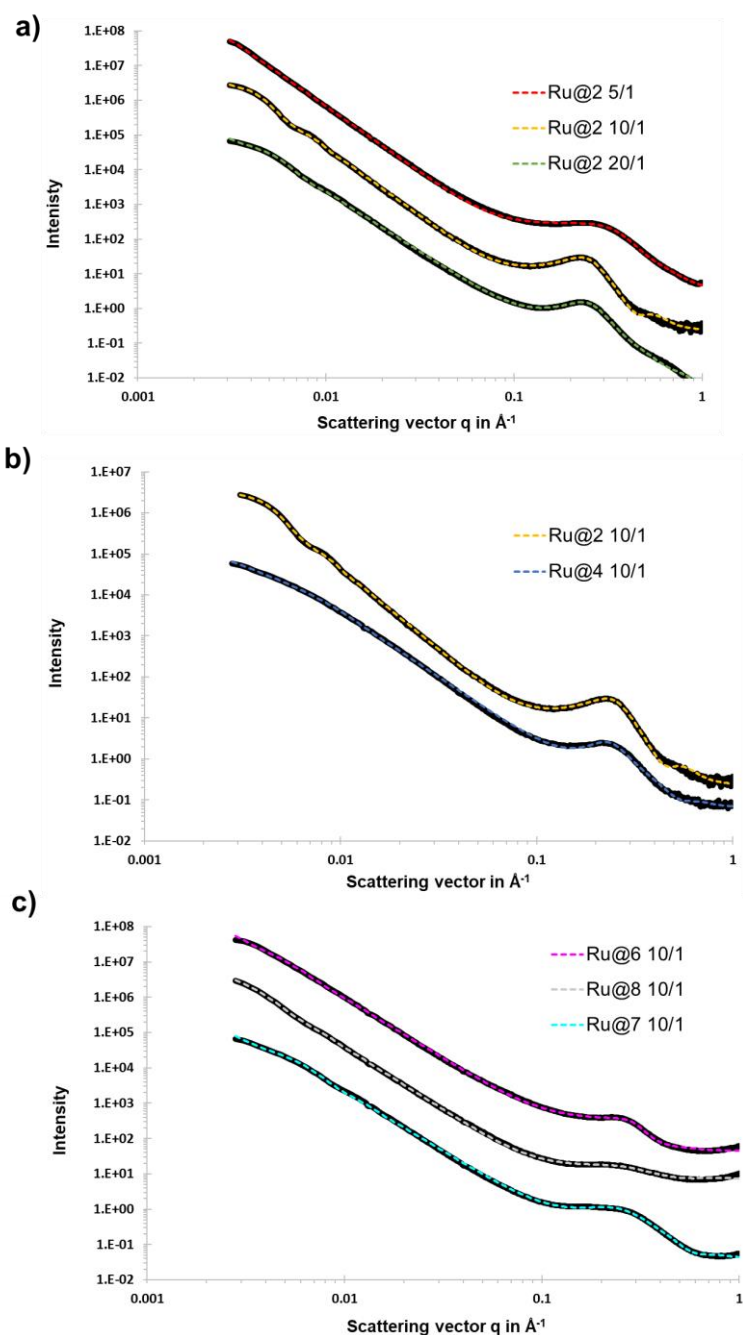


Figure 2.5 SAXS spectra of Ru NP assemblies produced from ligands **2**, **4**, **6**, **7** and **8**. The experimental SAXS curves are plotted in Log I(q) vs Log q representation in black lines and the fitting curves corresponding to the calculated SAXS curves from the model are plotted in dashed lines. a) SAXS curves corresponding to the complex **Ru@2** at different molar ratio: red line for Ru/L molar ratio 5/1, in yellow for the molar ratio 10/1 and in green for the molar ratio 20/1; b) SAXS curves corresponding to the complex **Ru@2** (yellow curve) and **Ru@4** (blue curve); and c) SAXS curves corresponding to the complex **Ru@6** (magenta curve), **Ru@8** (gray curve) and **Ru@7** (cyan curve).

At higher values of q ($q_{max} = 0.2-0.3 \text{ \AA}^{-1}$) we observed a peak interpreted as a correlation distance between the metallic NP (center-to-center distance between Ru NP in the superstructure).^{8,28} These correlation distances were found to vary between 2.2 and 2.9 nm, according to the nature of the ligand, and the Ru/L molar ratio (Table 2.1). Slightly larger correlation distances were measured in the case of dicarboxylic ligands compared to diamine ones. This is consistent with the dimensions of these ligands and the nanoparticle sizes. The self-assembly process can be directed to tune the inter-particle spacing by using BAd and DAd ligands; and with ligands **4**, **7** and **8**, larger correlation distances were measured compared to ligands **2** and **6**, respectively. For a given ligand, the increase of the Ru/L molar ratio contributes to enhance the spatial distribution of the NP, creating a more homogeneous particle network. Indeed, for ligand **2** the SAXS curve shows at intermediate angles a correlation peak larger for the Ru/L ratio 5/1 (Figure 2.5a), reflecting a change in distribution of inter-particle distance with an increase of the polydispersity.

Other effects are directly observable on the SAXS curves at small angles ($<0.01 \text{ \AA}^{-1}$). The oscillations are due to a contribution of structure factor $S(q) \neq 1$, reflecting the presence of large structures interacting each other with a correlation distance shorter than their diameter. For **Ru@2** with Ru/L ratio of 10 and 20, the formation of 3D assembly containing Ru NP was promoted with a regular spatial spacing ($>500 \text{ \AA}$). The value of the slope at small angle, reflecting the state of the surface of the large agglomerate, does not change significantly when increasing the Ru/**2** ratio. For **Ru@4**, the oscillations at very small angles disappeared and the decrease of the slope at the beginning indicates a significant change of the size of the agglomerate; the state of the surface showing more irregularity compared with **Ru@2**. By replacing in the global equation applied to fit the data (see experimental section) the term corresponding to the power law function with a “Guinier-Porod” function, we can evaluate the gyration radius R_g of the agglomerates, which is close to 90 \AA . For Ru NP connected through amine ligands, the oscillations are absent and this phenomenon is probably correlated to the loss of spatial organization of large assemblies. With this ligand, the NP assembly

is presented as amorphous aggregates of variable size.

2.2.1.4 Electron tomography analyses

To confirm the short-range order between the Ru NP, we performed an ET analysis on a typical aggregate obtained from ligand **2** at a Ru/L molar ratio of 10 (Figure 2.6a). The measures were performed by A. Falqui in King Abdullah University of Science and Technology.

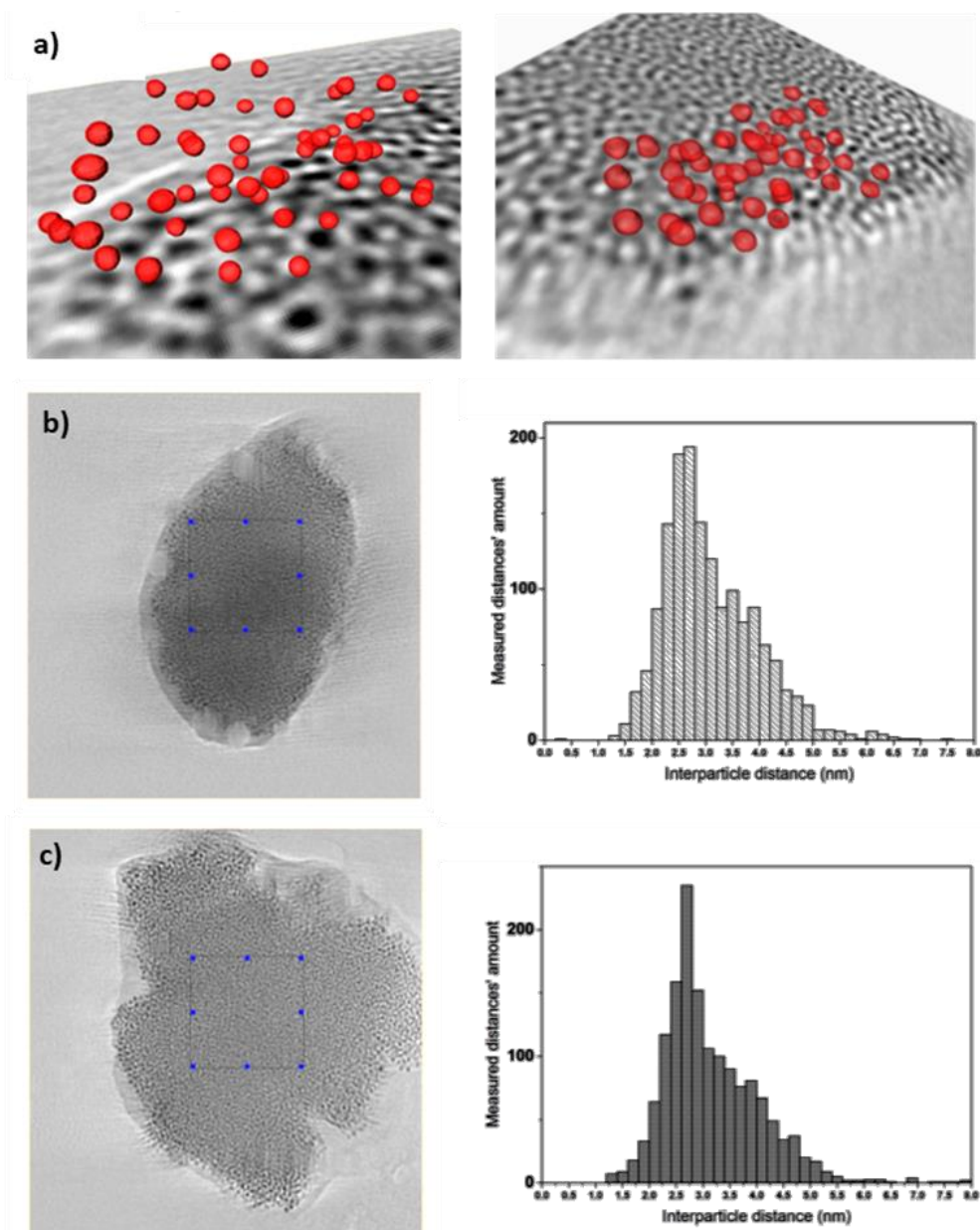


Figure 2.6 a) 3D manual reconstruction of some Ru NP from the corresponding tomogram. A slice of the latter was used just as a visual background for the NP. It should be noticed that not all the NP imaged by ET are reported, but just few of them, properly chosen in order to make it

clearly distinguishable. b) top part of the cluster and the correlation distance between Ru NP extracted from the square; c) center part of the cluster and the correlation distance between Ru NP extracted from the square.

After performing ET on large NP assemblies, it was possible to determine the distribution of their distance (Figure 2.6b, c) and to reconstruct the 3D shape of some of them, indicating a Ru NP mean size of 1.9 ± 0.3 nm and an inter-particle distance of 2.65 nm. The Ru NP mean size determined by ET for this sample is in excellent agreement with the WAXS data (Table 2.1, 2 nm), and the inter-particle distance is perfectly consistent with the one determined by SAXS analysis (Table 2.1, 2.71 nm).

2.2.2 Coordination of carboxylate and amine ligands on Ru nanoparticle surface

In the case of the use of carboxylic stabilizers for NP synthesis, different coordination modes of carboxylate on metallic surface have been reported: i) monodentate; ii) chelating bidentate; and iii) bridging bidentate.²⁹ The coordination of primary amine³⁰ ligands to Ru NP prepared by the decomposition of [Ru(COD)(COT)] has already been studied. NMR studies have unambiguously demonstrated the coordination of octylamine to the surface of the Ru NP.³¹ In our case, the coordination of **5** and **6** by the amine has been confirmed experimentally by X-ray photoelectron spectroscopy (XPS), infrared (IR) and solid-state NMR (SS-NMR) (see below).

2.2.2.1 Surface modeling from coordination complex analyses

In order to obtain better insight on the coordination mode of carboxylic acid derivatives onto the Ru NP surface we achieved the reaction of [Ru(COD)(COT)] with **1** and **2**. Reports concerning the reactivity of [Ru(COD)(COT)] with carboxylic acid derivatives have previously shown that reaction with 9-anthracenecarboxylic gives the complex [Ru(9-anthracenecarboxylate)₂(COD)],³² and with acetic acid gives the Ru complex [Ru(CH₃COO)(η^4 -1,4-COD)(η^5 -1,5-COT)].³³ [Ru(COD)(COT)] reacts smoothly with **1** at room temperature to give [Ru(κ^2 -AdCOO)(η^2 , η^2 -C₈H₁₂)(η^3 -C₈H₁₁)], **Ru1**, isolated as a pale yellow solid in 64% yield was characterized by NMR, IR and single crystal X-ray crystallography (XRD) (Figure 2.7).

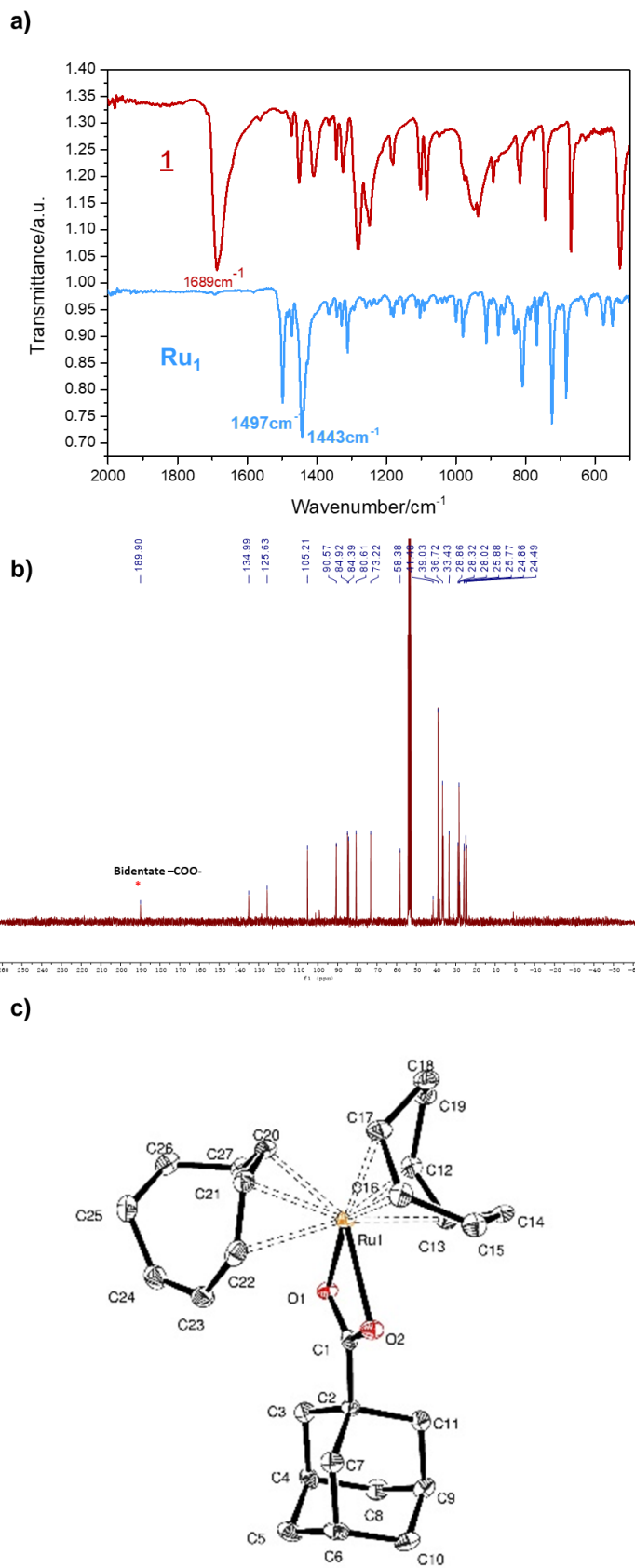
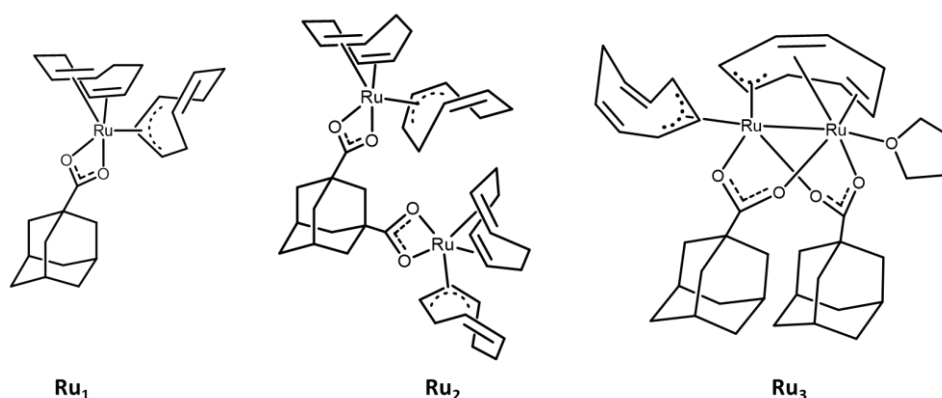


Figure 2.7 a) Infrared spectrum, b) $^{13}\text{C}\{^1\text{H}\}$ NMR characterization and c) crystal structure of $[\text{Ru}(\kappa^2\text{-AdCOO})(\eta^2, \eta^2\text{-C}_8\text{H}_{12})(\eta^3\text{-C}_8\text{H}_{11})] \text{Ru}_1$.

Ru₁ results from the coordination of the carboxylic acid (Scheme 2.3), through oxidative addition of the O–H bond inducing the reduction of cyclooctatriene to form an η^3 -allyl system. Likewise, the coordination of ligand **2** with [Ru(COD)(COT)] leads to the O–H bond cleavage of the ligand to produce a carboxylate Ru complex. In this case, the presence of two carboxylic acids on the ligand allowed synthesizing a bimetallic complex in which **2** in the carboxylate form acts as a bridge. **Ru₂** was isolated as yellow powder in 52% yield and characterized by NMR, IR and elemental analyses (Figure 2.8). Similar reactivity, *i.e.* oxidative addition followed by reduction of the cyclooctatriene molecule, has been previously reported with Si–H bonds, in which the reduced cyclooctatriene is coordinated to the Ru center through the three carbons in the allyl form and the two carbons of the double bond.³⁴⁻³⁵



Scheme 2.3 Structure of **Ru₁₋₃** complexes obtained by reaction of [Ru(COD)(COT)] with ligands **1** and **2**.

Upon heating these carboxylate Ru complexes in the presence of ligands, the unsaturated ligands of the Ru center are generally removed. We experimented a similar procedure, *i.e.* heating **Ru₁** at 55 °C in THF, but without any excess of ligand, in an attempt to reproduce the formation of Ru NP by loss of the unsaturated ligands. A mixture of **1**, **Ru₁**, and other species was obtained. Crystals grown from a saturated solution of the mixture in THF, which correspond to a bimetallic complex **Ru₃**, were isolated. **Ru₃** contains two ligand **1** coordinated, chelating both metallic centers with a THF molecule attached to one Ru atom (see Figure 2.9). This finding is in line with the

formation of Ru NP by the coordination of ligand **1** to the Ru NP surface.

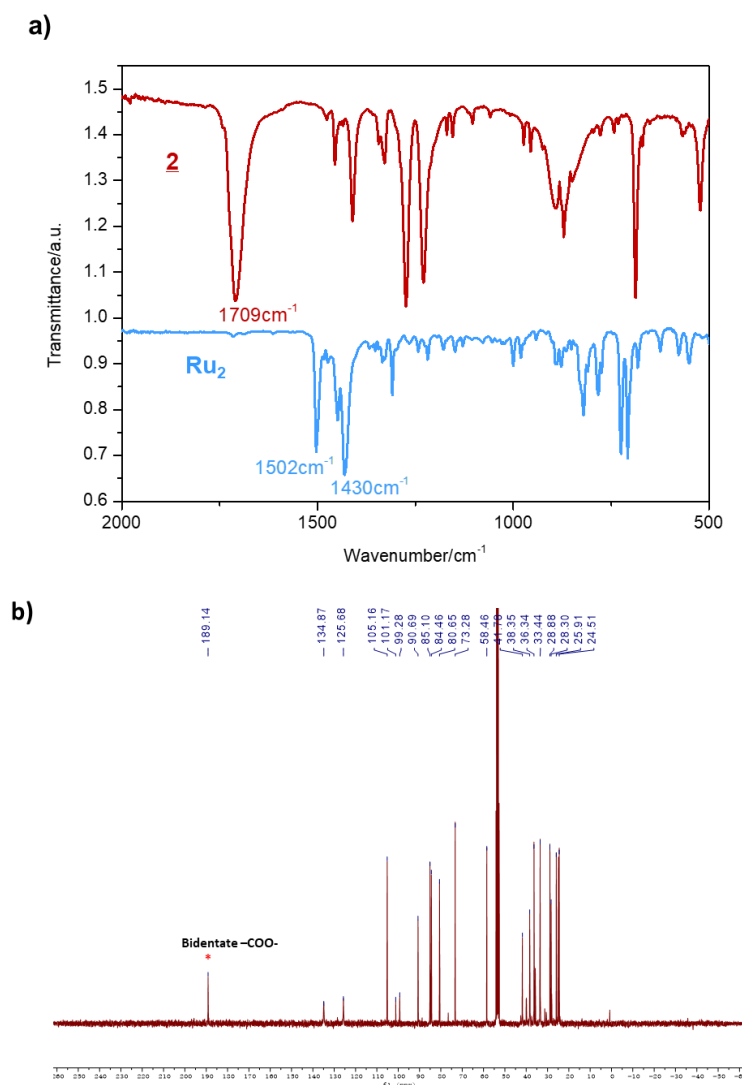


Figure 2.8 a) Infrared spectra and b) ¹³C{¹H} NMR spectrum of the dimer [Ru₂(κ²-Ad(COO)₂)(η²,η²-C₈H₁₂)₂(η³-C₈H₁₁)₂] **Ru₂**.

In the two isolated Ru complexes bearing ligands **1** and **2**, the carboxylic acids are easily deprotonated and the carboxylate ligands are chelating bidentate. Complexes **Ru₁** and **Ru₂** show in their respective IR spectra the typical ν_{as}(COO⁻) and ν_s(COO⁻) bands of the carboxylate ligand at 1497/1443 and 1502/1430 cm⁻¹, respectively. In IR, the difference in ν_{as}(COO⁻) and ν_s(COO⁻) (Δν), is generally used to determine the coordination mode of the carboxylate group. In that case, the Δν are 54 and 72 cm⁻¹ for **Ru₁** and **Ru₂**, respectively, which is in accordance with a chelating bidentate coordination (Δν < 110 cm⁻¹).³⁶ The ¹³C NMR spectra of these complexes show singlets

2.2.2.2 Infrared of Ru nanoparticles and Ru nanoparticle assemblies

As far as Ru NP stabilized by carboxylate (acetate) ligands are concerned, Poteau *et al.* reported a bridging bidentate coordination mode ($\Delta\nu = 145 \text{ cm}^{-1}$),²⁴ in accordance with data reported for molecular (or polymeric) Ru species bearing such ligands.³⁸⁻⁴¹

The IR spectra of **Ru@2** samples prepared at different Ru/L ratio are shown in Figure 2.10a and compared to the one of the free ligands.

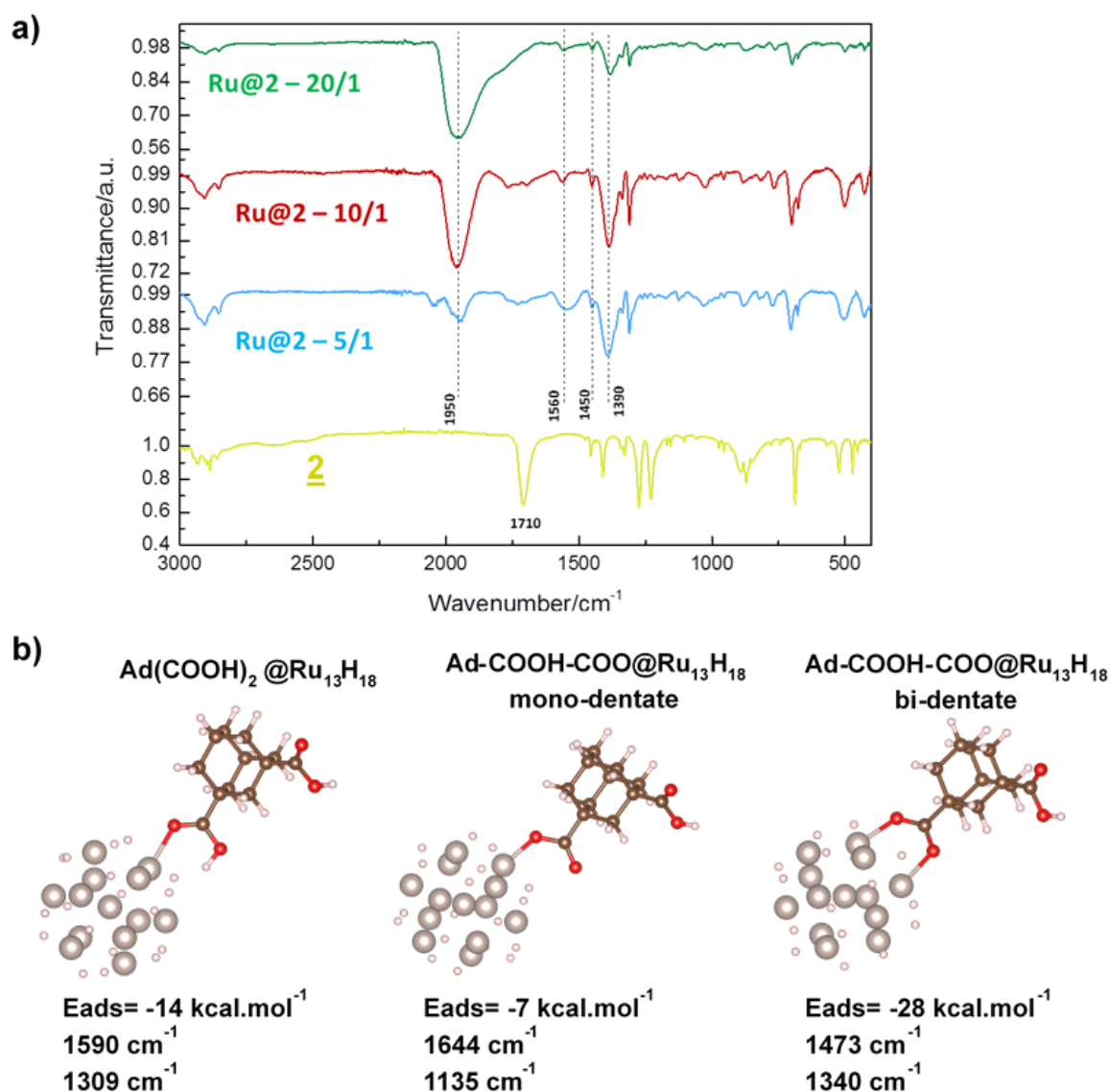


Figure 2.10 a) Infrared spectra of **Ru@2** prepared using different Ru/L ratio, together with ligand **2**; and b) simulated infrared frequencies of different coordination modes between Ru₁₃

cluster and ligand **2** by theoretical calculations.

First, it is clear as observed for coordination complexes **Ru1-3**, the ligand **2** has been deprotonated since no carboxylic acid (-C=OOH) stretching vibration bands are visible at 1710 cm^{-1} . Whatever the Ru/L ratio, several bands are visible in the $1600\text{-}1300\text{ cm}^{-1}$ region. As in the case of Ru NP stabilized by acetate ligands,²⁴ we identified bands at $1560/1390\text{ cm}^{-1}$ ($\Delta\nu = 170\text{ cm}^{-1}$), which are consistent with bridging bidentate carboxylate coordinated ligands. Density functional theory (DFT) calculations performed on a $\text{Ru}_{13}\text{H}_{18}@\text{(Ad-COOH-COO}^-)$ model predicted bands at 1473 and 1340 cm^{-1} ($\Delta\nu = 133\text{ cm}^{-1}$) (Figure 2.10b). The frequency of the $\nu_{\text{as}}(\text{COO}^-)$ mode is underestimated in our calculation, as similarly reported elsewhere.²⁴ Other bands are visible at 1450 , 1361 , 1337 and 1312 cm^{-1} . The band at 1450 cm^{-1} is characteristic of CH_2 scissoring. These bands are not consistent with the presence of monodentate carboxylate species, since monodentate species should give a $\Delta\nu > 200\text{ cm}^{-1}$. DFT calculations were performed on $\text{Ru}_{13}\text{H}_{18}@\text{Ad}(\text{COOH})_2$ model in two possible monodentate coordinations, the favorable model with high adsorption energy predicts bands at 1590 and 1309 cm^{-1} ($\Delta\nu = 281\text{ cm}^{-1}$) (Figure 2.10b). Additionally, monodentate carboxylate Ru complexes give bands for the $\nu_{\text{as}}(\text{COO}^-)$ mode at around 1600 cm^{-1} .³⁷ Although it is difficult at that point to safely assign these bands, we can propose the presence of chelate bidentate species.

Beside to the bands attributed to carboxylate species, a band at $1940\text{-}1960\text{ cm}^{-1}$ (according to the Ru/ligand ratio) is also observed, as in the work of Poteau *et al.* In our case, however, the intensity of this ν_{CO} band is very high and depends on the Ru/ligand ratio. At a Ru/ligand ratio of 5, two bands are visible at 2040 and 1942 cm^{-1} ; for a ratio of 10 a single broad band at 1962 cm^{-1} is observed, and at a ratio of 20 the band at 1957 cm^{-1} is very broad with a shoulder at 1800 cm^{-1} , which could correspond to bridged CO.⁴¹ The shift of the main band as well as the appearance of new bands could be due to an influence of the CO coverage.⁴²⁻⁴⁵ Interestingly, the adsorbed CO species could be removed easily by vacuum treatment as shown by IR (Figure 2.11).

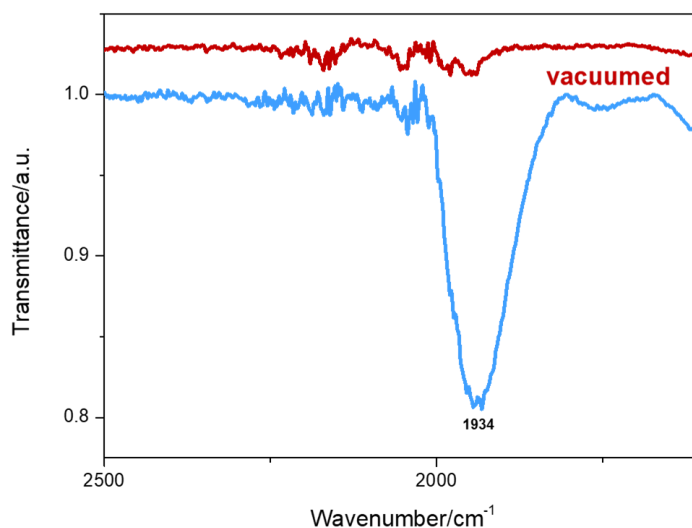


Figure 2.11 Infrared spectra of **Ru@2** at Ru/L ratio of 10 before (blue) and after vacuumed (red).

To determine whether the CO arises from ligand **2** or THF, we performed the synthetic reaction to produce Ru networks with labeled ligand **2** (Ad-(¹³COOH)₂) using a Ru/ligand ratio = 10. We recorded the IR for which a shift should be observed in the ν_{CO} band if the ¹³CO resulted from the decarbonylation of the ligand. Figure 2.12 shows the spectra obtained with unlabeled and labeled **2**.

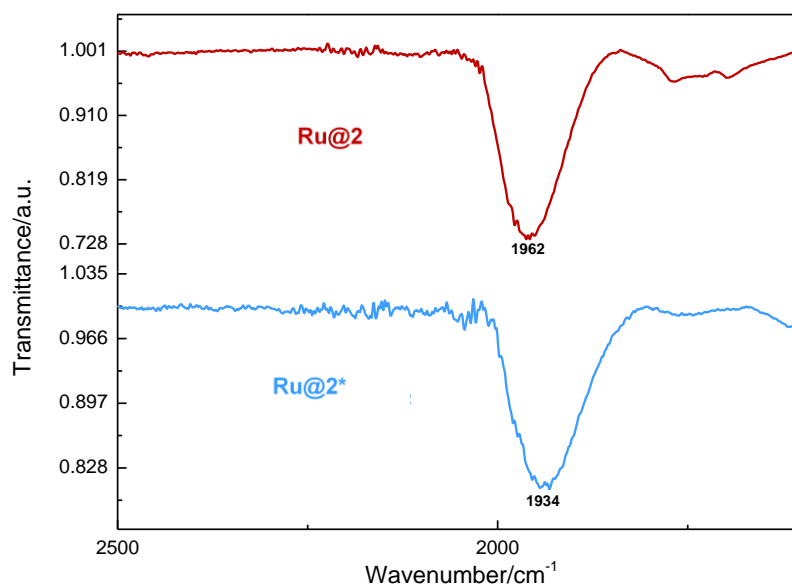


Figure 2.12 Infrared spectra of Ru NP assemblies with ¹³C labelled carboxylic group (**Ru@2***) and with unlabeled carboxylic group (**Ru@2**).

The CO band for the unlabeled **2** is observed at 1962 cm^{-1} , whereas for the labeled **2*** the ν_{CO} band is found at 1934 cm^{-1} . When $^{12}\text{C}^{16}\text{O}$ is replaced by $^{13}\text{C}^{16}\text{O}$ ($R = 0.978$), the differences between observed and calculated frequencies are generally low. In our case, the calculated frequency should be at 1918 cm^{-1} , so the difference (16 cm^{-1}) is relatively large. This could be because, in addition to ligand **2** decarbonylation, we may also observe some THF decomposition. The large envelopes at 1934 cm^{-1} could encompass two bands ($\text{Ru}(^{13}\text{CO})(^{12}\text{CO})$); the $\text{Ru}(^{13}\text{CO})$ arising from **2** decarbonylation and the $\text{Ru}(^{12}\text{CO})$ from THF decomposition. The fact that THF decomposition also occurs during the reaction of $[\text{Ru}(\text{COD})(\text{COT})]$ with H_2 and polymantane ligands was supported by the ν_{CO} band at $1914\text{--}1923\text{ cm}^{-1}$ observed in the case of the diamine ligands **5**, **6**, **7** and **8** (Figure 2.13).

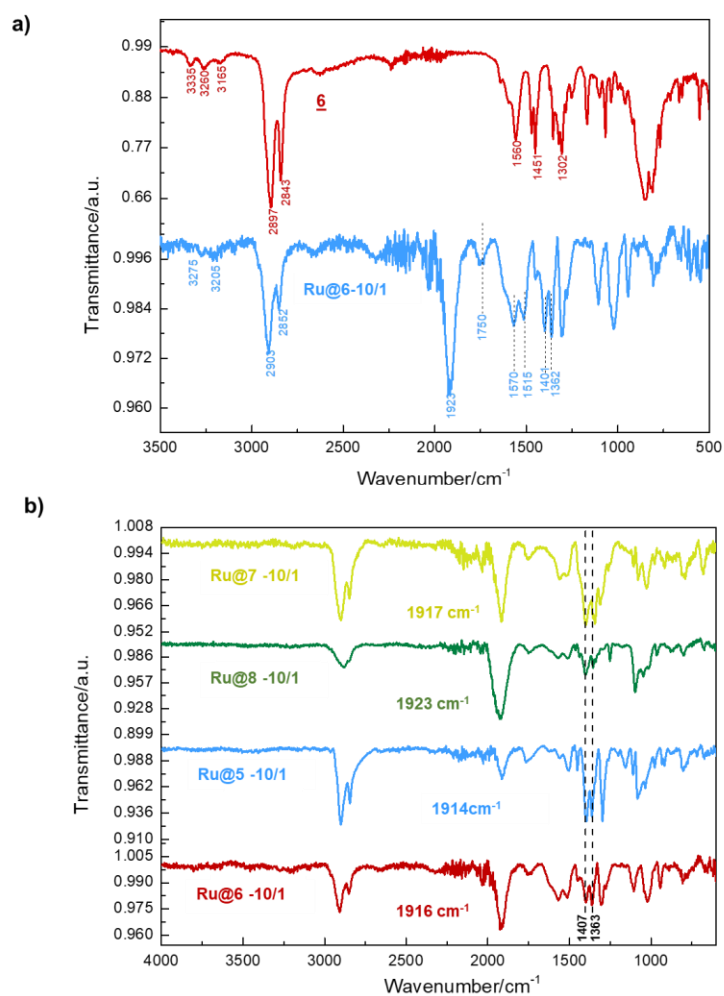


Figure 2.13 Infrared spectra of a) ligand **6** and Ru@6 and b) Ru@5, Ru@6, Ru@7 and Ru@8 at Ru/L ratio of 10.

The IR spectrum of **Ru@6** shows bands at 3275-3205 and 2903-2852 cm^{-1} (Figure 2.13a) corresponding to the N-H and C-H stretching bands of the ligand, respectively; confirming the presence of the amine ligands near the surface of the Ru particles. Bending vibration bands of the N-H bond at 1560 cm^{-1} are splitted into two peaks at 1570 and 1515 cm^{-1} . The peaks at 1350-1400 cm^{-1} are supposed to be related to C-C bonds adjacent to N-C bond. While the N-C stretching vibration peak at 1300 cm^{-1} was not detected in **Ru@6**, a slightly downshifted peak appears at 1296 cm^{-1} for **Ru@5**.

2.2.2.3 Solid-State NMR analyses

The ^{13}C MAS SS-NMR spectrum of **Ru@2** (Figure 2.14) has been recorded on a compound prepared with ^{13}C labeled **2** ($\text{Ad}-(^{13}\text{COOH})_2$) in order to obtain clear signals of the sp^2 carbons of carbonyl groups.

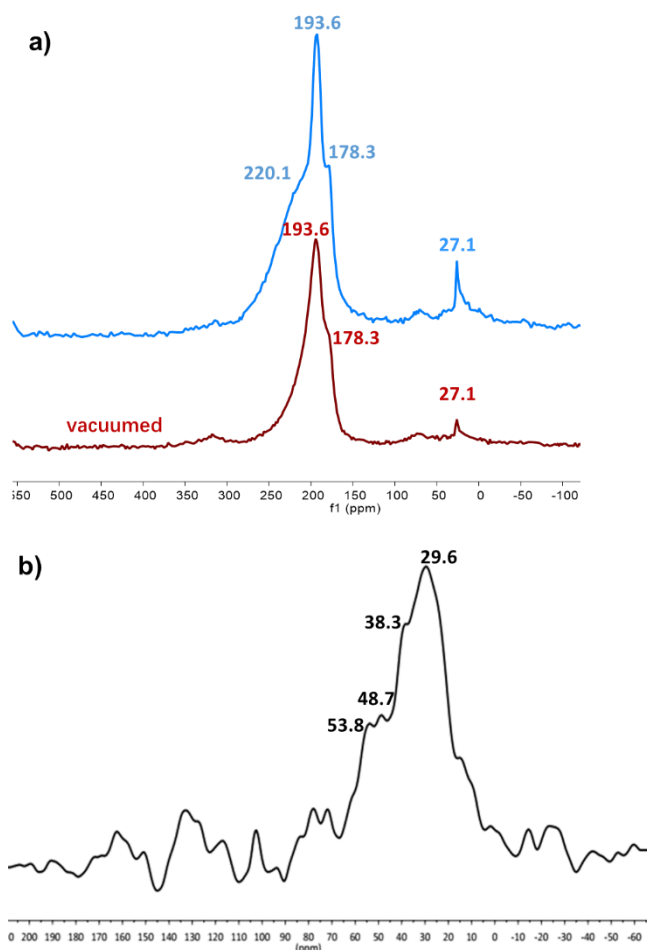


Figure 2.14 ^{13}C UDEFT (Uniform driven equilibrium Fourier transform) MAS SS-NMR spectrum of a) **Ru@2** (Ru/ligand ratio = 10) obtained with a ^{13}C labeled **2** ($\text{Ad}-(^{13}\text{COOH})_2$); and b) **Ru@6**.

Beside the peak at 27.1 ppm corresponding to the sp^3 carbons of the adamantane cage, carbonyl species are clearly detected at 178.3, 193.6 and 220.1 ppm. The peak at 220.1 ppm has been assigned to CO ligands on the Ru NP surface. Indeed, we independently checked by IR (Figure 2.11) and NMR that this adsorbed CO can be easily removed from the NP surface by a simple vacuum treatment of the sample at room temperature overnight. This treatment induces the disappearance of the CO peak in ^{13}C MAS SS-NMR at 220.1 ppm. The fact to observe an intense signal for this CO peak after labeling of **2** suggests that the carbonyl ligand results from **2** decarbonylation. The peak at 193.6 ppm has been attributed to the bridging bidentate carboxylate ligands (186.0 ppm in the work of Poteau *et al.*²⁴ and 198.4 ppm in **Ru₃**), whereas the peak at 178.3 ppm could be tentatively attributed to chelate bidentate species (a peak at 185.2 ppm was also observed in the mixture of **Ru₃** synthesis). ^{13}C -NMR studies on Ru complexes bearing chelate bidentate carboxylate ligands have reported chemical shifts (182-186 ppm), which are consistent with this attribution.³⁷ The ^{13}C MAS SS-NMR spectrum of **Ru@6** shows broad bands at 30-50 ppm characteristic of the sp^3 carbons of ligand **6**.

2.2.2.4 CO adsorption analyses

We used carbon monoxide adsorption on the Ru NP produced from ligands **2** (**Ru@2**) and **6** (**Ru@6**) to probe the charge transfer induced by the ligand coordination to the metallic surface by infrared spectroscopy. Prior to CO adsorption, the Ru NP were first outgassed under vacuum to eliminate the CO ligands arising from the decomposition reaction. After the treatment of the sample with CO (1 bar at room temperature), the IR spectra were recorded and the ν_{CO} stretching frequency were observed at 2050-1940 and 1980-1920 cm^{-1} for **Ru@2** and **Ru@6**, respectively (see Figure 2.15 for the corresponding spectra). The use of ligand **6**, a donor ligand, contributes to increase the electronic density on Ru NP, and consequently to a significant Ru \rightarrow CO π -donation. The increase of the electronic density in the π^* of the CO causes the C–O bond length to increase and thus the ν_{CO} to decrease. In the case of ligand **2**, the charge transfer occurs from the metal to the ligand, and consequently the CO band frequency shifted to higher wavenumber.

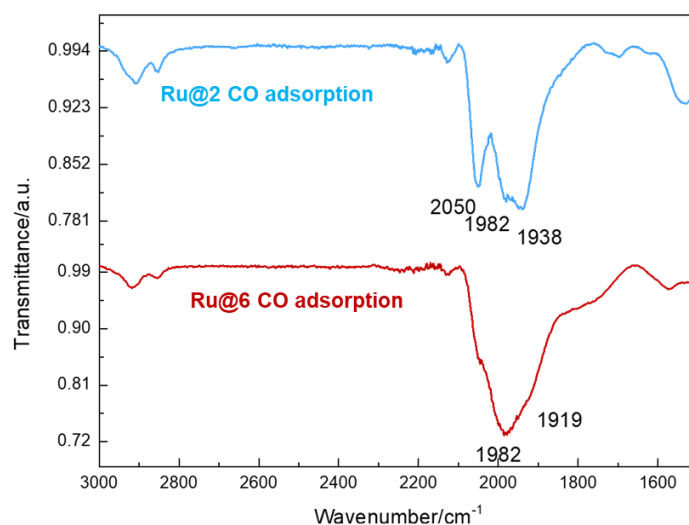


Figure 2.15 Infrared spectra of **Ru@2** and **Ru@6** after CO adsorption.

2.2.2.5 X-ray photoelectron spectroscopy analyses

XPS analyses support the charge repartition deduced from CO adsorption. The details of the analyses of **Ru@2** and **Ru@6** at a Ru/L molar ratio of 10 are depicted in Tables 2.2 and 2.3 and Figure 2.16. As far as the Ru(3d) and (3p) core levels are concerned, the data obtained for the Ru 3d_{5/2}, Ru 3d_{3/2} and Ru 3p_{3/2} peaks are consistent with metallic ruthenium.⁴⁶ A slight difference in the binding energy of the Ru 3p_{3/2} peaks between the product obtained from ligands **2** (461.3eV) and **6** (461.2 eV) is consistent with Ru NP that are more electro deficient in the case of ligand **2**.

The existence of C and O in the assembly is evidenced by peaks observed of C 1s (286.8 and 288.3 eV) and O 1s (531.2 and 532.9 eV). The mass fraction of Ru calculated with both ligands is in good agreement with ICP analyses (Table 2.1). For **Ru@6**, the binding energy of C1s at 286.8eV is assigned to C-N species. The nitrogen percentage is estimated to be 4.5%.

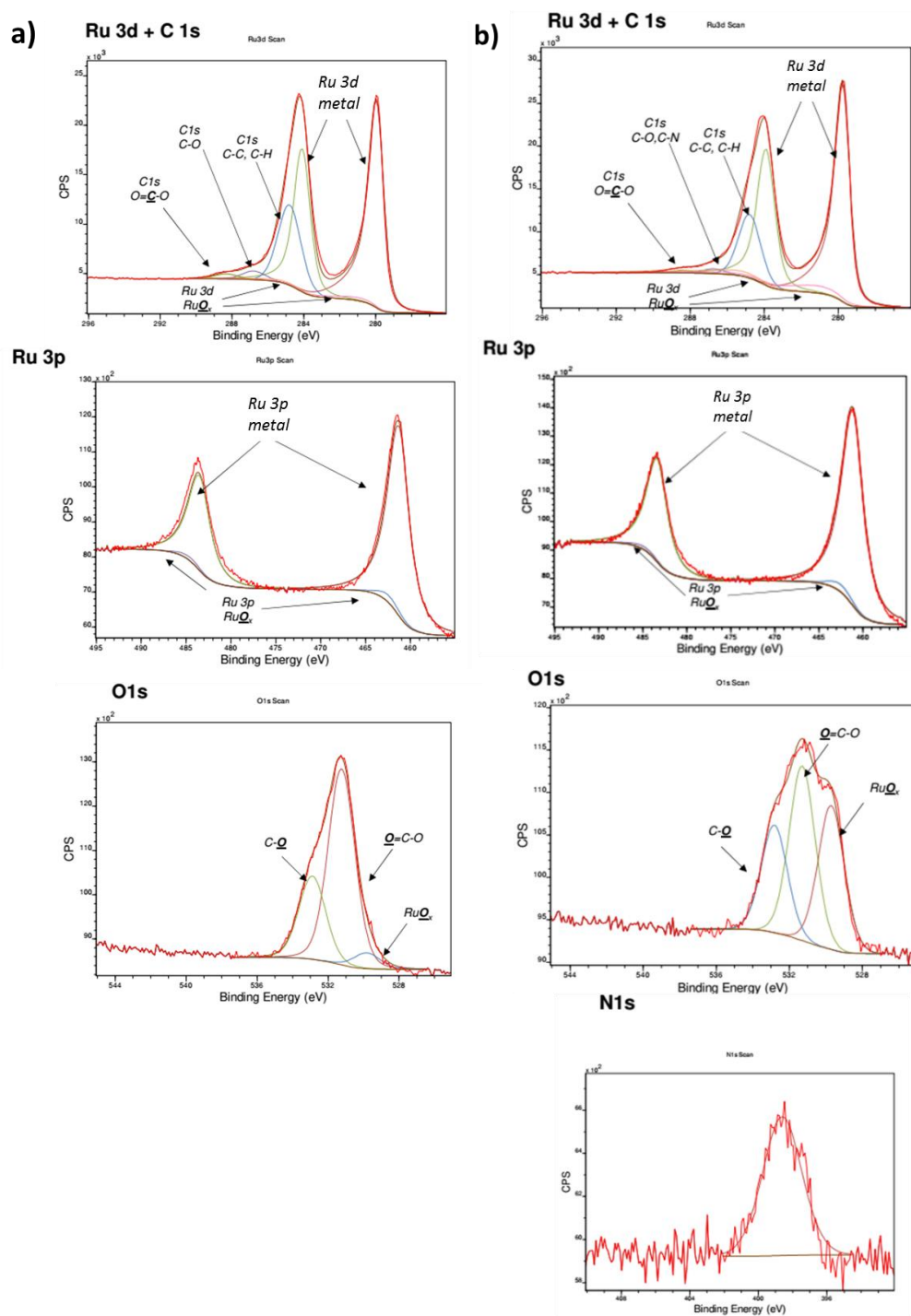


Figure 2.16 XPS spectra of Ru 3d + C 1s, Ru 3p, O 1s and N 1s of: a) Ru@2 and b) Ru@6.

Table 2.2 XPS analyses of Ru@2 (Ru/ligand = 10).

Name	Position	FWHM	% Conc.
Ru 3d	279.9-284.1	1.0-1.1	16.4
	280.7-284.9	2.2-2.2	0.7

			17.1
Ru 3p	461.3-483.5	2.8-2.7	-
	462.6-484.8	3.0-3.0	-
	285.0	1.5	54.6
C 1s	286.8	1.5	5.8
	288.3	1.5	3.4
			63.8
	529.8	1.8	0.9
O 1s	531.2	1.8	11.3
	532.9	1.8	4.8
			17.0

Considering the bonding energy of C-NH₂ and nitrides of metal at 400 and 397 eV, respectively, the N 1s spectrum of **Ru@6** shows a peak at 398.6 eV (Table 2.3 and Figure 2.16b) corresponds well to what might be expected for a nitrogen atom donating electron density to the Ru surface *via* its lone pair and, hence, is assumed to arise from the chemisorbed amine. It was reported that coordination of primary amine such as hexadecylamine to iron oxide NP gives a peak at 399.7 eV, whereas the free amine gives a peak at 397.2 eV.³¹

Table 2.3 XPS analyses of **Ru@6** (Ru/ligand = 10).

Name	Position	FWHM	% Conc.
Ru 3d	279.9-284.1	0.9-1.1	20.7
	280.7-284.9	2.2-2.2	2.3
			23.0
Ru 3p	461.2-483.4	2.8-2.7	-
	462.6-484.8	3.1-3.1	-
	285.0	1.4	50.7
C 1s	286.8	1.4	3.8
	288.3	1.4	1.9
			56.4
	529.7	1.7	4.4
O 1s	531.2	1.7	5.3
	532.9	1.7	3.2
			12.9
N 1s	398.6	2.7	4.5

2.2.2.6 Temperature programmed desorption analyses

Temperature programmed desorption (TPD) experiments couple with mass spectrometry (MS) analyses were performed to probe the stability of **Ru@1** and **Ru@2** samples under an inert (helium) atmosphere (Figure 2.17 and Table 2.4).

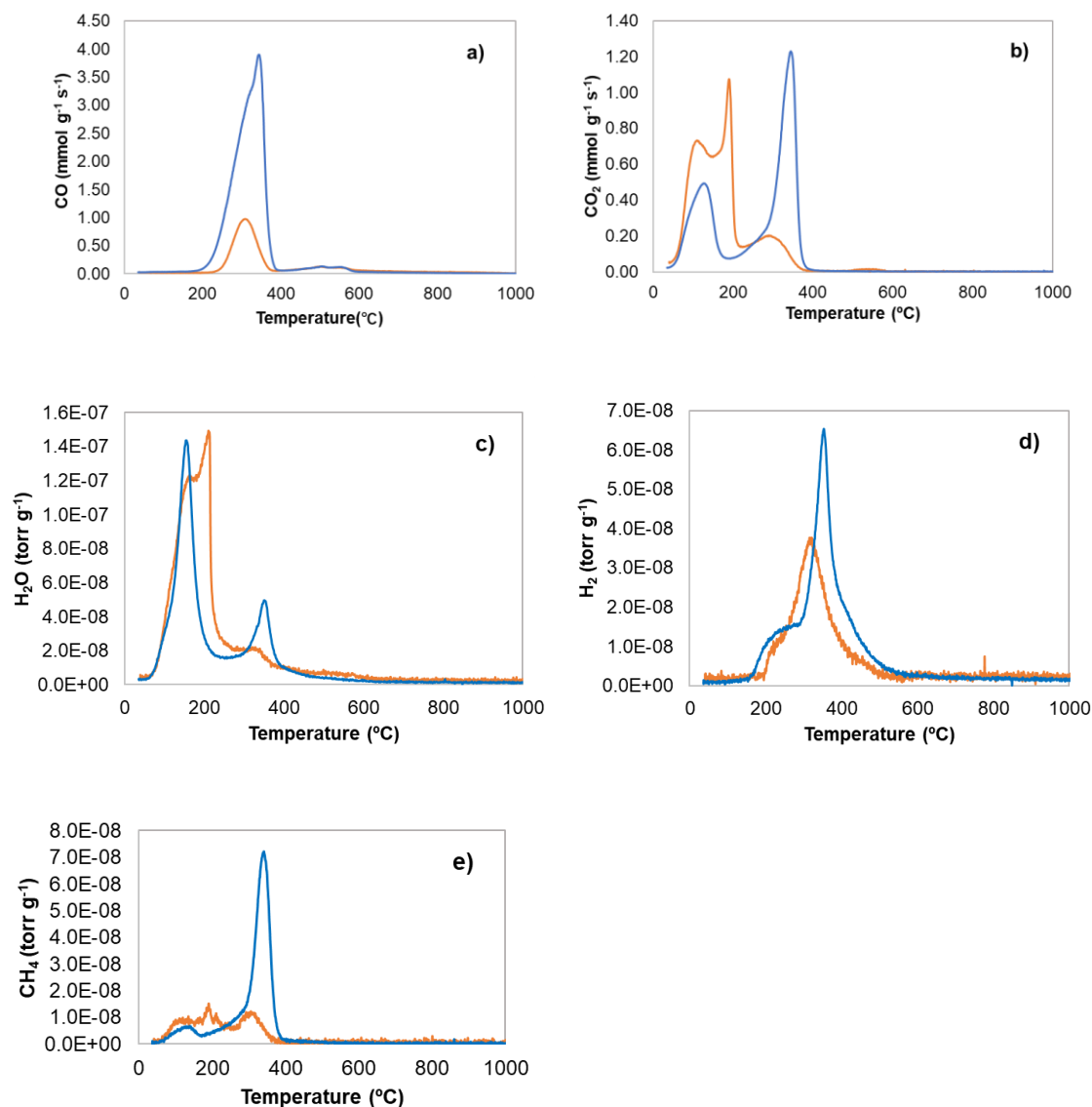


Figure 2.17 Temperature programmed desorption spectra of different desorption species: a) CO, b) CO₂, c) H₂O, d) H₂ and e) CH₄ for **Ru@1** (orange) and **Ru@2** (blue) at Ru/L ratio of 10.

The decarboxylation and decarbonylation reactions started at almost the same

temperature for both samples. For both samples the decarboxylation reaction is a two-step process. The first decarboxylation occurs at low temperature (110-130 °C) and the second one at higher temperature (300-345 °C).

Table 2.4 Temperatures of gas evolution in **Ru@1** and **Ru@2**.

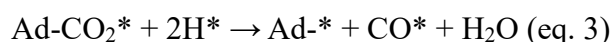
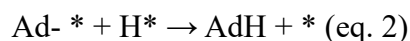
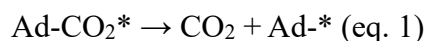
Sample	CO ₂	CO	H ₂ O T (°C)	H ₂	CH ₄
Ru@1	110/190/300	310	160/210/330	240/320	130/190/310
Ru@2	130/345	320/345	155/350	250/350	140/340

For **Ru@1** a narrow and intense peak is also observed at 190 °C. This narrow peak could be related to a Ru-assisted decarbonylation, since narrow peaks are characteristic of catalyzed reactions. While low temperature decarboxylation (< 200°C) prevails for **Ru@1**, for **Ru@2** high temperature decarboxylation (> 300°C) is the major route. Decarbonylation occurs above 300 °C for both samples. For the low-temperature process, CO₂ evolution is concomitant with H₂O and little CH₄ evolution. The high temperature process involves desorption of CO₂, large amount of CO, CH₄, H₂ and H₂O. It is worth noting that the CO/CO₂ ratio is significantly different for both samples (Table 2.5).

Table 2.5 Quantification of CO and CO₂ evolution in **Ru@1** and **Ru@2**.

Sample	CO (μmol.g ⁻¹)	CO ₂ (μmol.g ⁻¹)	CO/CO ₂
Ru@1	1307	1406	0.93
Ru@2	4115	1345	3.06

The fact that little amounts of CH₄ are associated to the low-temperature process could be rationalized by the fact that this decomposition should involve only the carboxylate groups of the adsorbed ligands and maybe adsorbed hydrogen present on the Ru surface. At low temperatures, the decomposition could thus involve different reactions:



The equation (3) is related to the reverse water-gas shift reaction, which produced CO that can remain adsorbed on the Ru surface. The high temperature process should involve the complete destabilization of the materials, during which, beside CO desorption, desorption of some water, hydrogen and methane is also observed. The formation of methane could arise from CO methanation (equation 4), since ruthenium is known as an active catalyst for this reaction.



From these TPD/MS analyses, it appears that the use of dicarboxylic adamantane **2** should induce the formation of thermally more stable materials than when using the monocarboxylic acid **1**. Our DFT calculations do agree with this statement, since the adsorption energy of **2** to a single Ru₅₅ cluster (64 kcal.mol⁻¹) or to two Ru₅₅ clusters (100 kcal.mol⁻¹) are significantly higher than the one of **1** to a single Ru₅₅ cluster (48 kcal.mol⁻¹).

2.2.2.7 Theoretical calculations

Theoretical calculations using DFT were performed in several systems in order to obtain a better insight on the coordination of ligands onto the Ru NP surface, and also to analyze further the origin of the decarbonylation of a carboxylic acid at room temperature in the presence of dihydrogen in the Ru NP surface.

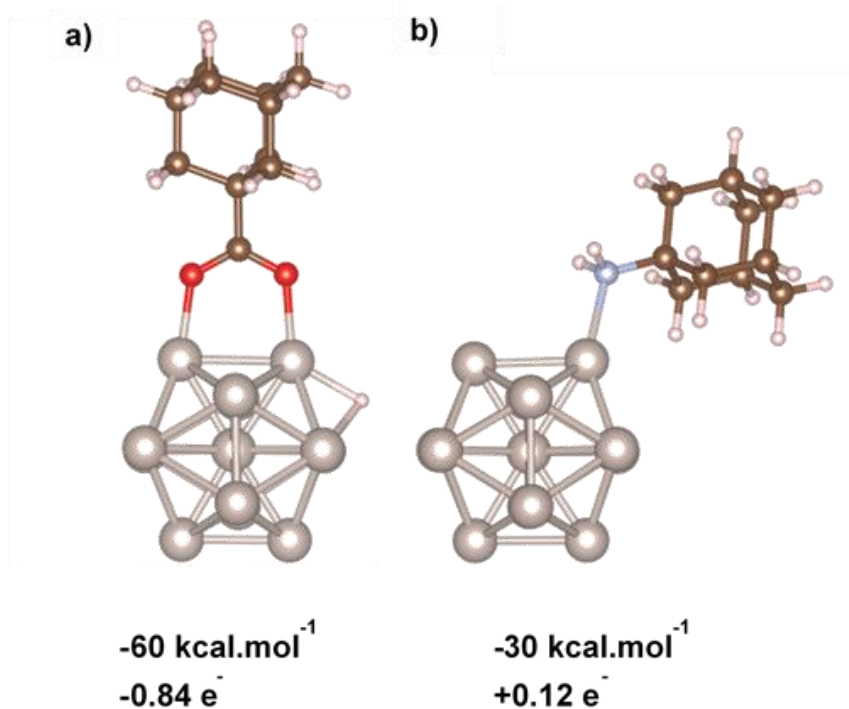


Figure 2.18 Optimized geometry (from DFT), ligand adsorption energy and charge transfer (CT) for a) 1@Ru₁₃ and b) 5@Ru₁₃ models.

A higher binding energy (Figure 2.18) of 1 compared to 5 to a Ru₁₃ cluster was predicted by DFT. Adsorption energy of $-60 \text{ kcal.mol}^{-1}$ was obtained for 1 on a bare Ru₁₃ cluster, presenting a *syn-syn* bridging coordination with two Ru–O distances of 2.0 and 2.1 Å after the spontaneous O–H bond dissociation on the cluster. Similar energies have been obtained in a previous work involving the coordination of acetic acid on Ru₅₅.²⁸ A significant charge transfer from the cluster to the ligand has been estimated by Bader charge analysis: -0.84 e^- , because of the oxygen lone pair sigma donation and π^* backdonation, with 0.27 e^- given to the hydride. Slightly smaller adsorption energy on a bare Ru₅₅ NP was calculated: $-48 \text{ kcal.mol}^{-1}$, with very similar charge transfer. In the case of 5, in agreement with previous results involving the coordination of amines on RuNP,⁴⁷ the adsorption energy is reduced to $-30 \text{ kcal.mol}^{-1}$. This difference can be associated to a top coordination, with a single Ru–N bond-length of 2.2 Å. In the same way, a lower charge transfer (0.12 e^-) from the ligand to the metal was obtained.

In the case of ligands **2** and **6**, DFT calculations have confirmed greater interactions of the carboxylate groups compared to the diamine ones with both Ru₁₃ and Ru₅₅ NP models. With a single ligand **2**, Ru–O interactions are strong enough to avoid the coalescence of two Ru₁₃ or Ru₅₅ clusters. For ligands **6**, larger clusters are obtained due to coalescence upon geometry optimizations. See Figure 2.19b for the coordination mode of ligand **2** bridging two Ru₅₅ clusters, the charge transfer corresponds to a loss of around 0.8 e⁻ for each NP. In this case, the Ru NP-Ru NP distance is 1.8 nm, measured from both NP centers.

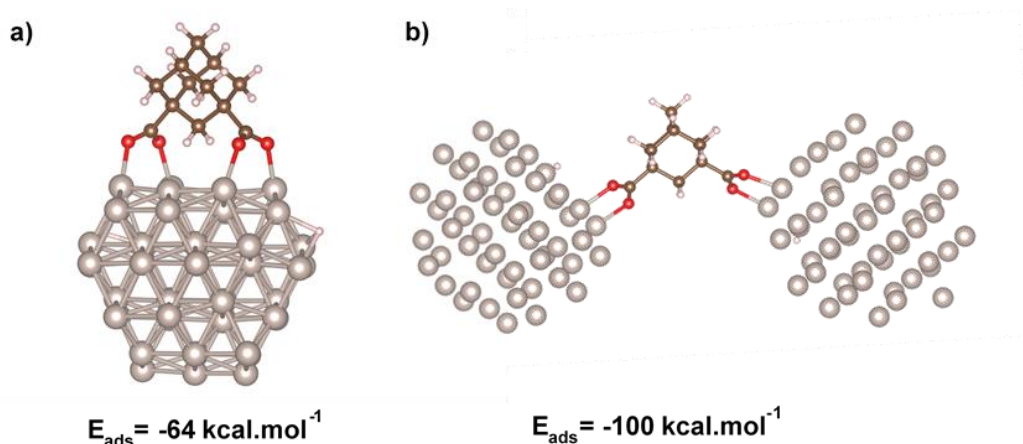


Figure 2.19 a) Optimized structure of one ligand **2** molecule on Ru₅₅ with a bi-carboxylate anchoring coordination; and b) optimized structure of the two **2**@Ru₅₅ species.

Confirmed by DFT, it is concluded that the use of ligands **1** and **5** lead to different charge transfer between the ligand and the Ru NP. DFT calculations, XPS and IR analyses show a similar tendency for possible charge transfer in the case of the ligands Ad-(COOH)₂, **2**, and Ad-(NH₂)₂, **6**: the charge transfer is from the ligand to the metal with the amine ligand, and from the metal to the ligand with the carboxylic ligand.

As far as the presence of CO ligands on the Ru NP is concerned, we were surprised by the intensity of the CO band. Then, the question about its origin arose. Chaudret *et al.*⁴⁸⁻⁴⁹ and Poteau *et al.*²⁴ have also observed the presence of CO ligands on Ru NP formed from [Ru(COD)(COT)] in THF solvent, and have attributed this CO to THF decomposition into propane and CO. In our case, CO could arise either from THF

decomposition or from **2** decarbonylation, as experimentally supported by IR and labelled ^{13}C MAS SS-NMR experiments. Decarbonylation of a carboxylic acid at room temperature in the presence of dihydrogen is very surprising since this reaction usually occurs on catalysts at much higher temperatures. Accordingly, the decarbonylation of propanoic acid in the presence of H_2 on Ru catalyst has been observed above $180\text{ }^\circ\text{C}$.⁵⁰⁻⁵¹ This can be rationalized by the energy barrier necessary to pass for C–C bond breaking, an essential step to produce CO.⁵¹ Our result suggests a very high reactivity of under-coordinated ruthenium species that are formed during the decomposition of $[\text{Ru}(\text{COD})(\text{COT})]$ in the presence of H_2 and **2**. To further investigate this unexpected reactivity, a DFT study was performed on a $\text{Ru}_{13}\text{H}_{16}$ model, as representative species of a small-size reactive intermediate in realistic conditions, and the ligand **2** was replaced by CH_3COOH species for sake of simplicity. Several reaction pathways were considered (Figure 2.20), but only the lowest energy ones are discussed here. The reference initial state is given by those two species infinitely separated. The reaction begins by the thermodynamically favorable coordination of **2** (-23 kcal.mol^{-1}). We will see in the following that among all the investigated pathways, it is very likely that $\text{CO}@_{\text{Ru}_{13}\text{H}_{16}}$ is formed on the surface with the help of an extra H_2 molecule and the release of one H_2O and one CH_4 molecule (-46 kcal.mol^{-1}). This pathway appears reasonable in terms of kinetics and thermodynamics. In this case, the reaction occurs first through the facile (10 kcal.mol^{-1}) C–OH bond dissociation leading to the formation of adsorbed CH_3CO^* and OH^* on the Ru NP surface. A C–C bond breaking with an even lower barrier height (5 kcal.mol^{-1}) follows this step. Yet this $(\text{CH}_3)^*(\text{CO})^*(\text{OH})^*$ intermediate is slightly less stable than the previous one (-35 vs. -43 kcal.mol^{-1}). Owing to the experimental conditions, under H_2 pressure, one dihydrogen molecule can easily react on the surface and act as a thermodynamic driving force, leading to the release of methane and water and finally yielding the final adsorbed CO product (-46 kcal.mol^{-1}).

Another possibility we have explored is a direct C–C dissociation, assuming that some surface hydrides are mobile enough to allow for the clearance of a facet composed by 3 Ru atoms. The corresponding barrier energy is 29 kcal.mol^{-1} , when the

$(\text{CH}_3)^*(\text{COOH})^*@\text{Ru}_{13}\text{H}_{16}$ final state remaining very high in energy (-1 kcal.mol^{-1}).

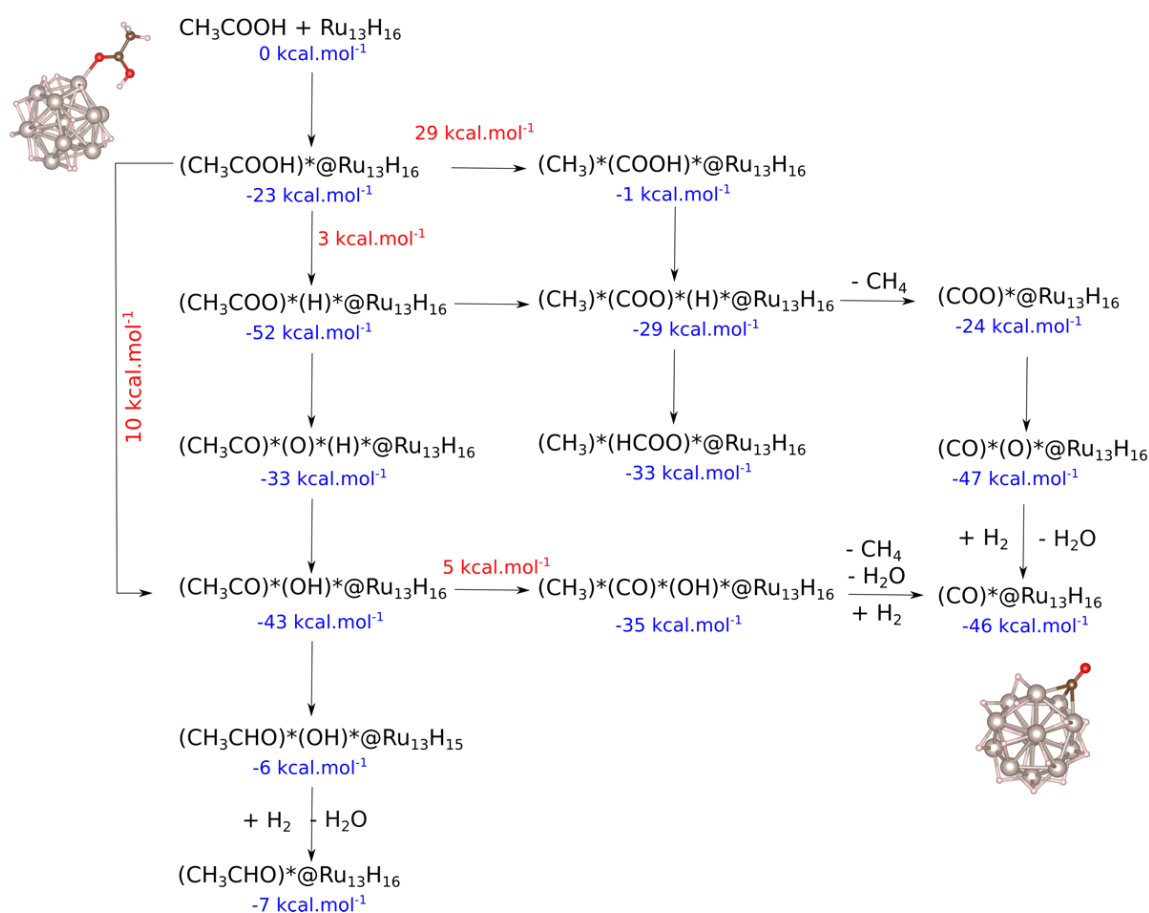


Figure 2.20 DFT investigation of the mechanism of the decarbonylation reaction. Blue values correspond to total energy differences with respect to the initial state, when red ones give energy barrier height.

A second possible pathway is a further dissociation of the carboxylic group (almost barrierless) that yields a very deep well in the potential energy landscape ($(\text{CH}_3\text{COO})^*(\text{H})^*$: $-52 \text{ kcal.mol}^{-1}$). This value is slightly lowered compared to the one reported above for $\mathbf{1}@\text{Ru}_{13}$. This is mainly due to the surface saturation by hydrides. This intermediate corresponds to a thermodynamic trap since neither a further C–C nor C–O dissociation could provide a more stable state. The question thus arising is which principle reaction favor the CO formation herein. Some reported semi-quantitative clues based on previous phase diagrams calculations are to be considered.^{24, 52} These diagrams show that under realistic conditions close to the present experimental ones, a

Ru₅₅ NP under acetic acid concentration and carbon monoxide pressure can respectively accommodate 16 (CH₃COO)*(H)* and up to 63 (CO)*. Owing to the average adsorption energy per ligand (-35 kcal.mol⁻¹ per (CH₃COO)*(H)* and -40 kcal.mol⁻¹ per (CO)*), the final decomposition of a large amount of acids into carbon monoxide can be considered as the strongest driving force.

2.3 Conclusion

We have successfully prepared materials based on well-defined nanometric-sized Ru NP (< 2 nm) surface stabilized by mono or difunctionalized adamantanes, bis-adamantanes and diamantanes ligands, bearing either carboxylic acid or amine functional groups. Monofunctionalized ligands lead to discrete NP, and defunctionalized ones to Ru NP covalent networks. We have shown that the mean NP size and the internal network inter-particle distances can be finely tuned by a proper choice of the ligand and the Ru/ligand ratio. We have also shown that the choice of the ligand is crucial to tune the electronic properties of the metal. In a systematic approach from molecular regime to nanoparticles and networks, the coordination chemistry of these species has been investigated, and it was shown that highly reactive Ru cluster or colloidal species are formed during NP synthesis, which were experimentally shown to be able to decarbonylate carboxylic acids at room temperature in the presence of 3 bar of H₂. DFT theoretical investigation, which support this high reactivity with small clusters, also allowed proposing a preferential low energy pathway for this innovative decarbonylation reaction.

From these fundamental experimental data and simulation, it can be anticipated that these two types of ligands, carboxylic acid vs amine, should induce very different surface states for Ru NP, possibly also different networks assembly, and certainly as a consequence contrasted catalytic performances, which will be demonstrated in the following chapter.

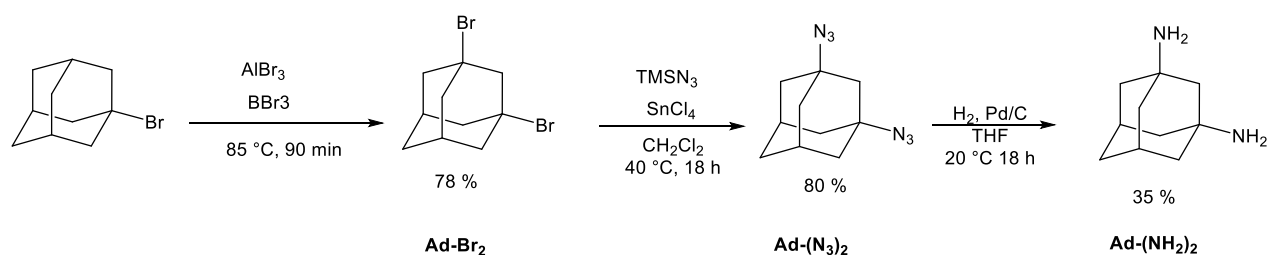
2.4 Experimental section

Materials

The solvents we used in this work were purified with a MBraun SPS-800 solvent purification system and degassed by freezing cycles. [Ru(COD)(COT)] was purchased from Nanomeps Toulouse. 1-Adamantanecarboxylic acid (AdCOOH, **1**) and 1-Adamantylamine (AdNH₂, **5**), phenylacetylene and decane were purchased from Sigma-Aldrich and used as received.

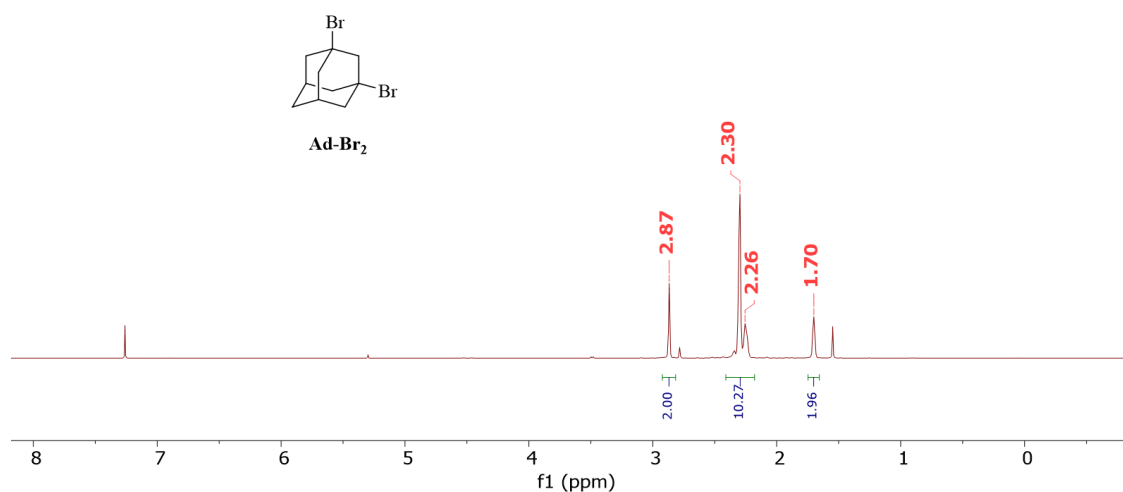
Synthesis of polymantane ligands

Ligand 6: 1,3-diaminoadamantane Ad-(NH₂)₂

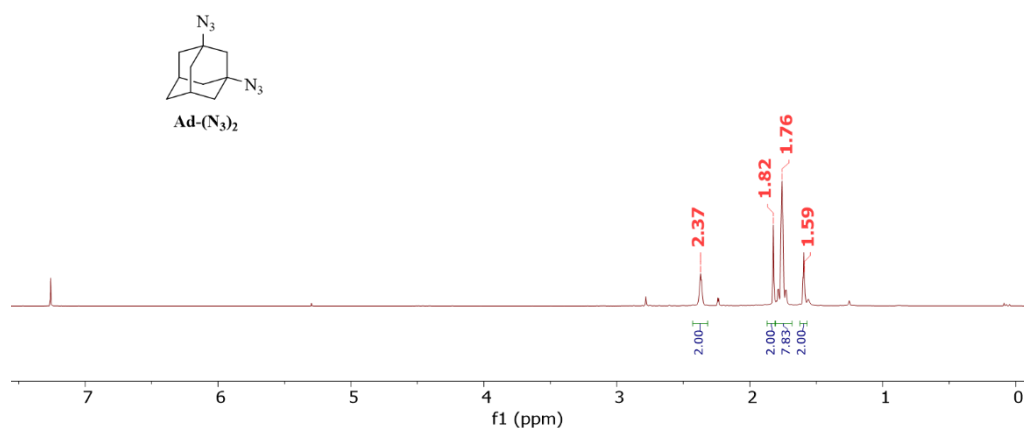


1,3-dibromoadamantane (Ad-Br₂). A dry 250 mL three-necked flask was fitted with a reflux condenser. At $-78\text{ }^\circ\text{C}$ aluminum tribromide (solution of 10 mg in 1 mL Br₂, 0.03 mmol) was added to a solution of dry Br₂ (5 mL) and BBr₃ (1 mL, 10 mmol). The resulting mixture was vigorously stirred and 1-bromoadamantane (2.07 g, 9.6 mmol) was added in one portion. The reaction was gradually heated to $85\text{ }^\circ\text{C}$ for 90 min, during which time HBr were evolved. The reaction mixture was then cooled to room temperature and poured into 100 mL of ice-water, and CH₂Cl₂ (20 mL) was added. With rapid stirring and external cooling (ice bath), the excess Br₂ was quenched by slow addition of solid NaHSO₃, until the red color disappeared. The resulting bilayer mixture was separated and the organic layers were combined, dried with MgSO₄, and concentrated. The residue was crystallized from hot methanol to afford 2.0 g (78 %) of Ad-Br₂ as a white powder. ¹H NMR (300 MHz, CDCl₃) δ (ppm): 1.73 (bs, 2H), 2.2-2.37

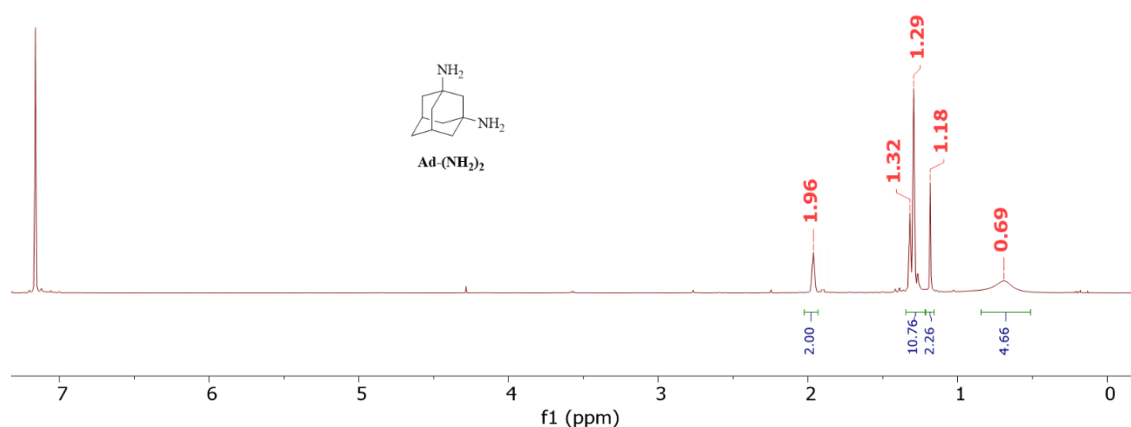
(m, 10H), 2.87 (s, 2H).



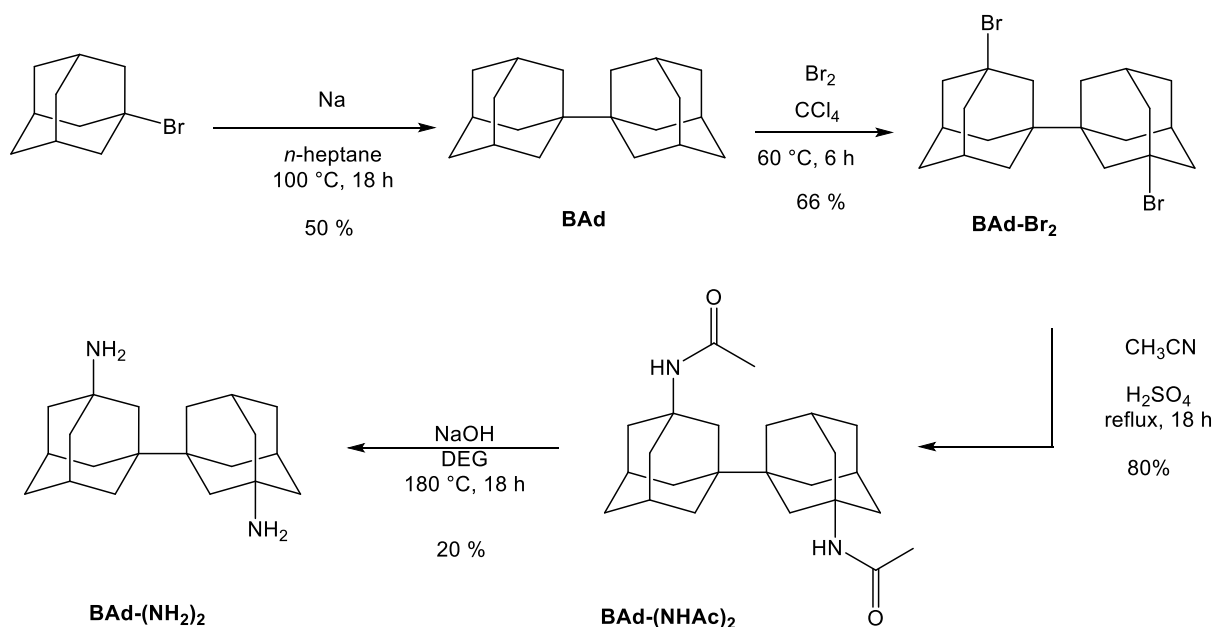
1,3-Diazidoadamantane Ad-(N₃)₂. A mixture of 880 mg of Ad-Br₂ (3 mmol), 2.5 mL of azidotrimethylsilane (2.2 g, 19 mmol, 6.4 equiv) and 1.92 g of SnCl₄ (7.4 mmol, 2.4 equiv) in 11 mL of CH₂Cl₂ was refluxed under argon for 5 h the overnight at room temperature. The mixture was poured onto crushed ice and H₂O. The mixture was stirred for 15 min and the organic phase was extracted. The organic phase was successively washed with H₂O, saturated aqueous NaHCO₃, and brine and then dried over anhydrous MgSO₄. After solvent evaporation the product was collected as a colorless liquid (508 mg, yield 77%). ¹H NMR (500 MHz, CDCl₃) δ (ppm): 1.59 (s, 2H), 1.76 (m, 8H), 1.82 (s, 2H), 2.37 (bs, 2H).



1,3-Diaminoadamantane Ad-(NH₂)₂. A mixture of 1.2 g of Ad-(N₃)₂ (0.005 mol) and 81 mg of Pd/C* 10% in 25 mL of THF was hydrogenated (2.7 bar) in a Fisher-Porter glass bottle at room temperature for 22 h. Hexane (12.5mL) was added to the mixture before filtering through celite on a coarse glass frit. The solvent was evaporated to collect 320 mg of Ad-(NH₂)₂ as a white solid (35 %). ¹H NMR (500 MHz, C₆D₆) δ (ppm): 0.69 (bs, 4H), 1.18 (s, 2H), 1.37–1.24 (m, 10H), 1.96 (m, 2H).

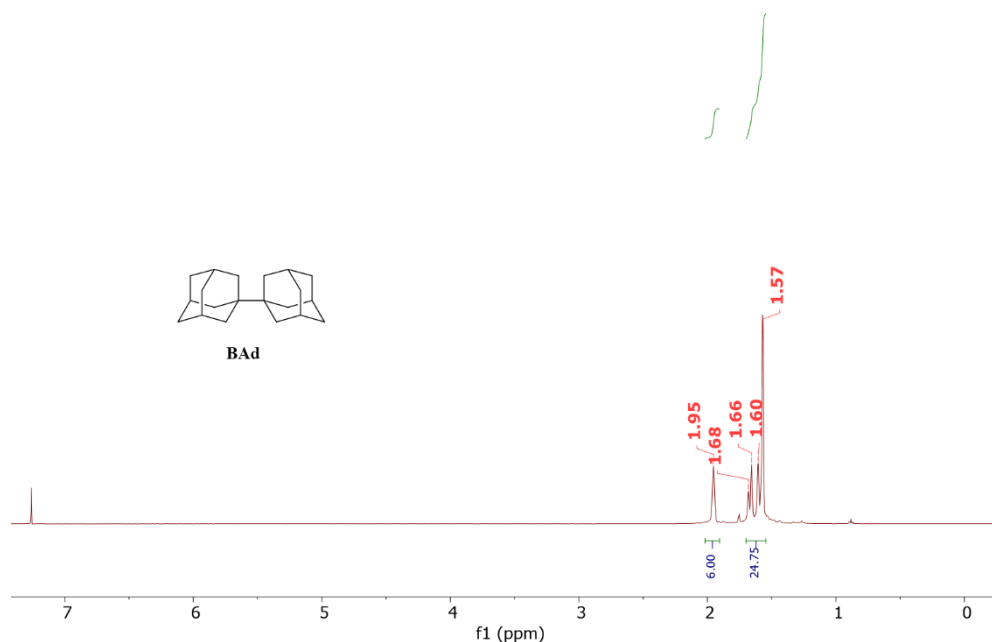


Ligand 7: 3,3'-diamino-1,1'-bisadamantane BAd-(NH₂)₂



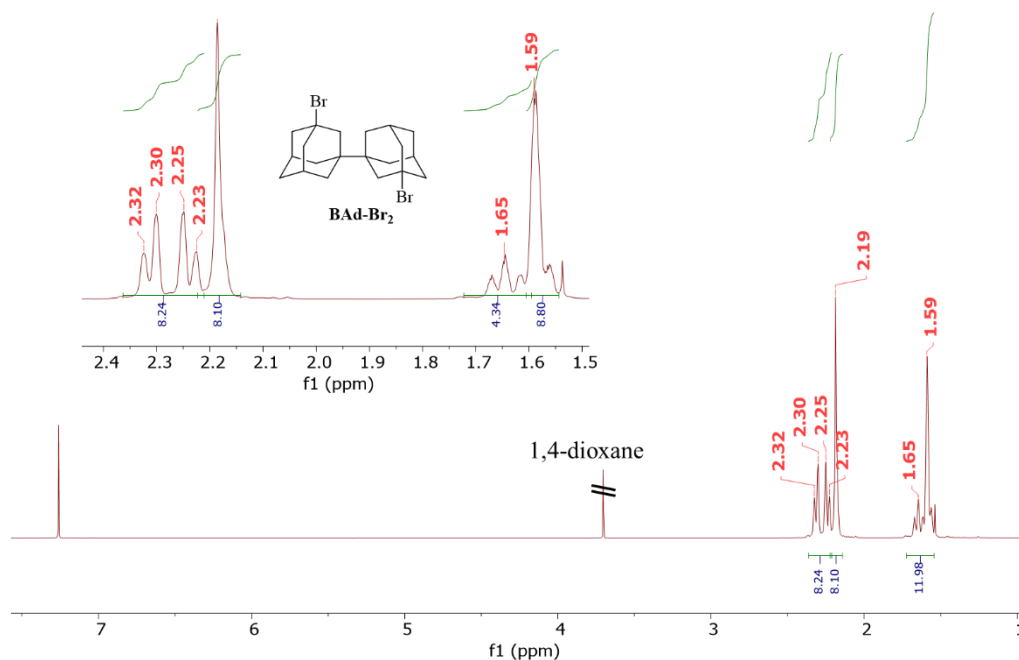
1,1'-Bisadamantane (BAd). 1.47 g (60 mmol) of metallic sodium in 64 ml of *n*-

heptane was introduced in a 250 mL two-necked flask equipped with a reflux tube. The temperature was cooled to 0 °C. 6.6 g (30 mmol) of 1-bromoadamantane dissolved in 34 ml of *n*-heptane were slowly dropwise added under vigorous stirring. The reaction was stirred overnight at 100 °C and, after cooling, the mixture was poured into ice-water. The reaction mixture was extracted with chloroform, and the organic phases collected were dried over anhydrous MgSO₄. After filtration and solvent evaporation a mixture of the desired bisadamantane and adamantane was obtained. BAd (2g, 50%) was purified by washing with cold *n*-hexane to remove adamantane. ¹H NMR (500 MHz, CDCl₃) δ (ppm): 1.50-1.70 (m, 24H, CH₂), 1.95 (s, 6H, CH).

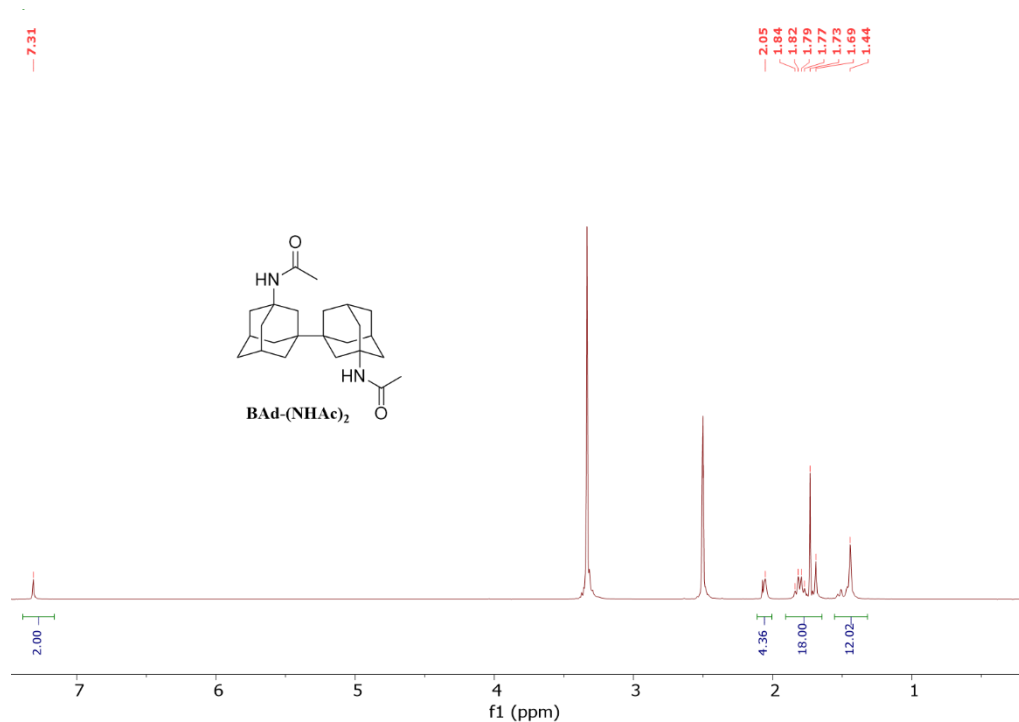


3,3'-dibromo-1,1'-bisadamantane (BAd-Br₂). A mixture of 1 g of 1,1'-bisadamantane (3.7 mmol) and 554 μL of CCl₄ in 7 mL liquid bromine (139 mmol) was stirred under reflux for 6 h. The reaction was monitored by evolution of hydrogen bromide gas. The reaction mixture was poured into iced water, and the excess bromine was carefully quenched by the addition of solid NaHSO₃. The layers were separated, and the aqueous layer was extracted three times with CHCl₃. The combined organic layers were dried over anhydrous MgSO₄ and then concentrated under reduced pressure. The light yellow residue obtained was recrystallized from 1,4-dioxane, giving the

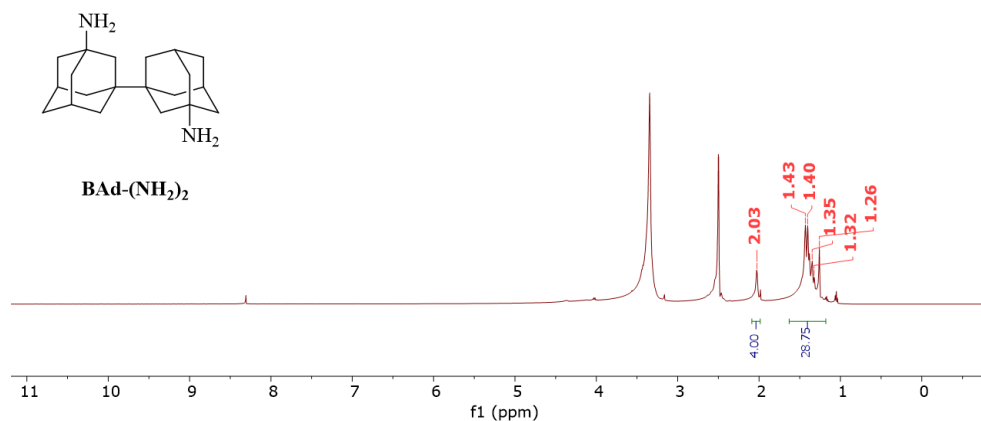
product desired as a colorless powder in 66% yield (1.05 g). $^1\text{H NMR}$ (500 MHz, CDCl_3) δ (ppm): 1.59 (m, 8H), 1.65 (t, $J = 10$ Hz, 4H), 2.19 (bs, m, 8H, CH_2), 2.28 (dd, $J = 10$ Hz, $J = 35$ Hz, 8H).

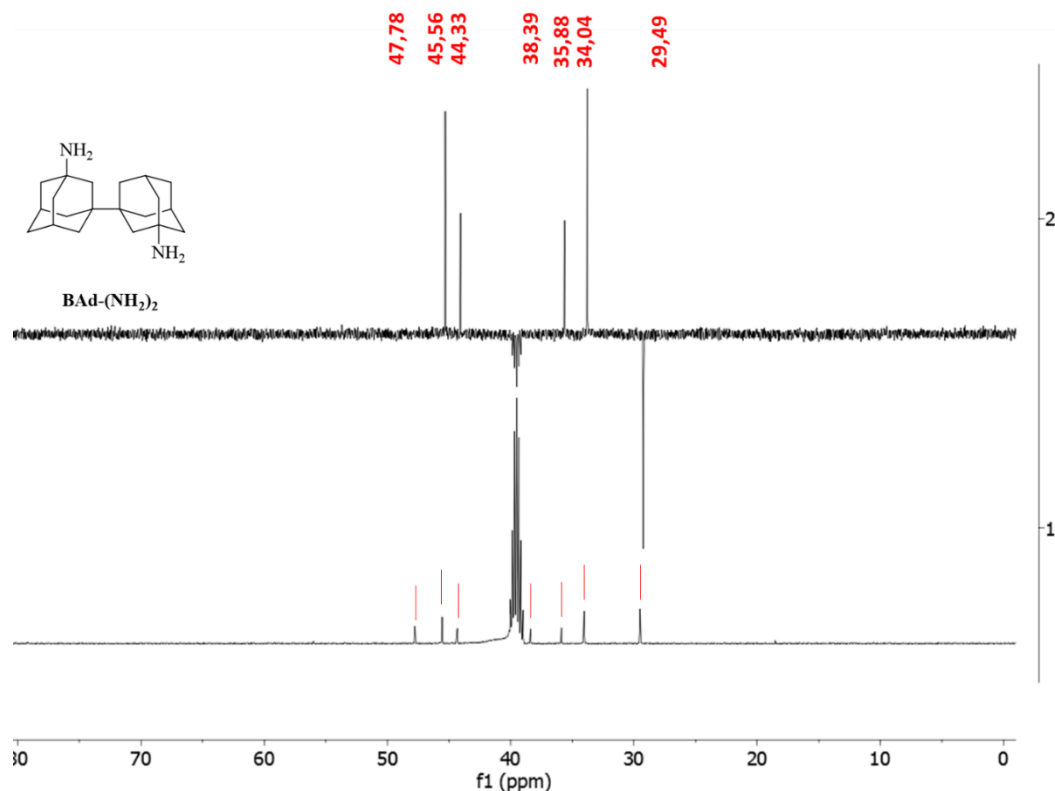


3,3'-diacetamido-1,1'-biadamantane BAD-(NHAc)_2 . To a suspension of BAD-Br_2 (620 mg, 1.4 mmol) in CH_3CN (10 mL) under vigorous stirring, concentrated H_2SO_4 (0.7 mL) was added. The solution was heated at reflux for 12 h. After cooling to room temperature, 10 mL of water was added and the solution was neutralized to pH 7 by addition of saturated $\text{NH}_4\text{OH}_{\text{aq}}$ solution. The white precipitate formed was filtered off, washed with water and air-dried, yielding 450 mg of BAD-(NHAc)_2 (80%): $^1\text{H NMR}$ (500 MHz, dmsO-d_6) δ (ppm): 1.48-1.58 (m, 12H), 1.64-1.87 (m, 18H), 2.05 (s, 4H), 7.31 (s, 2H, NH).

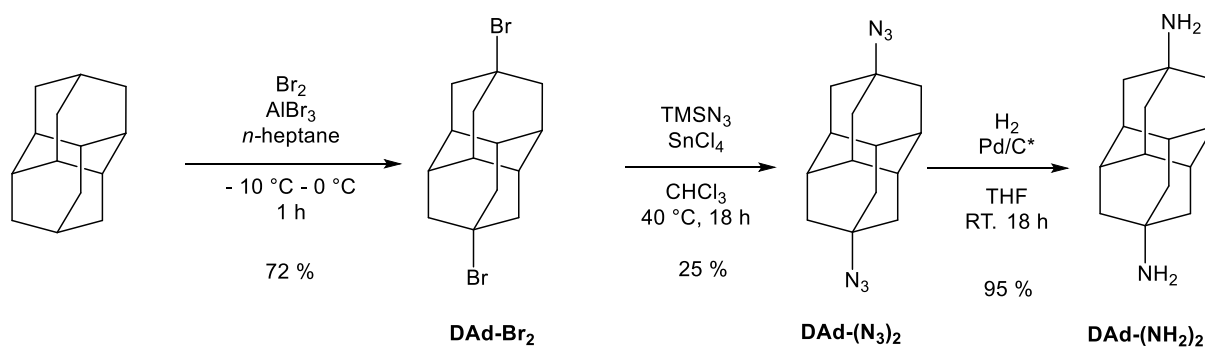


3,3'-diamino-1,1'-bisadamantane BAd-(NH₂)₂. 450 mg of BAd-(NHAc)₂ (, 1.17 mmol) was added to a hot solution of 1.1 g of NaOH (26 mmol) in 11 mL of diethyleneglycol. The mixture was stirred at 180 °C for 18 h. After cooling to room temperature, the residue was poured into 34 mL of water and cooled at –10°C in a fridge. The precipitate formed was filtered off, washed with water to neutral pH and air-dried. The resulting product was purified by sublimation under 0.001 mm Hg at 160 °C to give 70 mg of pure product (20%). ¹H NMR (500 MHz, dms_o-d₆) δ (ppm): 1.26-1.46 (m, 28H), 2.06 (s, 4H); ¹³C NMR (126 MHz, dms_o-d₆) δ (ppm): 24.5 CH, 34.0 CH₂, 35.9 CH₂, 38.4 C_{IV}, 44.3 CH₂, 45.6, CH₂, 47.8 C_{IV} (C–N).



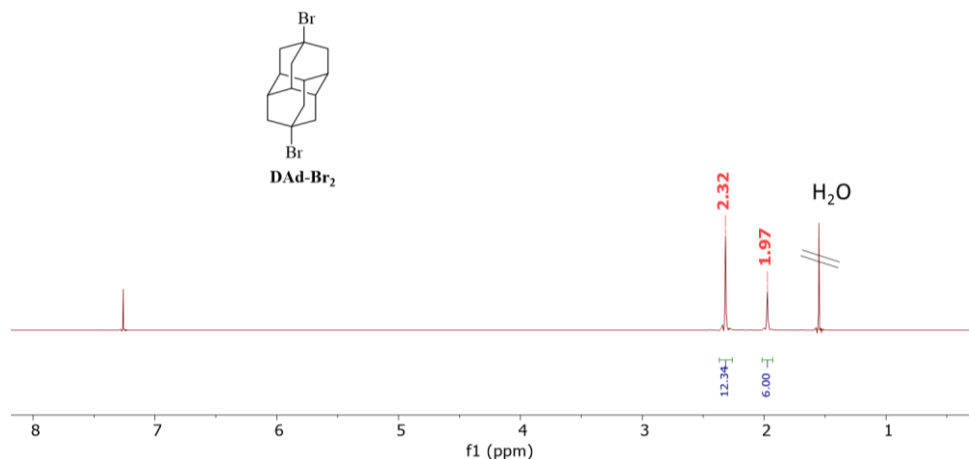


Ligand **8**, 4,9-Diaminodiamantane DAd-(NH₂)₂

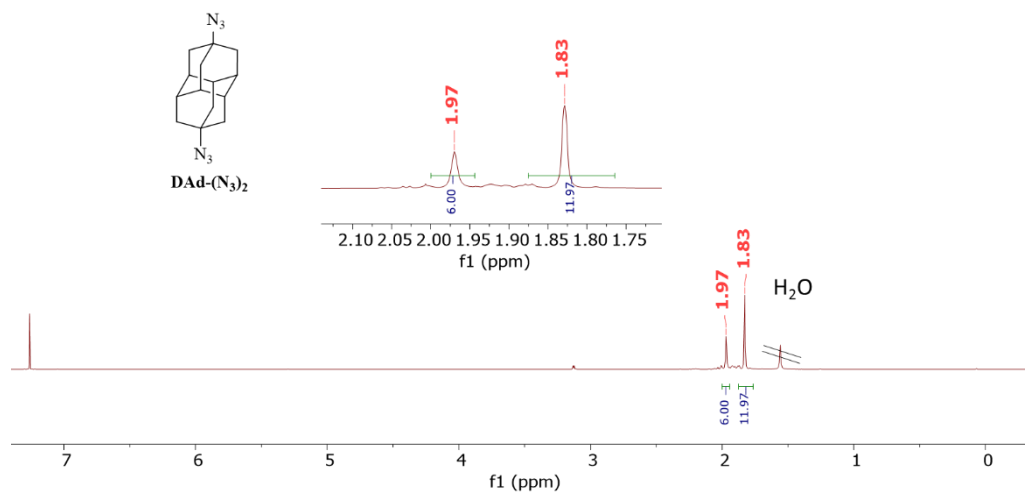


4,9-Dibromodiamantane DAd-Br₂. In a 25 mL two-necked round bottom flask fitted with a controlled addition funnel were added 1.0 g of diamantane (5.3 mmol) and 108 mg of AlBr₃ (0.41 mmol) in 6 mL *n*-heptane under Ar at -10 °C. 1.4 mL of Br₂ (27.2 mmol) in 2 mL of *n*-heptane was added dropwise over 2h at -10 °C. The reaction mixture was stirred for another 1 h at 0 °C, and then poured into iced water. To this mixture was added 6 mL of CCl₄ and then NaHSO₃ until the solution become colorless.

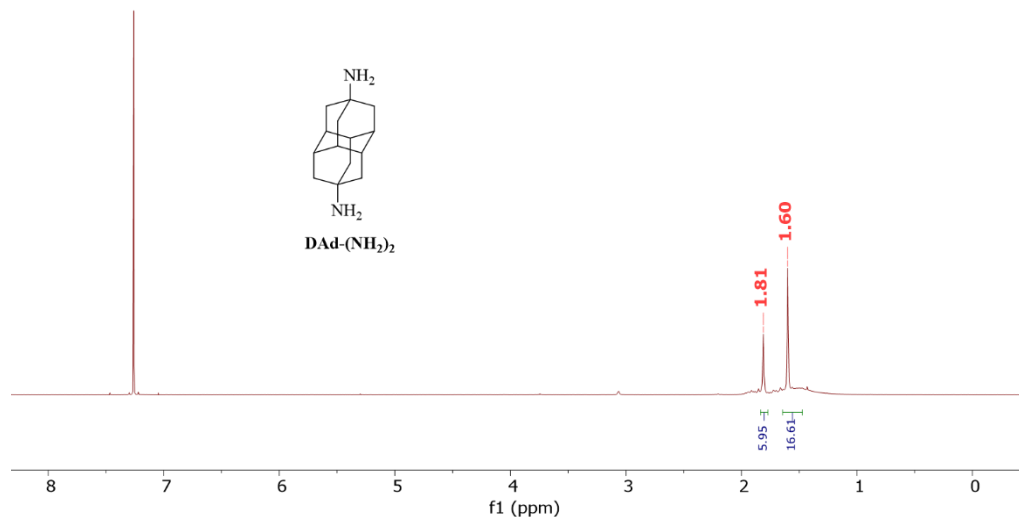
20 mL of CH_2Cl_2 was added and the mixture was extracted with Na_2CO_3 and brine. The organic layer was dried over MgSO_4 and concentrated. The organic residue was crystallized from acetone to give 1.3 g (72 %) of DAd-Br_2 as a white solid. ^1H NMR (500 MHz, CDCl_3) δ (ppm): 1.97 (s, 6H), 2.32 (s, 12H).



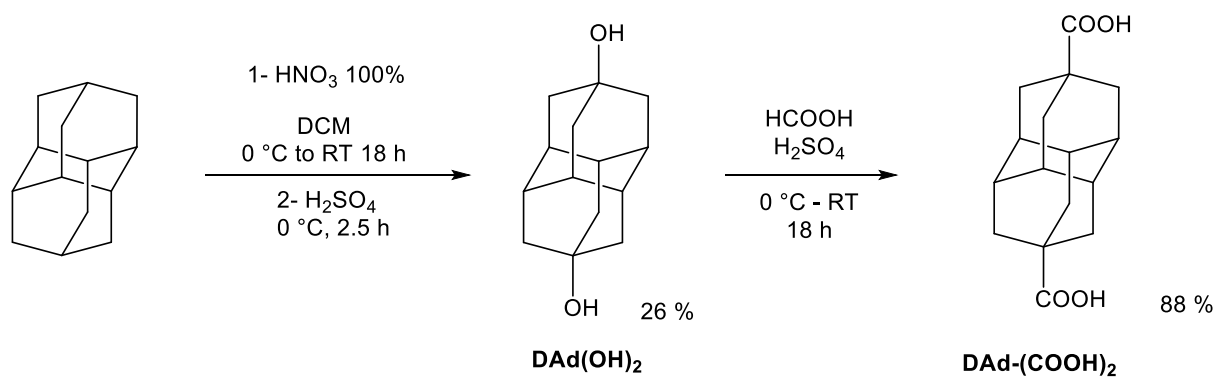
4,9-Diazidodiamantane $\text{DAd-(N}_3)_2$. A mixture of 500 mg of DAd-Br_2 (1.4 mmol), 1.3 g of azidotrimethylsilane (1.23 mL, 9.1 mmol, 6.5 equiv) and 754 mg of SnCl_4 (2.8 mmol, 2 equiv) in 6.5 mL of CH_2Cl_2 was refluxed under N_2 for 12 h. The mixture was poured onto crushed ice and H_2O . The mixture was stirred for 30 min and then separated. The organic phase was successively washed with H_2O , saturated aqueous NaHCO_3 , and brine, and then dried over anhydrous MgSO_4 . The solvent was evaporated and the resulting crude was washed by CH_3CN , yielding 100 mg of $\text{DAd-(N}_3)_2$ (25% yield). ^1H NMR (500 MHz, CDCl_3) δ (ppm): 1.83 (s, 12H), 1.97 (s, 6H).



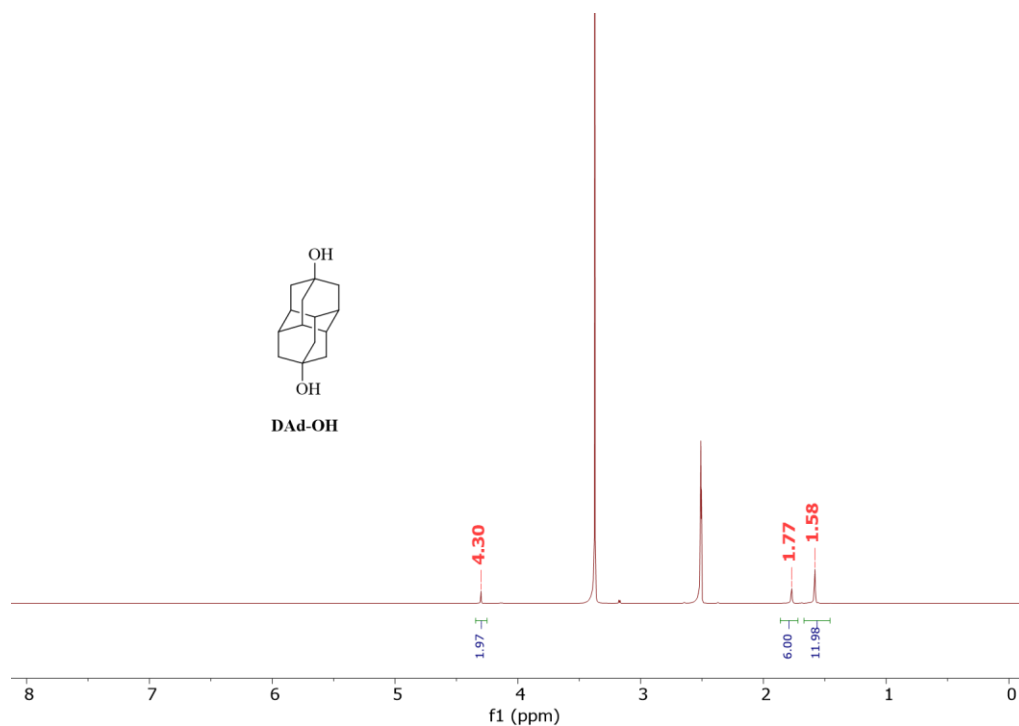
4,9-Diaminodiamantane DAd-(NH₂)₂. A mixture of 92 mg of DAd-(N₃)₂ (0.3 mmol) and 6 mg of Pd/C* in 2 mL of THF was hydrogenated (2.7 bar) in a Fisher-Porter glass bottle at room temperature for 22 h. 0.5 mL of hexane was added to the mixture before filtering through celite on a coarse glass frit. The solvent was evaporated and the residue was washed by *n*-hexane to get 70 mg of DAd-(NH₂)₂ as a white solid (95 %). ¹H NMR (500 MHz, CDCl₃) δ (ppm): 1.46-1.62 (m, 16H, CH₂, NH₂), 1.81 (s, 6H).



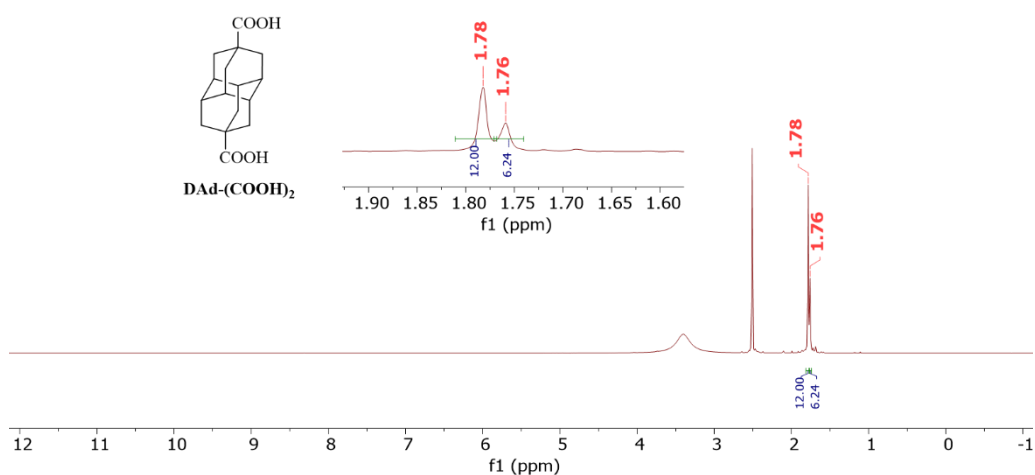
Ligand 4, 4,9-Diamantanedicarboxylic Acid DAd-(COOH)₂

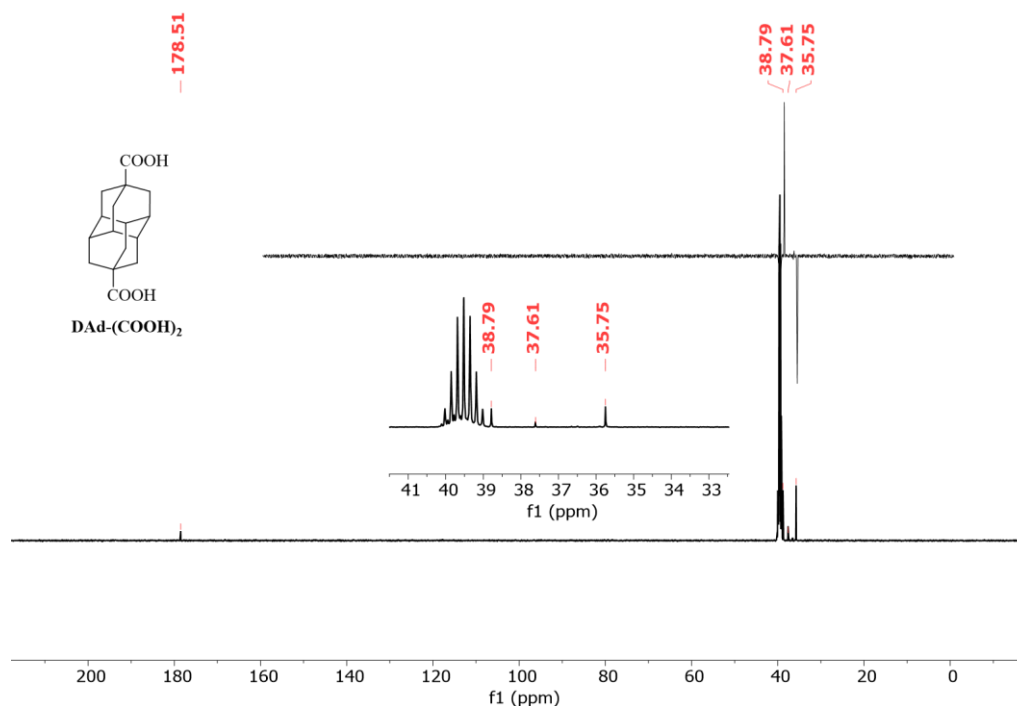


Diamantane-4,9-diol (DAd-OH). A suspension of finely triturated diamantane (1.66 g, 8.8 mmol) in 16 mL of CH_2Cl_2 was stirred in a cooling bath of iced water. To this suspension 9 mL of fuming HNO_3 (100%) was added dropwise over a period of 10 min. The reaction mixture was stirred at 0°C for 20 min, the iced water bath was removed, and the mixture was stirred overnight at room temperature. Afterwards, the reaction mixture was diluted with CH_2Cl_2 , and the excess of HNO_3 was neutralized with NaHCO_3 at 0°C under vigorous stirring. The precipitate formed was filtered and washed with CH_2Cl_2 which removed at reduced pressure affording 3 g of crude nitroso-diamantane. The crude product is added to 60 mL of 96% H_2SO_4 at 0°C and stirred 2.5 h at room temperature. Next, the reaction was poured onto 300 g of ice and extracted with CHCl_3 . Combined organic extracts were dried over MgSO_4 and solvent was removed at reduced pressure. Crystallization of the residue from methanol yield 0.5 g (26 %) of diamantane-4,9-diol. $^1\text{H NMR}$ (500 MHz, DMSO) δ : 1.58 (s, 12H), 1.77 (s, 6 H), 4.30 (s, 2H, OH).



4,9-Diamantanedicarboxylic Acid DAd-(COOH)₂. 0.2 g of diamantane-4,9-diol (0.9 mmol) was added to a 96% solution of 70 mL of H_2SO_4 cooled to 0 °C and containing several drops of HCOOH . 2 mL of HCOOH 98% were added dropwise with stirring within 4 h. The reaction was stirred overnight at room temperature. The mixture was afterwards poured into ice and the resulting precipitate was collected by filtration, washed with water, and dried to afford 0.22 g of DAd_c (88 %). ^1H NMR (500 MHz, $\text{dms}\text{-d}_6$) δ (ppm): 1.76 (s, 6 H), 1.78 (s, 12H). ^{13}C NMR (126 MHz, $\text{dms}\text{-d}_6$) δ (ppm): 35.8 CH, 37.6, 38.8 C_{IV}, 178.5 C_{IV} (COOH).





Synthesis of Ru NP stabilized by (di)carboxylic polymantane ligands

In a typical experiment $[\text{Ru}(\text{COD})(\text{COT})]$ complex and the desired ligand were introduced in a Fisher-Porter bottle, solubilized with THF, and stirred 1h in the glovebox. The resulting yellow solution was pressurized with 3 bar of H_2 . The solution, which turned black after few minutes of reaction, was kept under stirring overnight at room temperature. After this period of time, excess of H_2 was eliminated and the volume of solvent was reduced under vacuum. Pentane was then added to the colloidal suspension to precipitate the Ru nanoparticles. After filtration under argon with a cannula, the black solid powder was washed twice with pentane and filtrated again before drying under vacuum. For each ratio studied, the quantities of reactants are detailed hereafter. The products were all kept in glovebox to avoid oxidation. The assemblies and NP are stable in solution for several days in inert atmosphere.

Ru@1 - 5/1: 100 mg (0.32 mmol) of $[\text{Ru}(\text{COD})(\text{COT})]$, 70.4 mg (0.06 mmol) of AdCOOH, and 40 mL of THF. Yield: 30.5 mg. Ru loading: 77.9 % (mass).

Ru@1 - 10/1: 250 mg (0.79 mmol) of $[\text{Ru}(\text{COD})(\text{COT})]$, 14.3 mg (0.08 mmol) of

AdCOOH, and 100 mL of THF. Yield: 82.5 mg. Ru loading: 65.5 % (mass).

Ru@1 - 20/1: 150 mg (0.48 mmol) of [Ru(COD)(COT)], 4.3 mg (0.02 mmol) of AdCOOH, and 90 mL of THF. Yield: 46 mg. Ru loading: 78.7 % (mass).

Ru@2 - 5/1: 150 mg (0.48 mmol) of [Ru(COD)(COT)], 22.0 mg (0.10 mmol) of Ad(COOH)₂, and 60 mL of THF. Yield: 78.0 mg. Ru loading: 50.2 % (mass).

Ru@2 - 10/1: 150 mg (0.48 mmol) of [Ru(COD)(COT)], 17.8 mg (0.05 mmol) of Ad(COOH)₂, and 60 mL of THF. Yield: 49.4 mg. Ru loading: 61.8 % (mass).

Ru@2 - 20/1: 200 mg (0.634 mmol) of [Ru(COD)(COT)], 7.1 mg (0.03 mmol) of Ad(COOH)₂, and 60 mL of THF. Yield: 71.2 mg. Ru loading: 70.1 % (mass).

Ru@4 - 10/1: 250 mg (0.79 mmol) of [Ru(COD)(COT)], 21.9 mg (0.08 mmol) of DA(COOH)₂, and 100 mL of THF. Yield: 107.3 mg. Ru loading: 67.7 % (mass).

Ru@5 - 10/1: 150 mg (0.48 mmol) of [Ru(COD)(COT)], 7.2 mg (0.05 mmol) of AdNH₂, and 60 mL of THF. Yield: 41 mg. Ru loading: 82.5 % (mass).

Ru@6 - 10/1: 250 mg (0.79 mmol) of [Ru(COD)(COT)], 13.1 mg (0.08 mmol) of Ad(NH₂)₂, and 100 mL of THF. Yield: 85.8 mg. Ru loading: 80.1 % (mass).

Ru@7 - 10/1: 250 mg (0.79 mmol) of [Ru(COD)(COT)], 17.2 mg (0.08 mmol) of DA(NH₂)₂, and 100 mL of THF. Yield: 112.2 mg. Ru loading: 65.7 % (mass).

Ru@8 - 10/1: 88 mg (0.28 mmol) of [Ru(COD)(COT)], 8.4 mg (0.03 mmol) of BAd(NH₂)₂, and 35 mL of THF. Yield: 26 mg. Ru loading: 70.2 % (mass).

Synthesis of Ru complexes

Synthesis of [Ru(κ^2 -AdCOO)(η^2, η^2 -C₈H₁₂)(η^3 -C₈H₁₁)] – Ru₁

To a solution of [Ru(COD)(COT)] (100 mg, 0.32 mmol) in 10 mL of dry acetone, an excess of ligand **1** was added (62 mg, 0.35 mmol). The yellow solution was allowed to react 1h at room temperature in the glovebox. After this period, the solvent was slowly evaporated until a yellow precipitated appeared. The solvent was filtered off, the yellow

solid was cleaned twice with 3 mL of dry acetone, and dried under vacuum overnight. Yield: 111 mg (64%).

^1H NMR (300MHz, CD_2Cl_2): δ (ppm) = 5.48 (m, 1H, CH COT), 5.22 (m, 1H CH, COT), 5.22 (m, 1H CH, COD), 4.65 (m, 2H, CH, COD), 4.17 (m, H, CH, COT), 3.97 (m, 1H, CH, COT), 3.27 (m, CH, COT), 2.94 (m, CH, COD), 2.44 (m, 4H, CH_2 , COD), 2.05, 1.98, 1.81, 1.5, 1.37, 1.24 and 0.98 (m, 10H total, CH_2), 1.89 (m, 3H, CH_2 , adamantane), 1.78 (m, 6H, CH_2 , adamantane) and 1.62 (m, 6H, CH_2 , adamantane). ^{13}C NMR (75 MHz, CD_2Cl_2): δ (ppm) = 189.9 (-COO-), 135.0 (-CH=, COT), 125.8 (-CH=, COT), 105.2 (coordinated CH, COT), 90.6 (coordinated CH, COD), 84.9 (coordinated CH, COD), 80.6 (coordinated CH, COT), 73.2 (coordinated CH, COD), 58.4 (coordinated CH, COT), 41.5 (quaternary carbon), 39.0 (CH_2 , adamantane), 36.7 (CH_2 , COD), 33.4 (CH_2 , COD), 28.8 (CH_2 , COT), 28.3 (CH, adamantane), 25.9 and 25.8 (CH_2 , COD), 24.8(CH_2 , COT), 24.5 (CH_2 , COT). IR (neat) ν = 1497 cm^{-1} (s, $\nu_{\text{C-O}}$), 1443 cm^{-1} (s, $\nu_{\text{C-O}}$), 1309 cm^{-1} (m, $\nu_{\text{C-C}}$). Anal. calcd. (%) for $\text{C}_{27}\text{H}_{38}\text{O}_2\text{Ru}$ (495,67 g/mol): C,65.43; H, 7.73; Ru 20.39; found: C 65.59, H 8.39, Ru 20.99. Single crystals of **Ru1** suitable for X-ray diffraction were obtained by slow evaporation of a saturated solution of the complex in acetone.

Synthesis of $[\text{Ru}_2(\kappa^2\text{-Ad}(\text{COO})_2)(\eta^2, \eta^2\text{-C}_8\text{H}_{12})_2(\eta^3\text{-C}_8\text{H}_{11})_2] - \text{Ru}_2$

To a solution of ligand **2** (80 mg, 0.36 mmol) in 10 mL of dry acetone, $[\text{Ru}(\text{COD})(\text{COT})]$ (280 mg, 0.89 mmol) was added. The solution turned orange immediately, and after 20 min of agitation at room temperature in the glovebox a yellow precipitated appeared. The solvent was filtered off, and the yellow solid was cleaned twice with 5 mL of dry acetone, and dried under vacuum overnight. Yield: 160 mg (71%).

^1H NMR (300MHz, CD_2Cl_2): δ (ppm) = 5.44 (m,2H, CH, COT), 5.24 (m,2H, CH, COT), 5.21 (m,2H, CH, COD), 4.67 (m,4H, CH, COD), 4.17 (m, 2H, CH, COT), 3.99 (m, 2H, CH, COT), 3.28 (m, 2H, CH, COT), 2.95 (m, 2H CH, COT), 2.45 (m, 8H, CH_2 , COD), 1.83, 1.28, 1.52, 1.37, 0.99 and 0.94 (m, 20H total, CH_2), 2.04, 1.83, 1.72 and 1.58 (m, 14H total, CH and CH_2 , adamantane). ^{13}C NMR(75 MHz, CD_2Cl_2): δ (ppm)= 189.1 (-

COO-), 134.9 (-CH=, COT), 125.7 (-CH=, COT), 105.2 (coordinated CH, COT), 90.7 (coordinated CH, COD), 85.1 (coordinated CH, COD), 80.7 (coordinated CH, COT), 73.3 (coordinated CH, COD), 58.5 (coordinated CH, COT), 41.8 (quaternary carbon), 38.3(CH₂, adamantane), 36.3 (CH₂, COD), 35.7 (CH₂, adamantane), 33.4 (CH₂, COD), 28.9 (CH₂, COT), 28.3 (CH, adamantane), 25.9 and 25.8 (CH₂, COD), 24.9 (CH₂, COT), 24.5 (CH₂, COT). IR (neat) $\nu = 1502\text{ cm}^{-1}$ (s, $\nu_{\text{(C-O)}}$), 1430 cm^{-1} (s, $\nu_{\text{(C-O)}}$), 1451 cm^{-1} (m, $\nu_{\text{(C-C)}}$). Anal. calcd. (%) for C₄₄H₆₀O₄Ru₂ (855.1 g/mol): C, 61.8; H, 7.07, Ru, 23.6; found: C 60.5, H 7.2, Ru 23.3.

Synthesis of [Ru₂(μ -AdCOO)₂(μ - η^3, η^2, η^2 -C₈H₉)(η^3 -C₈H₉)(THF)] – Ru₃

A yellow solution of ligand **1** (70 mg, 0.36 mmol), Ru(COD)(COT)] (50 mg, 0.16 mmol) in 10 mL of dry acetone was allowed to react at room temperature. After 2h of stirring, the solution was evaporated to dryness. The crude was then solubilized with 10 mL of dry THF and stirred overnight at 55 °C. After this period THF was evaporated under vacuum and the ¹H NMR of the crude was recorded. Single crystals of **Ru₃** suitable for X-ray diffraction were obtained by slow evaporation of a saturated solution of the crude in THF. IR (neat) $\nu = 1691\text{ cm}^{-1}$ (s, $\nu_{\text{(C=O)}}$), 1553 cm^{-1} (s, $\nu_{\text{(C-O)}}$), 1407 cm^{-1} (s, $\nu_{\text{(C-O)}}$), 1451 cm^{-1} (m, $\nu_{\text{(C-C)}}$), 1258 cm^{-1} (vs, $\nu_{\text{(C-O)}}$).

Characterization

The ruthenium content in the products was measured by ICP performed at the LCC with a Thermo Scientific ICAP 6300 instrument. Elemental analyses of C, H, and N were carried out on a PERKIN ELMER 2400 serie II elemental analyzer.

TEM and HR-TEM analyses were performed at the “Centre de microcaracterisation Raimond Castaing, UMS 3623, Toulouse” by using a JEOL JEM 1011 CX-T electron microscope operating at 100 kV with a point resolution of 4.5 a and a JEOL JEM 1400 electron microscope operating at 120 kV. The high-resolution analyses were conducted by using a JEOL JEM 2100F equipped with a field emission gun (FEG) operating at 200 kV with a point resolution of 2.3 a and a JEOL JEM-ARM200F Cold FEG operating at 200 kV with a point resolution of > 1.9 a. The particle size distribution was

determined through a manual measurement of enlarged micrographs from different areas of the TEM grid (at least 200 particles).

SS- NMR spectroscopy (magic angle spinning, MAS NMR) with and without ^1H - ^{13}C cross polarization was performed at the LCC with a Bruker Avance 400WB instrument equipped with a 4 mm probe with the sample rotation frequency being set at 12/16 kHz, unless otherwise indicated. Measurements were carried out in a 4 mm ZrO_2 rotor. Liquid NMR spectra were obtained with Bruker Fourier 300 systems using CD_2Cl_2 / THF-d_8 as the solvent, TMS as internal standard, with proton and carbon resonances at 300 and 75 MHz, respectively.

The crystallographic data were collected on a Bruker Kappa Apex II diffractometer equipped with a 30 W air-cooled microfocus source using MoK_α radiation ($\lambda = 0.71073 \text{ \AA}$). An Oxford Cryosystems Cryostream cooler device was used to collect the data at low temperature (100(2)K). Phi- and omega- scans were performed for data collection. An empirical absorption correction with SADABS was applied [Bruker, SADABS, Bruker AXS Inc., Madison, Wisconsin, USA]. The structures were solved by intrinsic phasing method (SHELXT)⁵³ and refined by means of least-squares procedures on F^2 with SHELXL⁵³. All non-hydrogen were refined anisotropically and all hydrogen atoms were refined isotropically at calculated positions using a riding model.

IR spectra were recorded with a PerkinElmer GX2000 spectrometer installed in a glovebox, in the range 4000–400 cm^{-1} . WAXS measurements were performed at CEMES on a diffractometer dedicated to pair distribution function (PDF) analysis: graphite monochromatized molybdenum radiation (0.07169 nm), solid-state detection, and low background setup. Samples were sealed in Lindemann glass capillaries (diameter 1.0 mm) to avoid any oxidation after filling in a glovebox. For all samples, data were collected in an extended angular range ($2\theta = 1298$) with counting times of typically 150 s for each of the 457 data points, thus allowing for PDF analysis. Classic corrections (polarization and absorption in cylindrical geometry) were applied before reduction and Fourier transform.

XPS measurements were performed on a Thermo K α spectrometer working at a base pressure of 5×10^{-9} mbars and equipped with a monochromatic Al K α X-ray source (1486.7 eV). The spectra presented here were recorded with a Pass Energy of 20 eV. The data were processed with CasaXPS using Gaussian-lorentzian combinations and a Shirley background. Scofield photoionization cross-sections⁵⁵ corrected for the transmission function of the analyzer and the analysis depth were used for quantifications.

ET experiments were realized by a FEI Titan transmission electron microscope operating at 300 kV, equipped with a CT objective lens, a FEG electron source and a Gatan 2kX2k CCD camera. The tomogram was reconstructed by using the software Inspect3D (FEI) using the SIRT method (Simultaneous Iterative Reconstruction Technique) with 30 iterations, applied on several TEM images acquired with the sample tilted between +70 and -70 degrees, with an angular step of 2 degrees. The 3D-nanoparticles reconstruction was finally realized using the software AVIZO (FEI), while the calculation of the distance among their center was performed by a dedicated code developed at KAUST visualization lab.

SAXS measurements were performed on the XEUSS 2.0 laboratory source equipped with a pixel detector PILATUS 1M (DECTRIS) and an X-rays source provided by a GeniX3D with a fixed wavelength based on Cu K α radiation ($\lambda = 1.54 \text{ \AA}$). The sample to detector distance was fixed at 1216.5mm giving a q range starting from 0.005 \AA^{-1} to 0.5 \AA^{-1} assuming that q is the scattering vector equal to $4\pi/\lambda \sin \theta$ with 2θ the scattering angle. The distance was calibrated in the small angles region using silver behenate ($d_{001} = 58.34 \text{ \AA}$). The powders of nanoparticles were stored on sealed capillaries to prevent oxidation and placed on motorized sample holder. To remove scattering and absorption from air, a primary vacuum has been applied to the entire instrument. Acquisition time per sample was 1 hours and all scattering curves were corrected for the empty capillary contribution, divided by transmission factor, acquisition time and optical path in order to obtain SAXS curves in absolute units (cm^{-1}). The X-ray scattering curves at low q can be described as the scattering from multiscale organization of nanoparticle

assembly. The elementary particles can be assimilated as dense spherical objects showing interaction at small distances. In this case, we can describe the SAXS curves at medium and high angles (0.1 to 1 \AA^{-1}) with a form factor of sphere multiplied by a structure factor to take an account of interactions at low distances. At small and intermediate angles (0.01 - 0.1 \AA^{-1}), the increase of the intensity indicates the presence of large assemblies containing the nanoparticles, and the state of the surface of these large size objects can be described with a power law function. The total scattering is the sum of the different scattering contributions and the SASView program (SasView, <http://www.sasview.org/>) has been used to build the sum model and fit the data. The global equation applied to fit the data can be written as follow:

$$I(q)_{global} = I(q)_{agglomerates} + I(q)_{sphere} * S(q)$$

$$I(q)_{global} = Aq^{-P} + \frac{B}{V} \left[\frac{3V(\Delta\rho)(\sin(qr) - qr\cos(qr))}{(qr)^3} \right]^2$$

$$* \left[1 + \frac{1}{v1} 4\pi \int_0^\infty (g(r) - 1)r^2 \frac{\sin(qr)}{qr} dr \right]$$

where the A and B are factor scaling, P the slope providing information of the surface and the sphere is described by the volume V , the radius r and the contrast $\Delta\rho$. The form factor $S(q)$ used here correspond to the “hard sphere interaction model” described by Percus-Yevick.⁵⁴ Finally, three parameters such as radius of the sphere r , the state of the surface P and the inter-particle distance d are employed to fit the data.

At very small angles ($<0.01 \text{ \AA}^{-1}$), we are unable to determine the size of large assemblies but in some conditions we can observe oscillations coming from interaction at short distances between large size particles. By adding a term $I(q)_{sphere} * S(q)$ to give a contribution of large spheres with a spatial distribution at short distances, we can fit the beginning of the curve giving an approximation of the spatial distribution of these large particles.

Computational details section

The DFT calculations were performed using the Vienna *ab initio* simulation package (VASP),⁵⁵⁻⁵⁸ based on the full-potential projector augmented wave framework,⁵⁹⁻⁶⁰ Exchange-correlation effects have been approximated using the spin-polarized version of PBE functional.⁶¹ A kinetic-energy cutoff of 400 eV was found to be sufficient to achieve a total-energy convergence within several meV, considering the k-point sampling in Gamma-point only calculations for isolated molecules and complexes, in conjunction with a gaussian smearing with a width of 0.05 eV. During geometry optimization runs, all the atoms were fully relaxed until forces on individual atoms were smaller than 0.01 eV/Å. Calculation cells for isolated molecules and complexes were (25x26x27) Å³, to avoid spurious interactions between periodic images. Figures of the different geometries were produced thanks to the 3D visualization program VESTA.⁶² Bader charge analyses were performed using Henkelmann's group code.⁶³ The optimal geometries upon H₂ adsorption were constructed following the results of reference,⁶⁴ *i. e.* all available μ_3 sites were occupied and then the top sites and, if needed, some bridge sites were used to build the starting geometries. Reaction barriers were estimated by the climbing image nudge elastic band (CI-NEB) method⁶⁵⁻⁶⁷ with a spring force between images of 5 eV/Å² and a force tolerance of 0.05 eV/Å. The harmonic vibrational modes were systematically calculated to distinguish minima and saddle points using dynamical matrix extraction scheme of VTST tools.

2.5 References

1. Fendler, J. H., Self-Assembled Nanostructured Materials. *Chem. Mater.* **1996**, *8*, 1616-1624.
2. Fendler, J. H., Chemical Self-Assembly for Electronic Applications. *Chem. Mater.* **2001**, *13*, 3196-3210.
3. Vriezema, D. M.; Comellas Aragonès, M.; Elemans, J. A. A. W.; Cornelissen, J. J. L. M.; Rowan, A. E.; Nolte, R. J. M., Self-Assembled Nanoreactors. *Chem. Rev.* **2005**, *105*, 1445-1490.
4. Boles, M. A.; Engel, M.; Talapin, D. V., Self-Assembly of Colloidal Nanocrystals: From Intricate Structures to Functional Materials. *Chem. Rev.* **2016**, *116*, 11220-11289.
5. Lu, C.; Tang, Z., Advanced Inorganic Nanoarchitectures from Oriented Self-Assembly. *Adv. Mater.* **2016**, *28*, 1096-1108.
6. Wang, L.; Xu, L.; Kuang, H.; Xu, C.; Kotov, N. A., Dynamic Nanoparticle Assemblies. *Acc. Chem. Res.* **2012**, *45*, 1916-1926.
7. Sohn, B.-H.; Choi, J.-M.; Yoo, S. I.; Yun, S.-H.; Zin, W.-C.; Jung, J. C.; Kanehara, M.; Hirata, T.; Teranishi, T., Directed Self-Assembly of Two Kinds of Nanoparticles Utilizing Monolayer Films of Diblock Copolymer Micelles. *J. Am. Chem. Soc.* **2003**, *125*, 6368-6369.
8. Leng, F.; Gerber, I. C.; Lecante, P.; Bentaleb, A.; Muñoz, A.; Illescas, B. M.; Martín, N.; Melinte, G.; Ersen, O.; Martinez, H.; Axet, M. R.; Serp, P., Hexakis [60]Fullerene Adduct-Mediated Covalent Assembly of Ruthenium Nanoparticles and Their Catalytic Properties. *Chem. Eur. J.* **2017**, *23*, 13379-13386.
9. Schwertfeger, H.; Fokin, A. A.; Schreiner, P. R., Diamonds Are a Chemist's Best Friend: Diamondoid Chemistry Beyond Adamantane. *Angew. Chem. Int. Ed. Engl.* **2008**, *47*, 1022-1036.
10. Gunawan, M. A.; Hierso, J.-C.; Poinot, D.; Fokin, A. A.; Fokina, N. A.; Tkachenko, B. A.; Schreiner, P. R., Diamondoids: Functionalization and Subsequent Applications of Perfectly Defined Molecular Cage Hydrocarbons. *New J. Chem.* **2014**, *38*, 28-41.
11. Fang, Q.; Gu, S.; Zheng, J.; Zhuang, Z.; Qiu, S.; Yan, Y., 3d Microporous Base-Functionalized Covalent Organic Frameworks for Size-Selective Catalysis. *Angew. Chem. Int. Ed.* **2014**, *53*, 2878-2882.

12. Garcia, J. C.; Justo, J. F.; Machado, W. V. M.; Assali, L. V. C., Functionalized Adamantane: Building Blocks for Nanostructure Self-Assembly. *Phys. Rev.* **2009**, *80*.
13. Moncea, O.; Casanova-Chafer, J.; Poinot, D.; Ochmann, L.; Mboyi, C. D.; Nasrallah, H. O.; Llobet, E.; Makni, I.; El Atrous, M.; Brandes, S.; Rousselin, Y.; Domenichini, B.; Nuns, N.; Fokin, A. A.; Schreiner, P. R.; Hierso, J. C., Diamondoid Nanostructures as sp^3 -Carbon-Based Gas Sensors. *Angew. Chem. Int. Ed. Engl.* **2019**, *58*, 9933-9938.
14. Gunawan, M. A.; Moncea, O.; Poinot, D.; Keskes, M.; Domenichini, B.; Heintz, O.; Chassagnon, R.; Herbst, F.; Carlson, R. M. K.; Dahl, J. E. P.; Fokin, A. A.; Schreiner, P. R.; Hierso, J.-C., Nanodiamond-Palladium Core-Shell Organohybrid Synthesis: A Mild Vapor-Phase Procedure Enabling Nanolayering Metal onto Functionalized sp^3 -Carbon. *Adv. Funct. Mater.* **2018**, *28*, 1705786-1705800.
15. Davis, M. C.; Nissan, D. A., Preparation of Diamines of Adamantane and Diamantane from the Diazides. *Synth. Commun.* **2006**, *36*, 2113-2119.
16. Senchyk, G. A.; Lysenko, A. B.; Krautscheid, H.; Domasevitch, K. V., "Fluoride Molecular Scissors": A Rational Construction of New Mo(VI) Oxofluorido/1,2,4-Triazole Mofs. *Inorg. Chem. Commun.* **2011**, *14*, 1365-1368.
17. Reinhardt, H. F., Biadamantane and Some of Its Derivatives. *J. Org. Chem.* **1962**, *27*, 3258-3261.
18. Zhu, X.; Shao, B.; Vanden Bout, D. A.; Plunkett, K. N., Directing the Conformation of Oligo(Phenylenevinylene) Polychromophores with Rigid, Nonconjugatable Morphons. *Macromolecules* **2016**, *49*, 3838-3844.
19. Fokina, N. A.; Tkachenko, B. A.; Merz, A.; Serafin, M.; Dahl, J. E. P.; Carlson, R. M. K.; Fokin, A. A.; Schreiner, P. R., Hydroxy Derivatives of Diamantane, Triamantane, and [121]Tetramantane: Selective Preparation of Bis-Apical Derivatives. *Eur. J. Org. Chem.* **2007**, *2007*, 4738-4745.
20. Vodička, L.; Janků, J.; Burkhard, J., Synthesis of Diamantanedicarboxylic Acids with the Carboxy Groups Bonded at Tertiary Carbon Atoms. *Collect. Czech. Chem. Commun.* **1983**, *48*, 1162-1172.
21. Robinson, I.; Zacchini, S.; Tung, L. D.; Maenosono, S.; Thanh, N. T. K., Synthesis and Characterization of Magnetic Nanoalloys from Bimetallic Carbonyl Clusters. *Chem. Mater.*

- 2009**, *21*, 3021-3026.
22. Morris, T.; Zubkov, T., Steric Effects of Carboxylic Capping Ligands on the Growth of the Cdse Quantum Dots. *Colloids Surf. A* **2014**, *443*, 439-449.
23. Pan, C.; Pelzer, K.; Philippot, K.; Chaudret, B.; Dassenoy, F.; Lecante, P.; Casanove, M.-J., Ligand-Stabilized Ruthenium Nanoparticles: Synthesis, Organization, and Dynamics. *J. Am. Chem. Soc.* **2001**, *123*, 7584-7593.
24. Gonzalez-Gomez, R.; Cusinato, L.; Bijani, C.; Coppel, Y.; Lecante, P.; Amiens, C.; Del Rosal, I.; Philippot, K.; Poteau, R., Carboxylic Acid-Capped Ruthenium Nanoparticles: Experimental and Theoretical Case Study with Ethanoic Acid. *Nanoscale* **2019**, *11*, 9392-9409.
25. Martínez-Prieto, L. M.; Chaudret, B., Organometallic Ruthenium Nanoparticles: Synthesis, Surface Chemistry, and Insights into Ligand Coordination. *Acc. Chem. Res.* **2018**, *51*, 376-384.
26. Martinez-Prieto, L. M.; Cano, I.; Marquez, A.; Baquero, E. A.; Tricard, S.; Cusinato, L.; Del Rosal, I.; Poteau, R.; Coppel, Y.; Philippot, K.; Chaudret, B.; Campora, J.; van Leeuwen, P., Zwitterionic Amidinates as Effective Ligands for Platinum Nanoparticle Hydrogenation Catalysts. *Chem. Sci.* **2017**, *8*, 2931-2941.
27. Tristany, M.; Chaudret, B.; Dieudonné, P.; Guari, Y.; Lecante, P.; Matsura, V.; Moreno-Mañas, M.; Philippot, K.; Pleixats, R., Synthesis of Ruthenium Nanoparticles Stabilized by Heavily Fluorinated Compounds. *Adv. Funct. Mater.* **2006**, *16*, 2008-2015.
28. Tricard, S.; Said-Aizpuru, O.; Bouzouita, D.; Usmani, S.; Gillet, A.; Tassé, M.; Poteau, R.; Viau, G.; Demont, P.; Carrey, J.; Chaudret, B., Chemical Tuning of Coulomb Blockade at Room-Temperature in Ultra-Small Platinum Nanoparticle Self-Assemblies. *Mater. Horiz.* **2017**, *4*, 487-492.
29. Uznanski, P.; Zakrzewska, J.; Favier, F.; Kazmierski, S.; Bryszewska, E., Synthesis and Characterization of Silver Nanoparticles from (Bis)Alkylamine Silver Carboxylate Precursors. *J. Nanoparticle Res.* **2017**, *19*, 121-121.
30. Salas, G.; Santini, C. C.; Philippot, K.; Collière, V.; Chaudret, B.; Fenet, B.; Fazzini, P. F., Influence of Amines on the Size Control of in Situ Synthesized Ruthenium Nanoparticles in Imidazolium Ionic Liquids. *Dalton Trans* **2011**, *40*, 4660-4668.
31. Wood, M. H.; Welbourn, R. J. L.; Charlton, T.; Zorbakhsh, A.; Casford, M. T.; Clarke, S.

- M., Hexadecylamine Adsorption at the Iron Oxide–Oil Interface. *Langmuir* **2013**, *29*, 13735-13742.
32. Machado, B. F.; Oubenali, M.; Rosa Axet, M.; Trang Nguyen, T.; Tunckol, M.; Girleanu, M.; Ersen, O.; Gerber, I. C.; Serp, P., Understanding the Surface Chemistry of Carbon Nanotubes: Toward a Rational Design of Ru Nanocatalysts. *J. Catal.* **2014**, *309*, 185-198.
33. Osakada, K.; Grohmann, A.; Yamamoto, A., New Ruthenium Carboxylate Complexes Having a 1-5- η^5 -Cyclooctadienyl Ligand. *Organometallics* **1990**, *9*, 2092-2096.
34. Smart, K. A.; Grellier, M.; Coppel, Y.; Vendier, L.; Mason, S. A.; Capelli, S. C.; Albinati, A.; Montiel-Palma, V.; Munoz-Hernandez, M. A.; Sabo-Etienne, S., Nature of Si-H Interactions in a Series of Ruthenium Silazane Complexes Using Multinuclear Solid-State NMR and Neutron Diffraction. *Inorg. Chem.* **2014**, *53*, 1156-1165.
35. Smart, K. A.; Grellier, M.; Vendier, L.; Mason, S. A.; Capelli, S. C.; Albinati, A.; Sabo-Etienne, S., Step-by-Step Introduction of Silazane Moieties at Ruthenium: Different Extents of Ru–H–Si Bond Activation. *Inorg. Chem.* **2013**, *52*, 2654-2661.
36. Lopes, J. C. S.; Damasceno, J. L.; Oliveira, P. F.; Guedes, A. P. M.; Tavares, D. C.; Deflon, V. M.; Lopes, N. P.; Pivatto, M.; Batista, A. A.; Maia, P. I. S.; Von Poelhsitz, G., Ruthenium(II) Complexes Containing Anti-Inflammatory Drugs as Ligands: Synthesis, Characterization and in Vitro Cytotoxicity Activities on Cancer Cell Lines. *J. Braz. Chem. Soc.* **2015**, *26*, 1838-1847.
37. Jia, G.; Rheingold, A. L.; Haggerty, B. S.; Meek, D. W., Synthesis and Characterization of Ruthenium Acetate Complexes Containing Triphosphines. *Inorg. Chem.* **1992**, *31*, 900-904.
38. Toma, H. E.; Nikolaou, S., Self-Assembly of a Supramolecular Cyclic Polymer Containing Pyrazine Bridged Trinuclear μ -oxo-Ruthenium-Acetate Clusters. *J. Chem. Res.* **2000**, *2000*, 326-327.
39. Toma, Henrique E.; Alexiou, Anamaria D. P.; Dovidauskas, S., Extended Electronic Interactions in a Triangular μ -Oxotriruthenium Acetate Cluster Containing Nitric Oxide. *Eur. J. Inorg. Chem.* **2002**, *2002*, 3010-3017.
40. Kepert, C. M.; Deacon, G. B.; Spiccia, L.; Fallon, G. D.; Skelton, B. W.; White, A. H., A Facile and Benign Synthesis of Binuclear Ruthenium(I) “Sawhorse” Complexes. *J. Chem. Soc., Dalton Trans.* **2000**, 2867-2873.
41. Wang, S.; Sim, W.-S., Au Nanoparticles Encapsulated in Ru Carbonyl Carboxylate Shells.

- Langmuir* **2006**, *22*, 7861-7866.
42. Kellner, C. S.; Bell, A. T., Infrared Studies of Carbon Monoxide Hydrogenation over Alumina-Supported Ruthenium. *J. Catal.* **1981**, *71*, 296-307.
43. Dimakis, N.; Navarro, N. E.; Mion, T.; Smotkin, E. S., Carbon Monoxide Adsorption Coverage Study on Platinum and Ruthenium Surfaces. *J. Phys. Chem. C* **2014**, *118*, 11711-11722.
44. Pfnür, H.; Menzel, D.; Hoffmann, F. M.; Ortega, A.; Bradshaw, A. M., High Resolution Vibrational Spectroscopy of Co on Ru(001): The Importance of Lateral Interactions. *Surf Sci.* **1980**, *93*, 431-452.
45. Starr, D. E.; Bluhm, H., Co Adsorption and Dissociation on Ru(0001) at Elevated Pressures. *Surf Sci.* **2013**, *608*, 241-248.
46. Morgan, D. J., Resolving Ruthenium: XPS Studies of Common Ruthenium Materials. *Surf. Interface Anal.* **2015**, *47*, 1072-1079.
47. Taglang, C.; Martínez-Prieto, L. M.; del Rosal, I.; Maron, L.; Poteau, R.; Philippot, K.; Chaudret, B.; Perato, S.; Sam Lone, A.; Puente, C.; Dugave, C.; Rousseau, B.; Pieters, G., Enantiospecific C-H Activation Using Ruthenium Nanocatalysts. *Angew. Chem. Int. Ed. Engl.* **2015**, *54*, 10474-10477.
48. Martínez-Prieto, L. M.; Urbaneja, C.; Palma, P.; Cámpora, J.; Philippot, K.; Chaudret, B., A Betaine Adduct of N-Heterocyclic Carbene and Carbodiimide, an Efficient Ligand to Produce Ultra-Small Ruthenium Nanoparticles. *Chem. Commun.* **2015**, *51*, 4647-4650.
49. González-Gálvez, D.; Nolis, P.; Philippot, K.; Chaudret, B.; van Leeuwen, P. W. N. M., Phosphine-Stabilized Ruthenium Nanoparticles: The Effect of the Nature of the Ligand in Catalysis. *ACS Catal.* **2012**, *2*, 317-321.
50. Chen, L.; Zhu, Y.; Zheng, H.; Zhang, C.; Zhang, B.; Li, Y., Aqueous-Phase Hydrodeoxygenation of Carboxylic Acids to Alcohols or Alkanes over Supported Ru Catalysts. *J. Mol. Catal. A: Chem.* **2011**, *351*, 217-227.
51. Shanguan, J.; Olarte, M. V.; Chin, Y.-H., Mechanistic Insights on C-O and C-C Bond Activation and Hydrogen Insertion During Acetic Acid Hydrogenation Catalyzed by Ruthenium Clusters in Aqueous Medium. *J. Catal.* **2016**, *340*, 107-121.
52. Cusinato, L.; Martínez-Prieto, L. M.; Chaudret, B.; del Rosal, I.; Poteau, R., Theoretical

Characterization of the Surface Composition of Ruthenium Nanoparticles in Equilibrium with Syngas. *Nanoscale* **2016**, *8*, 10974-10992.

53. Sheldrick, G., Shelxt - Integrated Space-Group and Crystal-Structure Determination. *Acta Cryst. A* **2015**, *71*, 3-8.

54. Percus, J. K.; Yevick, G. J., Analysis of Classical Statistical Mechanics by Means of Collective Coordinates. *Phys. Rev.* **1958**, *110*, 1-13.

55. Kresse, G.; Furthmüller, J., Efficient Iterative Schemes for Ab Initio Total-Energy Calculations Using a Plane-Wave Basis Set. *Phys. Rev.* **1996**, *54*, 11169-11186.

56. Kresse, G.; Furthmüller, J., Efficiency of Ab-Initio Total Energy Calculations for Metals and Semiconductors Using a Plane-Wave Basis Set. *Comput. Mater. Sci.* **1996**, *6*, 15-50.

57. Kresse, G.; Hafner, J., Ab Initio Molecular-Dynamics Simulation of the Liquid-Metal–Amorphous-Semiconductor Transition in Germanium. *Phys. Rev.* **1994**, *49*, 14251-14269.

58. Kresse, G.; Hafner, J., Ab Initio Molecular Dynamics for Liquid Metals. *Phys. Rev.* **1993**, *47*, 558-561.

59. Blöchl, P. E., Projector Augmented-Wave Method. *Phys. Rev.* **1994**, *50*, 17953.

60. Kresse, G.; Joubert, D., From Ultrasoft Pseudopotentials to the Projector Augmented-Wave Method. *Phys. Rev.* **1999**, *59*, 1758.

61. Perdew, J. P.; Burke, K.; Ernzerhof, M., Generalized Gradient Approximation Made Simple. *Phys. Rev. Lett.* **1996**, *77*, 3865.

62. Momma, K.; Izumi, F., Vesta 3 for Three-Dimensional Visualization of Crystal, Volumetric and Morphology Data. *J. Appl. Crystallogr.* **2011**, *44*, 1272-1276.

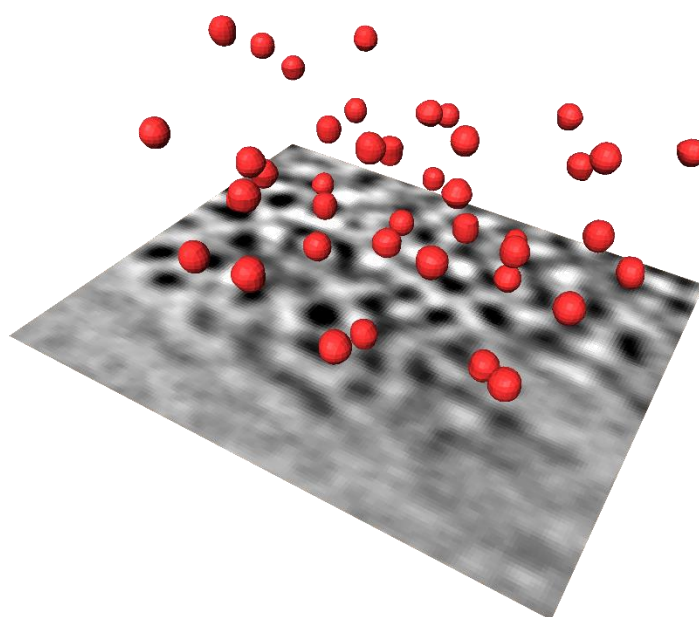
63. Tang, W.; Sanville, E.; Henkelman, G., A Grid-Based Bader Analysis Algorithm without Lattice Bias. *J. Phys.: Condens. Matter* **2009**, *21*, 084204.

64. Rosal, I.; Truflandier, L.; Poteau, R.; Gerber, I. C., A Density Functional Theory Study of Spectroscopic and Thermodynamic Properties of Surfacic Hydrides on Ru (0001) Model Surface: The Influence of the Coordination Modes and the Coverage. *J. Phys. Chem. C* **2010**, *115*, 2169-2178.

65. Henkelman, G.; Uberuaga, B. P.; Jónsson, H., A Climbing Image Nudged Elastic Band Method for Finding Saddle Points and Minimum Energy Paths. *J. Chem. Phys.* **2000**, *113*, 9901-9904.

66. Henkelman, G.; Jónsson, H., Improved Tangent Estimate in the Nudged Elastic Band Method for Finding Minimum Energy Paths and Saddle Points. *J. Chem. Phys.* **2000**, *113*, 9978-9985.
67. Sheppard, D.; Terrell, R.; Henkelman, G., Optimization Methods for Finding Minimum Energy Paths. *J. Chem. Phys.* **2008**, *128*, 134106.

Chapter 3 3D and 2D self-assemblies of Ru nanoparticles *via* multitopic ligands



3. 3D and 2D self-assemblies of Ru nanoparticles *via* multitopic ligands

3.1 Introduction

3.2 Results and discussion

3.2.1 3D Ru NP assemblies with hexa-substituted fullerene

3.2.1.1 Synthesis of hexa-substituted fullerene C₆₀ and their corresponding Ru NP assemblies

3.2.1.2 Characterization of the Ru@HF assembly

3.2.2 Synthesis and characterization of Ru NP assemblies through tricarboxylic-hexyloxy triphenylene

3.2.2.1 Synthesis of carboxylic/tricarboxylic-hexyloxy triphenylene and 2D assemblies with tricarboxylic-hexyloxy triphenylene

3.2.2.2 Wide-angle X-ray scattering analyses

3.2.2.3 Small-angle X-ray scattering analyses

3.2.2.4 Electron tomography analyses

3.2.2.5 Atomic force microscopy analyses

3.2.2.6 X-ray photoelectron spectroscopy analyses

3.2.2.7 Infrared analyses

3.2.2.8 Solid-state NMR analyses

3.2.2.9 Temperature-programmed desorption analyses

3.2.3 Synthesis and characterization of Ru NP assemblies through 9,10-dicarboxylic acid anthracene

3.3 Conclusion

3.4 Experimental section

3.5 References

3.1 Introduction

As described in Chapter 2, and in previous published works,¹⁻³ carboxylic acid groups strongly coordinate to the Ru NP surface. A previous work in our group has shown that the multitopic $C_{66}(\text{COOH})_{12}$ ligand provided $\text{Ru}@C_{66}(\text{COOH})_{12}$ nanostructures (Figure 3.1), which are ordered in assemblies.¹ The formation of the network was confirmed by SAXS and electron tomography analyses. Other fullerene derivatives have been also reported for the stabilization of Au NP providing similar assemblies.⁴⁻⁷

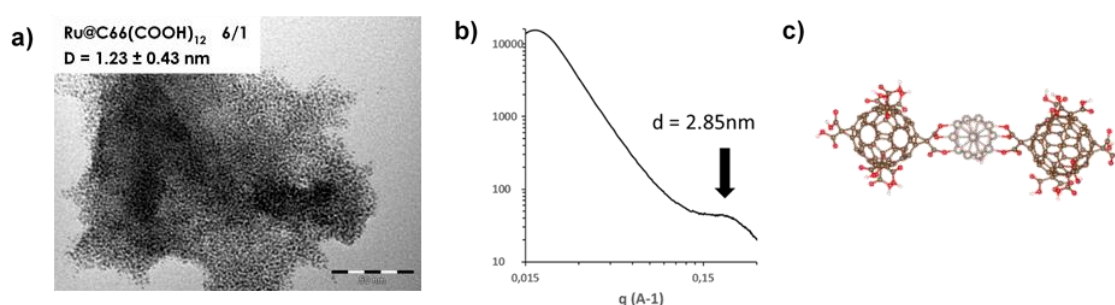
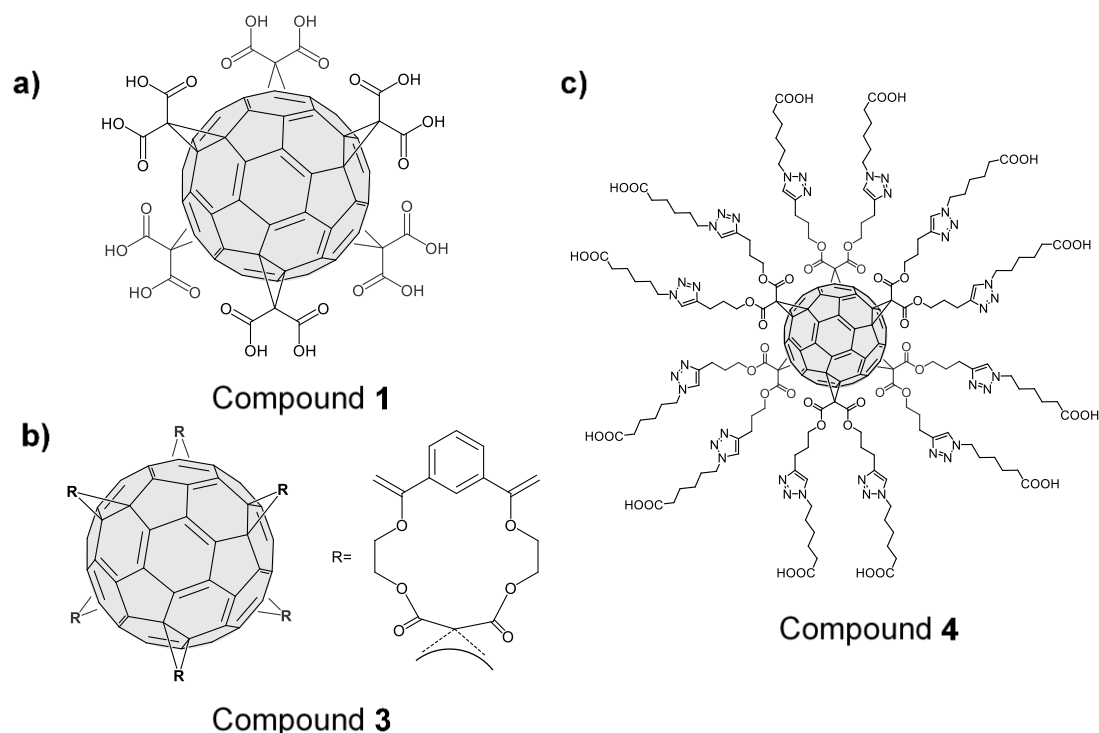


Figure 3.1 a) TEM image of the $\text{Ru}@C_{66}(\text{COOH})_{12}$ self-assembly displaying Ru NP mean size diameter of 1.2 nm; b) SAXS spectrum of the $\text{Ru}@C_{66}(\text{COOH})_{12}$ assembly; and c) optimized structure established through theoretical calculations of $C_{66}(\text{COOH})_{12}\text{-Ru}_{13}\text{-}C_{66}(\text{COOH})_{12}$ displaying a highly favourable formation ($-149 \text{ kcal}\cdot\text{mol}^{-1}$) and a monodentate and a bridging bidentate coordination of carboxylic acids groups to the Ru NP surface.¹

A ligand with the same fullerene structure but including spacers in between the cage and the anchoring groups ($-\text{COOH}$) can be of interest in order to build up similar Ru NP networks with a longer distance among the NP to control the porosity of the assembly. In this sense three ligands of hexa-adducted fullerene have been previously synthesised (Scheme 3.1),⁸ but only compound **1** was used for building up NP assemblies. The [60] fullerene hexakis-adduct synthesised through click chemistry (Scheme 3.1c, compound **4**, **HF**) allows obtaining a longer spacer between the acid moieties and the fullerene cage. Its synthesis is straightforward giving better yields than the other proposed compounds depicted in Scheme 3.1. In this chapter the synthesis and

use of this fullerene-based ligand for stabilizing Ru NP is described.



Scheme 3.1 Previously synthesized fullerene adducts bearing carboxylic acid groups: a) compound **1** $C_{66}(COOH)_2$; b) compound **3** and c) compound **4**.⁸

In this chapter it is also described the use of ligands having a triphenylene backbone as stabilizers of Ru NP. The triphenylene moieties with an extended aromatic sp^2 basal plane and six substituents at the periphery position of the polyaromatic core (Figure 3.2a) have been exploited as discotic liquid crystal.⁹⁻¹⁰ The disc-shaped molecules form mesophases, which are of primarily two types: nematic and columnar. In the discotic nematic phase, the arrangement of discs is orientationally ordered with no long-range translational order, while, in the columnar phase, the discs are stacked one on top of another to form columns (Figure 3.2b and c). The properties of mesomorphism and the presence of several binding sites lead to use widely these kind of molecules as building blocks to obtain self-assembled materials, such as metal complexes, polymers, metal-organic frameworks (MOFs), among others.¹¹⁻¹⁵

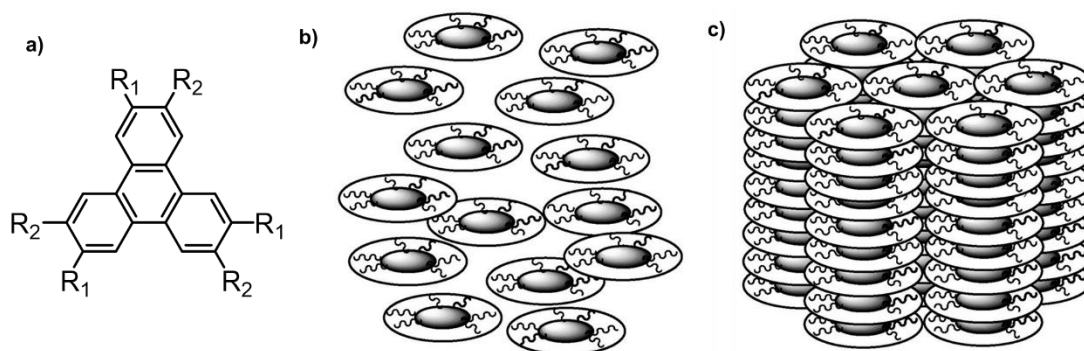


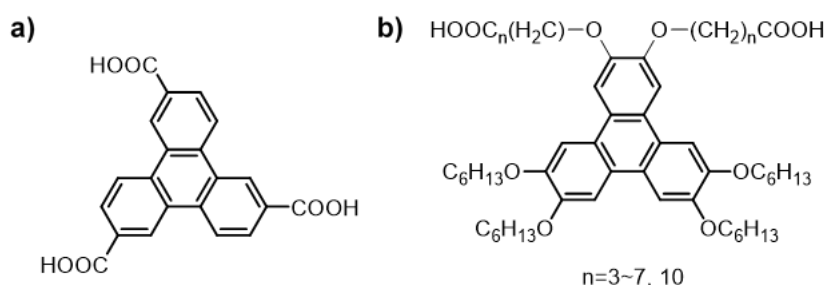
Figure 3.2 a) Functionalized triphenylene molecule; and schematic representations of b) the discotic nematic phase and c) the columnar phase.

For instance, triphenylene hexa-substituted derivatives afforded 2D MOFs because of the presence of the planar molecule, thus leading to extended sheets, which provided a significant electroactivity.¹⁶⁻¹⁸ Also, triphenylene-2, 6, 10-tricarboxylate was applied to construct dynamic fluorescent 3D MOFs along the c axis with Tb^{3+} , which was stable and highly selective sensor of nitroaromatic compounds.¹⁹ Furthermore, metal complexes containing triphenylene based ligands were found to display photonic properties, for example, Pt complexes are luminescent metallomesogens.²⁰ S. Coco, P. Espinet *et al.*²¹ reported mesophase organometallic complexes of isocyanotriphenylene molecule with several metals, including Au, Cu, Pd and Pt, which displayed promising properties for further applications as semiconductors. Columnar mesophases were detected resulting from π - π stacking of the triphenylene, and also due to inorganic columns formed through dipole-dipole interactions of the metallic moieties. It was also found that triphenylene based molecules can be well ordered and assembled on Ag (111) and Au (111) substrates.²²⁻²⁴

The nanocomposites of discotic liquid crystal hybridized with, or stabilizing, metal nanoparticles have been also reported; the associations of the compounds improved the liquid crystal properties leading to novel materials for device applications.²⁵⁻²⁶ As an illustration, Au NP was intercalated into a matrix of a discotic liquid crystals of hexapentyloxytriphenylene (TP) altering the thermophysical properties, leading to

enhanced conductivity and keeping the columnar mesophase.²⁷⁻³¹ The thermodynamic, electrical and optical properties of the TP liquid crystalline material could be also modified by supported Ag NP.³²⁻³³ Miyake *et al.*³⁴⁻³⁵ synthesized Au NP coated with hexaalkoxy-substituted triphenylene, which can be self-assembled to stripe-like arrangement of *hcp* structure due to the π - π interactions of ligands with the NP surface. The controllable arrangement of NP was achieved successfully by modifying the solvent ratio between methanol and toluene. Z. Shen *et al.* reported a simple method to transfer Au NP capped with triphenylene moiety into Au nanodisks by UV irradiation.³⁶ Wire-assembled Au NP were synthesized by template effect of star-shaped triphenylene columnar stacks.³⁷ Similarly, 2D hexagonal Au superlattices were produced by the confinement of NP stabilized by TP in the mesophase.³⁸ Other materials based on ZnO NP have also been reported. ZnO NP can coordinate with thiol-functionalized triphenylene ligand to obtain polymer/ZnO hybrid solar cells, with enhanced charge separation and transfer efficiency compared to polymer/ZnO without the ligand.³⁹

2D materials own remarkable physical and chemical properties, making it the focus of the forefront of material science. Due to their unique geometric and electronic properties, 2D materials can also find applications as catalysts.⁴⁰ The properties of extended 2D and mesophase of triphenylene derivative has been investigated by using carboxylic triphenylene (Scheme 3.2).⁴¹⁻⁴⁴



Scheme 3.2 a) Triphenylene-2,6,10-tricarboxylic acid;⁴¹ b) ester derivatives of triphenylene with two carboxylic groups.⁴²⁻⁴⁴

In this chapter, 3D Ru NP assemblies are synthesized by means of **HF** functionalized fullerene compound. In addition, the possibility to create 2D structures with a planar compound, tricarboxylic-hexyloxy triphenylene (**TPhTC**) compound, is also explored. For comparative purposes, mono carboxylic triphenylene (**TPhC**) ligand is discussed as well. Finally, 9,10-dicarboxylic acid anthracene (**AnDC**), which is commercial and presents a simple and planar structure is explored.

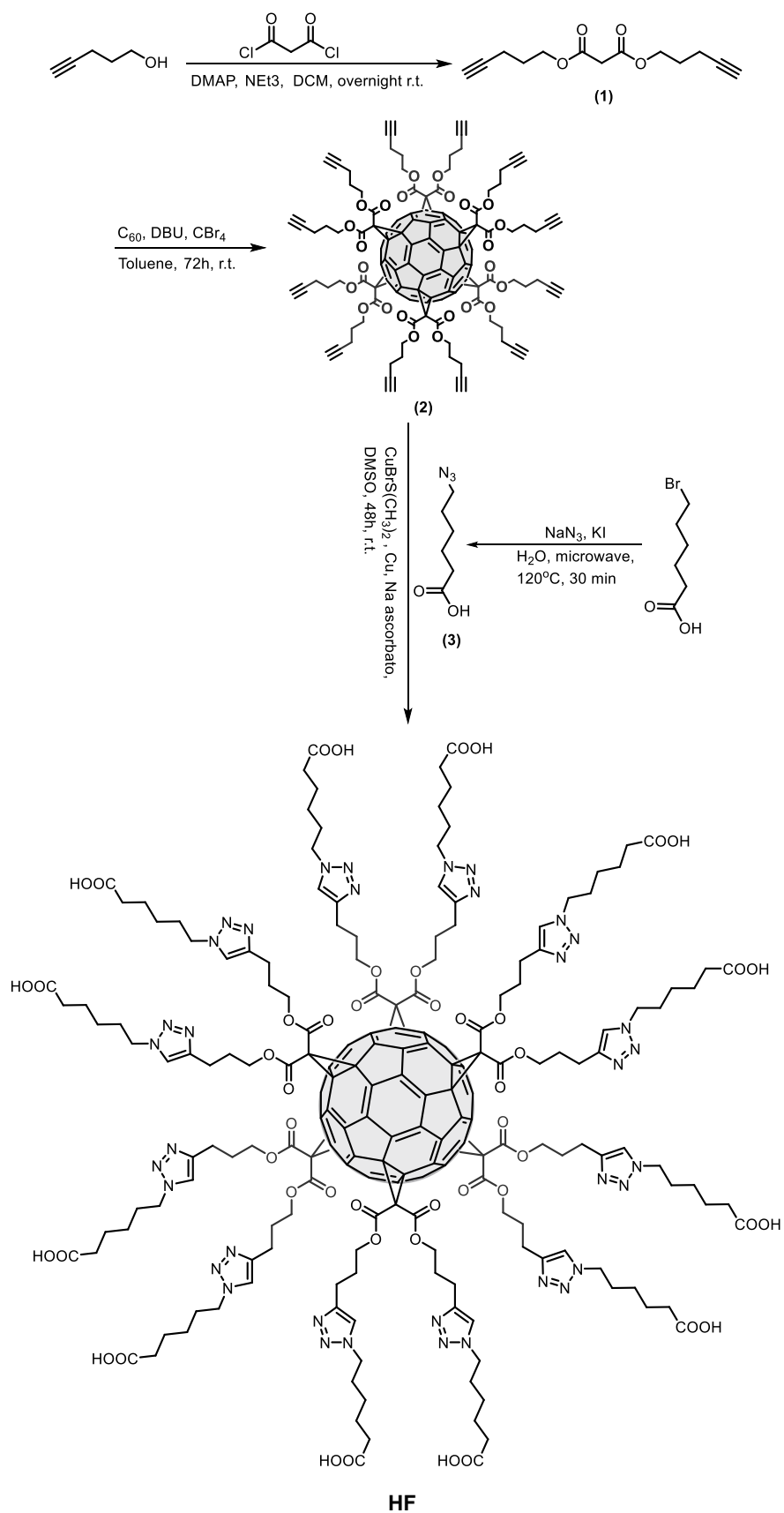
3.2 Results and discussion

3.2.1 3D Ru NP assemblies with hexa-substituted fullerene

Ru NP assemblies were produced through hexa-adducts functionalized C_{60} (**HF**) ligand (Scheme 3.1c) leading to similar 3D assemblies to the ones described with adamantane based ligands described in Chapter 2.

3.2.1.1 Synthesis of hexa-substituted fullerene C_{60} and their corresponding Ru NP assemblies

This compound was synthesized in the laboratory of Prof. Nazario Martin in Madrid (Spain) during three months internship. The synthesis of hexa-substituted fullerene C_{60} (**HF**) is depicted on Scheme 3.3. The cycloaddition of malonate to the [6, 6] double bonds of C_{60} through a Bingel-Hirsch reaction afforded T_h -hexa-adducts 4-pentyn malonate fullerene, compound (2). Via 'click' reaction,⁴⁵ hexanoic acid was attached to (2) through a triazole-link producing the desired multitopic carboxylic acid derivative. The detailed reaction procedure is described in the experimental section.

Scheme 3.3 Synthesis of the hexa-substituted fullerene C₆₀ (HF) using a Bingel-Hirsch

hexaadduct and click chemistry.⁴⁵⁻⁴⁷

The ^{13}C NMR spectrum of **HF** is depicted on Figure 3.3. A set of three peaks corresponding to the sp^2 carbons of the C_{60} fullerene cage appear at 145.5 and 141.2 ppm, and at 69.2 ppm due to the sp^3 carbons. Besides, a signal for the cyclopropane unit appears at 46.0 ppm. The signal at 163.3 ppm is attributed to the ester group. The expected resonances of the carbon atoms of the 1,2,3-triazole unit are clearly observed in 122.3 and 66.9 ppm. The presence of carboxylic acid is confirmed by the peak at 207 ppm.

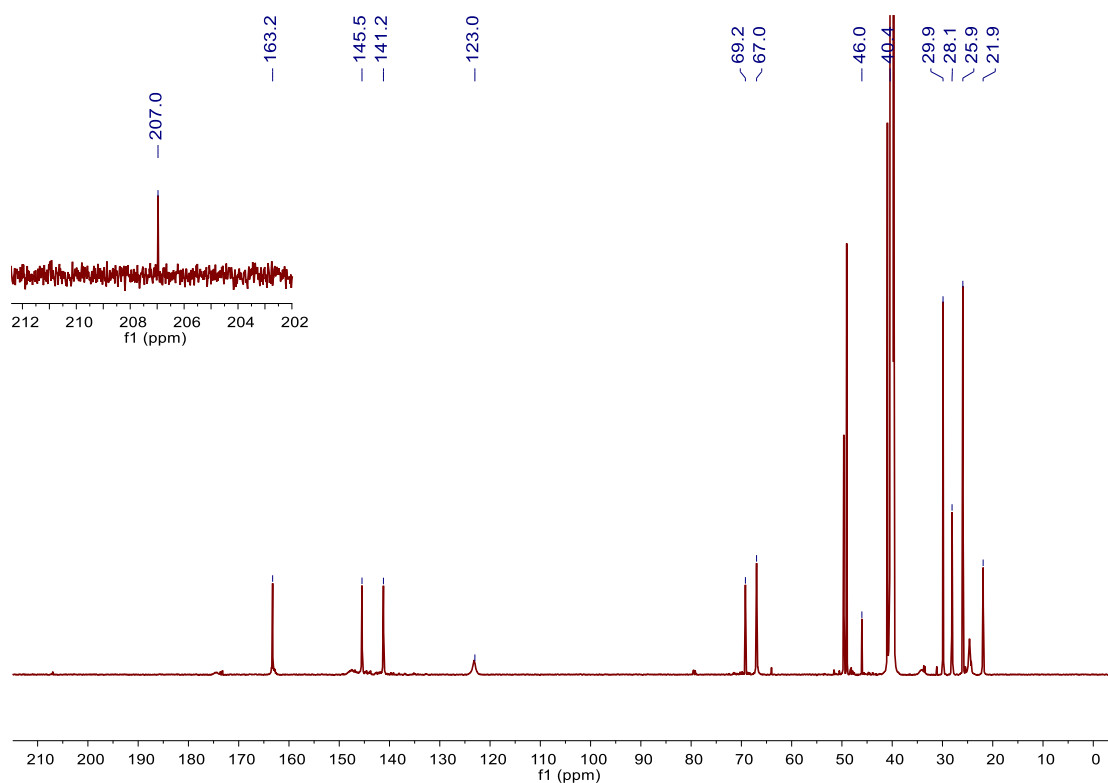
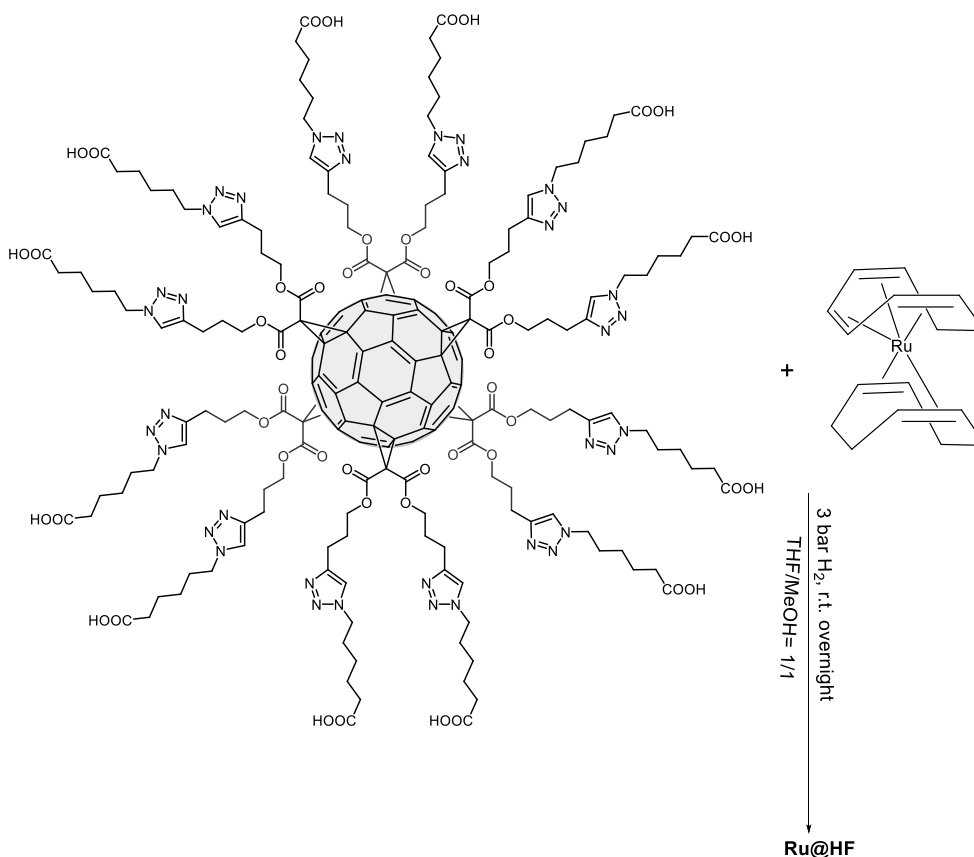


Figure 3.3 $^{13}\text{C}\{^1\text{H}\}$ NMR in DMSO-d_6 of **HF**.

With the ligand in hand, Ru nanostructures were synthesized by following the same procedure described for previous Ru NP assemblies, *i. e.* decomposition of $[\text{Ru}(\text{COD})(\text{COT})]$ in the presence of the ligand in a THF/MeOH mixture by using H_2 at room temperature (Scheme 3.4). In this case, due to the low amount of ligand available, only one Ru/L ratio was investigated (120/1). ICP analysis revealed that the

ruthenium content is 65.9% in the Ru based nanostructure, which is in agreement with the starting Ru to ligand ratio used. The detailed procedure is described in the experimental section.



Scheme 3.4 Synthesis of **Ru@HF**.

3.2.1.2 Characterization of the Ru@HF assembly

The **Ru@HF** assembly was characterized using several techniques, including TEM (Transmission electron microscopy analyses), ICP (Inductively Coupled Plasma analyses), IR (Infrared), SS-NMR (Solid-State NMR analyses), WAXS (Wide-angle X-ray scattering analyses) and SAXS (Small-angle X-ray scattering analyses).

TEM images of the as-synthesized Ru NP are shown in Figure 3.4a. **Ru@HF** is revealed to be, as observed for Ru NP structure synthesized in the presence of functionalized polyadamantane species (Chapter 2), an assembly of Ru NP, showing

the Ru NP mean size distribution of 2.2 ± 1.8 nm. The WAXS diffractogram shown in Figure 3.4b is consistent with Ru NP crystallized in the *hcp* structure. The coherence distance is estimated to 2.3 nm, which is in agreement with TEM measurements.

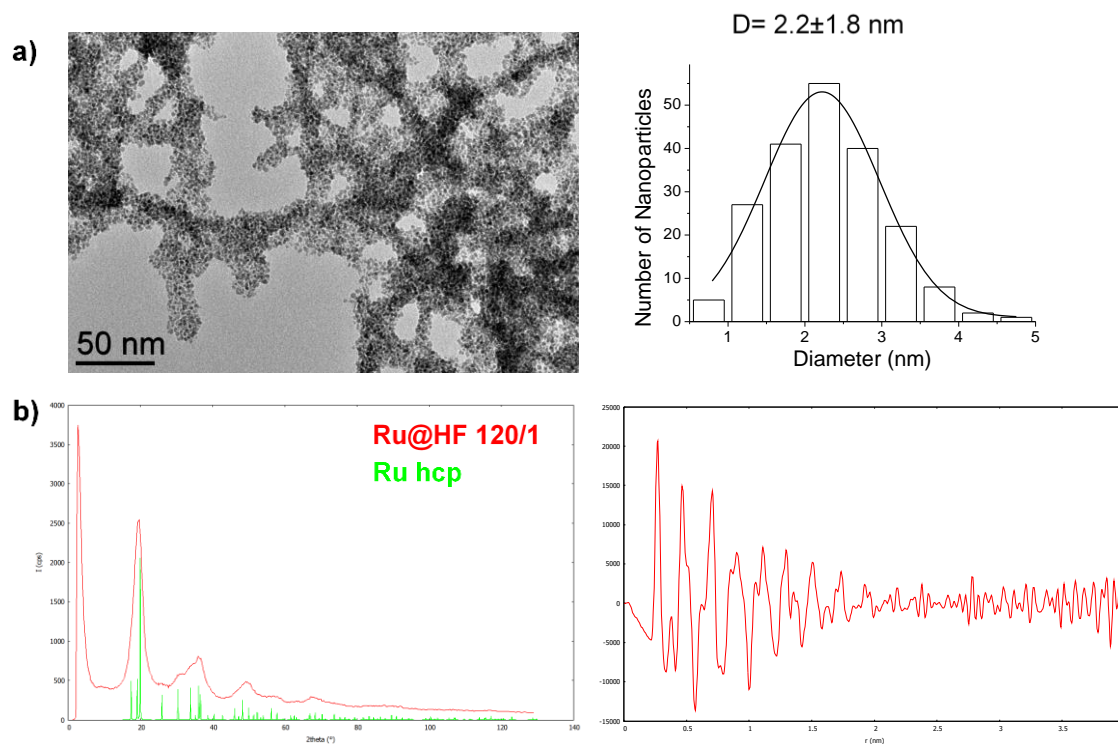


Figure 3.4 a) TEM image of **Ru@HF** - 120/1 (scale bar = 50 nm) together with the statistic distribution of NP size; and b) WAXS diffractogram (left) of **Ru@HF** - 120/1 together with Ru *hcp* as reference and related RDF (right).

SAXS analysis confirmed the formation of the assembly of Ru NP. The SAXS pattern depicted in Figure 3.5, showed a peak centered at 0.19 \AA^{-1} , which corresponds to an inter-particle distance of 3.3 nm. Comparing to the Ru NP assemblies described in a previous work by using the hexa-substituted fullerene C_{60} , $Ru@C_{66}(COOH)_{12}$,¹ the inter-particle size is larger with **HF**, since the inter-particle distance for $Ru@C_{66}(COOH)_{12}$ was 2.85 nm, which is mostly because that in our case Ru NPs are larger and with a broader size distribution (2.2 ± 1.8 nm) than for the $Ru@C_{66}(COOH)_{12}$ assembly (1.5 ± 0.8 nm).

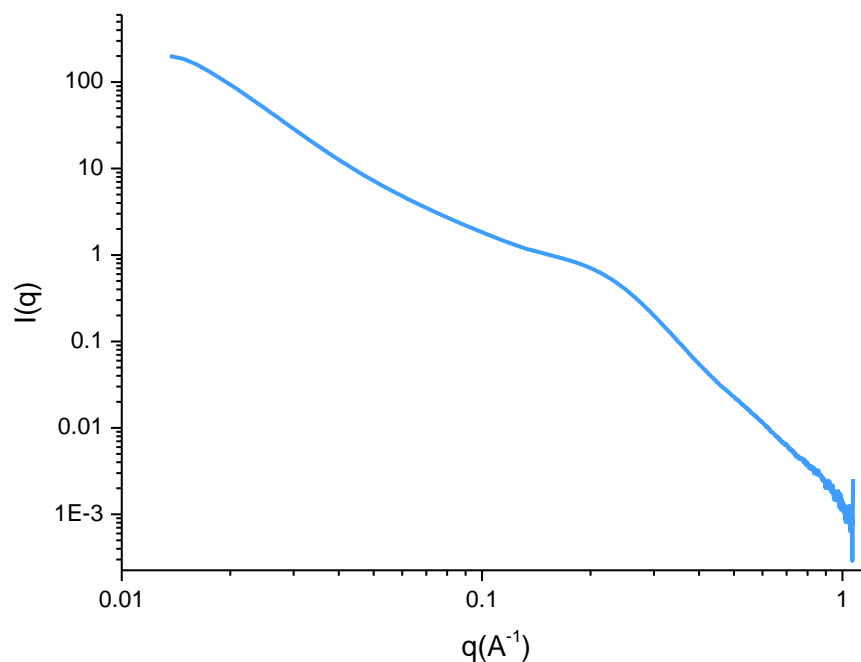


Figure 3.5 SAXS pattern of **Ru@HF**.

The coordination chemistry of the ligand **HF** on the surface of Ru NP was investigated by ATR-IR and SS-NMR.

Infrared analyses show that, upon coordination of the ligand **HF** on the Ru NP surface, two new bands appear at 1580 and 1395 cm^{-1} , (Figure 3.6a) together with the disappearance of the signals at 1720 cm^{-1} (C=O stretch) and 1244 cm^{-1} (C-O stretch) in the infrared spectrum, attributed to the coordination of the carboxylic acid moieties (Figure 3.6b). These signals, similar to the ones already described for **Ru@2** in Chapter 2, correspond to carboxylate species coordinating to the Ru surface through a bridging bidentate mode. The shift of the band of the C=O of the carboxylic acid due to the coordination to the Ru NP surface led to the C=O peak of the malonate at 1731 cm^{-1} observed. The triazole can be identified by a band at 1551 cm^{-1} due to the N=N bond,⁴⁸⁻⁴⁹ and 1440 cm^{-1} due to N-C stretching⁵⁰. Adsorbed CO species were also detected with a band at 1922 cm^{-1} .

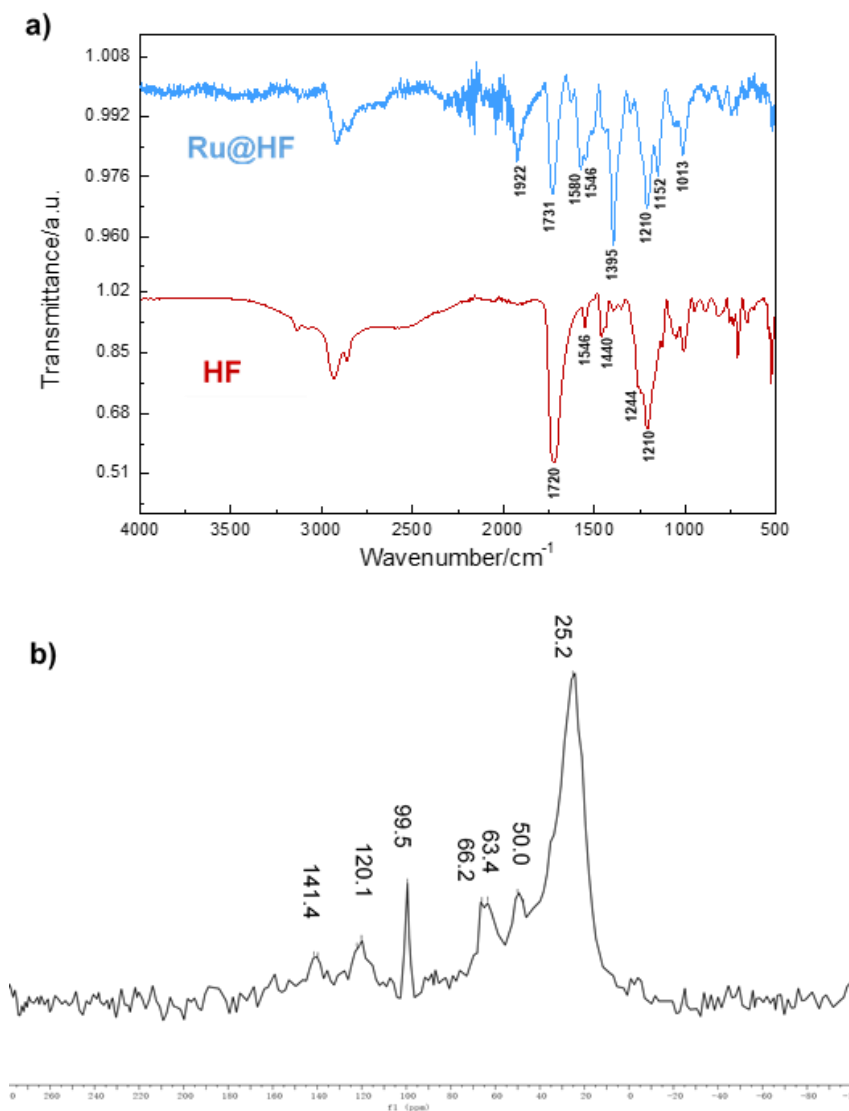


Figure 3.6 a) ATR-IR spectra of **Ru@HF** - 120/1 together with hexa-substituted fullerene C₆₀ ligand (**HF**); and b) ¹³C CP MAS SS-NMR of **Ru@HF** - 120/1.

The ¹³C SS-NMR spectra (Figure 3.6b) shows the presence of the ligand in the nanostructure through the characteristic peaks of carbon of the 1,2,3- triazole unit (120.1 and 63.4 ppm), the fullerene cage (141.4 and 66.2 ppm), quaternary carbon of the cyclopropane (50.0 ppm) and the carbon atoms of the alky chains (25.2 ppm). The signal of the coordinated carboxylate was not detected because of its low signal as mentioned in Chapter 2.

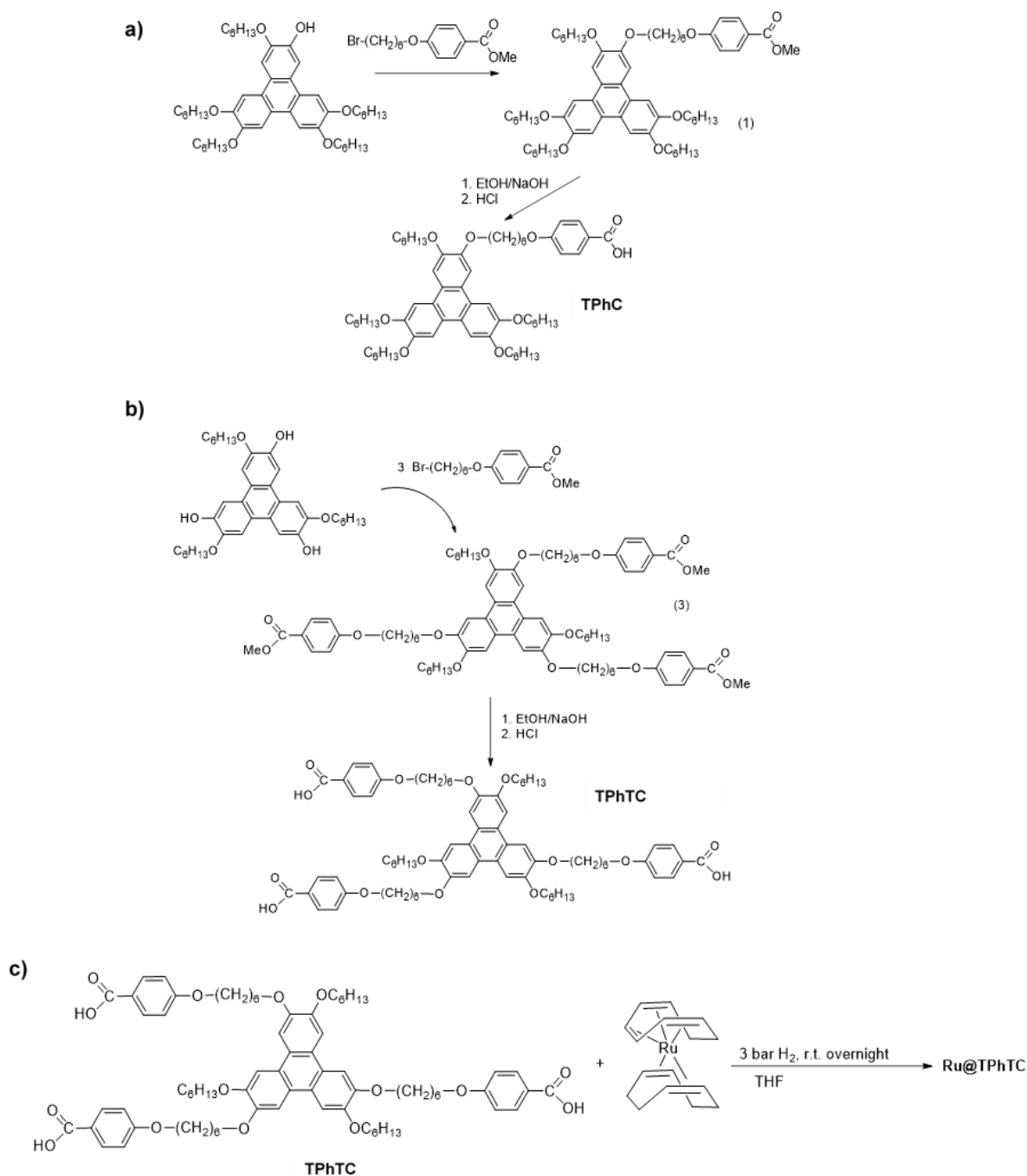
3.2.2 Synthesis and characterization of Ru NP assemblies through tricarboxylic-hexyloxy triphenylene

The use of tricarboxylic-hexyloxy triphenylene (**TPhTC**) compound as capping agent allows the self-assembly into a 2D nanostructure of Ru NP by following the straightforward organometallic synthesis method.

3.2.2.1 Synthesis of carboxylic/tricarboxylic-hexyloxy triphenylene and 2D assemblies with of tricarboxylic-hexyloxy triphenylene

The decomposition of $[\text{Ru}(\text{COD})(\text{COT})]$ under 3 bar of hydrogen pressure was performed in the presence of two different triphenylene derivatives, 2(6-(4-(carboxy)phenoxy)hexyloxy)-3,6,7,10,11-pentakis(hexyloxy)triphenylene (**TPhC**) and 2,6,10-tris(6-(4-(carboxy)phenoxy)hexyloxy)-3,7,11-trihexyloxytriphenylene (**TPhTC**) (Scheme 3.5 a, b) These molecules were provided by Prof. Silverio Coco (Liquid Crystal and New Materials Group of the Valladolid University), and the synthesis process (Scheme 3.5) is described in experimental part. Ru NP 2D assemblies were afforded by a one-step procedure, which was carried out at room temperature using THF as solvent and several Ru to ligand ratios were investigated.

The **TPhC** ligand that bears unique carboxylic group stabilized Ru NP, and as shown in the TEM images (Figure 3.7a), the sample consists of isolated NP. This differs from the material produced from the **TPhTC** ligand. Indeed, the presence of the multidentate ligand during the synthesis allows obtaining 2D assemblies of Ru NP (Figure 3.7b-f) no matter of the Ru to ligand ratio used.



Scheme 3.5 Synthesis of a) **TPhC**; b) **TPhTC**; and c) Ru NP assemblies with **TPhTC**.

On the other hand, the increase of the Ru content during the synthetic procedure leads to an increase of the Ru NP size, ranging from 1.3 ± 0.5 nm for the Ru/**TPhTC** ratio of 20 to 2.4 ± 1.2 nm for the ratio of 120. In contrast with the assemblies obtained with the adamantane ligands (Chapter 2), nanostructures stabilized by ligand **TPhTC** are thin tiled assemblies as revealed by TEM analyses, indicating the effect of the planar

character of the ligand.

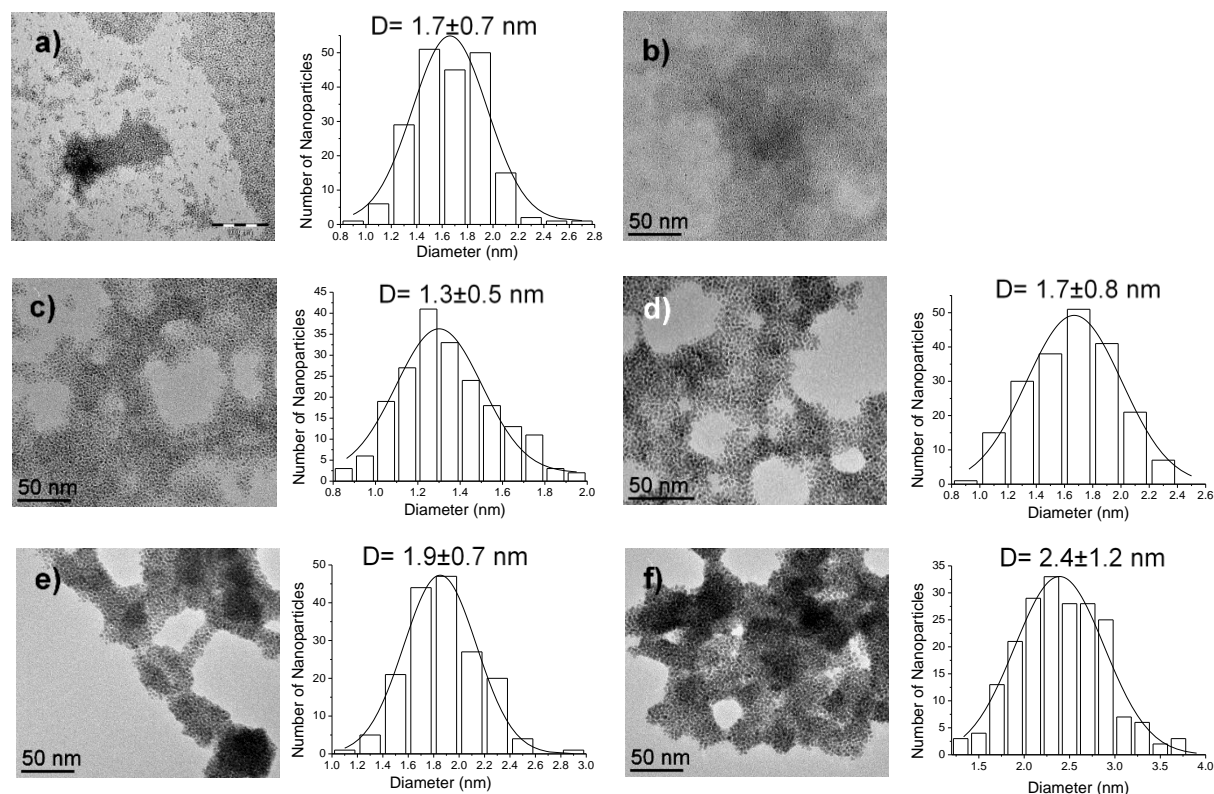


Figure 3.7 TEM images and corresponding size histograms of a) **Ru@TPhC** with a Ru/L ratio of 10/1; and **Ru@TPhTC** with Ru/L ratio of b) 4/1; c) 20/1; d) 40/1; e) 70/1; and f) 120/1.

HRTEM and HAADF-STEM analyses were performed on several samples (Figure 3.8) displaying Ru/L ratios from 6/1, 20/1 to 40/1. In the structural HRTEM analysis performed on assembly 6/1 (analysis performed by A. Falqui in King Abdullah University of Science and Technology - KAUST), two different shapes of NP are presented, one is spherical NP presenting single crystalline domains (Figure 3.8a right side panels and b left side panels), the other consists in elongated NP composed by different crystalline domains (Figure 3.8b right side panels). Interplanar distances and angular relationships measured by 2-Dimensional Fast Fourier Transform (2D-FFT) analysis for both types of particles are always consistent with the presence of Ru *hcp*.

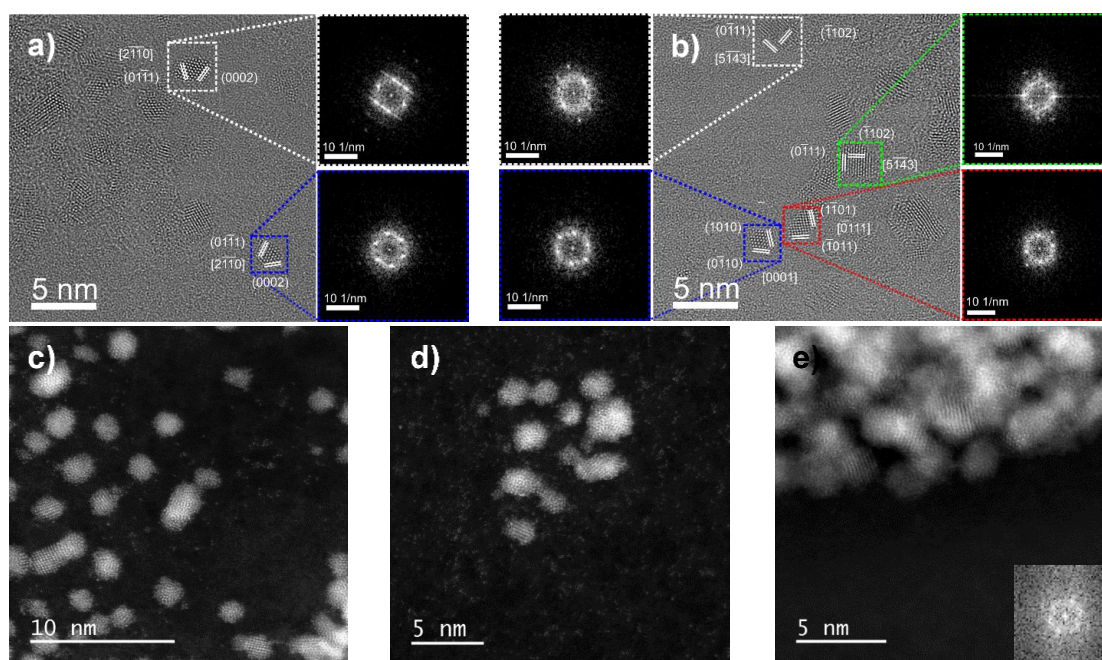


Figure 3.8 HRTEM images of Ru@TPhTC with a Ru/L ratio of a) and b) 6/1 together with 2-Dimensional Fast Fourier Transform (2D-FFT) analysis; HAADF-STEM images of: c) 20/1; d) 40/1 (reaction carried out at 0 °C for 7h); and e) 40/1.

At a Ru/L ratio of 20/1, small amounts of clusters and even Ru isolated atoms are shown around the NP in assemblies (Figure 3.8c). Similar result was obtained when the synthesis was carried at 0 °C for 7h with a 40/1 Ru/L ratio (Figure 3.8d). Following the typically synthesis procedure at room temperature for 16h, Ru NP assemblies of 40/1 only display NP with Ru *hcp* crystalline structure excluding Ru atoms (Figure 3.8e).

3.2.2.2 Wide-angle X-ray scattering analyses

The Ru@TPhTC nanostructures produced at different Ru/L ratios were examined by WAXS (Figure 3.9). The patterns show peaks in the corresponding reflections of Ru metallic *hcp*, indicating well-crystallized structures; except for the sample with a 4/1 Ru to ligand ratio. The strength of the signal is diluted because of the high amount of ligand, meanwhile, the small angle peak could indicate strong agglomeration.

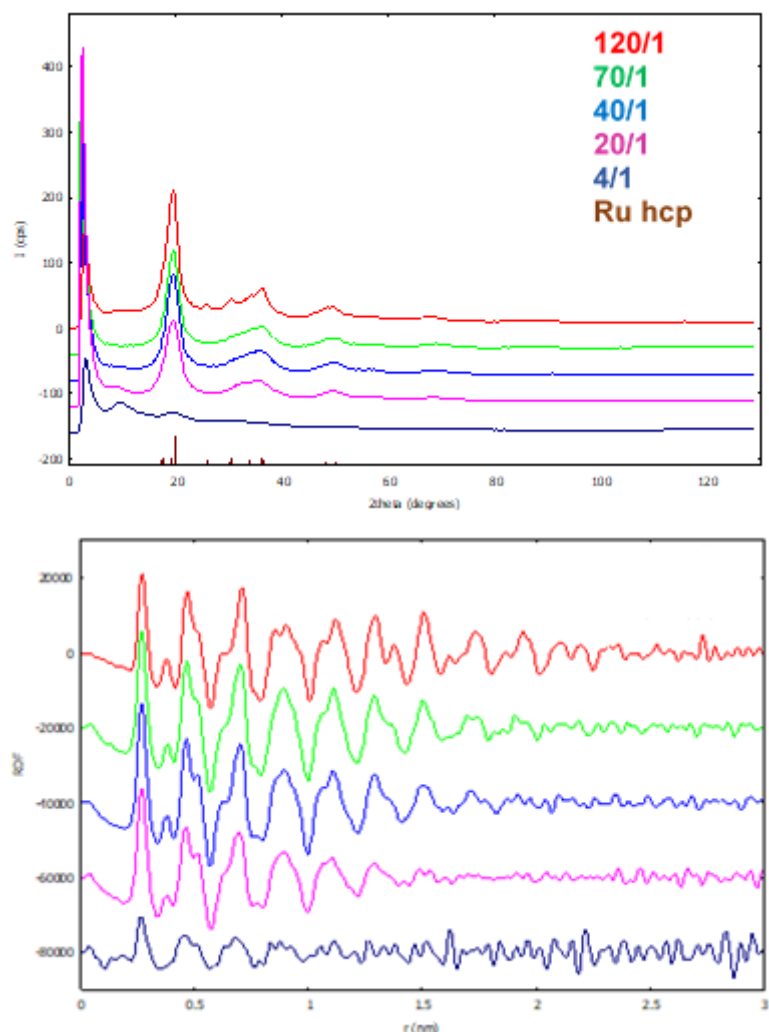


Figure 3.9 Diffractograms of **Ru@TPhTC** species displaying several Ru/L ratio (4 to 120 from bottom to top) together with the reference of Ru *hcp* structure (top); and related RDF (bottom).

After Fourier transformation, the RDF functions indicate that coherence distance is ranged from 1.8 nm to 2.2 nm for ratios from 20/1 to 70/1, for sample 120/1, the NP size is up to 2.7~2.8 nm; which is agreement with Ru NP sizes determined by means of TEM analyses. On the other hand, because of the weak signal of the **Ru@TPhTC** 4/1 sample, the determination of the coherence length is difficult and is estimated to be 1.3-1.4 nm.

3.2.2.3 Small-angle X-ray scattering analyses

SAXS analysis was performed to reveal the arrangement of Ru NP inside the assembly and the appearance of the assembly particle. The peaks at high angle ($> 0.1 \text{ \AA}^{-1}$) represent the average distance between NP detected at 0.18, 0.20 and 0.22 \AA for **Ru@TPhTC** samples 70/1, 40/1 and 20/1. The correlation distance is calculated by $q = 4\pi\sin\theta/\lambda$ and Bragg's law function $2d\sin\theta = n\lambda$, displaying center to center distance as 3.68, 3.56 to 3.11 nm, for samples 70/1, 40/1 and 20/1, respectively. As the length of the ligand is the same for all Ru NP series this variation on the distance is caused by the different Ru NP mean size diameter (1.9 ± 0.7 , 1.7 ± 0.8 , and 1.3 ± 0.5 nm, for **Ru@TPhTC** - 70/1, 40/1 and 20/1, respectively), which fits well with a distance of about 1.8 nm for all cases due to the presence of the ligand. Table 3.1 summarizes the Ru NP sizes of **Ru@TPhTC** series determined by TEM and SAXS, together with the inter-particle distance determined by SAXS.

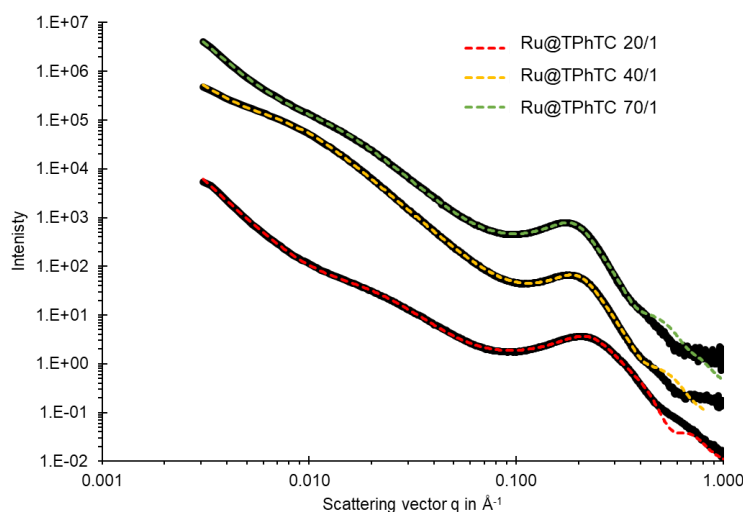


Figure 3.10 SAXS spectra of Ru NP assemblies with TPhTC ligands (red curve, **Ru@TPhTC** - 20/1, yellow curve, **Ru@TPhTC** - 40/1, and green curve, **Ru@TPhTC** - 70/1). The experimental SAXS curves are plotted in $\text{Log } I(q) \text{ vs } \text{Log } q$ representation in black line and the fitting curves corresponding to the calculated SAXS curves from the model are plotted in dashed line.

Table 3.1 Mean size distributions, inter-particle distances of the synthesized Ru NP and Ru NP

networks with **TPhTC** using different Ru/L ratio.

Ru/L (molar)	Ru NP size (nm) ^{a)}	Ru NP size (nm) ^{b)}	Inter-particle distance (nm) ^{c)}
4/1	-	1.3-1.4	-
20/1	1.3 ± 0.5 nm	1.8	3.11
40/1	1.7 ± 0.8 nm	2.1	3.56
70/1	1.9 ± 0.7 nm	2.2	3.68
120/1	2.4 ± 1.2 nm	2.7-2.8	-

^{a)} By TEM; ^{b)} by WAXS; ^{c)} by SAXS.

3.2.2.4 Electron tomography analyses

To confirm the short-range order between the Ru NP, an ET (Electron tomography) analysis was performed by A. Falqui in King Abdullah University of Science and Technology on a typical aggregate obtained at a Ru/L molar ratio of 40/1 (Figure 3.11). After performing ET on a large NP assembly, it was possible to determine the distribution of the inter-particle distance. For this the volume of the assembly was segmented into three small boxes (Figure 3.12a) to reconstruct the 3D shape, indicating an inter-particle distances of 3.4 nm (box 1), 3.5 nm (box 2) and 3.8 nm (box 3) in Figure 3.12b.

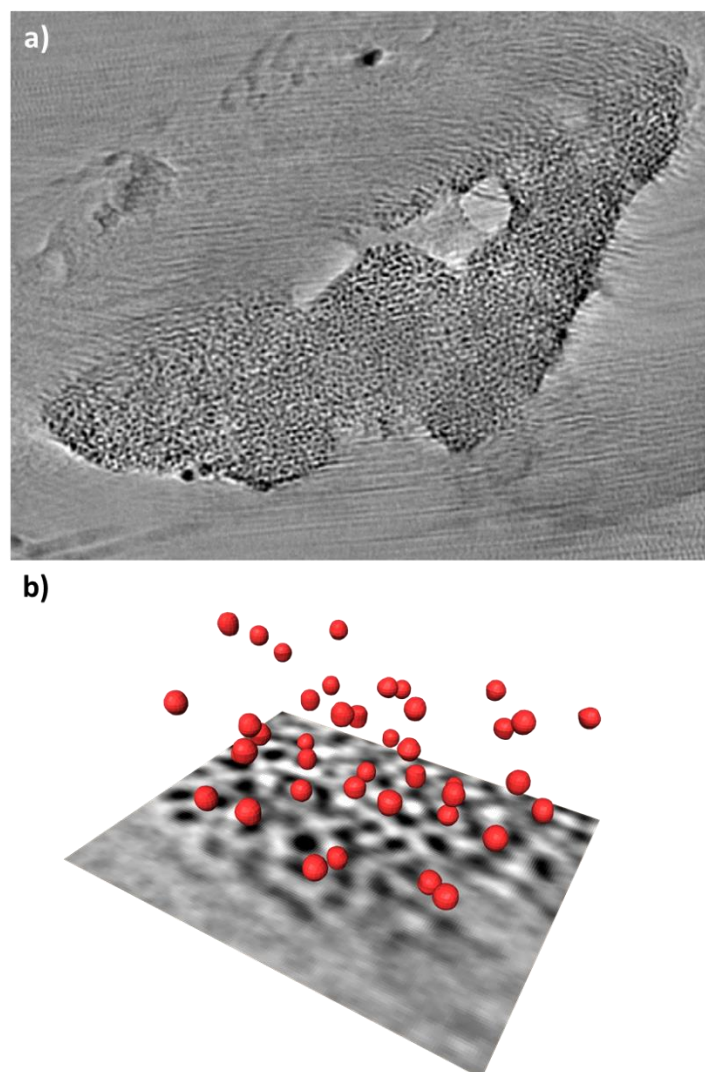


Figure 3.11 a) Tomogram of the Ru NP assembly produced from **TPhTC** using a 40/1 Ru/L ratio; and b) manual reconstruction of some Ru NP from the corresponding tomogram. A slice of the latter was used just as a visual background for the NP. It should be noticed that not all the NP imaged by ET are reported, but just few of them, properly chosen in order to make it clearly distinguishable.

The mean inter-particle distance determined by ET for this sample (3.57 nm) is in excellent agreement with the SAXS analysis (3.56 nm).

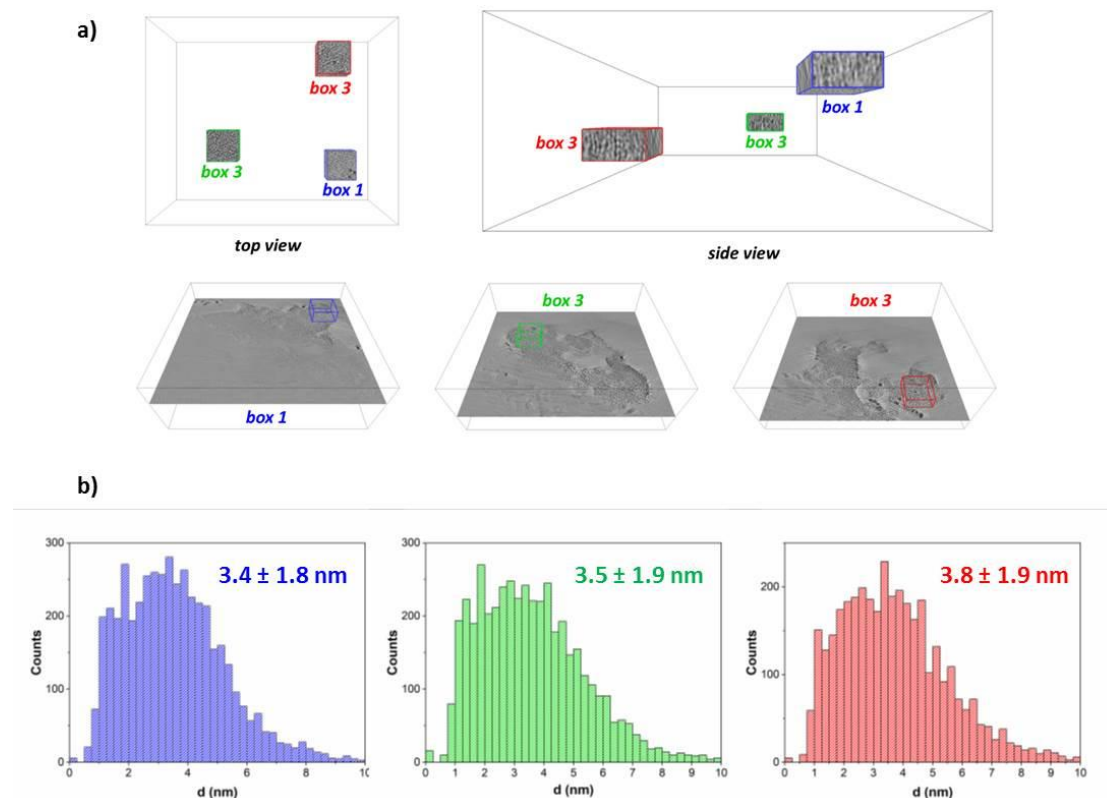


Figure 3.12 a) Volume segmentation of an assembly of Ru NP; and b) inter-particle distance distributions into the three boxes (measured on ~ 4000 distances for each boxes).

3.2.2.5 Atomic force microscopy analyses

AFM (Atomic Force Microscopy) analyses were performed to explore the surface morphology of the assembly, and to confirm their 2D structure. AFM image, height profile and 3D image of **Ru@TPhTC** with a Ru/L ratio of 40/1 are shown on Figure 3.13. The thickness of the sheets was measured to be 3 to 8 nm with some variations. Considering that the size of the Ru NP is around 2 nm, the thickness of the assembly corresponds to one to four NP in the assembly layer. Notably, the lateral size of the nanosheets ranges from 200 nm to 500 nm, presenting a high aspect ratio, thereby confirming their 2D layered structure.

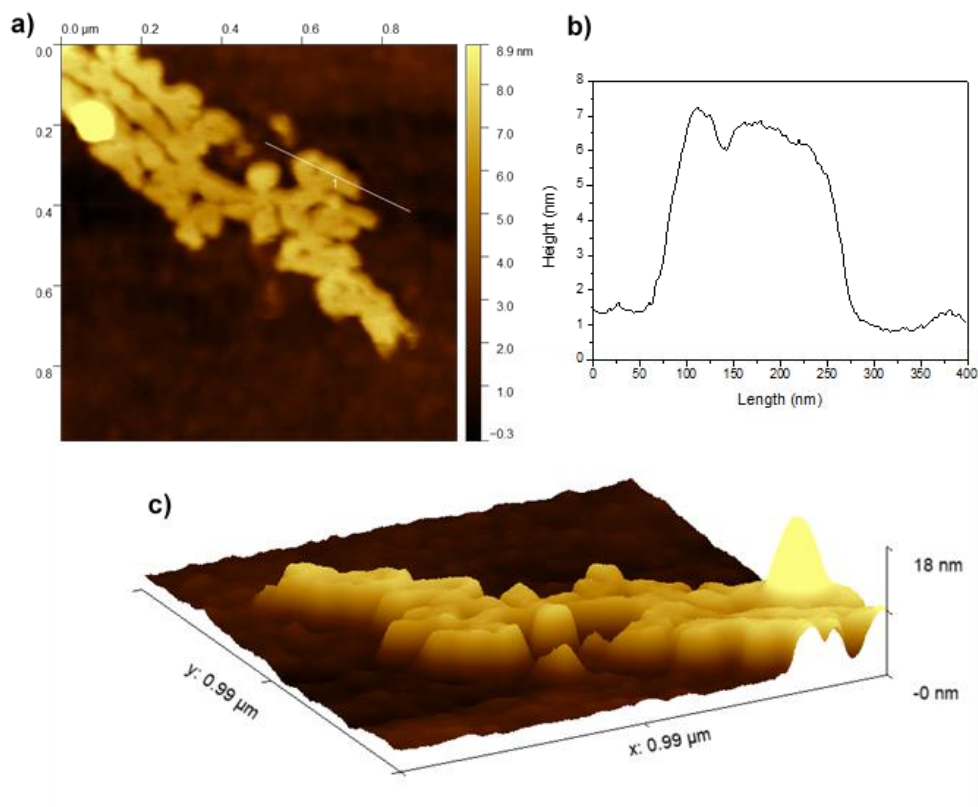


Figure 3.13 a) AFM image of **Ru@TPhTC** using 40/1 Ru/L ratio; b) height profile along the line depicted on a) line 1; and c) 3D image of the assembly.

3.2.2.6 X-ray photoelectron spectroscopy analyses

XPS (X-ray photoelectron spectroscopy) analyses of **Ru@TPhTC** were performed in an inert atmosphere. Two different Ru/L ratio, 4/1 and 40/1, were investigated, the spectra of which are depicted in Figure 3.14. The binding energies (BE), full width at half maximum (FWHM) and atomic composition are summarized in Tables 3.2 and 3.3. The elements identified in the nanostructures are Ru, C and O. For the **Ru@TPhTC** - 40/1 sample, metallic Ru is evidenced by two doublet peaks of Ru *3d* at 279.9 and 284.1 eV, and Ru *3p* at 461.5 and 483.7 eV. The C *1s* peak is deconvoluted into several peaks, which indicates different chemical environments: C-C and C-H (285.0 eV), 286.4 (C-O) and 288.1 eV (COO). Two peaks at 530.8 and 532.3 eV of O *1s* are in agreement with a carbonyl group and a weak peak at 529.5 eV with a Ru-O bond.

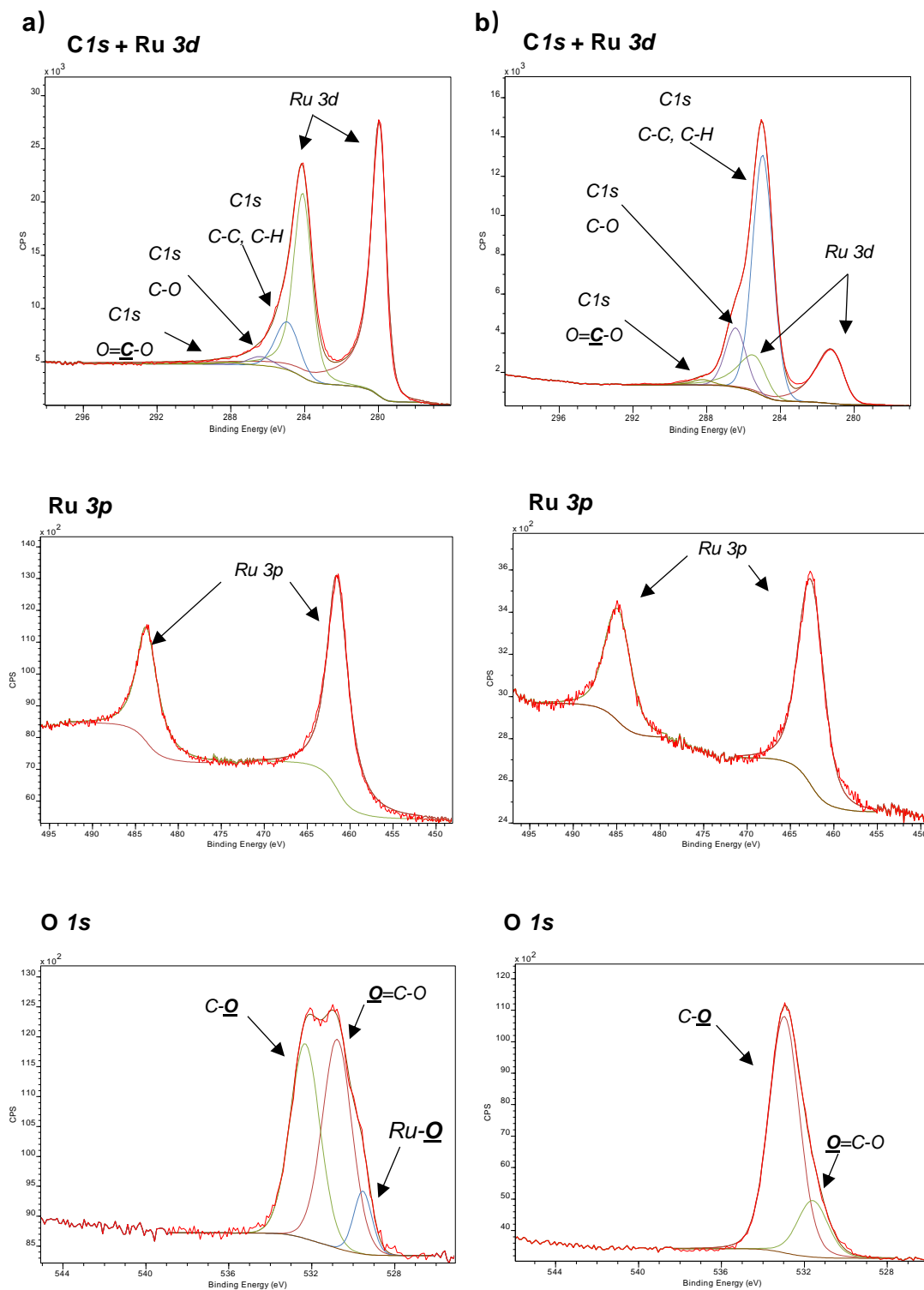


Figure 3.14 XPS spectra of: a) on the left, **Ru/TPhTC - 40/1**; b) on the right, **Ru/TPhTC - 4/1**.

In contrast, **Ru@TPhTC - 4/1** shows a clear shift of the Ru 3d peaks (281.1 and 285.3 eV) with respect to metallic Ru (279.9 and 284.0 eV), displaying values very close to the ones of RuO₂ (280.7 and 284.9 eV).⁵¹ The same situation is evidenced for the Ru

Table 3.2 Binding energy, FWHM and atomic composition of **Ru@TPhTC** - 40/1.

Bond	Ru 3p		Ru 3d			C1s		O 1s		
BE (eV)	461.5	483.7	279.9	284.1	285.0	286.4	288.1	529.5	530.8	532.3
FWHM (eV)	2.7	2.7	0.9	1.1	1.5	1.5	1.5	1.0	1.7	1.7
Atomic composition (%)	-		26.7		39.3	5.8	1.9	1.9	10.5	9.8
		26.7				47.0			22.2	

Table 3.3 Binding energy, FWHM and atomic composition of **Ru@TPhTC** - 4/1.

Bond	Ru 3p		Ru 3d			C1s		O 1s	
BE (eV)	462.6	484.9	281.1	285.3	285.0	286.4	288.1	531.6	533.0
FWHM (eV)	3.5	3.5	1.6	1.6	1.3	1.3	1.3	1.7	1.7
Atomic composition (%)	-		2.7		57.1	14.1	1.3	3.6	14.9
			2.7			72.5			16.5

$3p$ peak (462.6 eV), the peak of which is closer to the value expected for RuO_2 (462.6 eV) than for metallic Ru (461.2 eV).⁵¹ These findings suggested that the Ru is coordinated to the ligand through oxygen atoms as observed before for Ru-carboxylate nanostructures.¹ In addition and supporting this hypothesis, the O $1s$ binding energy peaks (533.0 eV) are deconvoluted into C-O and -COO or -OH species.¹ The atomic Ru percentages of **Ru@TPhTC** samples are in good agreement with the Ru/L ratio.

3.2.2.7 Infrared analyses

The series of Ru NP assemblies synthesized using **TPhTC** were characterized by ATR-IR and compared with the spectrum of the free ligand (Figure 3.15). The intense peaks at 1251 and 1164 cm^{-1} corresponding to the ether bonds, together with the peaks assigned to the triphenylene aromatic backbone, which appear in the range of 1500-1600 cm^{-1} , are observed in all spectra, pointing out that the ligand is stable under the synthesis conditions. On the other hand, the peak attributed to the C=O stretching of the carboxylic acid groups at 1680 cm^{-1} , vanished in the spectra of **Ru@TPhTC** nanomaterials, and a new set of peaks appeared at 1578 and 1367 cm^{-1} .

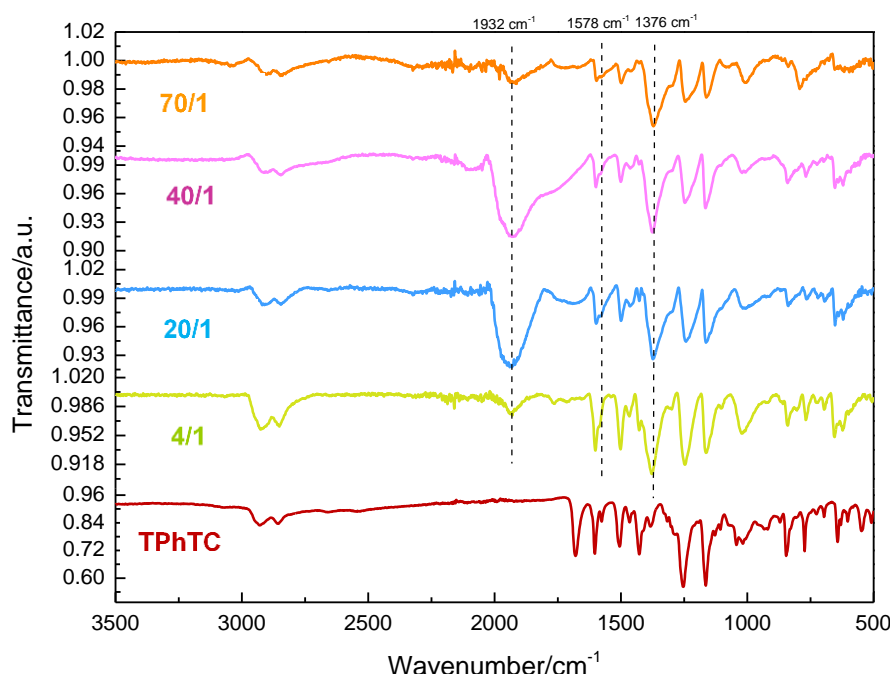


Figure 3.15 ATR-IR spectra of **TPhTC** and **Ru@TPhTC** with Ru/L ratio from 4/1 to 70/1 (from bottom to top).

These peaks are attributed to the formation of carboxylate species coordinated to the Ru surface. Giving the $\Delta\nu = 210 \text{ cm}^{-1}$, the carboxylate group is coordinated in a bridging bidentate mode. Chelating bidentate and monodentate carboxylate moieties cannot be safely ascribed. Also, adsorbed CO on the Ru NP surface is detected by IR with a band at 1932 cm^{-1} . This band is at a lower wavenumber than the ones obtained in the case of the polymantanes carboxylic ligands ($1940\text{-}1960 \text{ cm}^{-1}$).

3.2.2.8 Solid-state NMR analyses

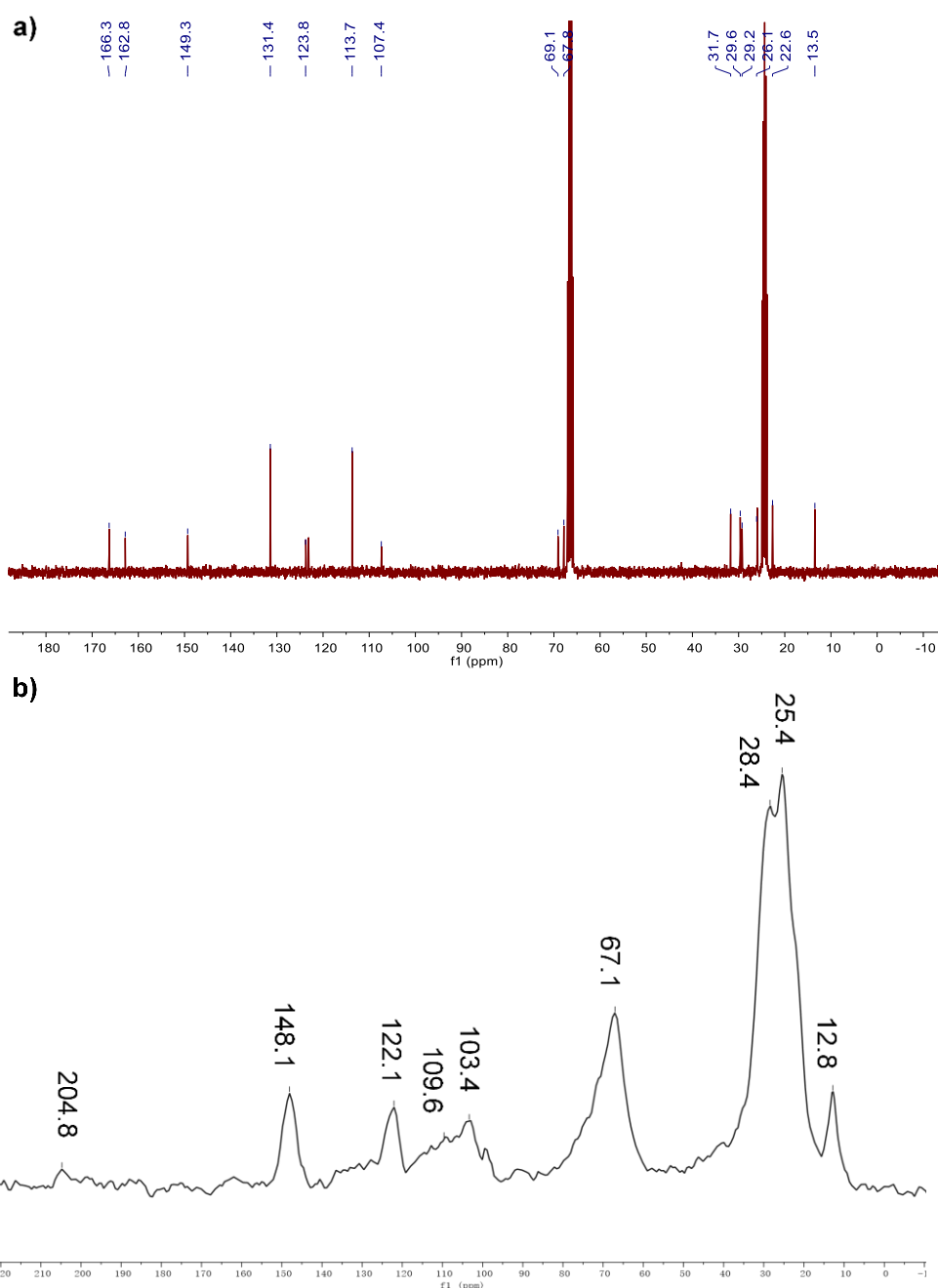
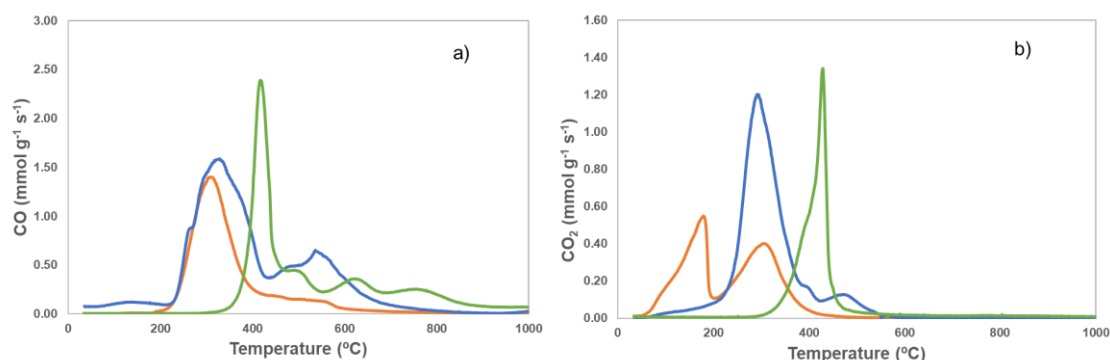


Figure 3.16 a) $^{13}\text{C}\{^1\text{H}\}$ NMR spectrum of **TPhTC** in $\text{THF-}d^8$ and; b) ^{13}C CP MAS SS-NMR spectrum of **Ru@TPhTC** with a Ru/L ratio of 40/1.

The ^{13}C NMR spectrum of the **TPhTC** in ligand in $\text{THF-}d^8$ is given in Figure 3.16a. The ^{13}C CP MAS SS-NMR of **Ru@TPhTC** - 40/1 was conducted under an inert atmosphere, the spectrum of which is displayed in Figure 3.16b. The peaks at 12.8, 25.4, 28.4 ppm are attributed to the carbons of the alkyl chain, which link the triphenylene core to the carboxylic acid moieties. The broad peak centered at 67.1 ppm corresponds to the saturated carbons of the ether bonds besides the aromatic ring. The aromatic carbons appear in the range of 103.4 to 148.1 ppm. The weak signal at 204.8 ppm is attributed to the carbon of the carboxylate species.

3.2.2.9 Temperature-programmed desorption analyses

TPD/MS analyses were performed to obtain information on the thermal stability and product decomposition of the **Ru@TPhTC** - 4/1 and 40/1 samples (Figure 3.17). TPD/MS was performed by heating the sample till 1000 °C at a rate of $5\text{ }^\circ\text{C}\cdot\text{min}^{-1}$ under He. Several fragment ions were monitored, including $m/z = 2$ (H_2), 16 (CH_4), 18 (H_2O), 28 (CO), and 44 (CO_2), in order to monitor the decomposition of the ligand on the Ru NP surface.



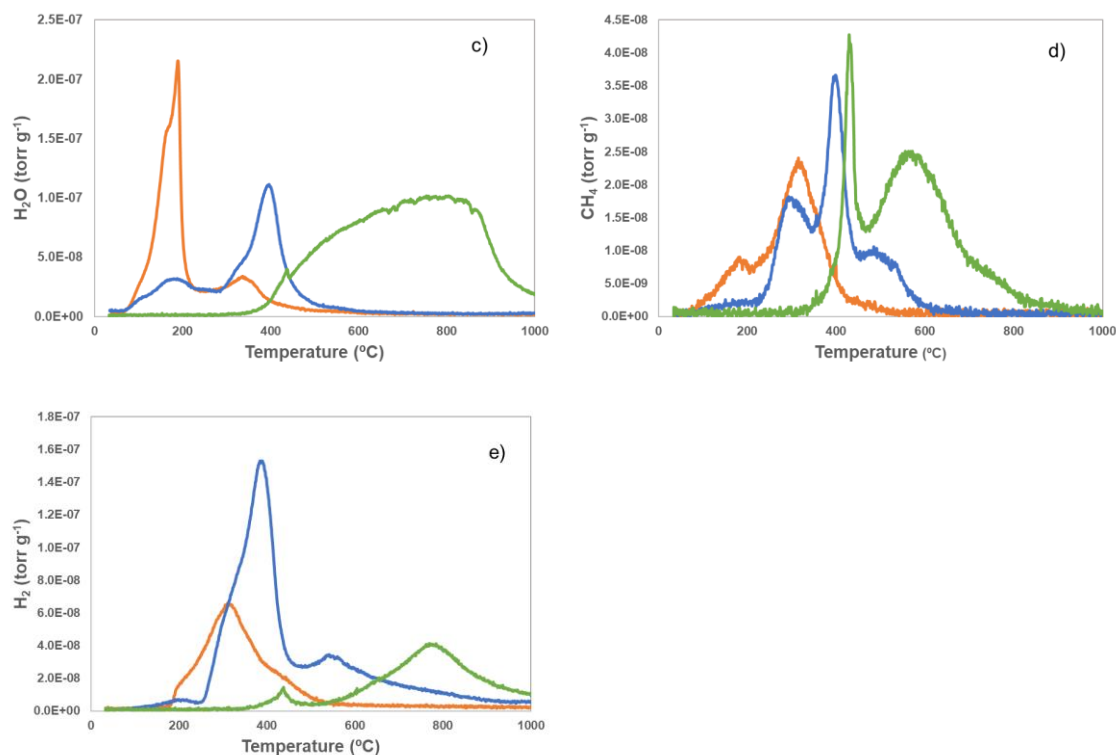
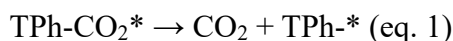


Figure 3.17 TPD patterns of **Ru@TPhTC** - 40/1 (in orange), 4/1 (in blue) and ligand **TPhTC** (in green): a) CO; b) CO₂; c) H₂O; d) CH₄ and e) H₂.

From these analyses, we can first notice that decarboxylation occurs more easily on the **Ru@TPhTC** - 40/1 assembly than on the **Ru@TPhTC** - 4/1 one, as shown by the detection of CO₂ at the temperature of 190 °C which is absent on the curve of 4/1 assembly (in blue Figure 3.17b). This difference could be due to a catalytic decomposition effect from the presence of more Ru in **Ru@TPhTC** - 40/1 compared to 4/1. As the temperature increases, a strong decarbonylation (CO desorption) and decarboxylation (CO₂ desorption) is detected at around 300~400 °C for both of the assemblies. As shown by the green curves in Figure 3.17a and 3.17b, the **TPhTC** ligand decomposed in the temperature range of 420~440 °C, which indicates a higher stability when compared with the **Ru@TPhTC** assemblies. A less significant CO and CO₂ evolution is also detected at higher temperatures (around 500 °C) of **Ru@TPhTC** - 4/1 (Figure 3.17a-b, blue lines).

H₂, CH₄ and H₂O were also detected (Figure 3.17c-e), but in much less quantity, which

could be due to simultaneous Ru-catalyzed reverse water-gas-shift side reaction⁵². The desorption of H₂ is suspected to proceed from the proton on the surface of NP. Therefore, the presence of traces of CH₄ and H₂O could be due to the following reactions:



As confirmed by the mass analyses (Table 3.4), the amount of desorbed CO is much higher than CO₂, indicating that the decomposition goes mainly by decarbonylation. Furthermore, with higher Ru loading, the CO/CO₂ mol ratio decreases from 2.66 to 2.12, and it is lower than the value found for the free ligand (CO/CO₂ = 3.33). It is worth noting, that, normalizing the value to the amount of ligand on the **Ru@TPhTC** samples, **Ru@TPhTC** - 40/1 releases more gaseous products followed by **Ru@TPhTC** - 4/1, which points out to the hypothesis that Ru promotes the decomposition of the ligand contained in the sample.

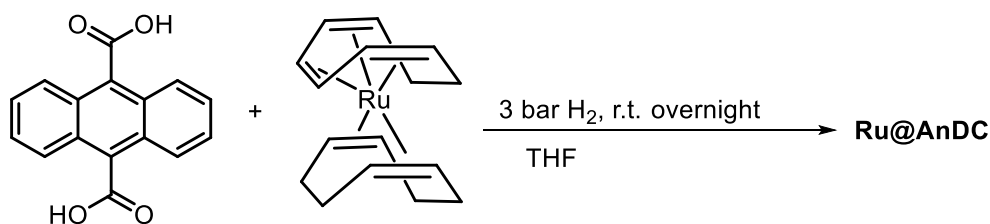
Table 3.4 Mass analyses of CO and CO₂ detected in TPD.

Sample	CO (μmol/g)		CO ₂ (μmol/g)		CO/CO ₂
	assembly	ligand ^{a)}	assembly	ligand ^{a)}	
Ru@TPhTC - 40/1	2118	6229	1001	2944	2.12
Ru@TPhTC - 4/1	4065	4748	1530	1787	2.66
Ligand		2695		809	3.33

^{a)} Ligand mass percentage is 34% and 85.6% for **Ru@TPhTC** - 40/1 and 4/1, respectively.

3.2.3 Synthesis and characterization of Ru NP assemblies through 9,10-dicarboxylic acid anthracene

Ru@AnDC nanostructures were synthesized by decomposing 10 and 20 equivalents of [Ru(COD)(COT)] in the presence of 9,10-dicarboxylic acid anthracene (**AnDC**) reduced by hydrogen.



Scheme 3.6 Synthesis of **Ru@AnDC**.

The black powder obtained by this synthetic procedure consisted in an assembly of Ru NP, in which the nanoparticles displayed a bimodal size distribution centered at 2.0 and 2.6 nm for 10/1 ratio. For Ru/**AnDC** ratio of 20/1, a similar result was obtained (Figure 3.18). Further analytical techniques, such as ICP, IR, SS-NMR, WAXS and SAXS, were used to fully characterize this material.

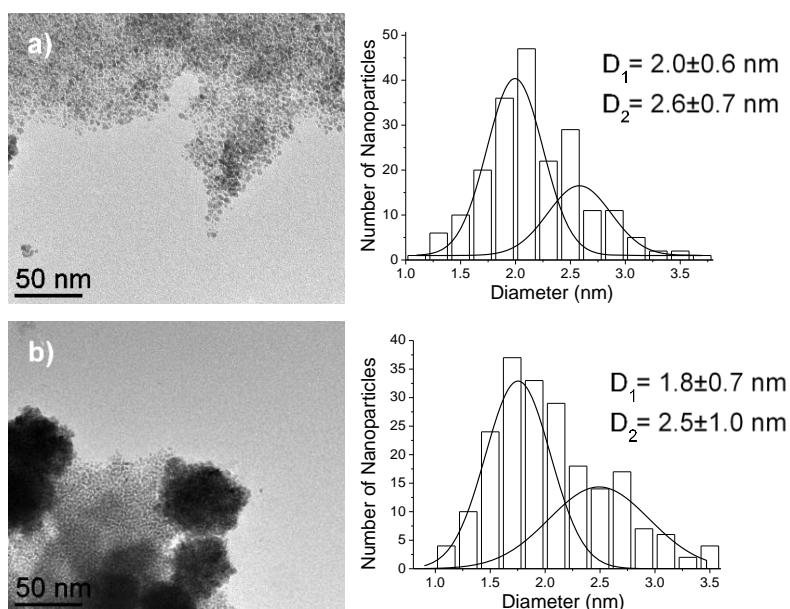


Figure 3.18 TEM images and size distribution histograms of **Ru@AnDC** with Ru/L ratio of a) 10/1 and b) 20/1.

WAXS analysis revealed well-crystallized nanoparticles in the *hcp* structure, with a coherence length of 3 nm for **Ru@AnDC - 20/1** (Figure 3.19). This NP size fits well with TEM observations, but only reflects the measured longer mean size distribution.

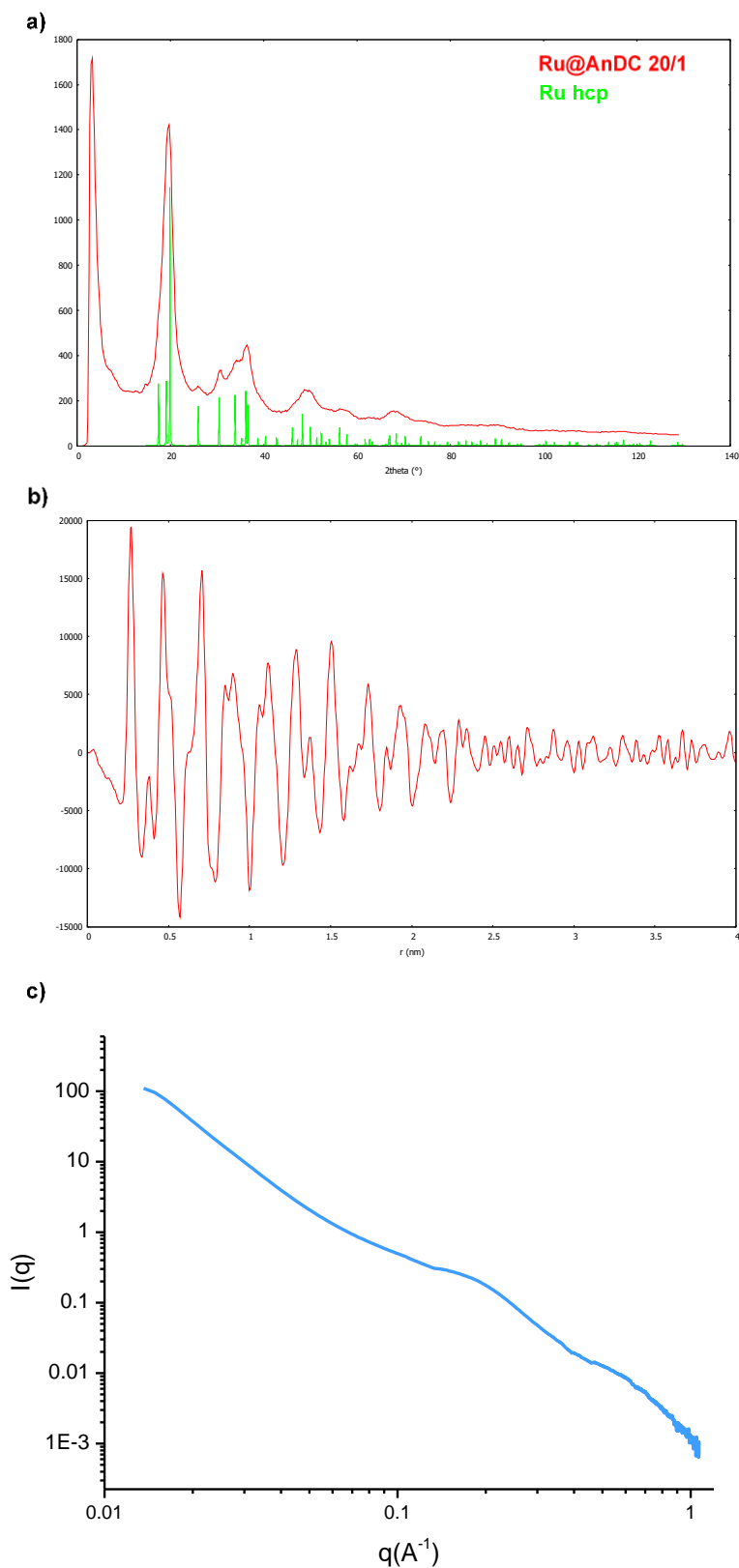


Figure 3.19 a) WAXS diffractogram together with the reference of Ru *hcp* structure; b) related RDF; and c) SAXS pattern of **Ru@AnDC** displaying a Ru/L ratio of 20.

SAXS analysis (Figure 3.19c) shows an angle beyond 0.1\AA representing the inter-particle distance that is weak and broad, inferring that the correlation distance is not as homogeneous as the assemblies produced with triphenylene ligand. The wide peaks shown on the curve which after calculation (equation: $q = 4\pi\sin\theta/\lambda$ and Bragg's law function $2d\sin\theta = n\lambda$) disclose to main distances of 3.2 nm.

The coordination of the ligand to the Ru NP surface was studied by means of IR and SS-NMR (Figure 3.20). The IR spectra of the **AnDC** ligand is depicted together with the spectrum of the **Ru@AnDC** nanostructure (Figure 3.20a). It is clearly seen, in line with previous results presented in this dissertation concerning the coordination mode of carboxylate moieties to the Ru NP surface, that the stretching C=O vibration peak at 1680 cm^{-1} is no longer detected in the **Ru@AnDC** IR spectrum. In addition, two intense peaks at 1523 cm^{-1} and 1395 cm^{-1} for a Ru/**AnDC** ratio of 10/1, and 1543 cm^{-1} and 1395 cm^{-1} for a Ru/**AnDC** ratio of 20/1 appear. These peaks are attributed to Ru carboxylate species, mainly coordinating in a bidentate bridging mode. Also, the vibration attributed to the CO coordinated to the Ru NP surface is detected at 2050 and 1946 cm^{-1} implying different adsorption sites. Some peaks present for the free ligand attributed to the arene moieties are no longer detected or the intensity is clearly lower on the **Ru@AnDC** structure, indicating the possible hydrogenation of the ligand during the synthetic procedure. Furthermore, **Ru@AnDC** displays two peaks in the C-H stretching region at 2923 cm^{-1} and 2855 cm^{-1} , which can be attributed to sp^3 C-H ($< 3000\text{ cm}^{-1}$). These observations support the hypothesis of a partial hydrogenation of the ligand. SS-NMR confirmed this assumption (Figure 3.20b). ^{13}C SS-NMR spectrum shows two peaks at 124.6 ppm and 26.5 ppm, which confirms the presence of sp^2 and sp^3 carbons in the sample. The intensity of the signal at 67.5 to 85.7 ppm is more intense when the SS-NMR is recorded by using cross-polarization, indicating that more protons are in the vicinity of the aforementioned peak. This partial hydrogenation could explain the inhomogeneity of the Ru NP size in these samples; as a mixture of compounds are

available for NP stabilization.

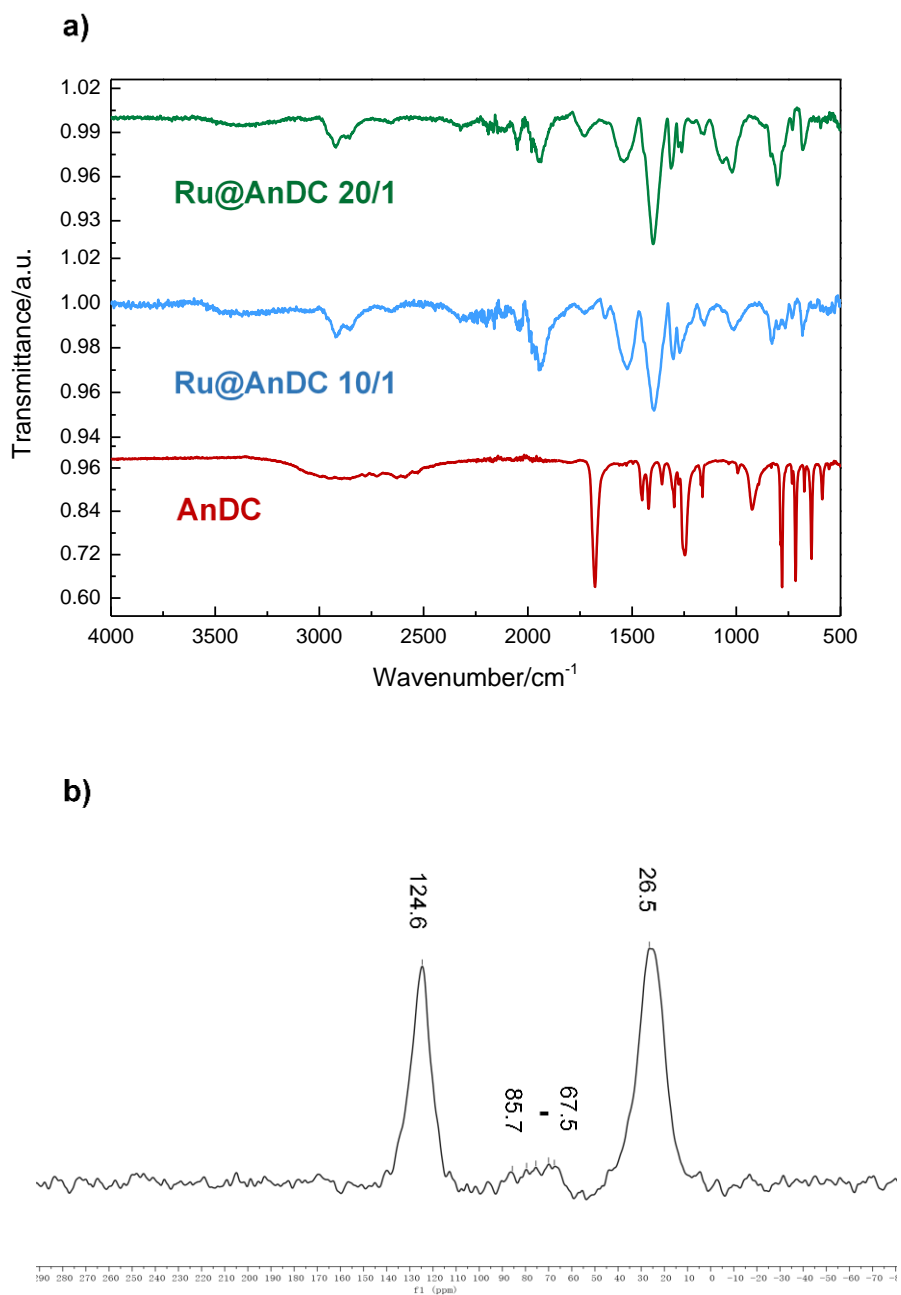


Figure 3.20 a) IR spectra of Ru@AnDC (10/1 and 20/1) and AnDC; and b) ¹³C CP MAS SS-NMR spectrum of Ru@AnDC with Ru/L ratio of 10.

3.3 Conclusion

Ru NP assemblies have been produced successfully using carboxylic functionalized

fullerene, triphenylene, and anthracene ligands. These ligands should allow tuning the assembly structure (3D with the **HF** ligand and 2D with the **TPhTC** or **AnDC** ligands) and inter-particle distance. Coordination *via* the carboxylate group on the surface of Ru NP was confirmed by IR, SS-NMR and XPS analyses. As same as for polymantanes ligands, CO was generated during the synthesis by ligand decarbonylation and/or solvent decomposition, which remains adsorbed on NP surface.

TPhTC leads to 2D assembly with 3-8 nm thickness and more than 200 nm extension as verified by AFM. The characterization by TEM, ET, WAXS and SAXS show well-ordered assembly with homogeneous NP size and a relatively large inter-particle distances (3.1-3.7 nm according to different Ru/**TPhTC** ratio). The thermal decomposition of the structure was followed by TPD, showing a thermal stability up to around 190 °C.

In comparison, ligand of **AnDC** is not stable during the synthesis as part of the arene backbone is hydrogenated. In consequence, the NP size is not homogeneous resulting in uneven correlation distance in between. While, the synthesized hexa-adduct fullerene hexanoic acid (**HF**) establish interweaved 3D assembly with average NP center to center distance of 3.3 nm and homogeneous NP. The Table 3.5 summarized the results of NP size and inter-particle distance obtained with the three ligands for a similar metal loading.

Table 3.5 Mean size distributions, inter-particle distances of the synthesized Ru NP networks using **HF**, **TPhTC** and **AnDC**.

Ligand	Ru/L (molar)	Ru loading (%)	Ru NP size (nm) ^{a)}	Ru NP size (nm) ^{b)}	Inter-particle distance (nm) ^{c)}
HF	120/1	65.9	1.5±0.8	2.3	3.3
TPhTC	40/1	66.0	1.7 ± 0.8	2.1	3.56
AnDC	20/1	66.5	1.8 ± 0.7 2.5 ± 1.0	3.0	3.2

^{a)} By TEM; ^{b)} by WAXS; ^{c)} by SAXS.

3.4 Experimental section

Materials

Solvents were purified by standard methods or by an MBraun SPS-800 solvent purification system. 4-pentyn-1-ol, triethylamine, 4-dimethylaminopyridine, malonyl chloride, CBr₄, C₆₀ fullerene, 1,8-diazabicyclo[5.4.0]undec-7-ene (DBU), sodium azide (NaN₃), 6-bromohexanoic acid, KI, CuBr•SMe₂, sodium ascorbate, QuadraSil[®] MP, sephadex LH-20 were purchased from Sigma-Aldrich and used as received.

Synthesis of hexa-substituted fullerene (HF)

Di(pent-4-yn-1-yl) malonate (Scheme 3.3 (1)). 4-pentyn-1-ol (0.88ml, 9.46 mmol), NEt₃ (1.34 mL) and 4-dimethylaminopyridine (DMAP) (11.56 mg, 0.0946 mmol) were successively dissolved in CH₂Cl₂ (25ml) under inert atmosphere. The mixture was cooled down to 0 °C, and a solution of malonyl chloride (0.47 mL, 4.73 mmol) in 1~2 mL CH₂Cl₂ was added dropwise. After 30 min, the reaction mixture was allowed to warm up to room temperature and stirred overnight. The reaction solution was treated with 20 mL HCl (1M) twice, and then by the same volume NaHCO₃ saturated solution for two times. After, the organic phase was washed once by 20 mL of brine, dried over MgSO₄ and filtered. After evaporation of the solvent the crude product was purified by flash chromatography (CH₂Cl₂/ hexane 3/1) to obtain colorless oily product. (616.2 mg, 55%). ¹H NMR (CDCl₃, 300MHz) δ(ppm) = 4.30 (t, J = 6.3 Hz, 4H), 3.4 (s, 2H), 2.31 (td, J = 7.0, 2.7 Hz, 4H), 1.99 (t, J = 2.7 Hz, 2H), 1.89 (m, 4H).

Compound (2) in Scheme 3.3. CBr₄ (8.8 g, 26 mmol), compound di(pent-4-yn-1-yl) malonate (616 mg, 2.6 mmol) and fullerene (187.4 mg, 0.26 mmol) were dissolved in dry toluene (500 mL). 1,8-diazabicyclo [5.4.0] undec-7-ene (DBU, 0.78 mL, 5.2 mmol) was introduced into the mixture dropwise. The color of the solution changed from violet to red. The mixture was kept stirring under inert atmosphere for 72 h at room temperature. After that, the organic solution was extracted with 100 mL saturated Na₂S₂O₃ solution, 150 mL HCl (1M), deionized water twice and finally with 100 mL of

brine. The organic layer was dried with MgSO_4 filtered and concentrated under reduced pressure. The crude product was purified by flash chromatography using CH_2Cl_2 as eluting solvent. The product was isolated as orange solid (289.9 mg, 53% yield). ^{13}C NMR (CDCl_3 , 75MHz) δ (ppm) = 164.0 (C=O), 146.1 ($\text{sp}^2\text{-C C}_{60}$), 141.4 ($\text{sp}^2\text{-C C}_{60}$), 82.8 ($\text{C}\equiv$), 70.2 ($\text{CH}\equiv$), 69.4 ($\text{sp}^3\text{-C C}_{60}$), 65.7 (CH_2), 45.7 (tert-C), 27.5 (CH_2), 15.5 (CH_2).

6-azido-hexanoic acid (Scheme 3.3 (3)). Sodium azide (NaN_3 , 1 g, 26 mmol), 6-Bromohexanoic acid (1 g, 5 mmol) and KI (170 mg, 1.02 mmol) were dissolved into deionized H_2O (15 mL) in a 30 mL glass vial. The reaction was carried out in a microwave at 120 °C for 30 min, and cooled down to 55 °C for removing. The mixture was extracted with diethyl ether (20 mL) three times. The organic layer was washed with brine once and dried with MgSO_4 . A colorless liquid was afforded after concentration at reduced pressure (436 mg, 69% yield). IR (cm^{-1}): 2090.19 (s, N_3), 1703.23 (s, C=O), 1250.95 (m, C-O). ^{13}C NMR (CDCl_3 , 175MHz) δ (ppm) = 180.3 (C=O), 51.5 (N- CH_2), 34.1 (CH_2), 28.8 (CH_2), 26.4 (CH_2), 24.4 (CH_2).

Compound HF. Compound (2) (120 mg, 0.056 mmol) and 6-azido-hexanoic acid (177.2 mg, 1.129 mmol) were dissolved in DMSO (3 mL). $\text{CuBr}\cdot\text{SMe}_2$ (81.2 mg, 0.395 mmol) and sodium ascorbate (134.2 mg, 0.677 mmol) were added into the mixture successively. The solution was stirred with a stirrer twined with copper wire under inert atmosphere at room temperature for 48 h. Then, QuadraSil[®] MP was added to the solution and stirred for 15 min to remove Cu. After filtration the solution was passed through a sephadex LH-20 column with $\text{CH}_2\text{Cl}_2/\text{MeOH}$ (1/1) as elution. The solution was washed by centrifugation with AcOEt (10 min, 6000 rpm) for three times. Red solid was isolated (79 mg, 36% yield). IR (cm^{-1}): 3140 (w, C-H), 1720 (s, C=O), 1459 (w, triazole), 1210 (s, C-O), 1006 (m, C-O). ^1H NMR (DMSO, 700 MHz): δ = 12.00 (s, 1H, COOH), 7.89 (s, 1H, N-CH=C), 4.33 (s, 2H, N- CH_2), 4.27 (s, 2H, O- CH_2 -), 2.63 (s, 2H, CH_2), 2.23 (s, 2H, CH_2), 1.95 (s, 2H, CH_2), 1.77 (s, 2H, CH_2), 1.49 (s, 2H, CH_2), 1.21 (s, 2H, CH_2). ^{13}C NMR (DMSO, 175MHz): δ = 163.3 (COOH), 145.5 ($\text{sp}^2\text{-C, C}_{60}$),

141.2 (sp^2 -C, C₆₀), 122.3 (N-CH=C), 69.2 (sp^3 -C, C₆₀), 67.0 (N-CH₂), 49.6 (O-CH₂), 46.0 ppm (tert-C), 29.9 (CH₂), 28.2 (CH₂), 26.0 (CH₂), 24.6 (CH₂), 21.8 (CH₂).

Synthesis of carboxylic functionalized triphenylene (TPhC) and tricarboxylic functionalized triphenylene (TPhTC)

2-(4-(methoxycarbonyl)phenoxy)hexyloxy)-3,6,7,10,11-pentakis(hexyloxy)triphenylene ((1) in Scheme 3.5)

A mixture of 3,6,7,10,11-pentakis(hexyloxy)triphenylen-2-ol⁵³ (1.22 g, 1.64 mmol), methyl-4-(6-bromohexyloxy)benzoate⁵³ (1.80 g, 5.73 mmol), and anhydrous K₂CO₃ (0.80 g, 1.44 mmol) in 100 mL of dry butanone was refluxed under nitrogen atmosphere for 24 h. After cooling to room temperature, the solvent was removed under vacuum, and then water (200 mL) was added. The mixture was extracted with dichloromethane (5 x 30 mL). The organic fractions were combined and dried over MgSO₄. Filtration followed by solvent removal afforded the crude product, which was purified by column chromatography (silica gel, dichloromethane/hexane 1:3 v/v). The compound was isolated as light yellow solid (1.33 g, 83 % yield). ¹H NMR (CDCl₃, 500 MHz) δ(ppm) = 7.97 (d, 2H, ArH, AA' part of AA'XX' spin system, $N = J_{AX} + J_{AX'} = 8.98$ Hz, $J_{AA'} \approx J_{XX'}$), 7.83 (s, 6H, TripH), 6.90 (d, 2H, ArH, XX' part of AA'XX' spin system, $N = J_{AX} + J_{AX'} = 8.98$ Hz, $J_{AA'} \approx J_{XX'}$), 4.23 (m, 12H, TriPh-O-CH₂), 4.04 (t, 2H, ArH-O-CH₂, $J = 6.40$ Hz), 3.88 (s, 3H, O-CH₃), 2.02-1.84 (m, 14H, CH₂), 1.71-1.56 (m, 14H, CH₂), 1.44-1.33 (m, 20H, CH₂), 0.93 (m, 15H, CH₃). IR (cm⁻¹): ν (C=O): 1722.

2(6-(4-(carboxy)phenoxy)hexyloxy)-3,6,7,10,11-pentakis(hexyloxy)triphenylene (TPhC) (TPhC in Scheme 3.5)

To a suspension of 2-(4-(methoxycarbonyl)phenoxy)hexyloxy)-3,6,7,10,11-pentakis(hexyloxy)triphenylene (1.33 g, 1.36 mmol) in 140 mL of absolute ethanol, NaOH (1.69 g, 42.25 mmol) was added. After refluxing for 5 h, the solvent was removed on a rotary evaporator. Water (120 mL) and dichloromethane (50 mL) were added to the solid residue obtained, and the stirred mixture was treated with 36% hydrochloric acid until pH = 2. The organic phase was collected and the water solution

extracted again with dichloromethane (4 x 50 mL). The dichloromethane extracts were dried over anhydrous magnesium sulfate and filtrated. The solvent was removed on a rotary evaporator to obtain the product as a light yellow solid, which was dried under vacuum. (1.21 g, 93 % yield). ^1H NMR (CDCl_3 , 500 MHz) δ (ppm) = 10.86 (s, 1H, OH), 8.04 (d, 2H, ArH, AA' part of AA'XX' spin system, $N = J_{AX} + J_{AX'} = 9.01$ Hz, $J_{AA'} \approx J_{XX'}$), 7.84 (s, 6H, TriPh), 6.93 (d, 2H, ArH, XX' part of AA'XX' spin system, $N = J_{AX} + J_{AX'} = 9.01$ Hz, $J_{AA'} \approx J_{XX'}$), 4.23 (m, 12H, TriPh-O-CH₂), 4.06 (t, 2H, ArH-O-CH₂, $J = 6.48$ Hz), 2.02-1.86 (m, 14H, CH₂), 1.72-1.54 (m, 14H, CH₂), 1.45-1.34 (m, 20H, CH₂), 0.93 (m, 15H, CH₃). IR (cm^{-1}): ν (C=O): 1690. Anal. calcd (%) for $\text{C}_{75}\text{H}_{96}\text{O}_{15}$: C, 72.79; H, 7.82; O, 19.39. Found: C, 72.81; H, 7.70.

2,6,10-tris(6-(4-(methoxycarbonyl)phenoxy)hexyloxy)-3,7,11-trihexyloxytriphenylene ((3) in Scheme 3.5)

A mixture of 2,6,10-trihydroxy-3,7,11-trihexyloxytriphenylene⁵⁴ (1.83 g, 3.17 mmol), methyl-4-(6-bromohexyloxy)benzoate⁵⁵ (9.00 g, 28.6 mmol), and anhydrous K_2CO_3 (15.79 g, 114.2 mmol) in 100 mL of dry butanone was refluxed under nitrogen atmosphere for 24 h. After cooling to room temperature, the solvent was removed under vacuum, and then water (100 mL) was added. The mixture was extracted with dichloromethane (3 x 30 mL). The organic fractions were combined and dried over MgSO_4 . Filtration followed by solvent removal afforded the crude product, which was purified by column chromatography (silica gel, ethyl acetate/hexane 3:1 v/v). The compound was isolated as a light yellow solid (2.25 g, 55.4 % yield). ^1H NMR (CDCl_3 , 500 MHz) δ (ppm) = 7.98 (s, 3H, TriPh), 7.96 (s, 3H, TriPh), 7.83 (d, 6H, ArH, AA' part of AA'XX' spin system, $N = J_{AX} + J_{AX'} = 8.92$ Hz, $J_{AA'} \approx J_{XX'}$), 6.90 (d, 6H, ArH, XX' part of AA'XX' spin system, $N = J_{AX} + J_{AX'} = 8.92$ Hz, $J_{AA'} \approx J_{XX'}$), 4.23 (m, 12H, TriPh-O-CH₂), 4.04 (t, 6H, ArH-O-CH₂, $J = 6.40$ Hz), 3.88 (s, 9H, O-CH₃), 2.02-1.84 (m, 18H, CH₂), 1.72-1.53 (m, 18H, CH₂), 1.38 (m, 12H, CH₂), 0.92 (t, 9H, CH₂, $J = 6.92$ Hz). IR (cm^{-1}): ν (C=O): 1716.

2,6,10-tris(6-(4-(carboxy)phenoxy)hexyloxy)-3,7,11-trihexyloxytriphenylene (TPhTC in Scheme 3.5)

To a solution of 2,6,10-Tris(6-(4-(methoxycarbonyl)phenoxy)hexyloxy)-3,7,11-trihexyloxytriphenylene (1.90 g, 1.48 mmol) in 100 mL of absolute ethanol, NaOH (3.56 g, 89.1 mmol) was added. After refluxing for 6 h, the solvent was removed on a rotary evaporator. Glacial acetic acid (125 mL) was added and the mixture refluxed for 2 h giving rise to a white solid. The solid was collected by filtration, washed first with cold water (3 x 50 mL), then with cold acetone (3 x 50 mL) and finally dried under vacuum. (1.60 g, 87.1 % yield). $^1\text{H NMR}$ (DMSO- d_6 , 500 MHz) δ (ppm)= 12.56 (s, 3H, OH), 7.92 (s, 3H, TriPh), 7.91 (s, 3H, TriPh), 7.85 (d, 6H, ArH, AA' part of AA'XX' spin system, $N = J_{AX} + J_{AX'} = 8.92$ Hz, $J_{AA'} \approx J_{XX'}$), 6.94 (d, 6H, ArH, XX' part of AA'XX' spin system, $N = J_{AX} + J_{AX'} = 8.92$ Hz, $J_{AA'} \approx J_{XX'}$), 4.19 (m, 12H, TriPh-O-CH₂), 3.98 (t, 6H, ArH-O-CH₂, $J = 6.42$ Hz), 1.75 (m, 18H, CH₂), 1.50 (m, 18H, CH₂), 1.27 (m, 12H, CH₂), 0.82 (t, 9H, CH₃, $J = 6.87$ Hz). IR (cm⁻¹): ν (C=O): 1678. Anal. calcd (%) for C₇₅H₉₆O₁₅: C, 72.79; H, 7.82; O, 19.39. Found: C, 72.81; H, 7.70.

Synthesis of Ru NP assemblies

In a typical experiment, ruthenium precursor [Ru(COD)(COT)] and the corresponding ligand were dissolved in THF in a Fisher-Porter bottle and the solution was stirred 1h (30 min for **HF**) at room temperature. After this period of time, 3 bar of hydrogen were introduced into the bottle. The reaction was allowed to react 16 h at room temperature. The excess of H₂ was eliminated and the volume of the solvent was reduced under vacuum. The black solid was precipitated after the addition of 200 mL of pentane. After filtration under argon with a cannula, the black solid powder was washed twice with pentane (200 mL) and filtered again before drying under vacuum. For typical ratio and ligand studied, the quantities of the reactants are detailed hereafter:

Ru@TPhC - 10/1: 50 mg (0.159 mmol) of [Ru(COD)(COT)], 13.8 mg (0.0143 mmol) of **TPhC**, and 20 mL of THF. Yield: 21.7 mg.

Ru@TPhTC - 4/1: 200 mg (0.634 mmol) of [Ru(COD)(COT)], 200 mg (0.162 mmol) of **TPhTC**, and 80 mL of THF. Yield: 156.1 mg. Ru loading: 14.4% (mass).

Ru@TPhTC - 20/1: 200 mg (0.634 mmol) of [Ru(COD)(COT)], 40.6 mg (0.033 mmol)

of **TPhTC**, and 80 mL of THF. Yield: 65.7 mg. Ru loading: 50.6% (mass).

Ru@TPhTC - 40/1: 200 mg (0.634 mmol) of [Ru(COD)(COT)], 20.3 mg (0.016 mmol) of **TPhTC**, and 80 mL of THF. Yield: 81.7 mg. Ru loading: 66.0% (mass).

Ru@TPhTC - 70/1: 200 mg (0.634 mmol) of [Ru(COD)(COT)], 10.7 mg (0.009 mmol) of **TPhTC**, and 80 mL of THF. Yield: 63.5 mg. Ru loading: 66.1% (mass).

Ru@TPhTC - 120/1: 75 mg (0.238 mmol) of [Ru(COD)(COT)], 2.5 mg (0.002 mmol) of **TPhTC**, and 30 mL of THF. Yield: 13.5 mg.

Ru@AnDC - 20/1: 100mg (0.317 mmol) of [Ru(COD)(COT)], 4.22 mg (0.016 mmol) of **AnDC**, and 40 mL of THF. Yield: 29.3 mg. Ru loading: 66.5% (mass).

Ru@HF - 120/1: 130 mg (0.412 mmol) of [Ru(COD)(COT)], 13.3 mg (0.0034 mmol) of **HF**, and 2.6 mL MeOH and 26 mL of THF. Yield: 50.4 mg. Ru loading: 65.9% (mass).

Characterization

Microwaved reactions were performed in a Anton Paar Microwave reactor Monowave 300, with a power of 850W, 2455MHz frequency.

The ruthenium content was measured by inductively coupled plasma optical emission spectroscopy (ICP-OES) performed in LCC with a Thermo Scientific ICAP 6300 instrument.

TEM and HRTEM analyses were performed at the “Centre de microcaracterisation Raimond Castaing, UMS 3623, Toulouse” by using a JEOL JEM 1011 CX-T electron microscope operating at 100 kV with a point resolution of 4.5 a and a JEOL JEM 1400 electron microscope operating at 120 kV. The high-resolution analyses were conduct by using a JEOL JEM 2100F equipped with a field emission gun (FEG) operating at 200 kV with a point resolution of 2.3 a and a JEOL JEM-ARM200F Cold FEG operating at 200 kV with a point resolution of > 1.9 a. The basic morpho-structural characterization and High-Resolution Transmission Electron Microscopy analysis of **Ru@TPhTC - 6/1** were performed on a Titan Themis transmission electron microscope

(TEM) equipped with an ultra-bright Schottky (FEI X-FEG) electron source, a double CS corrector, a FEI Ceta CMOS camera and operating at an acceleration voltage of 300kV. The particle size distribution was determined through a manual measurement of enlarged micrographs from different areas of the TEM grid (at least 200 particles).

Electron tomography experiments were realized by a FEI Titan transmission electron microscope operating at 300 kV, equipped with a CT objective lens, a FEG electron source and a Gatan 2kX2k CCD camera. The tomogram was reconstructed by using the software Inspect3D (FEI) using the SIRT method (Simultaneous Iterative Reconstruction Technique) with 30 iterations, applied on several TEM images acquired with the sample tilted between +70 and -70 degrees, with an angular step of 2 degrees. The 3D-nanoparticles reconstruction was finally realized using the software AVIZO (FEI), while the calculation of the distance among their center was performed by a dedicated code developed at KAUST visualization lab.

For AFM analyses a SmartsSPM-1000 AIST-NT microscope was used to explore the surface morphology of the samples. Topography was measured in tapping mode with a silicon tip of 12 to 18 μm length and 8 nm radius of curvature

Temperature-programmed desorption (TPD) spectra were obtained with a fully automated AMI-300 characterization instrument (Altamira Instruments), equipped with a quadrupole mass spectrometer (Dycor Dymaxion). Given that the samples were air-sensitive, about 70 mg of material was transferred to a U-shaped quartz tube and placed inside an electrical furnace inert atmosphere. Then, the sample was heated at 1000 $^{\circ}\text{C}$ at 5 $^{\circ}\text{C min}^{-1}$ using a constant helium flow of 25 $\text{cm}^3 \text{min}^{-1}$ (STP). During the analysis, different fragment ions were monitored, including $m/z = 2$ (H_2), 16 (CH_4), 18 (H_2O), 28 (CO), and 44 (CO_2). For quantification of the CO_2 and CO_2 released during the thermal analysis, the calibration of these gases was carried out after each analysis.

SS-NMR spectroscopy (magic angle spinning, MAS NMR) with and without ^1H - ^{13}C cross polarization (CP) was performed at the LCC with a Bruker Avance 400WB instrument equipped with a 4 mm probe with the sample rotation frequency being set

at 12/16 kHz, unless otherwise indicated. Measurements were carried out in a 4 mm ZrO₂ rotor. Liquid NMR spectra were obtained with Bruker Fourier 300 and 700 systems using TMS as internal standard, with proton and carbon resonances at 300/700 and 75/175 MHz, respectively.

ATR-IR spectra were recorded with a Perkin Elmer GX2000 spectrometer installed in a glovebox, in the range 4000-400 cm⁻¹.

Wide-angle X-ray scattering measurements were performed at CEMES on a diffractometer dedicated to pair distribution function (PDF) analysis: graphite monochromatized molybdenum radiation (0.07169 nm), solid-state detection, and low background setup. Samples were sealed in Lindemann glass capillaries (diameter 1.0 mm) to avoid any oxidation after filling in a glovebox. For all samples, data were collected in an extended angular range ($2\theta = 1298$) with counting times of typically 150 s for each of the 457 data points, thus allowing for PDF analysis. Classic corrections (polarization and absorption in cylindrical geometry) were applied before reduction and Fourier transform.

XPS measurements were performed on a Thermo K α spectrometer working at a base pressure of 5x10⁻⁹ mbar and equipped with a monochromatic Al K α X-ray source (1486.7 eV). The spectra presented here were recorded with a Pass Energy of 20 eV. The data were processed with CasaXPS using Gaussian-lorentzian combinations and a Shirley background. Scofield photoionization cross-sections⁵⁵ corrected for the transmission function of the analyzer and the analysis depth were used for quantifications.

SAXS measurements were performed on the XEUSS 2.0 laboratory source equipped with a pixel detector PILATUS 1M (DECTRIS) and an X-rays source provided by a GeniX3D with a fixed wavelength based on Cu K α radiation ($\lambda = 1.54 \text{ \AA}$). The sample to detector distance was fixed at 1216.5mm giving a q range starting from 0.005 \AA^{-1} to 0.5 \AA^{-1} assuming that q is the scattering vector equal to $4\pi/\lambda \sin \theta$ with 2θ the scattering angle. The distance was calibrated in the small angles region using silver behenate (d_{001}

= 58.34 Å). The powders of nanoparticles were stored on sealed capillaries to prevent oxidation and placed on motorized sample holder. To remove scattering and absorption from air, a primary vacuum has been applied to the entire instrument. Acquisition time per sample was 1 hour and all scattering curves were corrected for the empty capillary contribution, divided by transmission factor, acquisition time and optical path in order to obtain SAXS curves in absolute units (cm^{-1}). The X-ray scattering curves at low q can be described as the scattering from multiscale organization of nanoparticle assembly. The elementary particles can be assimilated as dense spherical objects showing interaction at small distances. In this case, we can describe the SAXS curves at medium and high angles (0.1 to 1Å^{-1}) with a form factor of sphere multiplied by a structure factor to take an account of interactions at low distances. At small and intermediate angles (0.01 - 0.1Å^{-1}), the increase of the intensity indicates the presence of a large assemblies containing the nanoparticles, and the state of the surface of these large size objects can be described with a power law function. The total scattering is the sum of the different scattering contributions and the SASView program (SasView, <http://www.sasview.org/>) has been used to build the sum model and fit the data. The global equation applied to fit the data can be written as follow:

$$I(q)_{global} = I(q)_{agglomerates} + I(q)_{sphere} * S(q)$$

$$I(q)_{global} = Aq^{-P} + \frac{B}{V} \left[\frac{3V(\Delta\rho)(\sin(qr) - qr\cos(qr))}{(qr)^3} \right]^2$$

$$* \left[1 + \frac{1}{v1} 4\pi \int_0^\infty (g(r) - 1)r^2 \frac{\sin(qr)}{qr} dr \right]$$

where the A and B are factor scaling, P the slope providing information of the surface and the sphere is described by the volume V , the radius r and the contrast $\Delta\rho$. The form factor $S(q)$ used here correspond to the “hard sphere interaction model” described by Percus-Yevick.⁵⁶ Finally, three parameters such as radius of the sphere r , the state of the surface P and the inter-particle distance d are employed to fit the data.

At very small angles ($<0.01\text{Å}^{-1}$), we are unable to determine the size of large assemblies

but in some conditions, we can observe oscillations coming from interaction at short distances between large size particles. By adding a term $I(q)_{sphere} * S(q)$ to give a contribution of large spheres with a spatial distribution at short distances, we can fit the beginning of the curve giving an approximation of the spatial distribution of these large particles.

3.5 References

1. Leng, F.; Gerber, I. C.; Lecante, P.; Bentaleb, A.; Muñoz, A.; Illescas, B. M.; Martín, N.; Melinte, G.; Ersen, O.; Martinez, H.; Axet, M. R.; Serp, P., Hexakis [60]Fullerene Adduct-Mediated Covalent Assembly of Ruthenium Nanoparticles and Their Catalytic Properties. *Chem. Eur. J.* **2017**, *23*, 13379-13386.
2. Gonzalez-Gomez, R.; Cusinato, L.; Bijani, C.; Coppel, Y.; Lecante, P.; Amiens, C.; Del Rosal, I.; Philippot, K.; Poteau, R., Carboxylic Acid-Capped Ruthenium Nanoparticles: Experimental and Theoretical Case Study with Ethanoic Acid. *Nanoscale* **2019**, *11*, 9392-9409.
3. Machado, B. F.; Oubenali, M.; Rosa Axet, M.; Trang Nguyen, T.; Tunckol, M.; Girleanu, M.; Ersen, O.; Gerber, I. C.; Serp, P., Understanding the Surface Chemistry of Carbon Nanotubes: Toward a Rational Design of Ru Nanocatalysts. *J. Catal.* **2014**, *309*, 185-198.
4. Rousseau, G.; Lavenn, C.; Cardenas, L.; Loridant, S.; Wang, Y.; Hahn, U.; Nierengarten, J.-F.; Demessence, A., One-Pot Synthesis of Sub-3 Nm Gold Nanoparticle Networks Connected by Thio-Based Multidentate Fullerene Adducts. *Chem. Commun.* **2015**, *51*, 6730-6733.
5. Fujihara, H.; Nakai, H., Fullerenethiolate-Functionalized Gold Nanoparticles: A New Class of Surface-Confined Metal-C₆₀ Nanocomposites. *Langmuir* **2001**, *17*, 6393-6395.
6. Geng, M.; Zhang, Y.; Huang, Q.; Zhang, B.; Li, Q.; Li, W.; Li, J., Functionalization of C₆₀ with Gold Nanoparticles. *Carbon* **2010**, *48*, 3570-3574.
7. Lu, F.; Xiao, S.; Li, Y.; Song, Y.; Liu, H.; Li, H.; Zhuang, J.; Liu, Y.; Gan, L.; Zhu, D., Fullerene-Functionalized Gold Core-Shell Nanoparticles: Preparation and Optical Limiting Properties. *Inorg. Chem. Commun.* **2004**, *7*, 960-962.
8. Leng, F. Controlled Synthesis and Characterization of Ru-Fullerene Nanostructures and Their Catalytic Applications. PhD Thesis, Université de Toulouse. 2016.
9. Kumar, S., Recent Developments in the Chemistry of Triphenylene-Based Discotic Liquid Crystals. *Liq. Cryst.* **2004**, *31*, 1037-1059.
10. Pal, S. K.; Setia, S.; Avinash, B. S.; Kumar, S., Triphenylene-Based Discotic Liquid Crystals: Recent Advances. *Liq. Cryst.* **2013**, *40*, 1769-1816.
11. Sonet, D.; Bibal, B., Triphenylene: A Versatile Molecular Receptor. *Tetrahedron Lett.* **2019**, *60*, 872-884.

12. Yang, L.-P.; Pan, C.-Y., A Non-Covalent Method to Functionalize Multi-Walled Carbon Nanotubes Using Six-Armed Star Poly(L-Lactic Acid) with a Triphenylene Core. *Macromol. Chem. Phys.* **2008**, *209*, 783-793.
13. Kresge, C. T.; Leonowicz, M. E.; Roth, W. J.; Vartuli, J. C.; Beck, J. S., Ordered Mesoporous Molecular-Sieves Synthesized by a Liquid-Crystal Template Mechanism. *Nature* **1992**, *359*, 710-712.
14. Sheraw, C. D.; Zhou, L.; Huang, J. R.; Gundlach, D. J.; Jackson, T. N.; Kane, M. G.; Hill, I. G.; Hammond, M. S.; Campi, J.; Greening, B. K.; Francl, J.; West, J., Organic Thin-Film Transistor-Driven Polymer-Dispersed Liquid Crystal Displays on Flexible Polymeric Substrates. *Appl. Phys. Lett.* **2002**, *80*, 1088-1090.
15. Das, S.; Irin, F.; Tanvir Ahmed, H. S.; Cortinas, A. B.; Wajid, A. S.; Parviz, D.; Jankowski, A. F.; Kato, M.; Green, M. J., Non-Covalent Functionalization of Pristine Few-Layer Graphene Using Triphenylene Derivatives for Conductive Poly (Vinyl Alcohol) Composites. *Polymer* **2012**, *53*, 2485-2494.
16. Mahringer, A.; Jakowetz, A. C.; Rotter, J. M.; Bohn, B. J.; Stolarczyk, J. K.; Feldmann, J.; Bein, T.; Medina, D. D., Oriented Thin Films of Electroactive Triphenylene Catecholate-Based Two-Dimensional Metal-Organic Frameworks. *ACS Nano* **2019**, *13*, 6711-6719.
17. Miner, E. M.; Wang, L.; Dinca, M., Modular O₂ Electroreduction Activity in Triphenylene-Based Metal-Organic Frameworks. *Chem. Sci.* **2018**, *9*, 6286-6291.
18. Yang, L.; He, X.; Dinca, M., Triphenylene-Bridged Trinuclear Complexes of Cu: Models for Spin Interactions in Two-Dimensional Electrically Conductive Metal-Organic Frameworks. *J. Am. Chem. Soc.* **2019**, *141*, 10475-10480.
19. Gong, Y. N.; Jiang, L.; Lu, T. B., A Highly Stable Dynamic Fluorescent Metal-Organic Framework for Selective Sensing of Nitroaromatic Explosives. *Chem Commun.* **2013**, *49*, 11113-11115.
20. Shi, J.; Wang, Y.; Xiao, M.; Zhong, P.; Liu, Y.; Tan, H.; Zhu, M.; Zhu, W., Luminescent Metallomesogens Based on Platinum Complex Containing Triphenylene Unit. *Tetrahedron* **2015**, *71*, 463-469.
21. Chico, R.; de Domingo, E.; Domínguez, C.; Donnio, B.; Heinrich, B.; Termine, R.; Golemme, A.; Coco, S.; Espinet, P., High One-Dimensional Charge Mobility in

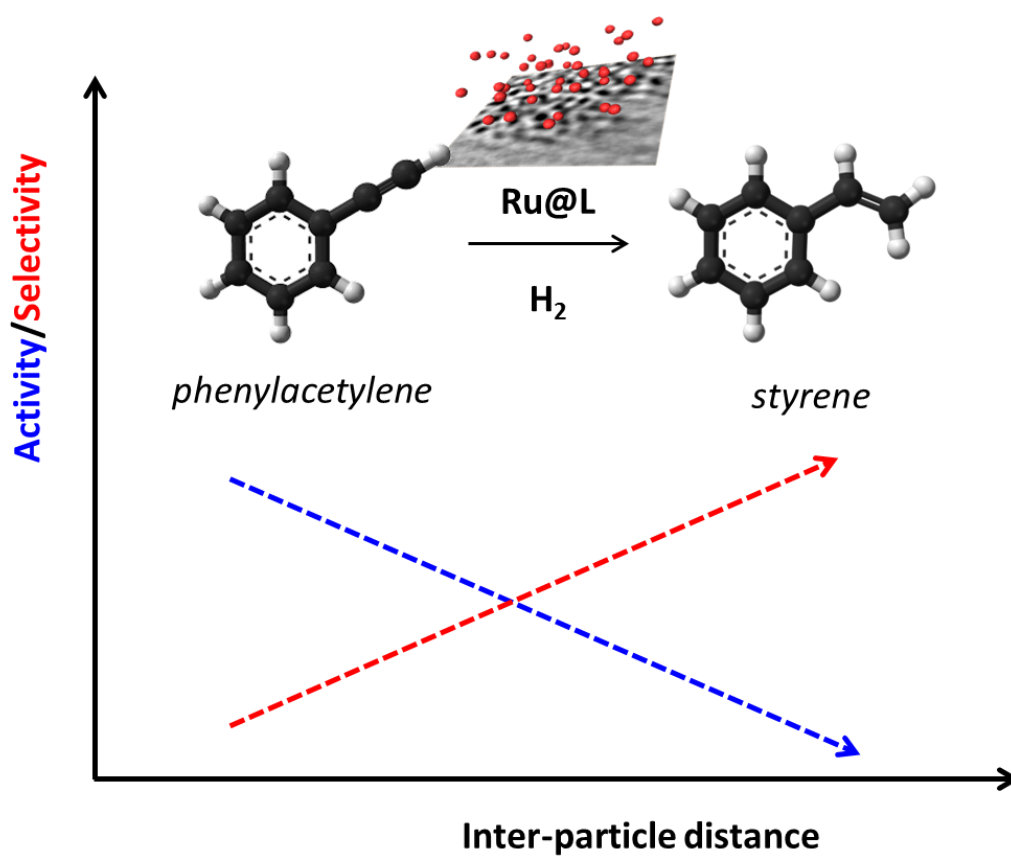
- Semiconducting Columnar Mesophases of Isocyano-Triphenylene Metal Complexes. *Chem. Mater.* **2017**, *29*, 7587-7595.
22. Zint, S.; Ebeling, D.; Ahles, S.; Wegner, H. A.; Schirmeisen, A., Subsurface-Controlled Angular Rotation: Triphenylene Molecules on Au(111) Substrates. *J. Phys. Chem. C* **2016**, *120*, 1615-1622.
23. Katsonis, N.; Marchenko, A.; Fichou, D., Substrate-Induced Pairing in 2,3,6,7,10,11-Hexakis-Undecalkoxy-Triphenylene Self-Assembled Monolayers on Au111. *J. Am. Chem. Soc.* **2003**, *125*, 13682-13683.
24. Muller, K.; Schmidt, N.; Link, S.; Riedel, R.; Bock, J.; Malone, W.; Lasri, K.; Kara, A.; Starke, U.; Kivala, M.; Stohr, M., Triphenylene-Derived Electron Acceptors and Donors on Ag(111): Formation of Intermolecular Charge-Transfer Complexes with Common Unoccupied Molecular States. *Small* **2019**, *15*, 1901741-1901751.
25. Kumar, S., Nanoparticles in Discotic Liquid Crystals. **2016**, *7*, 461-496.
26. Gowda, A.; Kumar, S., Recent Advances in Discotic Liquid Crystal-Assisted Nanoparticles. *Materials (Basel)* **2018**, *11*, 382-399.
27. Kumar, S.; Lakshminarayanan, V., Inclusion of Gold Nanoparticles into a Discotic Liquid Crystalline Matrix. *Chem Commun.* **2004**, 1600-1601.
28. Kumar, S.; Pal, S. K.; Lakshminarayanan, V., Discotic-Decorated Gold Nanoparticles. *Mol. Cryst. Liq. Cryst.* **2005**, *434*, 251-258.
29. Kumar, S.; Pal, S. K.; Kumar, P. S.; Lakshminarayanan, V., Novel Conducting Nanocomposites: Synthesis of Triphenylene-Covered Gold Nanoparticles and Their Insertion into a Columnar Matrix. *Soft Matter* **2007**, *3*, 896-900.
30. Holt, L. A.; Bushby, R. J.; Evans, S. D.; Burgess, A.; Seeley, G., A 106-Fold Enhancement in the Conductivity of a Discotic Liquid Crystal Doped with Only 1% (W/W) Gold Nanoparticles. *J. Appl. Phys.* **2008**, *103*, 063712.
31. Mishra, M.; Kumar, S.; Dhar, R., Gold Nanoparticles in Plastic Columnar Discotic Liquid Crystalline Material. *Thermochim. Acta* **2016**, *631*, 59-70.
32. Yaduvanshi, P.; Mishra, A.; Kumar, S.; Dhar, R., Effect of Silver Nanoparticles on Frequency and Temperature-Dependent Electrical Parameters of a Discotic Liquid Crystalline Material. *Liq. Cryst.* **2015**, *42*, 1478-1489.

33. Varshney, S.; Kumar, M.; Gowda, A.; Kumar, S., Soft Discotic Matrix with 0-D Silver Nanoparticles: Impact on Molecular Ordering and Conductivity. *J. Mol. Liq.* **2017**, *238*, 290-295.
34. Yamada, M.; Shen, Z.; Miyake, M., Self-Assembly of Discotic Liquid Crystalline Molecule-Modified Gold Nanoparticles: Control of 1d and Hexagonal Ordering Induced by Solvent Polarity. *Chem Commun.* **2006**, 2569-2571.
35. Shen, Z.; Yamada, M.; Miyake, M., Control of Stripelike and Hexagonal Self-Assembly of Gold Nanoparticles by the Tuning of Interactions between Triphenylene Ligands. *J. Am. Chem. Soc.* **2007**, *129*, 14271-14280.
36. Shen, Z.; Miyabayashi, K.; Higashimoto, M.; Shimoda, T.; Miyake, M., Single-Crystalline Gold Nanodisks Prepared by the Shape Transformation under Uv Irradiation from Nanoparticles Protected with Discotic Liquid Crystalline Ligands. *Chem. Lett.* **2008**, *37*, 1276-1277.
37. Ogoshi, T.; Hiramitsu, S.; Yamagishi, T.-a.; Nakamoto, Y., Columnar Stacks of Star- and Tadpole-Shaped Polyoxazolines Having Triphenylene Moiety and Their Applications for Synthesis of Wire-Assembled Gold Nanoparticles. *Macromolecules* **2009**, *42*, 3042-3047.
38. Vijayaraghavan, D.; Kumar, S., Self-Assembled Superlattices of Gold Nanoparticles in a Discotic Liquid Crystal. *Mol. Cryst. Liq. Cryst.* **2009**, *508*, 101-114.
39. Chen, X.; Chen, L.; Chen, Y., Self-Assembly of Discotic Liquid Crystal Decorated ZnO Nanoparticles for Efficient Hybrid Solar Cells. *RSC Adv.* **2014**, *4*, 3627-3632.
40. Henry, C. R., 2d-Arrays of Nanoparticles as Model Catalysts. *Catal. Lett.* **2014**, *145*, 731-749.
41. Gong, Y. N.; Meng, M.; Zhong, D. C.; Huang, Y. L.; Jiang, L.; Lu, T. B., Counter-Cation Modulation of Hydrogen and Methane Storage in a Sodalite-Type Porous Metal-Organic Framework. *Chem Commun.* **2012**, *48*, 12002-12004.
42. Wan, W.; Monobe, H.; Sugino, T.; Tanaka, Y.; Shimizu, Y., Mesomorphic Properties and Hydrogen Bonding Formation of Asymmetrical Triphenylene Discotic Liquid Crystals. *Mol. Cryst. Liq. Cryst.* **2006**, *364*, 597-603.
43. Setoguchi, Y.; Monobe, H.; Wan, W.; Terasawa, N.; Kiyohara, K.; Nakamura, N.; Shimizu, Y., Infrared Spectral Studies of Triphenylene Mesogens Possessing Terminal Functional Groups

- in the Peripheral Chains for Hydrogen-Bond Interaction. *Mol. Cryst. Liq. Cryst.* **2004**, *412*, 9-18.
44. Setoguchi, Y.; Monobe, H.; Wan, W.; Terasawa, N.; Kiyohara, K.; Nakamura, N.; Shimizu, Y., Infrared Studies on Hydrogen Bond Interaction in a Homologues Series of Triphenylene Discotic Liquid Crystals Having Carboxylic Acids at the Peripheral Chains. *Thin Solid Films* **2003**, *438-439*, 407-413.
45. Iehl, J.; Pereira de Freitas, R.; Delavaux-Nicot, B.; Nierengarten, J. F., Click Chemistry for the Efficient Preparation of Functionalized [60]Fullerene Hexakis-Adducts. *Chem Commun.* **2008**, 2450-2452.
46. Hirsch, A.; Vostrowsky, O., C₆₀ Hexakisadducts with an Octahedral Addition Pattern— a New Structure Motif in Organic Chemistry. *Eur. J. Org. Chem.* **2001**, *2001*, 829-848.
47. Sanchez-Navarro, M.; Munoz, A.; Illescas, B. M.; Rojo, J.; Martin, N., [60]Fullerene as Multivalent Scaffold: Efficient Molecular Recognition of Globular Glycofullerenes by Concanavalin A. *Chem. Eur. J.* **2011**, *17*, 766-769.
48. Li, H.; Zheng, Q.; Han, C., Click Synthesis of Podand Triazole-Linked Gold Nanoparticles as Highly Selective and Sensitive Colorimetric Probes for Lead(II) Ions. *Analyst* **2010**, *135*, 1360-1364.
49. Kamalraj, V. R.; Senthil, S.; Kannan, P., One-Pot Synthesis and the Fluorescent Behavior of 4-Acetyl-5-Methyl-1,2,3-Triazole Regioisomers. *J. Mol. Struct.* **2008**, *892*, 210-215.
50. Krishnakumar, V.; Xavier, R. J., Ft Raman and Ft–Ir Spectral Studies of 3-Mercapto-1,2,4-Triazole. *Spectrochim Acta A* **2004**, *60*, 709-714.
51. Morgan, D. J., Resolving Ruthenium: Xps Studies of Common Ruthenium Materials. *Surf. Interface Anal.* **2015**, *47*, 1072-1079.
52. Osojnik Črnivec, I. G.; Djinović, P.; Erjavec, B.; Pintar, A., Low-Temperature Catalytic Decarboxylation of Formic and Acetic Acid over a Ru/TiO₂ Catalyst: Prospects for Continuous Production of Energy-Rich Gaseous Mixtures. *RSC Adv.* **2015**, *5*, 54085-54089.
53. Feringán, B.; Romero, P.; Serrano, J. L.; Folcia, C. L.; Etxebarria, J.; Ortega, J.; Termine, R.; Golemme, A.; Giménez, R.; Sierra, T., H-Bonded Donor–Acceptor Units Segregated in Coaxial Columnar Assemblies: Toward High Mobility Ambipolar Organic Semiconductors. *J. Am. Chem. Soc.* **2016**, *138*, 12511-12518.

54. Ke-Qing, Z.; Bi-Qin, W.; Ping, H.; Quan, L.; Liang-Fu, Z., Synthesis of New Triphenylene-Containing Discotic Liquid Crystals and the Influence of Fluorophilic Effect and Molecular Symmetry on Mesomorphism. *Chin. J. Chem.* **2005**, *23*, 767-774.
55. Xiao, W.; He, Z.; Xu, M.; Wu, N.; Kong, X.; Jing, X., A Convenient One-Step Reaction Leading to a Key Discotic Intermediate: Mono-Hydroxy-Triphenylene at Multi-Gram Scale. *Tetrahedron Lett.* **2015**, *56*, 700-705.
56. Percus, J. K.; Yevick, G. J., Analysis of Classical Statistical Mechanics by Means of Collective Coordinates. *Phys. Rev.* **1958**, *110*, 1-13.

Chapter 4 Catalytic applications of Ru NP covalent assemblies



4. Catalytic application of Ru NP covalent assemblies

4.1 Introduction

4.2 Results and discussion

4.2.1 C-H activation - bromination

4.2.2 Hydrogenation of quinoline

4.2.3 Hydrogenation of phenylacetylene

4.2.3.1 Solvent selection for phenylacetylene hydrogenation

4.2.3.2 Catalytic performances of Ru NP assemblies produced from functionalized polymantanes

4.2.3.3 Electronic and confinement effects of Ru NP assemblies produced from functionalized polymantanes

4.2.3.4 Catalytic performances of Ru NP assemblies produced from functionalized triphenylene, fullerene and anthracene ligands

4.2.3.5 Stability of the Ru NP assemblies

4.3 Conclusion

4.4 Experimental section

4.5 References

4.1 Introduction

Transition metal nanoparticles (NP) are among the most important catalysts in chemical manufacture, which have been studied widely for decades.¹⁻² In contrast with heterogeneous catalysts where NP are supported,³⁻⁵ solvent-dispersed NP are considered featuring both classical homogenous and heterogeneous catalytic properties, making their *in situ* characterization accessible.⁶⁻⁷ The presence of a stabilizer for metal NP is prerequisite for application. Poorly stabilized NP tend to be more active but are more prone to turn into larger metallic aggregates hampering the catalyst activity. Therefore, metal NP covalent assemblies were put forward as robust and arranged against aggregation. However, limited studies are devoted to the use of covalent assemblies of metal NP as catalysts. Among the reported works, a large proportion is devoted to Au, and few about Pt or Pd as reviewed in Chapter 1. Our group has studied Ru NP assembled as Ru-fulleride spheres⁸ demonstrating high selectivity for the reduction of nitrobenzene,⁹ as well for hydrogenation of cinnamaldehyde.¹⁰ Another 3D Ru NP assembly displaying a short-range order was obtained with a multitopic ligand bearing -COOH anchoring groups of hexakis-fullerene adduct, and named as Ru@C₆₆(COOH)₁₂.¹¹ The Ru@C₆₆(COOH)₁₂ assembly was active in the hydrogenation of nitrobenzene, and TEM analyses performed after catalysis have shown that the 3D assembly is maintained. From an environmental point of view (*i.e.*, toxicity, endangered elements, life cycle assessment, etc.), it has been shown that ruthenium is a greener heterogeneous catalyst compared to widely used nickel, cobalt, or gold, among others.¹²

This chapter describes the catalytic properties of Ru NP assemblies in three different reactions, C-H activation (bromination), hydrogenation of quinoline and phenylacetylene. It is shown that the Ru NP carboxylate covalent assemblies are fragmented into isolated NP both in bromination and quinoline hydrogenation reactions even though showing good activity. For application in phenylacetylene hydrogenation, the short-range ordered assemblies keep their integrity and present a correlation between activity, selectivity and inter-particle distance and electronic properties of the Ru NP.

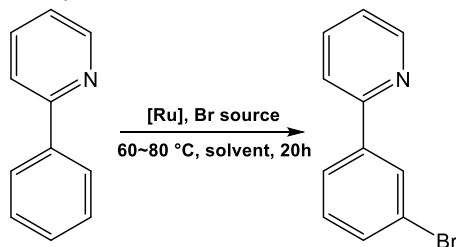
4.2 Results and discussion

4.2.1 C-H activation - bromination

C-H bond functionalization reactions have been extensively exploited due to their capability to create a variety of C-X and C-C bonds playing an important role in organic synthesis.¹³

Ruthenium is one of the most widely used metals to catalyze C-H activation reactions,¹⁴⁻¹⁵ for instance for arylation,¹⁶ alkylation,¹⁷⁻¹⁸ alkyne annulations,¹⁹ coupling reactions,²⁰ to cite a few. Specially, Ru-catalyzed σ -activation strategy to access *meta*-selective functional group reactions has rapidly developed,²¹ and has become one of the most effective methods for remote *meta* C-H bond selective activation, for example, cross-coupling,²² acylation,²³ carboxylation,²⁴ bromination,²⁵⁻²⁶ and so on. The group of Lutz Ackermann²⁷ disclosed the first heterogeneous ruthenium catalyst for *meta*-selective C-H functionalization-*meta*-C-H bromination. The catalyst is tolerant to a broad scope of substrates and show excellent positional selectivity and efficient catalyst reuse. The substitution of traditional homogeneous catalysts by heterogeneous catalysts can make C-H activation greener and more sustainable.²⁸

Herein, this part of work describes the bromination of 2-phenylpyridine (Table 4.1) with dispersed nanoparticles **Ru@1** and **Ru@5**, and Ru NP assemblies **Ru@2** and **Ru@6**. The study of the reaction was initiated by exploring the conditions, including the source of bromide, solvent, Ru content and the presence or not of additives. Dimethylacetamide (DMA) prove to be the optional solvent for reaction both with N-bromosuccinimide (NBS) and tetrabutylammonium tribromide (TBATB) (Table 4.1, Entry 1-10). The activity of Ru chloride hydrate is confirmed (Entry 1-2) and the results are in good agreement with the literature.²⁷

Table 4.1 Bromination of 2-phenylpyridine using Ru based catalyst.^{a)}

Entry	Catalyst	T(°C)	Ru (mol%)	Bromide source	Atmosphere	Additives	Solvent	Conversion (%) ^b
1	RuCl₃.nH₂O	80	8	NBS	Ar	-	DMA	75
2	RuCl₃.nH₂O	80	8	NBS	air	-	DMA	85
3	Ru@1	80	8	NBS	Ar	-	DMA	18
4	Ru@1	80	8	NBS	air	-	DMA	67
5	Ru@2	80	8	NBS	Ar	-	DMA	54
6	Ru@2	80	8	NBS	air	-	DMA	72
7	Ru@2	80	10	TBATB	Ar	-	DMA	84
8	Ru@2	80	10	TBATB	Ar	-	CH ₃ CN	traces
9	Ru@2	80	10	TBATB	Ar	-	dioxane	28
10	Ru@2	80	10	TBATB	Ar	-	MEOH	traces
11	Ru@2	80	5	TBATB	Ar	-	DMA	51
12	Ru@2	60	5	TBATB	Ar	-	DMA	39
13	Ru@2	80	10	TBATB	Ar	K ₂ CO ₃ ^c	DMA	traces
14	Ru@1	80	10	TBATB	Ar	-	DMA	46
15	Ru@6	80	10	TBATB	Ar	-	DMA	22
16	Ru@5	80	10	TBATB	Ar	-	DMA	55

^{a)} Conditions: Ru catalysts with Ru/L ratio 10/1 (the amount is according to substrate in column 4), 46.6 mg (0.30 mmol) of 2-phenylpyridine, 231.4 mg (0.48 mmol) of TBATB, or 85.4 mg (0.48mmol) of NBS, 0.9 mL solvent, 42.7 mg (0.3 mmol) of decane as standard; ^{b)} Conversions were determined by GC analyses. ^{c)} 82.9 mg (0.6 mmol) of additives.

Particularly, conducting the reaction under controlled atmosphere (Ar) or open air had a large impact on the achieved conversion. This effect was observed when using NBS as bromination agent in both isolated Ru NP and Ru NP assemblies (Entry 3-6). The open air increases the conversion of substrate but at the cost of oxidizing the metallic Ru NP. The use of 10 mol% of Ru with respect to 2-phenylpyridine at 80 °C performed better than lower catalysts loading (Entry 7, 11-12). The addition of K₂CO₃ to the reaction media, which is often used in homogeneous bromination catalysis,²⁶ stopped the reaction (Entry 13).

Interestingly, under the optimized conditions, *i.e.* 10 mol% of Ru, 80 °C in DMA using TBATB as brominating agent, carboxylate coordinated NP assemblies **Ru@2** (Entry 7) outperformed the isolated Ru NP (carboxylate and amine, Entries 14 and 16) or the Ru NP assemblies stabilized with amine groups (Entry 15), reaching the conversion of 84 %. In addition, TEM analyses of the catalyst after reacted for 2 h and 20 h (Figure 4.1) reveal dispersed NP on the grid, indicating a partial disassembly of the nanostructure during the bromination reaction. Several reasons could be responsible for the damage of the assembly, such as the possibility of strong coordination of bromide to Ru, the reactivity of pyridine as a Lewis-base, or of the product.

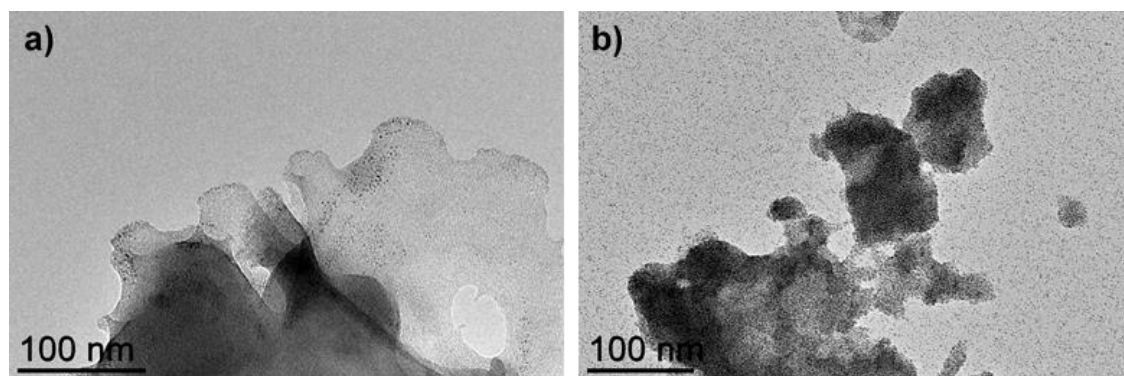


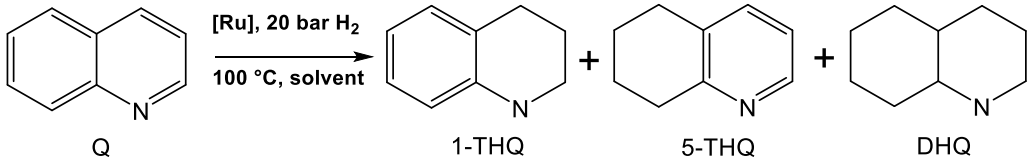
Figure 4.1 TEM images of **Ru@2** catalyst (Ru/L ratio 10/1) after a) 2h of reaction; and b) 20h.

4.2.2 Hydrogenation of quinoline

Hydrogenation of quinoline is an important reaction producing 1,2,3,4-tetrahydroquinoline (1-THQ, Table 4.2) by reduction of the heteroarene ring, which is

widely used in pharmaceuticals.²⁹⁻³⁰ Heterogeneous catalysts based on different metals have been investigated for this reaction, for instance, Ni,³¹ Au,³² Rh,³³ Pt and Pd.³⁴ Our group investigated the use of Rh/C₆₀ catalysts, which catalyze the hydrogenation of quinoline efficiently, displaying high TOFs and reaching high selectivity, up to 99 % to 1-THQ.³⁵ Supported Ru NP have also been applied in this reaction as catalysts.³⁶⁻⁴¹ Therefore, the catalytic performances of Ru NP covalent assemblies were investigated for this reaction, and compared to the isolated Ru NP. The results obtained with **Ru@1**, **Ru@2**, and **Ru@6** are summarized in Table 4.2.

Table 4.2 Hydrogenation of quinoline using Ru based catalysts.^{a)}



Entry	Catalysts	Conv. (%) ^{b)}	Select. (%) ^{c)}	TOF (h ⁻¹) ^{d)}	TOF(h ⁻¹) ^{f)}
1	Ru@1 - 10/1	96.1	83.2	99.5	178.6
2	Ru@2 - 10/1	95.4	81.6	106.3	190.8
3 ^{g)}	Ru@6 - 10/1	100.0	83.5	134.3	241.0

^{a)} Reaction conditions: 0.02 mmol of Ru, 404 mg (3.1 mmol) of quinoline, 75 mg (0.41 mmol) of dodecane (internal standard), 20 bar H₂, temperature 100 °C, 25 mL THF, 1h of reaction. ^{b)} Conversion (Conv.) was determined by GC analysis using internal standard technique. ^{c)} Selectivity to 1-THQ determined by GC analysis using internal standard technique. ^{d)} TOF calculated at 1 h (2 h for entry 3) of reaction per Ru atom. ^{f)} TOF calculated according to Ru surface content at 1 h (2 h for entry 3). ^{g)} 2 h of reaction.

The reaction was followed over the time and the time-concentration curves obtained for **Ru@1** and **Ru@2** are presented in Figure 4.2. Besides the target product 1-THQ the other two hydrogenated products, 5,6,7,8-tetrahydroquinoline (5-THQ) and decahydroquinoline (DHQ), were also produced. The reactivity displayed by the dispersed and the assembled Ru NP, **Ru@1** and **Ru@2**, respectively, is similar in terms of activity and selectivity, indicating no effect of the assembled structure. The TEM analyses of the **Ru@2** and **Ru@6** spent catalyst (Figure 4.3) reveal that the ordered structure of the assembled NP is lost at the end of the catalytic reaction, producing

isolated NP and explaining the similar catalytic results between **Ru@1** and **Ru@2**. The size of the Ru NP after catalysis are 2.0 ± 1.0 nm, 1.5 ± 0.7 nm and 1.5 ± 0.9 nm for **Ru@1**, **Ru@2** and **Ru@6** catalysts, respectively, indicating that the size of the NP remains similar to those before catalysis.

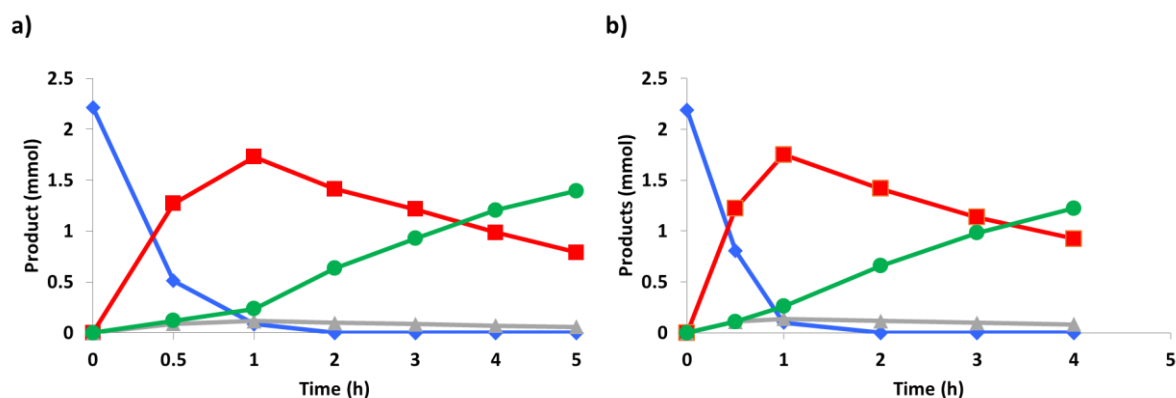


Figure 4.2 Time-concentration curves for quinolone hydrogenation using a) **Ru@1**, and b) **Ru@2** (Ru/ligand = 10) as catalysts (blue diamonds = quinoline; red squares = 1-THQ; green circles = DHQ; and grey triangle= 5-THQ).

The strong coordination of the N-containing compounds to the Ru NP surface could explain the disassembly of the nanostructure during catalysis by competition with the stabilizing agent. Nevertheless, further analyses are needed to verify this hypothesis.

Considering the previous results in C-H activation and hydrogenation of quinoline, in which the 3D ordering was damaged after catalysis, the Ru NP assemblies were tested in the selective hydrogenation of phenylacetylene. This reaction can be performed under milder reaction conditions, circumventing the loss of the nanostructure and thus allowing the study of the effect of the Ru NP ordering in an adequate manner.

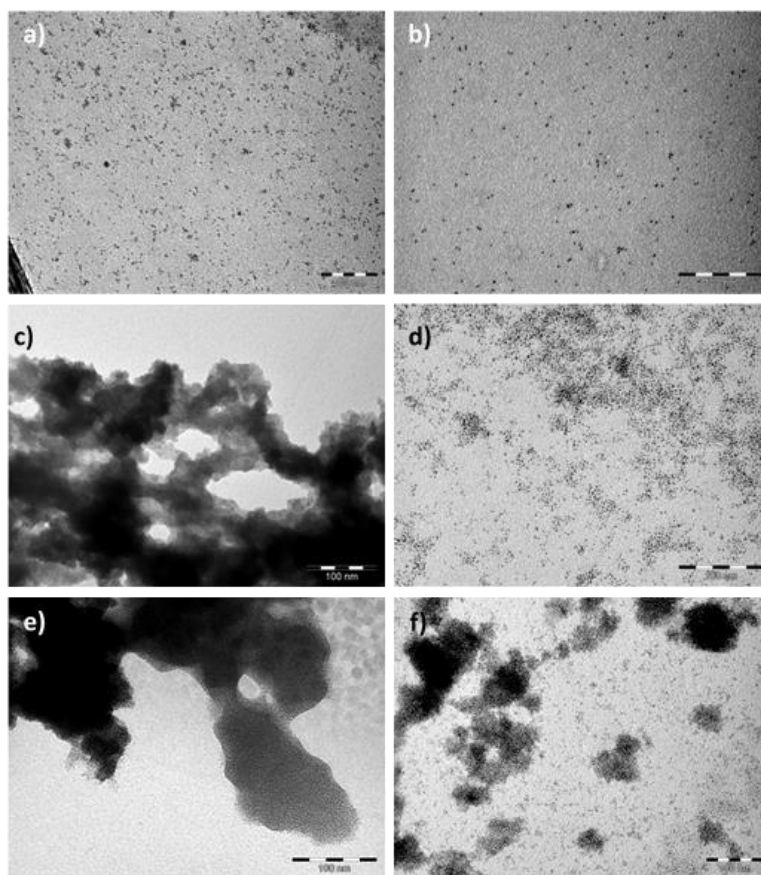


Figure 4.3 TEM images of catalysts: a) and b) **Ru@1**; c) and d) **Ru@2**; and e) and f) **Ru@6** (Ru/ligand = 10/1) before and after hydrogenation of quinoline (scale bar = 100 nm).

4.2.3 Hydrogenation of phenylacetylene

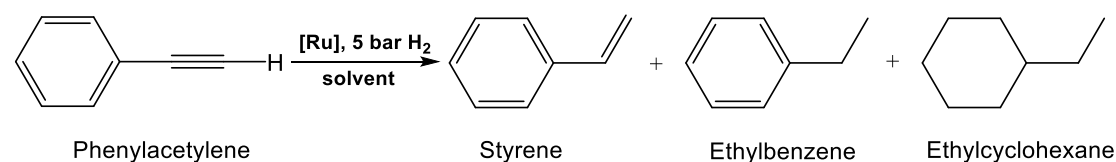
The selective hydrogenation of alkynes to alkenes is a particularly valuable reaction in synthetic organic chemistry. The hydrogenation of phenylacetylene in liquid phase is a benchmark method for assessing catalytic activity and selectivity of palladium NP.⁴² Although there is a need for selective hydrogenation catalysts that are less expensive than conventional Pd-based catalysts, Ru NP have been little studied.⁴³⁻⁵⁰ Ru NP supported on polymer were reported to reach 90 to 100 % selectivity to styrene at almost full conversion.⁴⁸⁻⁴⁹ The hydrogenation catalyzed by isolated Ru NP stabilized by NHC ligands concerned mainly the selectivity towards the aromatics, providing no information about styrene.⁴⁶ Herein, we study the catalytic behavior of the Ru NP and covalent NP assemblies prepared with the different ligands in the semi-

hydrogenation of phenylacetylene to styrene at room temperature and a constant H₂ pressure of 5 bar.

4.2.3.1 Solvent selection for phenylacetylene hydrogenation

Several different common solvents were used for the catalysis using **Ru@2** as catalyst, as shown in Table 4.3. The reaction proceeds faster using THF, MeOH, isopropanol or the mixture of MeOH and CH₂Cl₂ than with toluene or CH₂Cl₂ alone, although CH₂Cl₂ could help to reach highest selectivity to styrene.

Table 4.3 Hydrogenation of phenylacetylene in different solvents.^{a)}



Entry	Solvent	Time (h)	Conv. (%)	S _{20%} (%)	TOF (h ⁻¹) ^{b)}	TOF (h ⁻¹) ^{d)}
1	THF	3	56.9	74.7	41.4	71.2
2	CH ₂ Cl ₂	4	10.0	79.3 ^{c)}	5.5	9.5
3	MeOH	4	66.7	68.9	37.8	65.0
4	MeOH:CH ₂ Cl ₂ = 1:1	6	63.6	76.2	23.9	41.1
5	Isopropanol	5	58.6	68.0	26.1	44.9
6	Acetone	4	2.1	60.6 ^{d)}	1.0	1.7
7	Toluene	6	19.5	71.6	7.5	12.9

^{a)} Reaction conditions: 0.02 mmol of Ru (**Ru@2 -5/1**), 412 mg (4.00 mmol) of phenylacetylene, 71 mg (0.50 mmol) of decane (internal standard), room temperature, 5 bar H₂, 25 mL solvent; ^{b)} TOF in mol_{PAconverted}·mol_{Ru}⁻¹·h⁻¹ calculated at the time given in column 3; ^{c)} selectivity at 20% conversion; ^{d)} selectivity was corresponding to the conversion of 2.1%. ^{d)} TOF calculated according to Ru surface content at given time in column 3.

As shown on the TEM images of the catalysts after the reaction in different solvent (Figure 4.4), the integrity of the assemblies' structure is maintained only

in alcoholic solvent, and methanol behaved better than isopropanol as none isolated NP were detected on the grid.

Ru NP assemblies presents the highest hydrogenation activity in the aprotic polar solvent THF, followed by the alcoholic protic solvents. In aprotic and apolar solvents (toluene and CH_2Cl_2), a lower hydrogenation activity was observed. This was also the case with acetone, an aprotic polar solvent. However, only in methanol, the assemblies do not fall apart, which could be the result from the NP's stabilization ability of methanol as reported before.⁵¹

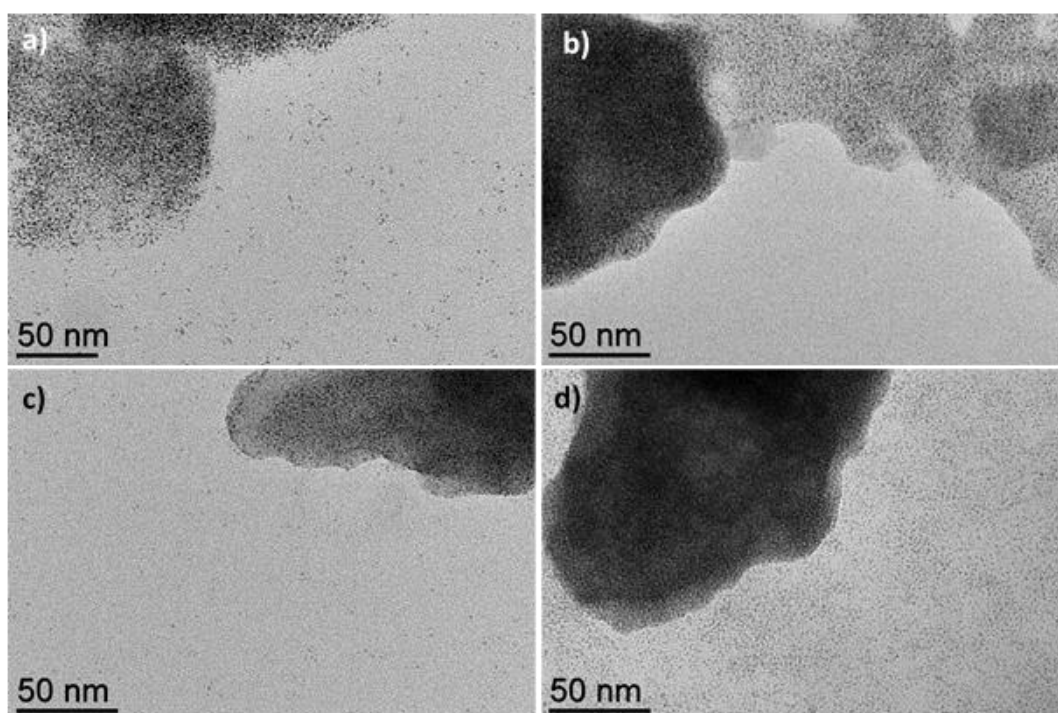


Figure 4.4 TEM images of **Ru@2** (Ru/ligand = 5/1) after hydrogenation of phenylacetylene in different solvents: a) THF; b) MeOH; c) isopropanol and d) CH_2Cl_2 : MeOH = 1:1.

4.2.3.2 Catalytic performances of Ru NP assemblies produced from functionalized polymantanes

A series of catalysts, Ru NP and Ru NP assemblies produced from polymantane based ligands, were used for the hydrogenation reaction using methanol as solvent. The performances of them are listed in Table 4.4.

The evolution of activity and selectivity over time (Figure 4.5) shows that for most of the polymantane stabilized catalysts, at the exception of the less active **Ru@4**, the selectivity to styrene decreases abruptly at high conversions (> 85%) due to the formation of ethylbenzene and the fully hydrogenated product, ethyl cyclohexane.

Table 4.4 Hydrogenation of phenylacetylene catalyzed by Ru catalysts.^{a)}

Entry	Catalysts	Time (h)	Conv. (%)	S _{20%} (%)	S _{60%} (%)	TOF (h ⁻¹) ^{b)}	TOF (h ⁻¹) ^{c)}	TOF (h ⁻¹) ^{d)}
1	Ru@1 - 5/1	2	84.4	62.3	58.3	57.9	83.5	61.6
2	Ru@1 - 10/1	3	73.1	64.5	61.5	57.3	113.5	112.9
3	Ru@1 - 20/1	4	73.2	63.5	61.7	38.3	80.6	45.6
4	Ru@2 - 5/1	4	66.7	68.9	66.7	37.8	70.6	30.3
5	Ru@2 - 10/1	3	71.6	66.7	63.6	52.0	102.5	64.9
6	Ru@2 - 20/1	3	79.1	66.7	63.6	64.5	100.2	74.2
7	Ru@4 - 10/1	5	62.1	71.3	65.4	28.0	59.8	18.9
8	Ru@5 - 10/1	2	72.7	64.3	59.6	79.0	129.5	99.2
9	Ru@6 - 10/1	2	65.9	62.5	58.9	68.4	126.8	101.4
10	Ru@7 - 10/1	3	66.8	60.5	56.3	48.5	82.3	66.6
11	Ru@8 - 10/1	3	72.6	65.2	64.9	60.3	89.8	74.9
12	1.6% Ru/CNT_O	8	10.6	67.8 ^{e)}	-	3.8	-	-
13	0.8% Ru/CNT_N	4	9.0	67.4 ^{e)}	-	11.3	-	-

^{a)} Reaction conditions: 0.02 mmol of Ru, 412 mg (4.00 mmol) of phenylacetylene, 71 mg (0.50 mmol) of decane (internal standard), room temperature, 5 bar H₂, 25 mL MeOH. ^{b)} TOF in mol_{PAconverted}·mol_{Ru}⁻¹·h⁻¹ calculated at the time given in column 3; ^{c)} TOF calculated according to surface Ru content at the time given in column 3; ^{d)} TOF calculated according to the surface Ru content at 1h.

Comparing the slope of the selectivity curves, the decreasing rate of Ru NP assembly with amine groups is higher than the ones with carboxylate, which is due to higher activity of the former. The poorly active **Ru@4** presents a smooth decline of selectivity (Figure 4.5g).

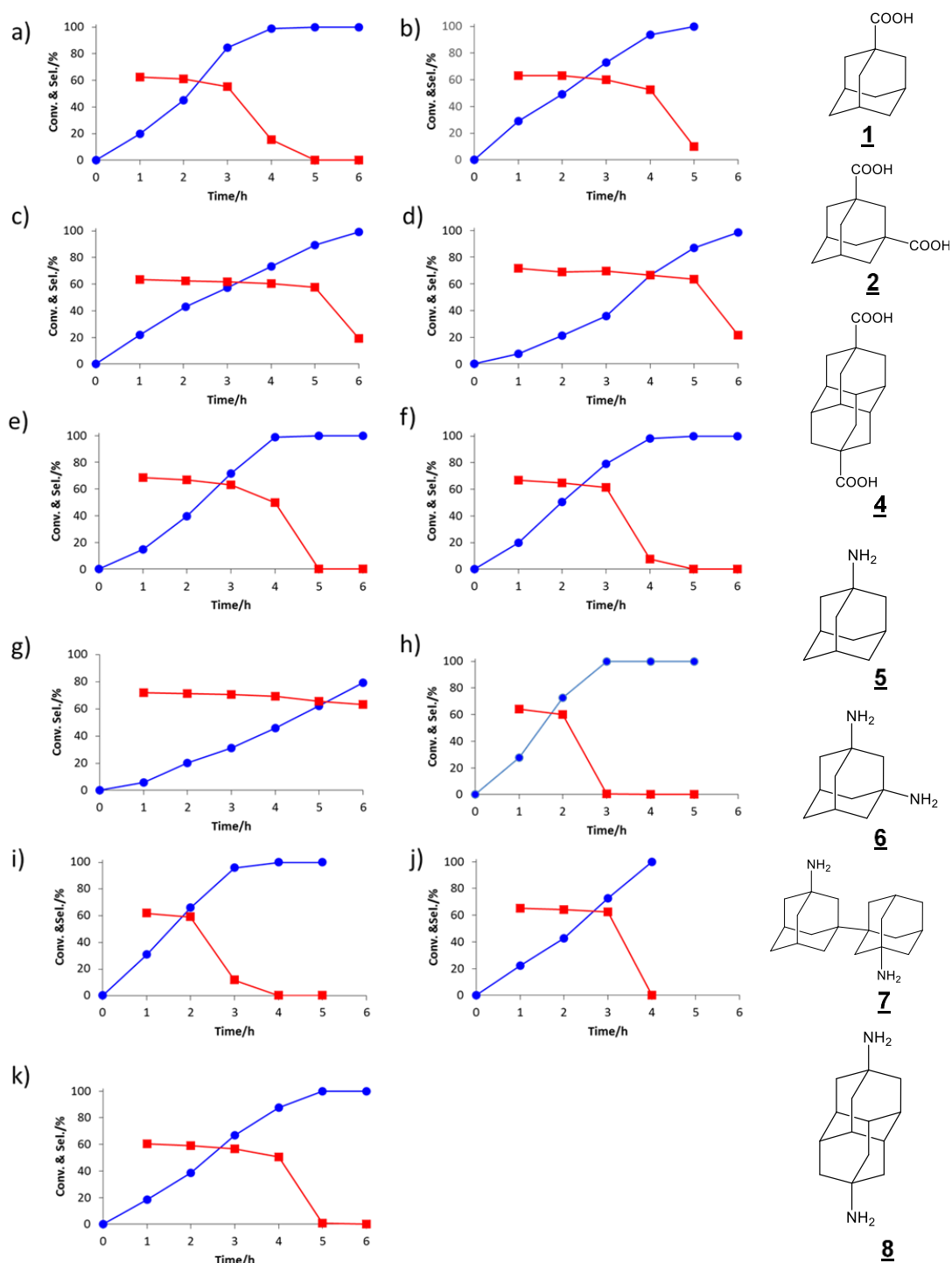


Figure 4.5 Evolution of activity (blue lines) and selectivity toward styrene (red lines) over time for the investigated catalysts: a) **Ru@1** - 5/1; b) **Ru@1** - 10/1; c) **Ru@1** - 20/1; d) **Ru@2** - 5/1; e) **Ru@2** - 10/1; f) **Ru@2** - 20/1; g) **Ru@4** - 10/1; h) **Ru@5** - 10/1; i) **Ru@6** - 10/1; j) **Ru@7** - 10/1; and k) **Ru@8** - 10/1.

A representative product distribution over time is shown on Figure 4.6 for **Ru@2** catalyst (Ru/ligand = 10). The alkyne group is firstly hydrogenated giving ethylbenzene with up to 95% selectivity. Afterwards ring hydrogenation occurs. The hydrogenation of arenes under mild reaction conditions using (supported or colloidal) Ru NP as catalysts has already been reported,⁵²⁻⁵⁵ and is not surprising, even at room temperature. The fully hydrogenation into ethylcyclohexane could be accomplished at prolonged reaction time.

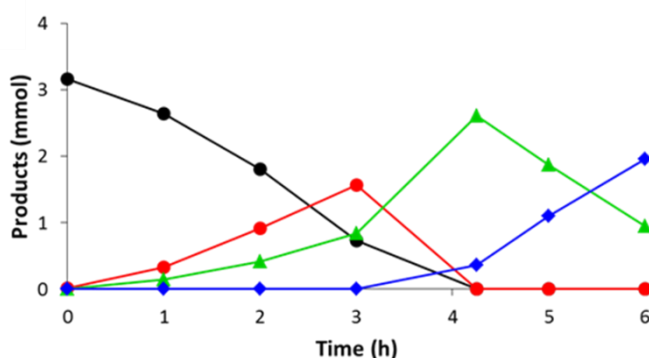


Figure 4.6 Product distribution (black squares = phenylacetylene; red circles = styrene; green triangles = ethylbenzene; and blue diamond's = ethylcyclohexane) for **Ru@2** (Ru/ligand = 10).

The catalytic activity shows some distinctive features related to the nature of the ligand. Table 4.4 column 8 shows the calculated TOF according to predicted active sites, *i.e.* surface Ru content affected by the nature of the ligand. For each series of ligands (acids and amines family), the use of Ru discrete NP (from **1** and **5**, adamantane monoacid and monoamine, respectively) provides higher TOF than the use of Ru NP networks (from **2** and **6**, adamantanes, and **4** and **8**, diamantanes, diacids and diamines, respectively).

To explain the difference of activity between discrete Ru NP and Ru NP networks, we rely on an important difference between these materials, which is the presence of significant amount of adsorbed CO on the Ru NP networks (see Chapter 2). This adsorbed CO poisons the Ru NP in the network, which are finally less active

that the discrete NP. Additional experiments were performed to validate this hypothesis. Thus, we tested catalyst as a Ru NP network (**Ru*@2 - 10/1**) that have been vacuum treated to remove the adsorbed CO, as confirmed by IR, and compared the TOF (based on total Ru) at 98% conversion of **Ru@1 - 10/1**, **Ru@2 - 10/1** and **Ru*@2 - 10/1**. The TOF (total Ru content) obtained were respectively 63.6, 56.8, and 65.4 h⁻¹, these data point out that the adsorbed CO decreases the activity of the networks and when removed, a similar TOF to that of the isolated Ru NPs can be observed for a Ru NP network.

4.2.3.3 Electronic and confinement effects of Ru NP assemblies produced from functionalized polymantanes

It has been shown that soft confinement effects, such as reactant enrichment or rapid diffusion, will directly affect the kinetics of the reaction. Hard effects, like the charge transfer between the metal and the support, will also affect activity/selectivity and stability.

Figure 4.7 displays a comparison of the activity and selectivity of the Ru based catalysts studied here. It is visible that the use of donating amino ligands (**5-8**, in blue) allows reaching higher TOF than with the carboxylic ligands (in red). The fact that amine ligands, which insure a higher electronic density on Ru, allow reaching higher TOF for phenylacetylene hydrogenation is in accordance with results reported in the literature. Thus, it was reported that for the hydrogenation of various unsaturated compounds on stabilized Ru NP, the use of σ -donor ligands increases the activity of the Ru NP.⁵⁶⁻⁵⁷ Similarly, Ru/N-doped carbon catalysts were reported to be very efficient catalysts for arene hydrogenation.⁵⁸

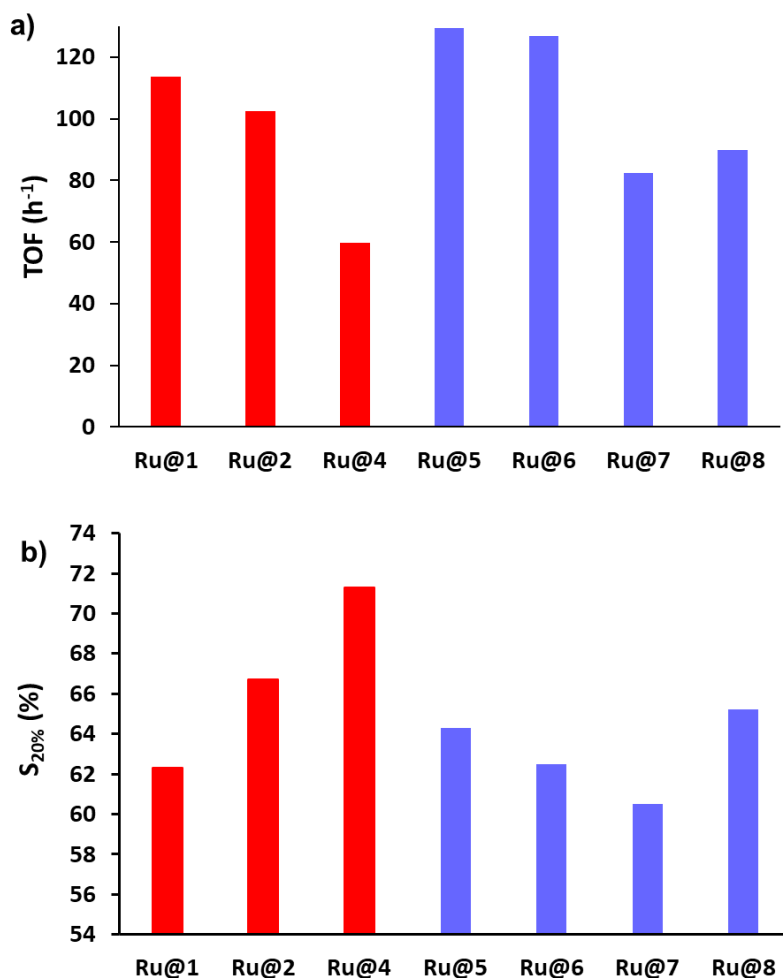


Figure 4.7 a) Activity for catalysts **Ru@1**, **Ru@2**, **Ru@4**, **Ru@5**, **Ru@6**, **Ru@7** and **Ru@8** (Ru/ligand = 10/1), TOF calculated with respect to surface Ru content at the time given in column 3 Table 4.4; and b) styrene selectivity at 20% conversion for catalysts **Ru@1**, **Ru@2**, **Ru@4**, **Ru@5**, **Ru@6**, **Ru@7** and **Ru@8** (Ru/ligand = 10/1). Red = carboxylic ligands; and blue = amine ligands.

We assume that the amine, a σ -donor ligand, increases the electron density at the NP surface, favoring thus the π -back donation from the d Ru orbitals to the antibonding π^* orbital of the alkyne/alkene, which facilitates rapid hydrogenation. Accordingly, a slightly higher selectivity towards styrene was observed when using carboxylic acid ligands (Figure 4.7b). Indeed, in that case, the charge transfer from the metal to the ligand results in electro-deficient Ru NP

that provide less π -back donation to the alkene, which weakens Ru-alkene bonding and favors its quick desorption, thus avoiding over hydrogenation to produce ethylbenzene.

Meanwhile, for the acid ligand series, a correlation exists between the surface electronic density and the selectivity of the catalyst, which was probed *via* the IR frequency of CO adsorbed on the catalysts after their synthesis (Figure 4.8, red squares). As expected, an increase of the selectivity is obtained when the electronic density on the Ru NP decreased (higher ν_{CO} frequency). For the σ -donor amine ligands (blue spheres in Figure 4.8), which provide a higher electronic density on the Ru NP, the selectivity is lower. However, differences of ν_{CO} shifts between the amine ligands are too close to show a clear tendency.

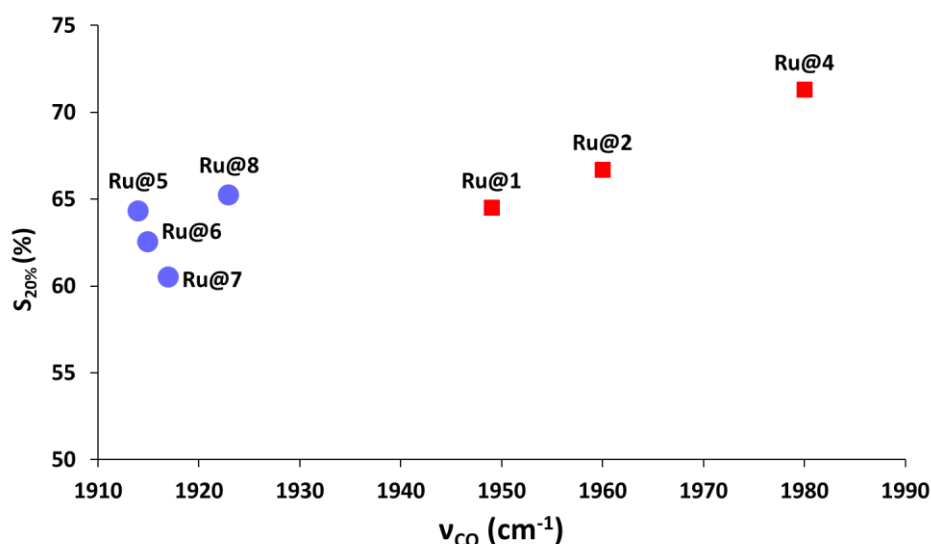


Figure 4.8 Styrene selectivity at 20% conversion as a function of the electronic density on Ru (probed *via* the IR ν_{CO} frequency of CO adsorbed on the catalysts after their synthesis in Table 4.6, blue spheres amine ligands, and red squares acid ligands). The Ru/ligand ratio in these catalysts is 10/1.

A correlation between the activity and the electronic properties is also obtained for the polymantane ligand series (Figure 4.9). Comparing the series with the

same polymantane cage (adamantane, **1**, **5**, **2**, **6** and diamantane, **4**, **8**), the activity decreases with the electronic density on Ru decreasing. On the other hand, **Ru@7** does not follow the trend, which could be attributed to its flexible backbone

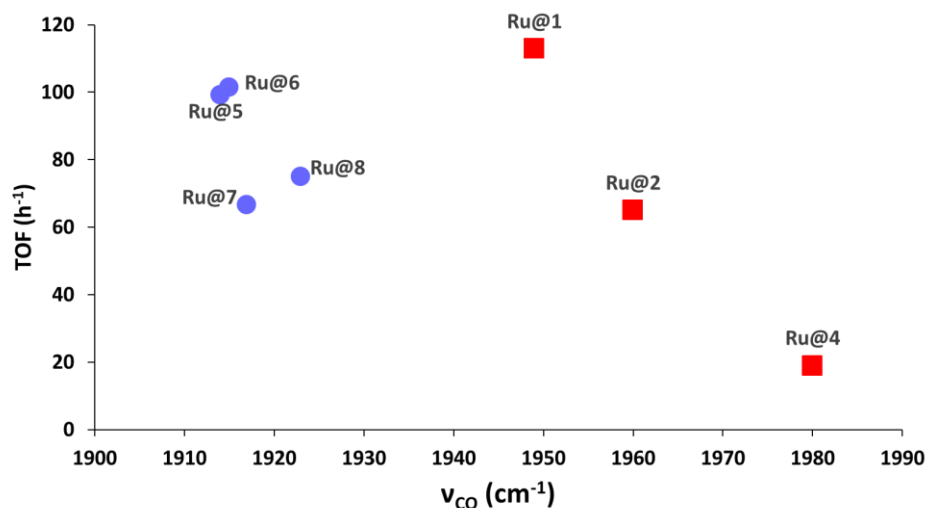


Figure 4.9 Correlation between the electronic density on Ru (probed *via* the IR ν_{CO} frequency of CO adsorbed on the catalysts after their synthesis in Table 4.6, blue sphere for amine, and red squares acid ligands, and the TOF (TOF calculated according to the Ru surface content at 1h of reaction) for the Ru catalysts.

In the series of Ru NP networks produced from acid or amines ligands, some differences attributed to the molecule background structure can also be noted. The use of bulkier ligands such as bis-adamantane (BAd), and diamantane (DAd) is detrimental to the activity. We also observed a confinement effect in relation with shorter inter-particle distances. Notably, the inter-particle distance is not affected by changes in Ru NP size since all the catalysts present very similar size (1.7-1.9 nm). Whatever the functional group of the ligand (carboxylic or amine), a correlation between the inter-particle distance and the catalyst activity is obtained (Figure 4.10), especially for the same polymantane family of ligands: the closer the particles are in the network, the higher the activity. The effects of confinement in carbon materials have been identified as possible levers to modify catalytic performances.⁵⁹ It has been shown that soft confinement effects, such

as reactant enrichment or rapid diffusion, will directly affect the kinetics of the reaction. Hard effects, like the charge transfer between the metal and the support, will also affect activity/selectivity and stability. In our case, it is clear that for the same family of functionalized ligand the more confined Ru NP are more active. The confinement effect occurs for Ru NP networks produced from different ligands (amines and acids) presenting very different electronic effects. Considering that reactant concentration enrichment (as well as high diffusion rates) have been regularly reported as explanation of “soft” confinement effects, we preferred to rely on this explanation. It should nevertheless be noted that the search for a detailed explanation of the observed confinement effects would require a study in itself, which falls outside the scope of our study.

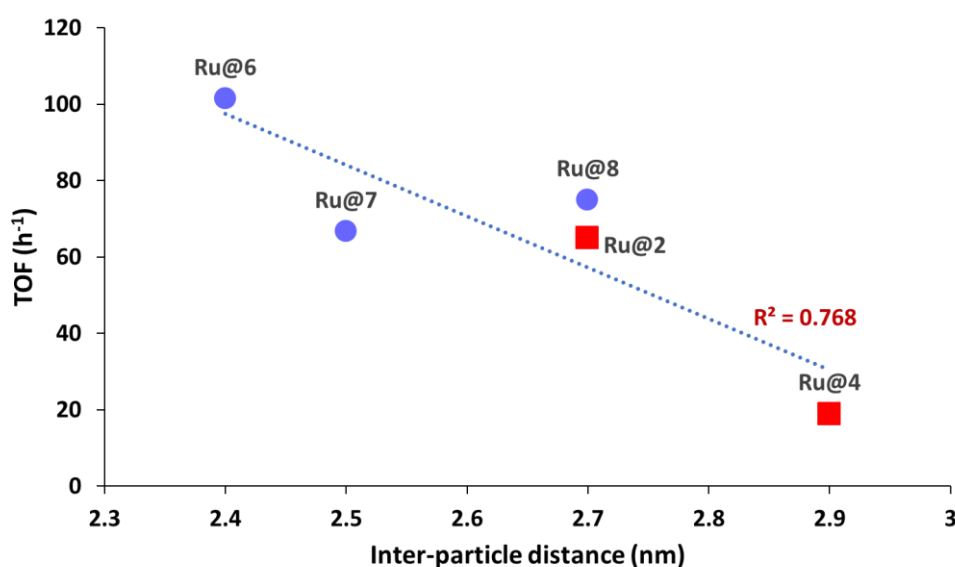


Figure 4.10 Activity as a function of the inter-particle distance in Table 4.6 (blue sphere for amine, and red squares acid ligands), the Ru/ligand ratio in these catalysts is 10/1 (TOF calculated according to the Ru surface content at 1h of reaction).

Both confinement and electronic effects concerning different type of carbon skeleton of molecules thus influence the activity. The TOF obtained with Ru NP networks nicely illustrate the promises concerning the use of NP networks in relation with inedited confinement effects, in which short-range interactions

between NP may greatly improve their catalytic activity when the electronic properties are similar.

A correlation can also be drawn between the inter-particle distance and selectivity (Figure 4.11) considering both amine and acid as ligands, which is reverse to the correlation observed between inter-particle distance and activity (Figure 4.10). That means, when increasing the confinement inside the assemblies, the catalysts are more active but less selective. Larger distance induces a decrease of the activity; in that case styrene could be desorbed before further hydrogenation, leading to higher selectivity.

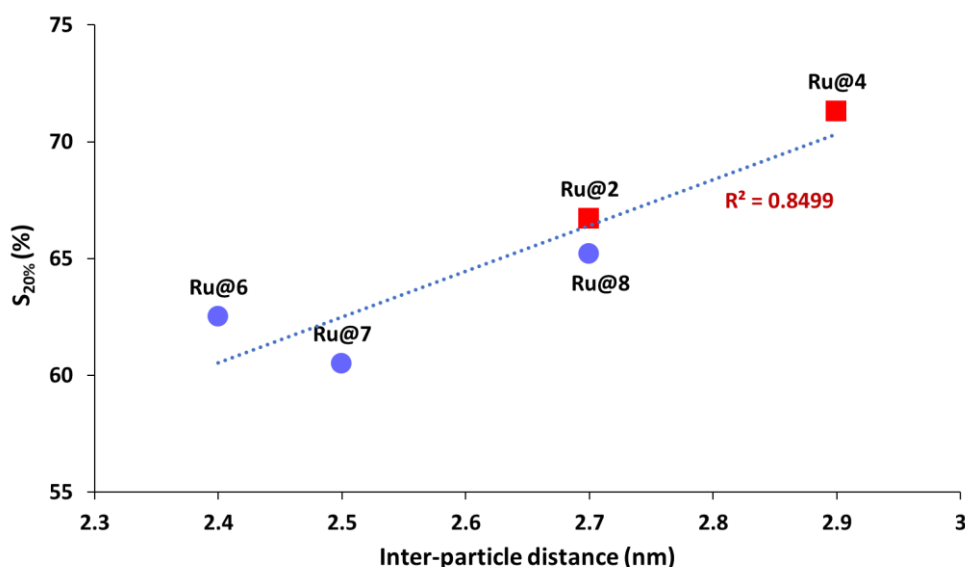


Figure 4.11 Styrene selectivity at 20% conversion as a function of the inter-particle distance in Table 4.6 (blue spheres amine ligands, and red squares acid ligands), Ru/ligand = 10/1.

Finally, to better delineate the performances of the Ru NP and NP networks prepared from the functionalized polymantane ligands we compared their reactivity with the ones of individual unprotected Ru NP deposited on functionalized carbon nanotubes (CNT). Two types of CNT were used, CNT functionalized with nitric acid (CNT_O) that contains significant amounts of carboxylic groups able to stabilize Ru NP,⁶⁰ and CNT

prepared from acetonitrile, which contains different types of nitrogen groups (CNT_N), such as pyridinic or amines.⁶¹ Both catalysts present similar Ru NP size (1-2 nm) and show much lower TOF (Table 4.4, entries 12 and 13) than the NP networks. However, the same tendency as the one observed for the Ru NP networks was observed, *i.e.* a higher TOF is obtained with the catalyst containing nitrogen functionalities. As for the Ru NP networks at low conversion (Figure 4.5), these two Ru/CNT catalysts show similar selectivity.

4.2.3.4 Catalytic performances of Ru NP assemblies produced from functionalized triphenylene, fullerene and anthracene ligands

The Ru NP assemblies presented in Chapter 3 were also used as catalysts for the hydrogenation of phenylacetylene. The catalytic results of these catalysts are listed in Table 4.5 together with those of one **Ru@C₆₀** catalyst.

Table 4.5 Hydrogenation of phenylacetylene using **Ru@TPhTC**, **Ru@HF**, **Ru@AnDC** and **Ru@C₆₀** catalyst.^{a)}

Entry	Catalysts	Time (h)	Conv. (%)	S _{20%} (%)	S _{60%} (%)	TOF (h ⁻¹) ^{b)}	TOF _s (h ⁻¹) ^{d)}
1	Ru@TPhTC - 40/1	5	64.0	57.5	53.5	27.0	15.6
2	Ru@TPhTC - 40/1 ^{c)}	4	53.8	67.6	65.2	25.4	2.6
3	Ru@TPhTC - 4/1	8	9.1	73.4 ^{e)}	-	4.4	16.0 ^{g)}
4	Ru@TPhTC - 4/1 ^{d)}	3	60.6	72.9	69.3	46.1	44.8 ^{g)}
5	Ru@HF - 120/1	3	86.1	59.5	51.2	64.1	70.2
6	Ru@AnDC - 10/1	3	66.2	58.8	55.1	48.8	91.8 ^{h)}
7	Ru@AnDC - 20/1	3	75.2	62.4	59.5	58.5	66.9 ⁱ⁾
8	Ru@C₆₀ - 10/1	3	53.8	58.6	52.4	46.3	18.1

^{a)} Reaction conditions: 0.02 mmol of Ru, 412 mg (4.00 mmol) of phenylacetylene, 71 mg (0.50 mmol)

of decane (internal standard), room temperature, 5 bar H₂, 25 mL MeOH; ^{b)} TOF in mol_{PAconverted}·mol_{Ru}⁻¹·h⁻¹ calculated at the time given in column 3; ^{c)} under 2 bar H₂; ^{d)} reaction temperature at 80 °C; ^{e)} Selectivity given at 10% of conversion; ^{f)} TOF calculated according to surface Ru content at 1h; ^{g)} The diameter calculating Ru surface content is 1.3 nm by WAXS; ^{h)} The Ru NP diameter calculating Ru surface content is 2.0 nm by TEM; ⁱ⁾ The Ru NP diameter used for calculating Ru surface is 1.8 nm by TEM.

The same distribution of products with different levels of hydrogenation (styrene, ethylbenzene and cyclohexane) was obtained as in the case of the polymantane stabilized catalysts. The highest selectivity for styrene (73 %) was obtained using the **Ru@TPhTC** catalyst with a Ru/L ratio of 4/1 at a reaction temperature of 80 °C with moderate activity. **Ru@TPhTC**- 4/1 is less metallic and possesses much smaller clusters compared to higher Ru/L ratio, meaning that Ru complex/single atoms may play a role in catalysis, which require higher temperature (80 °C) to reach high selectivity. The **Ru@TPhTC** - 40/1 catalyst leads to higher selectivity under 2 bar H₂ (Table 4.5 Entry 2) compared to 5 bar H₂. The TOF at 60 % conversion is almost the same for both catalysts, but the initial activity (column 8) decreases significantly. The trends along time for phenylacetylene conversion and styrene selectivity for the catalysts are presented in Figure 4.12. The decrease of selectivity over time for **Ru@TPhTC** with ratio of 4/1 and 40/1 are less pronounced than with the other catalysts. For two different Ru/L ratio of **Ru@AnDC**, the one with 20/1 behaves a little better than the one of 10/1 both in selectivity and activity.

The **Ru@C₆₀** catalyst, consisting in Ru NP decorating fulleride nanosphere, that was already used in our group for nitrobenzene hydrogenation⁹ shows lower selectivity and activity than Ru NP and Ru NP assemblies with carboxylic functionalized ligands due to different electronic properties and morphology.

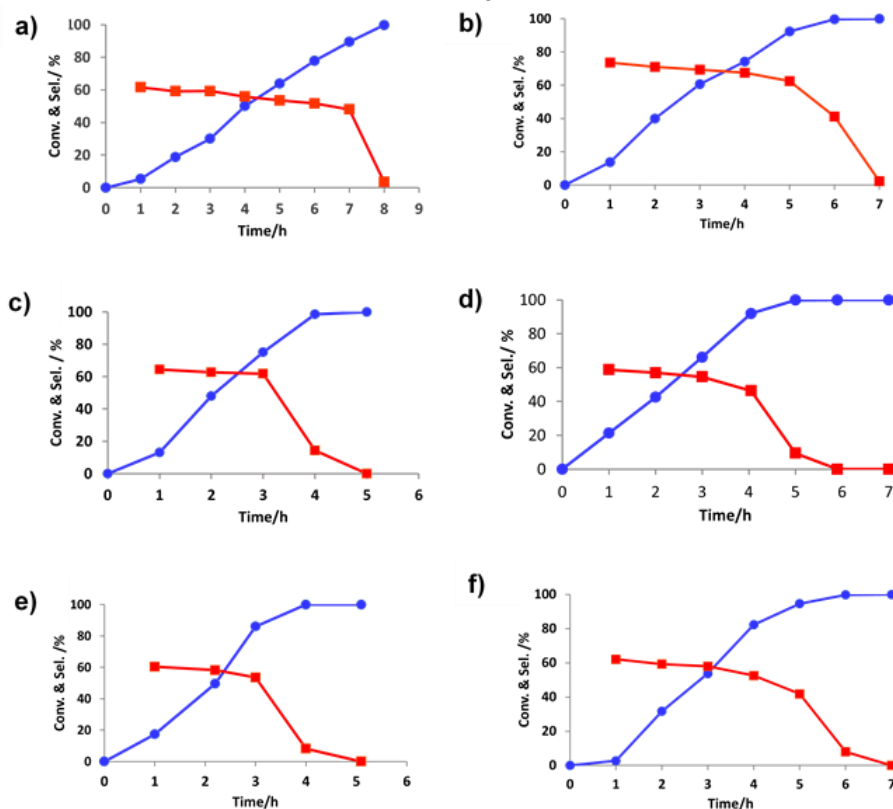


Figure 4.12 Evolution of activity (conversion blue lines) and selectivity toward styrene (red lines) over time for the investigated catalysts: a) **Ru@TPhTC** - 40/1; b) **Ru@TPhTC** - 4/1 at 80 °C; c) **Ru@AnDC** - 20/1; d) **Ru@AnDC** - 10/1; e) **Ru@HF** - 120/1; f) **Ru@C₆₀** - 10/1.

Considering that five different carboxylic functionalized ligands have been used in the hydrogenation of phenylacetylene, we examined the data to find possible correlations between selectivity and activity and the electronic properties or inter-particle distance.

The correlation between styrene selectivity and the electronic density on Ru NP is shown in Figure 4.13. A lower electronic density on Ru (higher ν_{CO} wavenumber), results in higher styrene selectivity, which is consistent with the discussion for polymantane catalysts due to electro-deficient Ru NP weakening Ru-alkene bonding and favoring its quick desorption.

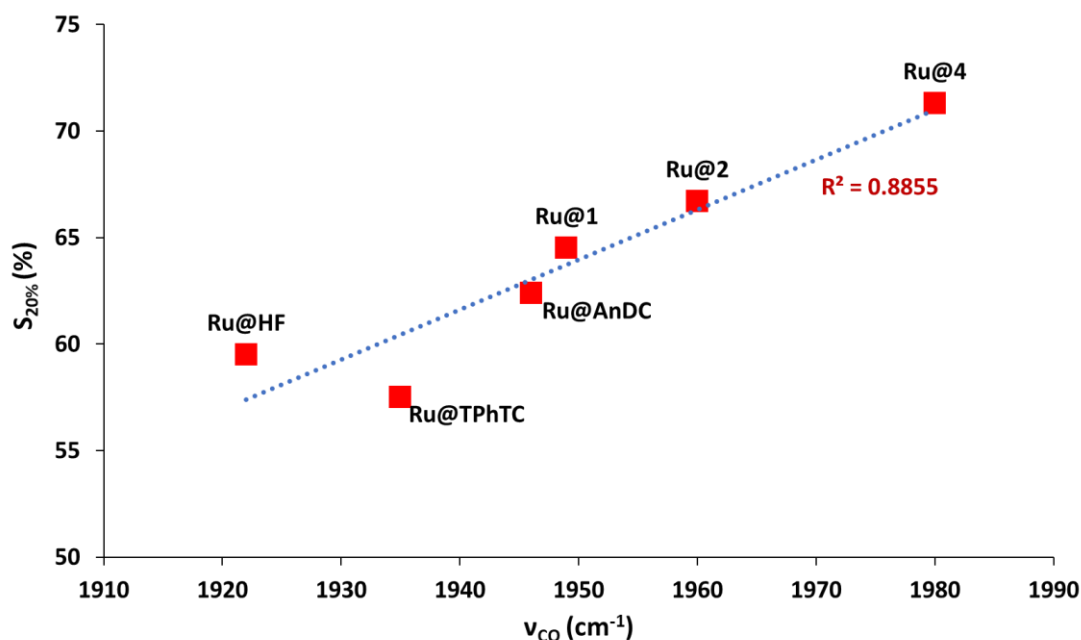


Figure 4.13 Styrene selectivity at 20% conversion as a function of the electronic density on Ru (probed *via* the IR ν_{CO} frequency of CO adsorbed on the catalysts in Table 4.6). The Ru/L ratios are 120, 40, 20, 10, 10, 10 for **HF**, **TPhTC**, **AnDC**, **4**, **2**, and **1**, respectively.

The activity of the NP assemblies can be affected by the charge transfer as well as the Ru NP inter-distance. As **Ru@HF** and **Ru@AnDC** possess larger and heterogeneous NP size, the correlation of inter-particle distance with TOF in Figure 4.14a only incorporates three ligands: **2**, **4** and **TPhTC**. With the elongation of the distance, the activity is decreased as shown before, which allows concluding that the use of bulky ligands is detrimental to the activity.

However, in an attempt to establish a correlation between charge transfer and TOF (Figure 4.14b), we found that the **Ru@TPhTC** catalyst is clearly out of the trend, in which the decrease of Ru electron density leads to the decrease of activity. For **Ru@TPhTC** the TOF is much lower than it should be, indicating that the influence of confinement is a determining factor obliterating the positive effect of the charge transfer. The **Ru@HF** could reach higher activity than all other acids, because the ν_{CO} bond representing the electron density is in that case as high as for Ru NP stabilized with amine ligands ($\sim 1920\text{ cm}^{-1}$).

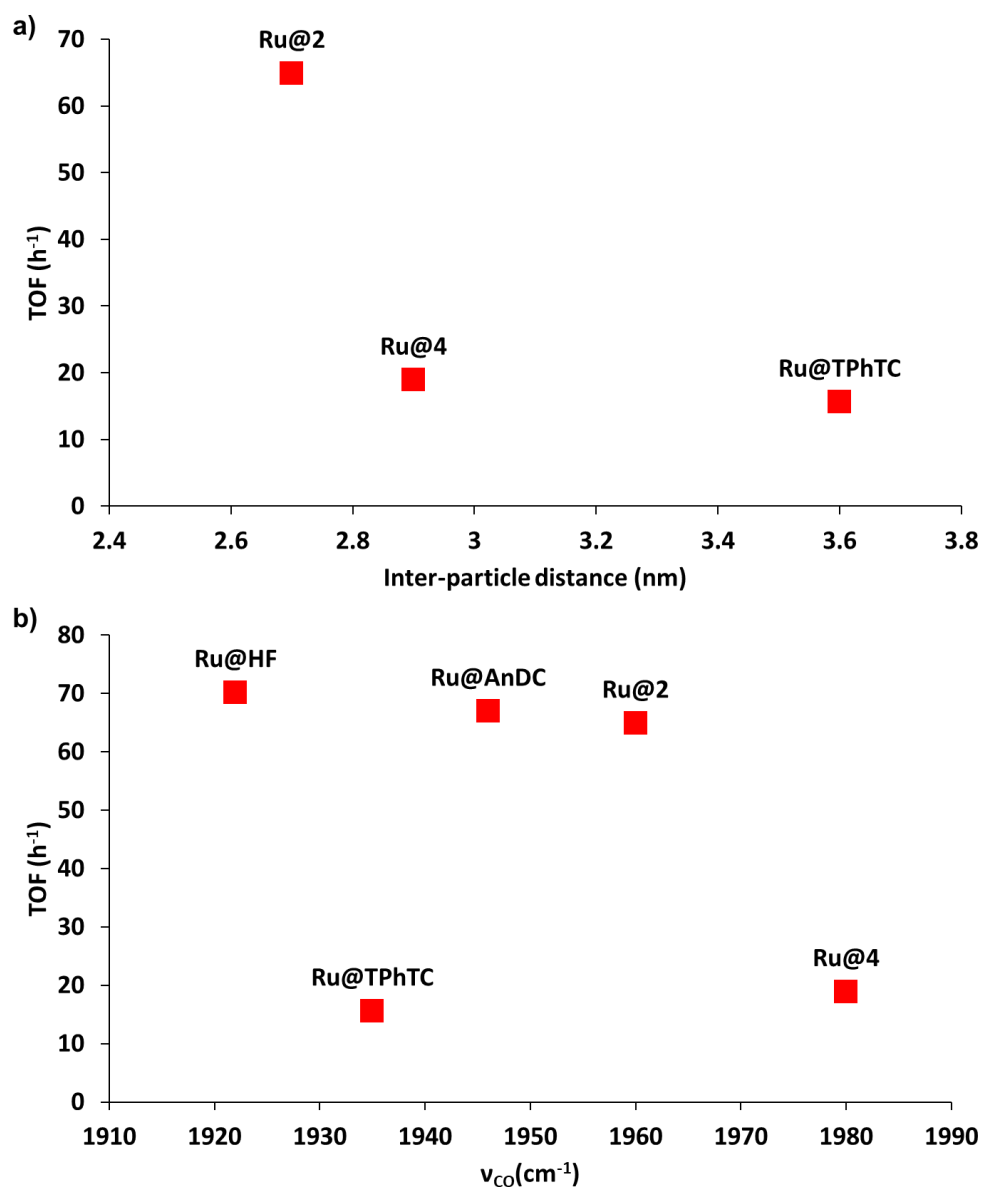


Figure 4.14 Correlation between the electronic density on Ru (probed *via* the IR ν_{CO} frequency of CO adsorbed on the catalysts after their synthesis in Table 4.6) and the TOF (calculated at 1h according to surface Ru content for the Ru catalysts. The Ru/L ratios are 120, 30, 20, 10, 10 for HF, TPhTC, AnDC, 4 and 2).

The Table 4.6 shows the main characterization of the catalysts before and after catalysis.

Table 4.6 Mean size distributions, interparticle distances, ruthenium content, CO infrared frequency band of the synthesised Ru NP and Ru NP networks and the NP size distribution after catalysis.

Entry	Catalyst	Ratio	Ru content (%) ^{a)}	Ru surface content (%)	NP size (nm) ^{b)}	Inter-particle distance (nm) ^{c)}	ν_{CO} (cm ⁻¹) ^{d)}	NP size after catalysis (nm) ^{f)}
1	Ru@1	10/1	65.5	36.5	1.8 ± 0.5	-	1949	1.5±0.8
2	Ru@2	10/1	61.8	34.4	1.8 ± 0.8	2.7	1960	1.1±0.5
3	Ru@4	10/1	67.7	37.7	1.8 ± 0.6	2.9	1980	1.4 ± 0.6
4	Ru@5	10/1	82.5	50.1	1.6 ± 0.7	-	1914	1.4 ± 0.7
5	Ru@6	10/1	80.1	44.6	1.8 ± 0.7	2.4	1915	1.1 ± 0.5
6	Ru@7	10/1	65.7	38.2	1.7 ± 0.6	2.5	1917	1.3 ± 0.6
7	Ru@8	10/1	70.2	40.8	1.7 ± 0.7	2.7	1923	1.2 ± 0.6
8	Ru@TPhTC	40/1	66.0	38.4	1.7 ± 0.8	3.6	1935	1.5 ± 0.6
9	Ru@AnDC	20/1	66.5	37.1 ^{e)}	1.8 ± 0.7 2.5 ± 1.0	-	1946	1.3 ± 0.5
10	Ru@HF	120/1	65.9	31.5	2.2 ± 1.8	3.3	1922	1.8 ± 1.0

^{a)} By ICP; ^{b), f)} by TEM; ^{c)} by SAXS; ^{d)} by IR; ^{e)} diameter is taken as 1.8 nm which is highest statistic frequency.

4.2.3.5 Stability of the Ru NP assemblies

The stability of Ru NP assemblies was evaluated by means of a recycling test for an adamantane-based catalyst, and the effect of a thermal treatment on a **Ru@TPhTC**- 40/1 catalyst was studied.

Figure 4.15 shows TEM micrographs of the spent catalysts of Ru NP assemblies with ligand **2**, **4**, **6**, **7**, **8**, **TPhTC**, **HF** and **AnDC**. After catalysis, the assemblies that are stabilized by carboxylic acid display no change in the network while for the ones with amine ligand isolated nanoparticles could be observed on the grid. Mean sizes of Ru NP (Table 4.6 column 9) after test indicates that the NP are not aggregated into larger NP after catalysis. It is clear from the micrographs (Figure 4.15) that the networks prepared from acid ligands provide more robust catalysts, as expected from the DFT calculations discussed in Chapter 2.

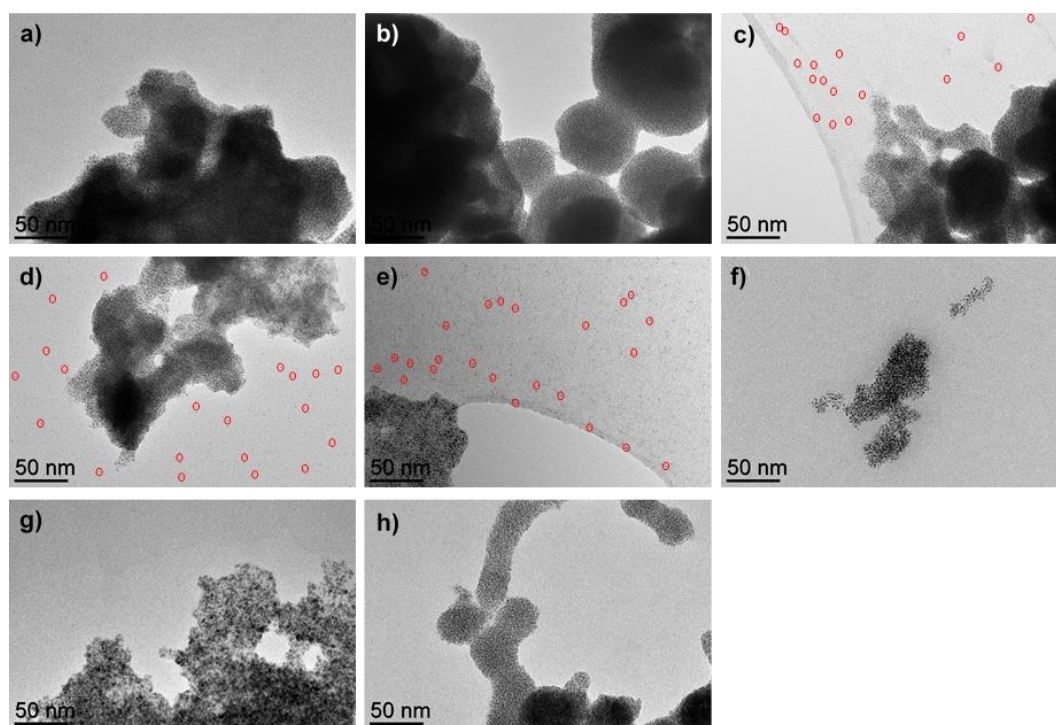


Figure 4.15 TEM images of spent catalysts: a) **Ru@2** - 10/1; b) **Ru@4** - 10/1; c) **Ru@6** - 10/1; d) **Ru@7** - 10/1; e) **Ru@8** - 10/1; f) **Ru@TPhTC** - 40/1; g) **Ru@HF** - 120/1; h) **Ru@AnDC** - 20/1.

The recyclability of the catalyst system was studied at partial conversion (3 hour of reaction) under the optimized conditions, *i.e.* room temperature, 5 bar H₂, and MeOH

as solvent, using **Ru@2** – 10/1 as catalyst. After each run, the supernatant was separated from the Ru catalyst, and after removal of the volatiles by reduced pressure, the Ru content on the remaining product was analyzed by ICP. The results are summarized in Table 4.7.

Table 4.7 Catalytic recycling tests for phenylacetylene hydrogenation with **Ru@2**. ^{a)}

Entry	Conv. (%)	Selec. (%)	Ru (mmol) ^{b)}	TOF(h ⁻¹) ^{c)}
Fresh	78.6	65.9	0.022	57.2
1 st recycling	67.6	64.5	0.018	62.0
2 nd recycling	63.3	64.4	0.015	67.7
3 rd recycling	47.8	64.3	0.014	52.8
4 th recycling	32.1	66.6	0.013	35.8

^{a)} Reaction conditions: 0.02 mmol of Ru, 412 mg (4.00 mmol) of phenylacetylene, 71 mg (0.50 mmol) of decane (internal standard), room temperature, 5 bar H₂, 25 mL MeOH, 3h. ^{b)} Ru content related to the loss of Ru due to Ru leaching as ascertained by ICP. ^{c)} TOF calculated according to the actual Ru content (column 4) at the time of 3h.

The selectivity towards styrene remains constant in all four recycling experiments being about 65% towards styrene. On the other hand, the activity decreased after recycling for two times, which is consistent with the Ru detected by ICP in the supernatant (Table 4.7). The leaching was attributed to the recycling procedure itself, as the precipitation of the Ru catalyst was difficult to achieve. On the other hand, TEM analyses reveal that the network is stable after three recycling tests, but significantly lost its structure after the fourth test (Figure 4.16). The mean size diameter of the recycled NP after 4 times is 1.1 ± 0.5 nm, which is similar to the size of the spent fresh **Ru@6**.

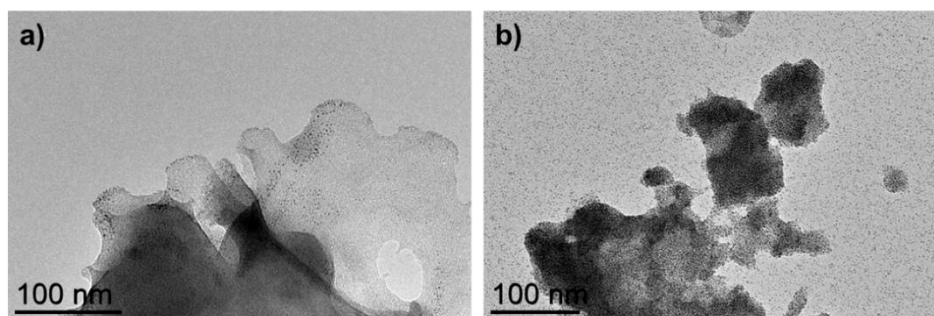


Figure 4.16 TEM images of catalyst **Ru@2** after a) 3rd recycling and b) 4th recycling tests.

In order to try to improve the stability of NP assemblies, thermal treatment was performed on the catalysts, with the aim to remove the carboxylate group and to anchor the ligand to NP by the remaining carbene-like carbon atom. Figure 4.17a shows the TGA (Thermogravimetric analysis) curve of **Ru@TPhTC** with a Ru/L ratio of 40/1. At a temperature of around 190 °C, the first stage of mass loss happened, in good agreement with TPD experiments (Figure 4.17b), which confirmed that the first decarboxylation occurs at around 180 °C to finish at around 200 °C. These two temperatures (181 and 201 °C) were chosen to thermal-treat the catalyst.

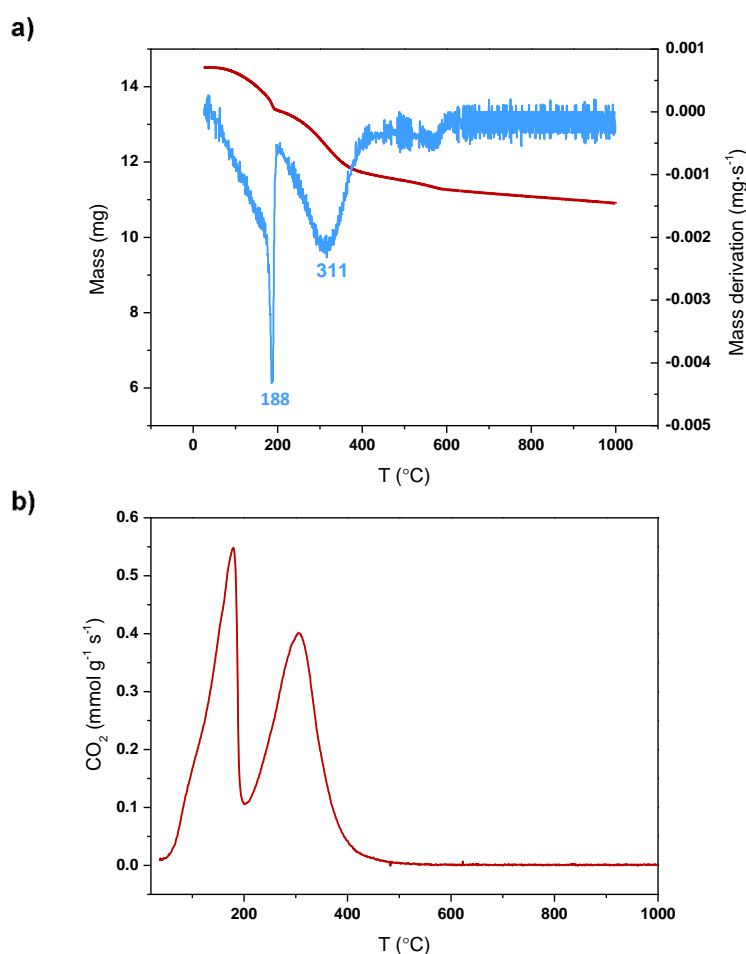


Figure 4.17 a) TGA (red curve) and derivation curve (blue curve) of **Ru@TPhTC** predicting the Ru loading after thermal treatment at 181 °C is 70% and 72% at 201 °C; and b) TPD/MS of CO₂ of **Ru@TPhTC**.

The thermal treatment of **Ru@TPhTC** - 40/1 was conducted by heating the sample in a furnace under Ar flow reaching a final temperature of 181 or 201 °C at a rate of 10 °C.min⁻¹ (**Ru@TPhTC**₁₈₁ and **Ru@TPhTC**₂₀₁, respectively). The final temperatures are chosen according to the results of the thermal analyses of **Ru@TPhTC**; 181 °C leading to a partially decarboxylated material, and 201 °C to a fully decarboxylated one in first stage (Figure 4.17). TEM analyses (Figure 4.18) show that Ru NPs networks remain qualitatively similar for sample **Ru@TPhTC**₁₈₁ than their parent material (Figure 4.18a vs. 4.18c), while the sample treated at a higher temperature qualitatively displayed a more compact structure (Figure 4.18a vs. 4.18e) indicating a probable change of the linking ligand. Mean size distributions of the untreated and thermal treated Ru NP networks are summarized in Table 4.8 column 3, presenting similar NP size. Both thermal treated and original **Ru@TPhTC** catalysts were used for the phenylacetylene hydrogenation using THF as solvent and the obtained results are summarized in Table 4.8. As the hydrogenation in THF shows good selectivity but disassembled structure into isolated NP, it can be an indication of whether the stability of the NP assemblies is improved or not.

Table 4.8 Catalytic hydrogenation of phenylacetylene with **Ru@TPhTC** (ratio of 40/1) before and after thermal treatment at 181 and 201 °C.

Entry	Catalyst	NP size (nm)	Time (h)	Conv. (%)	S _{20%} (%)	S _{60%} (%)	TOF (h ⁻¹) ^{b)}	TOF (h ⁻¹) ^{c)}
1	Ru@TPhTC	1.7 ± 0.8	5.4	66.8	68.4	66.1	24.2	41.6
2	Ru@TPhTC ₁₈₁	1.6 ± 0.7	4.0	52.8	68.7	66.9	26.1	43.0
3	Ru@TPhTC ₂₀₁	1.5 ± 0.8	5.0	75.9	61.6	60.8	23.9	37.6

^{a)} Reaction conditions: 0.02 mmol of Ru, 412 mg (4.00 mmol) of phenylacetylene, 71 mg (0.50 mmol) of decane (internal standard), room temperature, 5 bar H₂, 25 mL of THF; ^{b)} TOF calculated according to the Ru content at the time given in column 3, the Ru content of **Ru@TPhTC**₁₈₁ is 70% according to TGA, and 72% for **Ru@TPhTC**₂₀₁; ^{c)} TOF calculated according to the Ru surface content at the time in column 3.

TEM analyses of the catalysts after the hydrogenation reaction (Figure 4. 18b, d and f) show the beneficial effect of the thermal treatment over the stability. Indeed, **Ru@TPhTC** network is not stable after one catalytic run and produced isolated Ru NP (Figure 4.18a vs. 4.18b). This loss of the nanostructure is also observed for **Ru@TPhTC₁₈₁**, nevertheless some assemblies are still observed on the TEM grid (Figure 4.18c vs. 4.18d), thus indicating that the ligands in the network are basically acting in the same manner. The beneficial effect of the heat treatment in terms of stability of the networks is clearly observed for **Ru@TPhTC₂₀₁**. In this case, the network is almost unchanged before and after catalysis (Figure 4.18e vs. 4.18f) with slightly disassembled NP and a Ru NP size distribution of 1.5 ± 0.6 nm after catalysis.

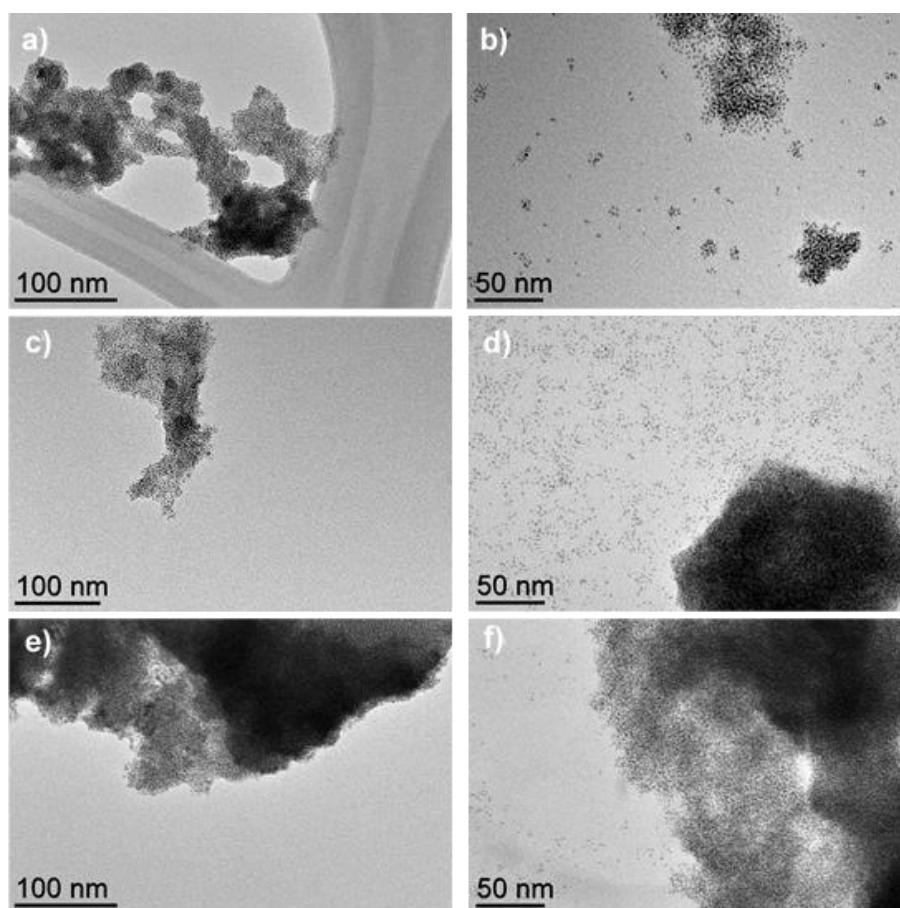


Figure 4.18 TEM images of catalyst **Ru@TPhTC** a) before and b) after the catalytic hydrogenation of phenylacetylene; **Ru@TPhTC** catalyst after thermal treatment at 181 °C c) before and d) after catalysis; and **Ru@TPhTC** catalyst after thermal treatment at 201 °C e) before and f) after catalysis.

In terms of catalytic performances, the thermal treatment seems to be less attractive.

While **Ru@TPhT**, **Ru@TPhTC₁₈₁** and **Ru@TPhTC₂₀₁** display similar catalytic activity (Table 4.8); even if more robust the **Ru@TPhTC₂₀₁** catalyst is slightly less selective when compared to the other catalysts. These results are in line with the thermal analyses, while 181 °C treatment produces a similar catalyst than **Ru@TPhT** due to the limited decarboxylation, a slightly higher temperature is able to decarboxylate the sample and produce a more robust catalyst. Nevertheless, the loss of the carbonyl groups together with the change on the network lead to different catalytic results, which are probably due to changes of the inter-particle distance and of the electronic density on the metal. These parameters need a deeper study to be fully understood.

4.3 Conclusion

Isolated Ru NP and Ru NP covalent assemblies stabilized by functional polymantane ligands bearing carboxylic and amine groups have been tested as catalyst for C-H activation - bromination and hydrogenation of quinoline and phenylacetylene reactions. In the case of the C-H activation and hydrogenation of quinoline reactions, the Ru NP networks dissembled into isolated NP after catalysis. This was tentatively attributed to the harsh conditions used or, in the case of the carboxylate ligands to the presence of Lewis-bases in the medium.

In the hydrogenation of phenylacetylene catalyzed by Ru NP assemblies, milder reaction conditions were used. Several Ru NP assemblies bearing different ligands (bi-functional polymantane, **TPhTC** and **HF**) were recovered intact after catalysis, and reached good selectivity to styrene. These nanoparticle networks constitute a unique set to investigate structural and electronic effects in heterogeneous catalysis. Confinement effects were evidenced that affect both catalyst activity and selectivity.

For the NP assemblies produced from the acid ligand series including polymantane, triphenylene, fullerene and anthracene, the selectivity varies with the inter-particle distance and the electronic properties. A higher selectivity towards styrene was obtained with Ru NP networks presenting electro-deficient Ru NP. The activity is also related to both the inter-particle distance and electron density. A higher activity is obtained with electron-rich Ru NP and short inter-particle distances.

We also demonstrated that the stability of the assemblies is still a problem for phenylacetylene hydrogenation since the structure cannot stand after recycling tests. It appears from this study that the choice of carboxylate (or amine) linkers to build the network of Ru NP is not an optimal choice. Other ligands such as phosphine or carbene, which can bind stronger to Ru could be investigated in the future.

Finally, a thermal treatment was investigated to improve the anchoring strength in the network by ligand decarboxylation. Although an improvement in stability was obtained, the changes in electronic effect and/or inter-particle distance associated to this heat-treatment induce a decrease in styrene selectivity.

4.4 Experimental section

Material and methods

All manipulations were carried on under Ar atmosphere *via* standard Shlenck techniques and in an MBraun glovebox. The solvent we used in this work are purified by standard methods or by an MBraun SPS-800 solvent purification system and degassed by a freeze-pump-thaw protocol. [Ru(COD)(COT)] [(1,5-cyclooctadiene)(1,3,5-cyclooctatriene)ruthenium] was purchased from Nanomeps Toulouse. Fullerene, TBATB, K₂CO₃, NaHCO₃, phenylacetylene and decane were purchased from Sigma-Aldrich, NBS was purchased from TCI and 2-phenylpyridine from Alfa Aesar. These products were used as received.

Synthesis of Ru NP on functionalized carbon nanotubes

9.6 mg [Ru(COD)(COT)] were dissolved in 20 mL THF and this solution was added to 150 mg of dried functionalized carbon nanotubes (CNT_O or CNT_N). After stirred under inert atmosphere overnight, the mixture was filtered and washed with pentane to obtain a black solid, which was reduced under H₂/Ar gas flow (flow ratio of Ar:H₂= 4:1) at 200 °C for 1h using a rate of 7 °C.min⁻¹. The final products were kept under inert atmosphere for further uses. % Ru content: Ru/CNT_O 1.6% w/w; Ru/CNT_N, 0.8% w/w.

Synthesis of Ru@C₆₀ with Ru/L ratio of 10/1

Fullerene C₆₀ (24.4 mg, 0.034 mmol) was dissolved in 135 mL of dichloromethane in

a 500 mL volume Fisher-Porter bottle, afterwards [Ru(COD)(COT)] (140.2 mg, 0.444 mmol) was added to the purple solution. After 1h of stirring under Ar at room temperature, hydrogen (3 bar) was introduced into the Fisher-Porter bottle. After 16 h of reaction at room temperature, the solvent volume was reduced and the black solid was washed by pentane (3 x 200 mL) and finally dried under vacuum overnight. Ru content: 48.7%.

Calculation of Ru surface content

The fraction of Ru atoms on the surface is given by $f = \frac{\text{Atoms surface}}{\text{Atoms total}}$ (in percentage x100). Atoms in total, in the core and in the shell are calculated following: $\text{Unitcells}_{total} = \frac{V_{total}}{V_{unit}}$; $\text{Atoms}_{total} = (\text{Unitcells}_{total}) \cdot (\text{atoms per unit cell})$; $\text{Unitcells}_{core} = \frac{V_{core}}{V_{unit}}$; $\text{Atoms}_{core} = (\text{Unitcells}_{core}) \cdot (\text{atoms per unit cell})$; $\text{Unitcells}_{shell} = \frac{V_{shell}}{V_{unit}}$; $\text{Atoms}_{surface} = (\text{Unitcells}_{shell}) \cdot (\text{atoms per unit cell})$; where the volume of the nanoparticles is: $V_{total} = \frac{4}{3}\pi(r)^3$; $V_{core} = \frac{4}{3}\pi(r-shell\ thickness)^3$; $V_{shell} = V_{total} - V_{core}$; and the volume of a single unit cell (a and c lattice parameters) using: $V_{unit} = (\text{atoms per unit cell}) \frac{a^2\sqrt{3}}{4} c$. Crystallographic data of Ru:⁶² shell thickness = half the lattice constant; $V_{unit} = 0.0817\text{ nm}^3$ ($a = 0.271$; $c = 0.428$); atoms per unit cell = 6; r determined using TEM images.

General procedure for the bromination of 2-phenylpyridine

4.8 mg of catalyst (Ru, 0.03 mmol) were added to a 2-phenylpyridine (46.9 mg, 0.3 mmol) solution in DMA (0.9 mL). Bromination agents (TBATB or NBS, 231.4 mg and 84.2 mg, respectively, 0.48 mmol) were subsequently added. The reaction mixture was heated to the desired temperature and allowed to react. After 20 h of reaction, the solution was cooled down and decane (45 mg, 0.258 mmol) was introduced as an internal standard. The final reaction solution was diluted in 10 mL CH₂Cl₂, then washed with 10 mL NaHCO₃ (1M) and 10 mL of brine successively. The organic layer was concentrated using a rotary evaporator and analyzed by GC and GC-MS.

General procedure for the hydrogenation of quinoline

The hydrogenation of quinoline was performed in a 75 mL stainless steel high-pressure batch reactor. Typically, the Ru NP catalyst (0.02 mmol of Ru) was introduced into a solution of dodecane (75 mg, 0.44 mmol) and quinoline (404 mg, 3.12 mmol) in 25 mL

of THF as solvent under an Ar atmosphere. The autoclave was purged three times with H₂; heated at 100 °C and charged with 20 bar of H₂. The stirring rate was fixed to 1500 rpm. Samples of the reaction mixture were taken out at different time intervals and analysed by gas chromatography.

General procedure for the hydrogenation of phenylacetylene

In a typical catalytic reaction, a mixture of phenylacetylene (4 mmol, 412 mg), decane (0.5 mmol, 71 mg) and Ru NP catalyst (0.02 mmol of Ru) were dispersed in MeOH (25 mL) in a magnetically stirred autoclave with Teflon inner cylinder. The autoclave was purged three times with H₂. The autoclave was pressurized with 5 bar of H₂ at room temperature. The stirring rate was fixed to 1500 rpm. Samples of the reaction mixture were taken out at different time intervals and analysed by gas chromatography.

Recycling test

Phenylacetylene (4 mmol, 412 mg), decane (0.5 mmol, 71 mg) and Ru NP catalyst (Ru atom amount 0.02 mmol) were dispersed in MeOH (25 mL) in a magnetically stirred autoclave with Teflon inner cylinder. The autoclave was purged three times with H₂ and pressurized with 5 bar of H₂ keeping the stirring rate at 1500 rpm. After 3h of reaction, the catalyst was recovered in the glovebox by precipitation and washed with diethyl ether, then dried under vacuum. The catalyst was then reused in a subsequent catalytic test carried out following the same procedure.

Thermal treatment of Ru@TPhTC - 40/1

30 mg of Ru@TPhTC - 40/1 was introduced in a furnace under an Ar flow. The temperature was raised using a rate of 10 °C.min⁻¹ until 181 or 201°C, to produce Ru@TPhTC₁₈₁ and Ru@TPhTC₂₀₁, respectively. When the corresponding temperature was reached, the furnace was cooled down to room temperature under 140 mL.min⁻¹ of Ar flow.

Characterization

The ruthenium content was measured by inductively coupled plasma optical emission spectroscopy (ICP-OES) performed at the LCC with a Thermo Scientific ICAP 6300 instrument.

TEM analyses were performed at the “Centre de microcaractérisation Raimond

Castaing, UMS 3623, Toulouse” by using a JEOL JEM 1011 CX-T electron microscope operating at 100 kV with a point resolution of 4.5 Å and a JEOL JEM 1400 electron microscope operating at 120 kV. The particle size distribution was determined through a manual measurement of enlarged micrographs from different areas of the TEM grid (at least 200 particles).

GC analyses were performed on a PerkinElmer Autosystem GC equipped with an Elite-5MS Capillary Column (30 m × 0.25 mm × 0.25 μm). Quantitative analyses of reaction mixtures were performed via GC using calibration solutions of commercially available products.

GC-MS analyses were performed in a PerkinElmer Autosystem GC equipped with an Elite-5MS Capillary Column (30 m*0.25 mm*0.25 μm) coupled to a Turbo Mass mass spectrometer.

Liquid NMR spectra were obtained on a Bruker Fourier 300 systems using CD₂Cl₂, CDCl₃, or THF-d₈ solvent, TMS as internal standard, with proton and carbon resonances at 300 and 75 MHz, respectively.

Thermogravimetric analyses (TGA) were obtained with TGA 2 METTLER TOLEDO instrument. The sample was heated up to 1000 °C at 10 °C.min⁻¹ using a constant nitrogen flow of 20 cm³.min⁻¹.

4.5 References

1. Wieckowski, A.; Savinova, E. R.; Vayenas, C. G., *Catalysis and Electrocatalysis at Nanoparticle Surfaces*. CRC Press: 2003.
2. Astruc, D., *Nanoparticles and Catalysis*. John Wiley & Sons: 2008.
3. Gates, B. C., Supported Metal Clusters: Synthesis, Structure, and Catalysis. *Chem. Rev.* **1995**, *95*, 511-522.
4. Mondloch, J. E.; Bayram, E.; Finke, R. G., A Review of the Kinetics and Mechanisms of Formation of Supported-Nanoparticle Heterogeneous Catalysts. *J. Mol. Catal. A: Chem.* **2012**, *355*, 1-38.
5. Fan, J.; Gao, Y., Nanoparticle-Supported Catalysts and Catalytic Reactions – a Mini-Review. *J. Exp. Nanosci.* **2006**, *1*, 457-475.
6. Yan, N.; Xiao, C.; Kou, Y., Transition Metal Nanoparticle Catalysis in Green Solvents. *Coord. Chem. Rev.* **2010**, *254*, 1179-1218.
7. Yan, N.; Yuan, Y.; Dyson, P. J., Nanometallic Chemistry: Deciphering Nanoparticle Catalysis from the Perspective of Organometallic Chemistry and Homogeneous Catalysis. *Dalton Trans.* **2013**, *42*, 13294-13304.
8. Leng, F.; Gerber, I. C.; Lecante, P.; Bacsa, W.; Miller, J.; Gallagher, J. R.; Moldovan, S.; Girleanu, M.; Axet, M. R.; Serp, P., Synthesis and Structure of Ruthenium-Fullerides. *RSC Adv.* **2016**, *6*, 69135-69148.
9. Leng, F.; Gerber, I. C.; Lecante, P.; Moldovan, S.; Girleanu, M.; Axet, M. R.; Serp, P., Controlled and Chemoselective Hydrogenation of Nitrobenzene over Ru@C₆₀ Catalysts. *ACS Catal.* **2016**, *6*, 6018-6024.
10. Leng, F.; Gerber, I. C.; Axet, M. R.; Serp, P., Selectivity Shifts in Hydrogenation of Cinnamaldehyde on Electron-Deficient Ruthenium Nanoparticles. *C. R. Chim.* **2018**, *21*, 346-353.
11. Leng, F.; Gerber, I. C.; Lecante, P.; Bentaleb, A.; Muñoz, A.; Illescas, B. M.; Martín, N.; Melinte, G.; Ersen, O.; Martinez, H.; Axet, M. R.; Serp, P., Hexakis [60]Fullerene Adduct-Mediated Covalent Assembly of Ruthenium Nanoparticles and Their Catalytic Properties. *Chem. Eur. J.* **2017**, *23*, 13379-13386.
12. Bystrzanowska, M.; Petkov, P.; Tobiszewski, M., Ranking of Heterogeneous Catalysts Metals by Their Greenness. *ACS Sustain. Chem. Eng.* **2019**, *7*, 18434-18443.
13. Yu, J.-Q.; Shi, Z., *CH Activation*. Springer: 2010; Vol. 292.
14. Arockiam, P. B.; Bruneau, C.; Dixneuf, P. H., Ruthenium(II)-Catalyzed C-H Bond Activation and Functionalization. *Chem. Rev.* **2012**, *112*, 5879-5918.
15. Ritleng, V.; Sirlin, C.; Pfeffer, M., Ru-, Rh-, and Pd-Catalyzed C–C Bond Formation Involving C–H Activation and Addition on Unsaturated Substrates: Reactions and Mechanistic

- Aspects. *Chem. Rev.* **2002**, *102*, 1731-1770.
16. Ackermann, L.; Vicente, R.; Potukuchi, H. K.; Pirovano, V., Mechanistic Insight into Direct Arylations with Ruthenium(II) Carboxylate Catalysts. *Org. Lett.* **2010**, *12*, 5032-5035.
 17. Ackermann, L.; Novak, P.; Vicente, R.; Hofmann, N., Ruthenium-Catalyzed Regioselective Direct Alkylation of Arenes with Unactivated Alkyl Halides through C-H Bond Cleavage. *Angew. Chem. Int. Ed. Engl.* **2009**, *48*, 6045-6048.
 18. Engle, K. M.; Mei, T. S.; Wasa, M.; Yu, J. Q., Weak Coordination as a Powerful Means for Developing Broadly Useful C-H Functionalization Reactions. *Acc. Chem. Res.* **2012**, *45*, 788-802.
 19. Ackermann, L., Carboxylate-Assisted Ruthenium-Catalyzed Alkyne Annulations by C-H/Het-H Bond Functionalizations. *Acc. Chem. Res.* **2014**, *47*, 281-295.
 20. Park, S.; Kim, M.; Koo, D. H.; Chang, S., Use of Ruthenium/Alumina as a Convenient Catalyst for Copper-Free Sonogashira Coupling Reactions. *Adv. Synth. Catal.* **2004**, *346*, 1638-1640.
 21. Leitch, J. A.; Frost, C. G., Ruthenium-Catalysed Sigma-Activation for Remote Meta-Selective C-H Functionalisation. *Chem. Soc. Rev.* **2017**, *46*, 7145-7153.
 22. Li, G.; Li, D.; Zhang, J.; Shi, D.-Q.; Zhao, Y., Ligand-Enabled Regioselectivity in the Oxidative Cross-Coupling of Arenes with Toluenes and Cycloalkanes Using Ruthenium Catalysts: Tuning the Site-Selectivity from the Ortho to Meta Positions. *ACS Catal.* **2017**, *7*, 4138-4143.
 23. Jing, K.; Li, Z.-Y.; Wang, G.-W., Direct Decarboxylativemeta-Selective Acylation of Arenes Via Anortho-Ruthenation Strategy. *ACS Catal.* **2018**, *8*, 11875-11881.
 24. Barlow, H. L.; Teskey, C. J.; Greaney, M. F., Ruthenium-Catalyzed Meta-Carboxylation. *Org. Lett.* **2017**, *19*, 6662-6665.
 25. Yu, Q.; Hu, L. a.; Wang, Y.; Zheng, S.; Huang, J., Directedmeta-Selective Bromination of Arenes with Ruthenium Catalysts. *Angew. Chem. Int. Ed.* **2015**, *54*, 15284-15288.
 26. Teskey, C. J.; Lui, A. Y.; Greaney, M. F., Ruthenium-Catalyzed Meta-Selective C-H Bromination. *Angew. Chem. Int. Ed. Engl.* **2015**, *54*, 11677-11680.
 27. Warratz, S.; Burns, D. J.; Zhu, C.; Korvorapun, K.; Rogge, T.; Scholz, J.; Jooss, C.; Gelman, D.; Ackermann, L., Meta-C-H Bromination on Purine Bases by Heterogeneous Ruthenium Catalysis. *Angew. Chem. Int. Ed.* **2017**, *56*, 1557-1560.
 28. Liu, L.; Corma, A., Metal Catalysts for Heterogeneous Catalysis: From Single Atoms to Nanoclusters and Nanoparticles. *Chem. Rev.* **2018**, *118*, 4981-5079.
 29. Sridharan, V.; Suryavanshi, P. A.; Menéndez, J. C., Advances in the Chemistry of Tetrahydroquinolines. *Chem. Rev.* **2011**, *111*, 7157-7259.
 30. Katritzky, A. R.; Rachwal, S.; Rachwal, B., Recent Progress in the Synthesis of 1,2,3,4,-Tetrahydroquinolines. *Tetrahedron* **1996**, *52*, 15031-15070.

31. Chen, F.; Surkus, A.-E.; He, L.; Pohl, M.-M.; Radnik, J.; Topf, C.; Junge, K.; Beller, M., Selective Catalytic Hydrogenation of Heteroarenes with N-Graphene-Modified Cobalt Nanoparticles (Co₃O₄-Co/NGr@ α -Al₂O₃). *J. Am. Chem. Soc.* **2015**, *137*, 11718-11724.
32. Ren, D.; He, L.; Yu, L.; Ding, R.-S.; Liu, Y.-M.; Cao, Y.; He, H.-Y.; Fan, K.-N., An Unusual Chemoselective Hydrogenation of Quinoline Compounds Using Supported Gold Catalysts. *J. Am. Chem. Soc.* **2012**, *134*, 17592-17598.
33. Karakulina, A.; Gopakumar, A.; Akcok, I.; Roulier, B. L.; LaGrange, T.; Katsyuba, S. A.; Das, S.; Dyson, P. J., A Rhodium Nanoparticle-Lewis Acidic Ionic Liquid Catalyst for the Chemoselective Reduction of Heteroarenes. *Angew. Chem. Int. Ed. Engl.* **2016**, *55*, 292-296.
34. Deraedt, C.; Ye, R.; Ralston, W. T.; Toste, F. D.; Somorjai, G. A., Dendrimer-Stabilized Metal Nanoparticles as Efficient Catalysts for Reversible Dehydrogenation/Hydrogenation of N-Heterocycles. *J. Am. Chem. Soc.* **2017**, *139*, 18084-18092.
35. Luo, Z.; Min, Y.; Nechiyil, D.; Bacsá, W.; Tison, Y.; Martínez, H.; Lecante, P.; Gerber, I. C.; Serp, P.; Axet, M. R., Chemoselective Reduction of Quinoline over Rh-C₆₀ Nanocatalysts. *Catal. Sci. Technol.* **2019**, *9*, 6884-6898.
36. Yu, X.; Nie, R.; Zhang, H.; Lu, X.; Zhou, D.; Xia, Q., Ordered Mesoporous N-Doped Carbon Supported Ru for Selective Adsorption and Hydrogenation of Quinoline. *Micropor. Mesopor. Mat.* **2018**, *256*, 10-17.
37. Tang, M.; Deng, J.; Li, M.; Li, X.; Li, H.; Chen, Z.; Wang, Y., 3D-Interconnected Hierarchical Porous N-Doped Carbon Supported Ruthenium Nanoparticles as an Efficient Catalyst for Toluene and Quinoline Hydrogenation. *Green Chem.* **2016**, *18*, 6082-6090.
38. Sánchez-Delgado, R. A.; Machalaba, N.; Ng-a-qui, N., Hydrogenation of Quinoline by Ruthenium Nanoparticles Immobilized on Poly(4-Vinylpyridine). *Catal. Commun.* **2007**, *8*, 2115-2118.
39. Jiang, H.-y.; Zheng, X.-x., Tuning the Chemoselective Hydrogenation of Aromatic Ketones, Aromatic Aldehydes and Quinolines Catalyzed by Phosphine Functionalized Ionic Liquid Stabilized Ruthenium Nanoparticles. *Catal. Sci. Technol.* **2015**, *5*, 3728-3734.
40. Sun, B.; Khan, F.-A.; Vallat, A.; Süß-Fink, G., NanoRu@Hectorite: A Heterogeneous Catalyst with Switchable Selectivity for the Hydrogenation of Quinoline. *Appl. Catal. A- Gen.* **2013**, *467*, 310-314.
41. Zhou, L.; Qi, X.; Jiang, X.; Zhou, Y.; Fu, H.; Chen, H., Organophilic Worm-Like Ruthenium Nanoparticles Catalysts by the Modification of CTAB on Montmorillonite Supports. *J. Colloid Interface Sci.* **2013**, *392*, 201-205.
42. McCue, A. J.; Anderson, J. A., Recent Advances in Selective Acetylene Hydrogenation Using Palladium Containing Catalysts. *Front. Chem. Sci. Eng.* **2015**, *9*, 142-153.
43. Support Effect on Cu-Ru/SiO₂ Sol-Gel Catalysts. *Mater. Lett.* **1999**, *41*, 309 - 316.

44. Dhiman, M.; Chalke, B.; Polshettiwar, V., Efficient Synthesis of Monodisperse Metal (Rh, Ru, Pd) Nanoparticles Supported on Fibrous Nanosilica (KCC-1) for Catalysis. *ACS Sustain. Chem. Eng.* **2015**, *3*, 3224-3230.
45. Li, C.; Shao, Z.; Pang, M.; Williams, C. T.; Zhang, X.; Liang, C., Carbon Nanotubes Supported Mono- and Bimetallic Pt and Ru Catalysts for Selective Hydrogenation of Phenylacetylene. *Ind. Eng. Chem. Res.* **2012**, *51*, 4934-4941.
46. Rakers, L.; Martinez-Prieto, L. M.; Lopez-Vinasco, A. M.; Philippot, K.; van Leeuwen, P.; Chaudret, B.; Glorius, F., Ruthenium Nanoparticles Ligated by Cholesterol-Derived NHCs and Their Application in the Hydrogenation of Arenes. *Chem. Commun.* **2018**, *54*, 7070-7073.
47. Ruzicka, J.-Y.; Anderson, D. P.; Gaw, S.; Golovko, V. B., Platinum-Ruthenium Nanoparticles: Active and Selective Catalysts for Hydrogenation of Phenylacetylene. *Aust. J. Chem.* **2012**, *65*, 1420.
48. Niu, M.; Wang, Y.; Li, W.; Jiang, J.; Jin, Z., Highly Efficient and Recyclable Ruthenium Nanoparticle Catalyst for Semihydrogenation of Alkynes. *Catal. Commun.* **2013**, *38*, 77-81.
49. Noël, S.; Bourbiaux, D.; Tabary, N.; Ponchel, A.; Martel, B.; Monflier, E.; Léger, B., Acid-Tolerant Cyclodextrin-Based Ruthenium Nanoparticles for the Hydrogenation of Unsaturated Compounds in Water. *Catal. Sci. Technol.* **2017**, *7*, 5982-5992.
50. Maximov, A.; Zolotukhina, A.; Kulikov, L.; Kardasheva, Y.; Karakhanov, E., Ruthenium Catalysts Based on Mesoporous Aromatic Frameworks for the Hydrogenation of Arenes. *React. Kinet. Mech. Catal.* **2016**, *117*, 729-743.
51. Vidoni, O.; Philippot, K.; Amiens, C.; Chaudret, B.; Balmes, O.; Malm, J.-O.; Bovin, J.-O.; Senocq, F.; Casanove, M.-J., Novel, Spongelike Ruthenium Particles of Controllable Size Stabilized Only by Organic Solvents. *Angew. Chem. Int. Ed.* **1999**, *38*, 3736-3738.
52. Pechtl, M. H. G.; Scariot, M.; Scholten, J. D.; Machado, G.; Teixeira, S. R.; Dupont, J., Nanoscale Ru(0) Particles: Arene Hydrogenation Catalysts in Imidazolium Ionic Liquids. *Inorg. Chem.* **2008**, *47*, 8995-9001.
53. Nowicki, A.; Le Boulaire, V.; Roucoux, A., Nanoheterogeneous Catalytic Hydrogenation of Arenes: Evaluation of the Surfactant-Stabilized Aqueous Ruthenium(0) Colloidal Suspension. *Adv. Synth. Catal.* **2007**, *349*, 2326-2330.
54. Rossi, L. M.; Machado, G., Ruthenium Nanoparticles Prepared from Ruthenium Dioxide Precursor: Highly Active Catalyst for Hydrogenation of Arenes under Mild Conditions. *J. Mol. Catal. A: Chem.* **2009**, *298*, 69-73.
55. Zahmakiran, M.; Özkaz, S., Intrazeolite Ruthenium(0) Nanoclusters: A Superb Catalyst for the Hydrogenation of Benzene and the Hydrolysis of Sodium Borohydride. *Langmuir* **2008**, *24*, 7065-7067.
56. Salas, G.; Campbell, P. S.; Santini, C. C.; Philippot, K.; Costa Gomes, M. F.; Pádua, A. A. H., Ligand Effect on the Catalytic Activity of Ruthenium Nanoparticles in Ionic Liquids.

Dalton Trans. **2012**, *41*, 13919-13926.

57. Tschan, M. J. L.; Diebolt, O.; van Leeuwen, P. W. N. M., Ruthenium Metal Nanoparticles in Hydrogenation: Influence of Phosphorus-Ligands. *Top. Catal.* **2014**, *57*, 1054-1065.

58. Cui, X.; Surkus, A. E.; Junge, K.; Topf, C.; Radnik, J.; Kreyenschulte, C.; Beller, M., Highly Selective Hydrogenation of Arenes Using Nanostructured Ruthenium Catalysts Modified with a Carbon-Nitrogen Matrix. *Nat. Commun.* **2016**, *7*, 11326.

59. Gerber, I. C.; Serp, P., A Theory/Experience Description of Support Effects in Carbon-Supported Catalysts. *Chem. Rev.* **2019**.

60. Morris, T.; Zubkov, T., Steric Effects of Carboxylic Capping Ligands on the Growth of the CdSe Quantum Dots. *Colloids Surf. A* **2014**, *443*, 439-449.

61. Susi, T.; Pichler, T.; Ayala, P., X-Ray Photoelectron Spectroscopy of Graphitic Carbon Nanomaterials Doped with Heteroatoms. *Beilstein J. Nanotechnol.* **2015**, *6*, 177-192.

62. Arblaster, J. W., Crystallographic properties of ruthenium. *Platinum Met. Rev.* **2013**, *57*, 127-136.

General conclusions and perspectives

General conclusions and perspectives

In this thesis we have investigated a series of innovative Ru NP covalent assemblies with di- or multi-functionalized polymantane, triphenylene, anthracene and fullerene molecules. These well-defined structures that present a narrow mean particle size distribution and a short-range order have been applied to catalyze the semi-hydrogenation of phenylacetylene. In such NP networks, we expected to have:

- i. a good control of NP size and electronic interactions as a result of the chemical nature of the ligand;
- ii. a good control of inter-particle distance due to the bulkiness of the ligand;
- iii. a control of the dimensionality of the network (2D or 3D) directed by the geometry of the ligand;
- iv. a facile catalyst separation as a consequence of the macroscopic shape of the final material.

Firstly, various carboxylic acid and amine polymantanes were synthesized and used as ligands and linkers for building up 3D Ru NP assemblies by decomposition of an organometallic Ru precursor under 3 bar H₂ in THF. Among all the ligands tested, mono carboxylic adamantane and mono amine adamantane direct to isolated Ru NP, while dicarboxylic and diamine adamantane, bisadamantane, and diamantane result in covalent NP assemblies. The Ru NP present a metallic *hcp* structure, as confirmed by WAXS analyses. Meanwhile, the mean Ru NP size can be controlled by adjusting the Ru/L ratio, showing in all cases a narrow size distribution. With increasing the Ru/L ratio from 5/1, 10/1 to 20/1, the NP size increased slightly. SAXS and electronic tomography analyses revealed a short-range order in the assembly, with a homogeneous inter-particle distance. Furthermore, this inter-particle distance can be tuned by changing the polymantane block in between the functional groups, in good agreement with ligand size established by theoretical calculations. For the carboxylic acid series, the connected nodes on the surface of NP consist in bidentate carboxylate species, as shown by IR, isotopic labeling, SS-NMR and isolation of intermediate Ru carboxylate complexes formed during the NP synthesis. The differences of electronic density on the surface of Ru NP due to the charge transfer between amine and acid groups and Ru have been quantified by IR from CO adsorption experiment, as well as by XPS analyses and DFT calculations. The charge transfer is from Ru to ligand for carboxylate networks,

resulting in electro-deficient Ru NP. The opposite situation is obtained in the case of the amine ligands. DFT calculations support the electronic properties and show a stronger binding energy of carboxylate groups than amine groups, leading to more stable assemblies as shown by TPD/MS results. Remarkably, a decarbonylation reaction of the carboxylic ligands has been evidenced during the material synthesis at room temperature under 3 bar of hydrogen, which should be catalyzed by intermediate Ru cluster or colloidal species. A preferential low energy pathway for this reaction has been proposed based on DFT calculations. To the best of our knowledge, it is the first time that carboxylic acid decarbonylation is reported under such mild conditions.

Secondly, another series of ligands composed of sp^2 or sp^3 backbone has been synthesized containing carboxylic acid functional groups: tri-carboxylic triphenylene (**TPhTC**), twelve-carboxylic hexa-adducted fullerene (**HF**). In addition, commercially available dicarboxylic anthracene (**AnDC**) has been used. The three compounds were utilized to synthesis Ru NP assemblies following the same organometallic method, expecting that the geometry of the ligand (2D or 3D) will control the formation of 2D or 3D assemblies. In a previous published work from our group, a twelve-carboxylic hexa-adducted fullerene, $C_{66}(\text{COOH})_{12}$ was used to produce self-assemblies with a short-range order. Herein, a hexa-fullerene bearing long alkyl chains terminated with carboxylic acid (**HF**) was applied leading to 3D assemblies with Ru NP mean diameter of 2.2 ± 1.8 nm and long inter-particle distance of 3.3 nm (2.85 nm for $\text{Ru}@C_{66}(\text{COOH})_{12}$). The bidentate carboxylate coordination mode on the NP surface as well as the presence of functionalized fullerene were evidenced by IR and SS-NMR. As a consequence of the planar geometry of the liquid crystal molecule, **TPhTC**, a 2D Ru NP assembly was produced with well-crystalized *hcp* structure, homogeneous NP diameters and controlled inter-particle distance. AFM analyses have shown that the assemblies are layered two-dimensional, and present a high aspect ratio. A wide range of Ru/L ratio have been used, from 4/1 to 120/1, allowing varying the NP size from around 1.3 nm to 2.8 nm. Specially, single Ru atoms can be detected at low Ru/L ratio (20/1) in the assemblies. The distance between NP is larger than the ones obtained in assemblies produced from polymantanes as shown by SAXS and electronic tomography. The coordination chemistry on the surface was studied by IR and SS-NMR that show the existence of bidentate carboxylate groups on the Ru NP surface as well as the maintain of the integrity of the ligand in the material, *i.e.* aromatic ring and ether group

nodes. As for polymantane ligands, adsorbed CO is present on the Ru surface. The thermal stability of **Ru@TPhTC** (40/1 and 4/1) and **TPhTC** ligand was evaluated by TPD/MS. The **Ru@TPhTC** 40/1 material is less stable than **Ru@TPhTC** 4/1 and **TPhTC**, presumably because Ru catalyzed the decomposition of the network. Another planar ligand, anthracene dicarboxylic acid was also used. In that case, the Ru NP size is not homogeneous, which is suspected to result from the partial hydrogenation of the aromatic ring of the ligand during the synthesis, as evidenced by SS-NMR analyses.

In the last chapter of the thesis, the Ru NP assemblies were applied to three different catalytic reactions: bromination, hydrogenation of quinoline, and the selective hydrogenation of phenylacetylene. It is shown that the Ru NP carboxylate covalent assemblies are fragmented into isolated NP both in bromination and quinoline hydrogenation reactions even though showing good activity. During the hydrogenation of phenylacetylene requiring milder conditions, the Ru NP assemblies kept its integrity and displayed good selectivity to styrene. From the set of assemblies produced we investigated structure/performance relationships. We particularly investigated the effect of the electronic density on Ru and the inter-particle distance. This could be done without an additional impact of particle size, since most of the sample produced show similar Ru mean NP size. Considering the catalytic behavior of polymantane NP assemblies, the electron rich Ru NP are more active and less selective than electron deficient one. Longer inter-particle distance between NP hampers activity but benefits the selectivity. When comparing all the carboxylate Ru NP assemblies, electron deficient of Ru NP present higher selectivity. The activity of the catalysts is influenced synergistically by the inter-particle distance as well as by the electron density of Ru NP surface. The assembly displayed good stability, activity and selectivity during catalysis; although a partial collapse of the nanostructure was displayed after four successive catalytic runs performed to test the recyclability of the system. Thermal treatment was attempted to enhance the stability of the nanostructure but additional efforts are needed to explore this approach.

The work described in this doctoral thesis provides inspired perspectives for future research:

i) The possibility of producing 2D or 3D covalent assemblies of metallic nanoparticles by a simple method that can be applied on a large scale has been

validated. We have demonstrated that the choice of ligand strongly influences: the dimensionality of the structure, the inter-particle distance and the electronic density on the metal. In some cases, an effect of the ligand on the particle size has been noted. Considering the huge number of ligands available as well as the choice of metal, the assembly possibilities are only limited by the imagination and of course by their application. Particularly, it would be interesting to: use ligands bearing more functional groups of different types, in order to achieve a larger modulation of the key characteristics of the assemblies; and to extend the study to more applications such as electrocatalysis or sensors, for which high metal loadings are pursued.

ii) The correlations found between the catalytic activity/selectivity and the NP arrangement and electronic effects provide clues for further catalyst design at the molecular level. The detailed characterization of the assemblies helps to better understand heterogeneous catalysts, which are hardly fully characterized nowadays, as for metal supported carbon catalysts. The work opens interesting perspectives for the rational design of heterogeneous catalysts, and offer interesting model catalysts to better understand carbon-supported catalysts.

iii) The main issue our work has raised is the stability of the assemblies under catalytic conditions. The main reason for choosing carboxylic or amine acid ligands to stabilize the assemblies came from the fact that it is well known for catalysts supported on carbon materials that the presence of surface functional groups of acid or amine type allows better dispersion of the active phase, and insures a good stability. Our work demonstrates that the presence of this group, indeed allows a sharp control over NP size, but is not sufficient to strongly stabilize the NP, at least in the case of ruthenium. A Ru-C contribution to the final bonding is in fact needed to stabilize NP on carbon materials.¹ Based on our results, an interesting perspective will be to use other types of ligand showing higher affinity for a metal like ruthenium as diphosphines or di-carbenes, or ligands bearing different functionalities as phosphine plus carboxylates.

iv) The exciting discovery of carboxylic acid decarbonylation occurring under mild conditions in the synthesis procedure is worthy to be exploited for catalysis application. Our work also suggests that the adsorption of CO on the metal should

be problematic to make this reaction catalytic under the condition of the reaction. However, considering that Ru is active for the preferential CO oxidation in hydrogen-rich environments,² it could be interesting to perform this reaction in the presence of small amounts of oxygen.

References

1. Machado, B. F.; Oubenali, M.; Rosa Axet, M.; Trang Nguyen, T.; Tunckol, M.; Girleanu, M.; Ersen, O.; Gerber, I. C.; Serp, P., Understanding the Surface Chemistry of Carbon Nanotubes: Toward a Rational Design of Ru Nanocatalysts. *J. Catal.* **2014**, *309*, 185-198.
2. Nilekar, A. U.; Alayoglu, S.; Eichhorn, B.; Mavrikakis, M., Preferential Co Oxidation in Hydrogen: Reactivity of Core-Shell Nanoparticles. *J. Am. Chem. Soc.* **2010**, *132*, 7418-7428.

Chapitre 5 Résumé

5. Résumé

5.1 Introduction

5.2 Assemblage covalent de nanoparticules métalliques - stratégies de synthèse et applications catalytiques

5.3 Synthèse contrôlée d'assemblages covalents de nanoparticules de ruthénium 3D à partir de ligands polymantanes

5.4 Auto-assemblages 3D et 2D de nanoparticules de Ru produits à partir des ligands multitopiques

5.5 Applications catalytiques des assemblages covalents de NP de Ru

5.6 Perspectives à ces travaux de thèse

5.7 Références

5.1 Introduction

La conception des premiers catalyseurs industriels date de près de deux cents ans¹ et les premiers procédés catalytiques importants, comme le procédé Haber-Bosch sont apparus il y a un siècle. Depuis lors, les progrès en catalyse et en développement de catalyseurs ont considérablement changé le mode de vie humain² et la catalyse est aujourd'hui essentielle pour le développement d'un monde durable. Le but principal de la recherche scientifique en catalyse est de trouver comment orienter les réactions chimiques, en obtenant une activité et une sélectivité élevées dans des conditions douces, tout en atteignant une stabilité maximale du catalyseur et de faibles coûts de production.³ Les recherches les plus récentes s'attachent à établir une description fine des étapes cruciales des réactions chimiques, afin de proposer des théories pouvant guider la conception du catalyseur, qui comprend une grande variété de méthodes et de matériaux.⁴⁻¹⁰

En raison de la demande de développer une chimie durable et verte, les catalyseurs hétérogènes tels que les catalyseurs supportés sont considérés comme supérieurs aux homogènes, en particulier au niveau industriel, du fait de leur recyclabilité et de leur séparation facile.¹¹ Cependant, les catalyseurs supportés souffrent de certains inconvénients, tels que: a) des centres actifs et des interactions métal/support mal définis, b) une large distribution de la taille des particules métalliques, et c) aucun contrôle de la distance inter-particules (Figure 5.1a). D'un autre côté, les catalyseurs homogènes sont attrayants en raison de la nature bien définie de leurs sites actifs, qu'il est possible d'ajuster finement pour atteindre des activités et/ou sélectivité importantes. Les nanoparticules (NP) colloïdales sont des nanomatériaux combinant les caractéristiques des catalyseurs homogènes et hétérogènes, pour lesquels la chimie de coordination de surface joue un rôle prépondérant.¹² Les techniques de préparation de NP colloïdales peuvent fournir un contrôle précis de la taille, la forme et la composition chimique, de sorte que l'hétérogénéité des matériaux catalytiques peut être considérablement réduite (Figure 5.1b).¹³ Cependant, leur séparation du mélange réactionnel est difficile, voire impossible à grande échelle.

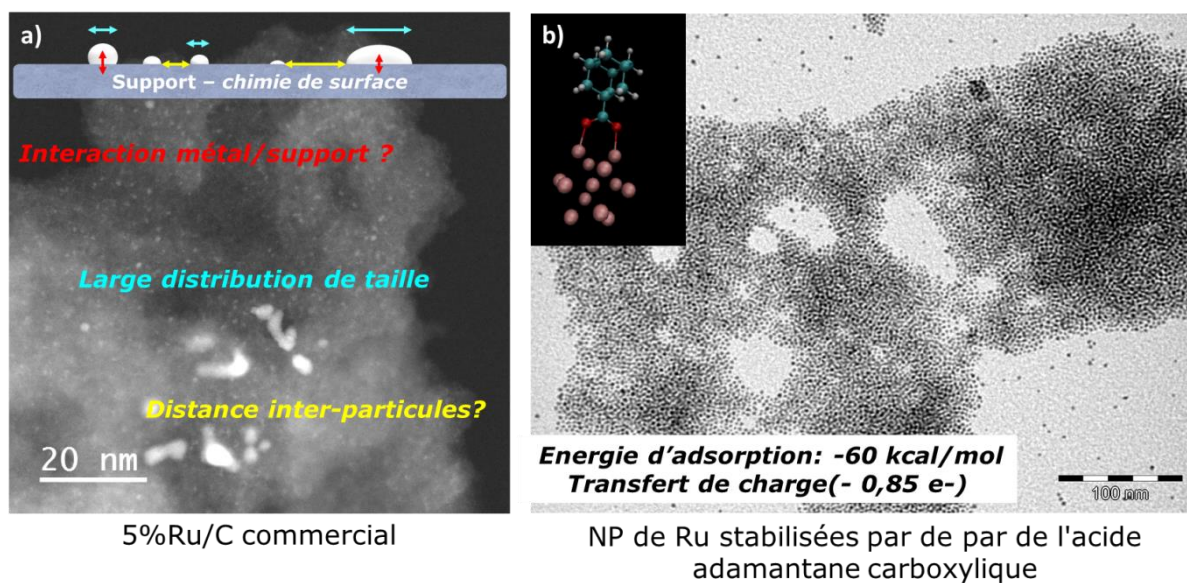


Figure 5.1 a) Micrographie STEM-HAADF d'un catalyseur Ru/C commercial; et b) micrographie TEM de NP de Ru préparées dans ce travail et stabilisées par de l'acide adamantane carboxylique.

Pour contourner ce problème, les NP colloïdales peuvent être déposées sur un support, comme par exemple sur un polymère, un matériau carboné ou des supports inorganiques,¹⁴⁻¹⁶ ou encore stabilisées dans une phase spécifique tel qu'un liquide ionique.^{17,18} Cependant, dans ce cas également, il est difficile de contrôler la distance inter-particules, qui est un paramètre important en catalyse¹⁹⁻²¹ et le fait de déposer les NP sur un support modifie considérablement les propriétés électroniques des NP stabilisées par le ligand d'origine.

Par conséquent, il pourrait être intéressant d'utiliser l'assemblage covalent de NP métalliques en catalyse compte tenu de l'obtention d'un espace confiné et d'un réseau potentiellement, qui sont souhaitables pour des applications en catalyse. Néanmoins, l'assemblage covalent de NP métalliques a reçu relativement peu d'attention pour les applications en catalyse. L'objectif de cette thèse est de concevoir des nanomatériaux innovants contenant des NP de ruthénium métallique et des ligands di- ou multifonctionnels assurant une liaison covalente entre les NPs. Dans de tels réseaux de NP, nous nous attendons à avoir: i) un bon contrôle de la taille des NP et des interactions électroniques avec le ligand, ii) un bon contrôle de la distance inter-particules grâce au choix du ligand, et iii) une séparation facile du catalyseur grâce à la forme macroscopique du matériau final. Étant donné que la structure du catalyseur peut être conçue et bien définie, il sera possible de comprendre la relation structure-performance et de développer une catalyse hétérogène prévisible, ce qui est la plupart du temps très difficile.

Ainsi, une série de nanostructures hybrides originales et auto-assemblées contenant des NP de Ru et divers ligands portant des groupes carboxyliques ou amines ont été produites et caractérisées. Le choix de ces fonctions a été dicté par le fait qu'il s'agit là de groupes de surfaces reconnus pour assurer une bonne dispersion et un bon ancrage des NP métalliques sur les supports carbonés. Le squelette organique, qui peut également être considéré comme le support, est constitué de molécules de différentes tailles contenant du carbone sp^2 (anthracène, fullerène, triphénylène) ou sp^3 (polymantanes). Différents assemblages de NP de Ru tridimensionnels ou bidimensionnels ont été synthétisés et entièrement caractérisés. Des calculs théoriques ont été effectués pour étayer les résultats expérimentaux concernant la stabilité des assemblages et la nature de la chimie de coordination à la surface des NP. Enfin, nous avons évalué les performances catalytiques de ces nanostructures pour différentes réactions. Une attention particulière a été consacrée à l'hydrogénation sélective du phénylacétylène en styrène. Il est démontré que les propriétés intrinsèques des assemblages tels que la distance interparticules et les effets électroniques ont des influences associées sur l'activité catalytique et la sélectivité.

Ce manuscrit est composé d'un chapitre bibliographique et de trois chapitres détaillant les résultats expérimentaux.

5.2 Assemblage covalent de nanoparticules métalliques - stratégies de synthèse et applications catalytiques

Le premier chapitre est consacré à une étude bibliographique exhaustive sur les assemblages covalents de nanoparticules métalliques, se concentrant notamment sur les différentes stratégies de synthèse et sur les rares exemples d'applications catalytiques. En ce qui concerne la synthèse des assemblages covalents de NP métalliques, alors que les premiers assemblages ont été produits avec des méthodes simples, des systèmes efficaces et plus complexes ont été conçus et appliqués récemment, comme la formation de réseaux covalents réversibles de NP métalliques. Si l'interaction métal-ligand est suffisamment forte, les principaux avantages des assemblages covalents de NP métallique en catalyse sont leur stabilité et leur robustesse, ce qui a conduit dans certains cas à un meilleur recyclage, par rapport aux NP de métal non assemblés. De plus, dans certains cas, les NP métalliques assemblées présentaient de meilleures performances catalytiques que les NP métalliques isolées.

Le Tableau 5.1 présente les avantages et les inconvénients des catalyseurs hétérogènes traditionnels, des NP colloïdales et des réseaux covalents de NP. D'après ce Tableau, il semble

que l'utilisation d'assemblages covalents de NP métalliques en catalyse pourrait constituer un bon compromis entre NP colloïdales et catalyseurs hétérogènes conventionnels.

Tableau 5.1 Comparaison du NP colloïdal, des réseaux covalents de NP et des catalyseurs hétérogènes conventionnels supportés en termes de paramètres pertinents pour les performances catalytiques.

Catalyseur	Taille NP	Distance inter-particulaire	Présence de ligand	Interaction avec le support	Robustesse	Séparation
NP colloïdales	+	-	-	-	-	✗
Réseau covalent de NP	+	+	-	-	-	-
Catalyseur hétérogène	✗	✗	+	✗	+	+

Les deux chapitres suivants présentent une série d'assemblages covalents de NP de Ru avec des molécules de polymantane, triphénylène et fullerène fonctionnalisées. Ces structures bien définies dont la synthèse est contrôlée ont été appliquées pour catalyser la semi-hydrogénation du phénylacétylène qui est décrite dans le quatrième et dernier chapitre.

5.3 Synthèse contrôlée d'assemblages covalents de nanoparticules de ruthénium 3D à partir de ligands polymantanes

Dans le chapitre deux, plusieurs ligands polymantanes portant des fonctions acide carboxylique et amine ont été synthétisés (Schéma 5.1) et utilisés comme ligands et lieux dans la construction d'assemblages de NP par décomposition d'un précurseur de Ru sous 3 bar de H₂ dans le THF. Parmi ces ligands, le mono carboxylique adamantane et le mono amine adamantane (**1** et **5**) conduisent à la formation de NP de Ru isolées, tandis que les composés dicarboxyliques et diamines de l'adamantane/bis-adamantane/diamantane conduisent à la formation d'assemblages de NP, les images MET correspondantes sont présentées sur la Figure 5.2.

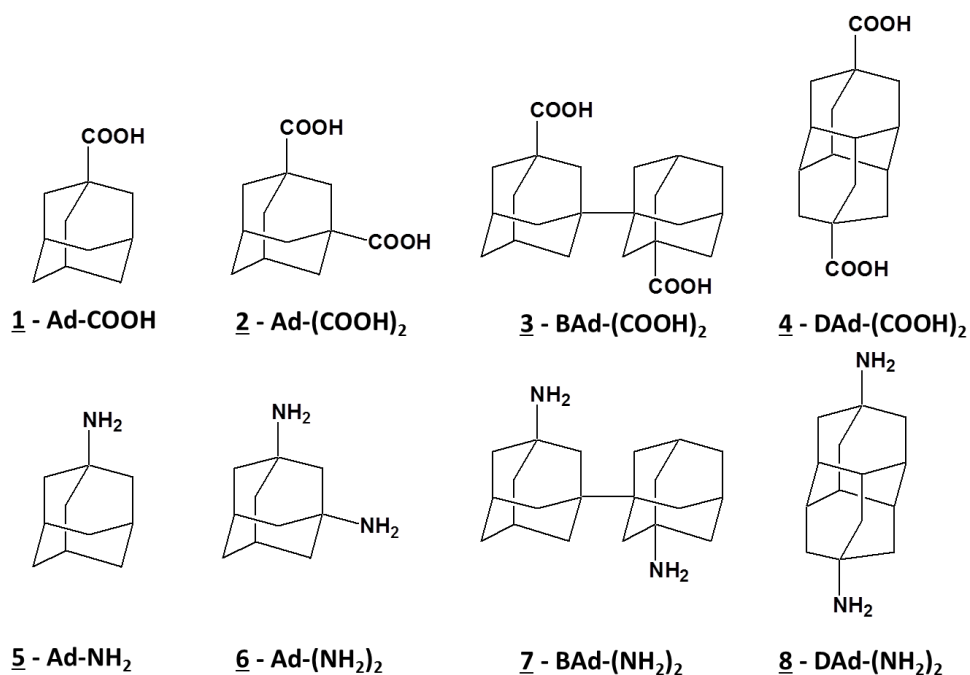


Schéma 5.1 Série de ligands polymantanes, y compris l'adamantane, le bis-adamantane et le squelette diamantane, utilisés pour la synthèse de NP de Ru et de réseaux de NP de Ru.

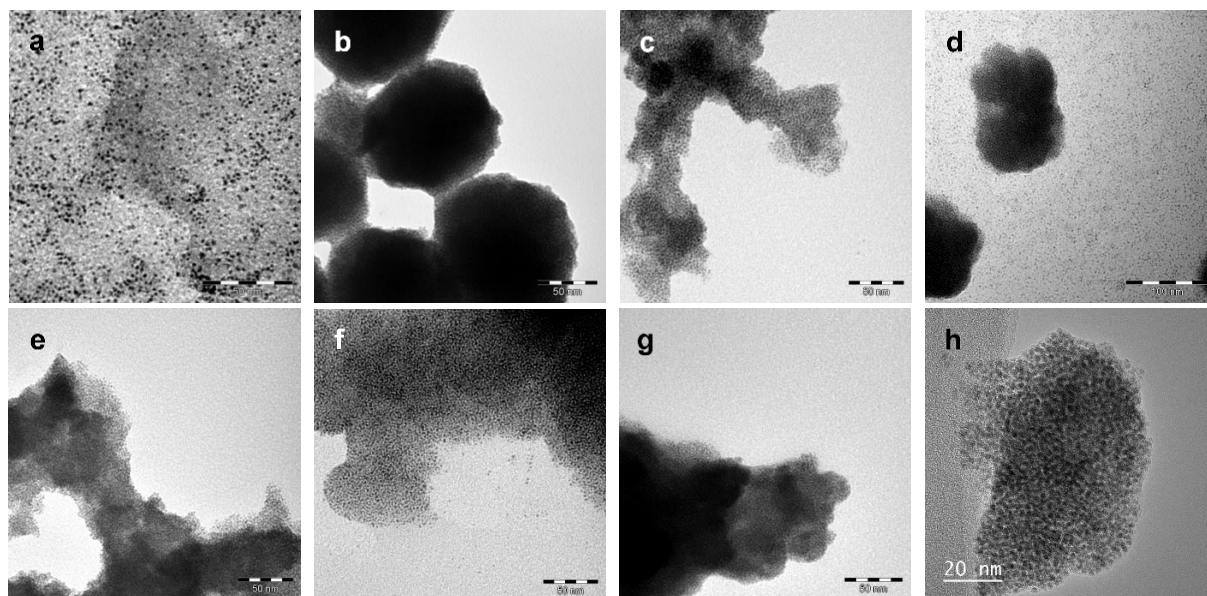


Figure 5.2 Micrographies MET de réseaux de NP de Ru et de NP isolées obtenus à un rapport molaire Ru/L de 10 pour les ligands: a) **1** (barre d'échelle = 50 nm); b) **2** (barre d'échelle = 50 nm); c) **4** (barre d'échelle = 50 nm); d) **5** (barre d'échelle = 100 nm); e) **6** (barre d'échelle = 50 nm); f) **7** (barre d'échelle = 50 nm); g) **8** (barre d'échelle = 50 nm); et h) HRTEM de **Ru@2** (barre d'échelle = 20 nm)

Les nanostructures présentent une structure métallique *hcp* confirmée par l'analyse WAXS. La taille des NP est modifiée avec succès en modulant le rapport Ru/L, montrant un diamètre homogène modéré d'environ 2 nm. Avec l'augmentation du rapport Ru/L de 5/1, 10/1 à 20/1, la taille NP est légèrement augmentée, comme résumé dans le Tableau 5.2.

Tableau 5.2 Distribution de taille moyenne, distances inter-particules et de la teneur en ruthénium des réseaux de NP de Ru et des NP de Ru isolées synthétisés à partir des ligands polymantanes.

Ligand	Ru/L (molaire)	Ru charge (%)	Taille NP (nm) ^{a)}	Taille NP taille (nm) ^{b)}	Réseau NP	Distance inter-particules (nm) ^{c)}
1	5/1	77,9	1,5 ± 0,6	1,5	no	-
	10/1	65,5	1,8 ± 0,5	2,2	no	-
	20/1	78,7	1,9 ± 0,6	2,5	no	-
2	5/1	50,2	1,7 ± 0,7	1,7	yes	2,2
	10/1	61,8	1,8 ± 0,8	2,0	yes	2,7
	20/1	70,1	1,9 ± 0,7	2,2	yes	2,7
4	10/1	67,7	1,8 ± 0,6	2,1	yes	2,9
5	10/1	82,5	1,6 ± 0,7	1,5	no	-
6	10/1	80,1	1,8 ± 0,7	1,9	yes	2,4
7	10/1	65,7	1,7 ± 0,6	1,2	yes	2,5
8	10/1	70,2	1,7 ± 0,7	2,1	yes	2,7

^{a)} Par TEM. ^{b)} Par WAXS. ^{c)} Par SAXS.

En particulier, les auto-assemblages de NP de Ru démontrent un ordre à courte distance avec une distance inter-particules homogène. Le pic à un angle élevé dans les spectres SAXS (Figure 5.3a) est interprété comme une distance de corrélation, et la tomographie électronique (Figure 5.3b) montre un arrangement tridimensionnel des NP à l'intérieur de l'assemblage. De plus, la distance peut être ajustable en modifiant la taille de la molécule de polymantane entre les groupes fonctionnalisés, en bon accord avec la valeur théorique obtenue en sommant la taille des NP et celle de la molécule. Les principales informations issues des analyses MET, WAXS et SAXS sont répertoriées dans le Tableau 5.2.

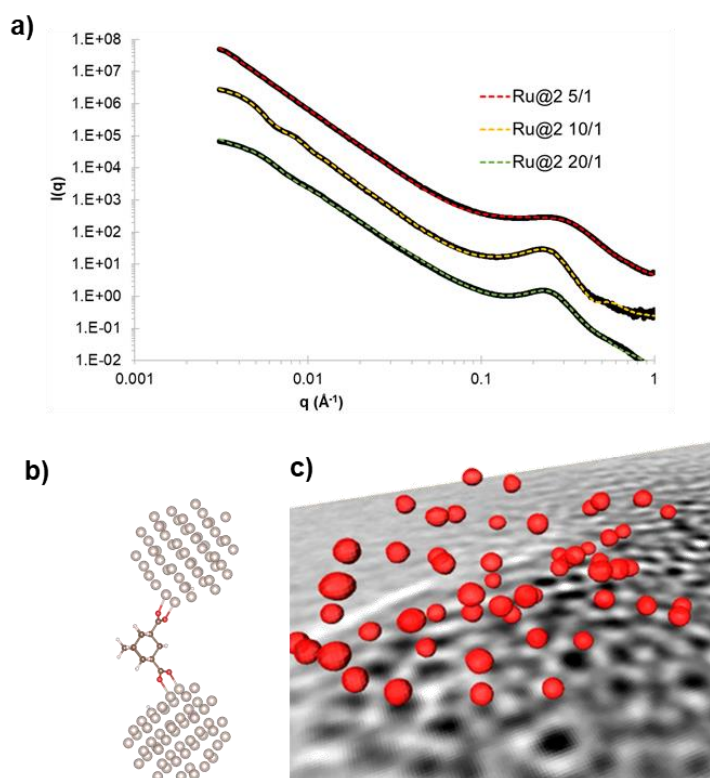


Figure 5.3 a) Analyses SAXS des assemblages de NP de Ru produits à partir du ligand **2** à différents rapports molaires Ru/L 5: 1, 10: 1 et 20: 1; b) Structure optimisée des espèces $(\text{Ru}_{55})_2@Ad-(\text{COO})_2$; et c) reconstruction manuelle 3D de certaines NP de Ru à partir du tomogramme correspondant. Leur taille est calculée à $1,9 \pm 0,3$ nm.

Des analyses IR, et par RMN du solide nous ont permis de mettre en évidence que les ligands carboxyliques sont coordonnés à la surface des nanoparticules *via* un mode carboxylate bidentate (Figure 5.4). Des complexes carboxylates du Ru formés lors des premières étapes de la réaction ont également pu être isolés et caractérisés. Nous avons identifié que les bandes IR à $1560/1390 \text{ cm}^{-1}$ ($\Delta\nu = 170 \text{ cm}^{-1}$) sont cohérentes avec les ponts ligands carboxylates bidentés. Le pic à 220,1 ppm en RMN a été attribué à du CO adsorbé sur les NP de Ru. Le pic à 193,6 ppm a été attribué aux ponts ligands carboxylates bidentés, tandis que le pic à 178,3 ppm pourrait être provisoirement attribué à des espèces chélatées bidentées.

Les différences de densité électronique en surface des NP de Ru dues au transfert de charge entre les groupes amine et acide et le Ru ont été sondées par IR après adsorption de CO et par analyses XPS. Les électrons sont transférés du Ru vers le ligand pour les réseaux carboxylates provoquant la formation de NP de Ru pauvres en électrons. La situation est inversée avec les ligands de type amine.

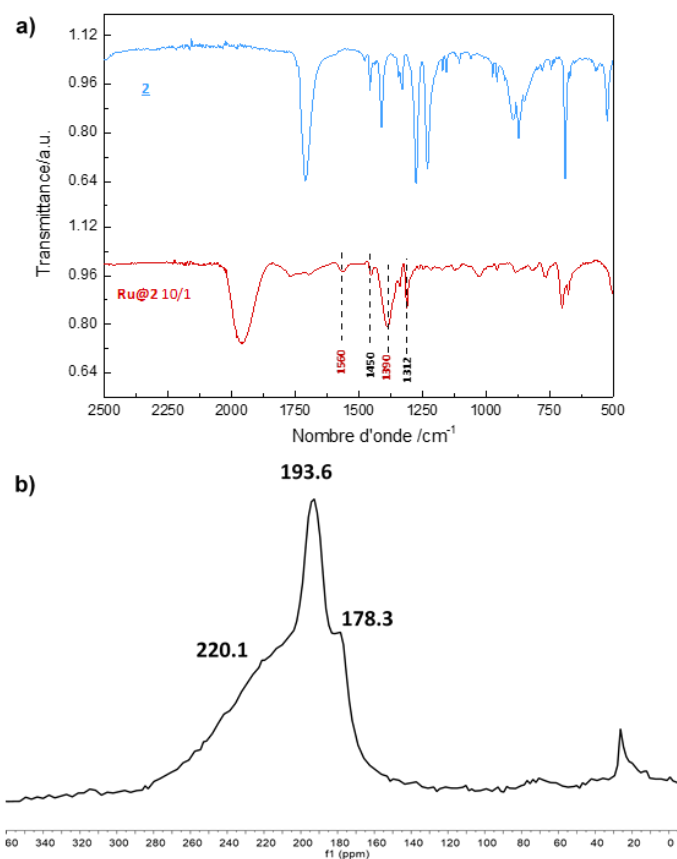


Figure 5.4 a) Spectres IR de **2** et **Ru@2** (rapport Ru/ligand = 10), et b) Spectre RMN ¹³C à l'état solide de **Ru@2** (rapport Ru/ligand = 10) obtenu avec du ligand marqué au ¹³C (Ad-(¹³COOH)₂).

Les calculs DFT (Figure 5.5) prennent en charge les propriétés électroniques et montrent une énergie de liaison plus forte des groupes carboxylates que des groupes amines conduisant à des assemblages plus stables comme le montrent des résultats obtenus par TPD/MS.

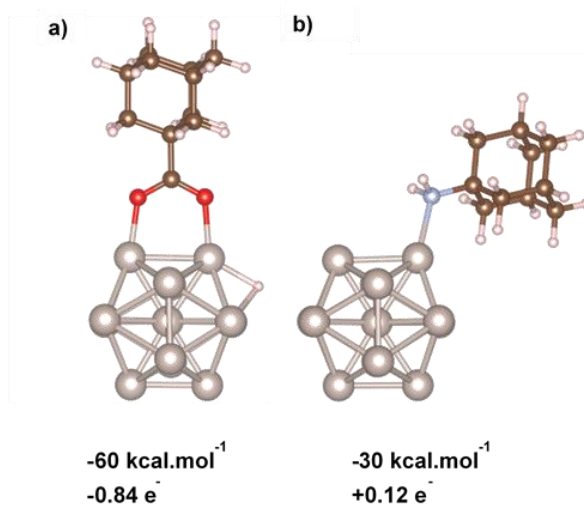


Figure 5.5 Géométrie optimisée (à partir de calculs DFT), énergie d'adsorption des ligands et transfert

de charge pour les modèles a) $\text{Ru}_{13}@1$ et b) $\text{Ru}_{13}@5$.

Remarquablement, nous avons mis en évidence une réaction de décarbonylation des ligands carboxyliques, produisant du CO adsorbé en surface des NP de Ru (ν_{CO} entre 1920 et 1980 cm^{-1}) se produit pendant la synthèse du matériau à température ambiante sous 3 bar d'hydrogène. Cette réaction doit être catalysée par des clusters de Ru et une voie préférentielle de faible énergie a été proposée à partir de calculs DFT (Figure 5.6). C'est à notre connaissance la toute première fois que la réaction de décarbonylation d'acides carboxyliques est observée dans des conditions aussi douces.

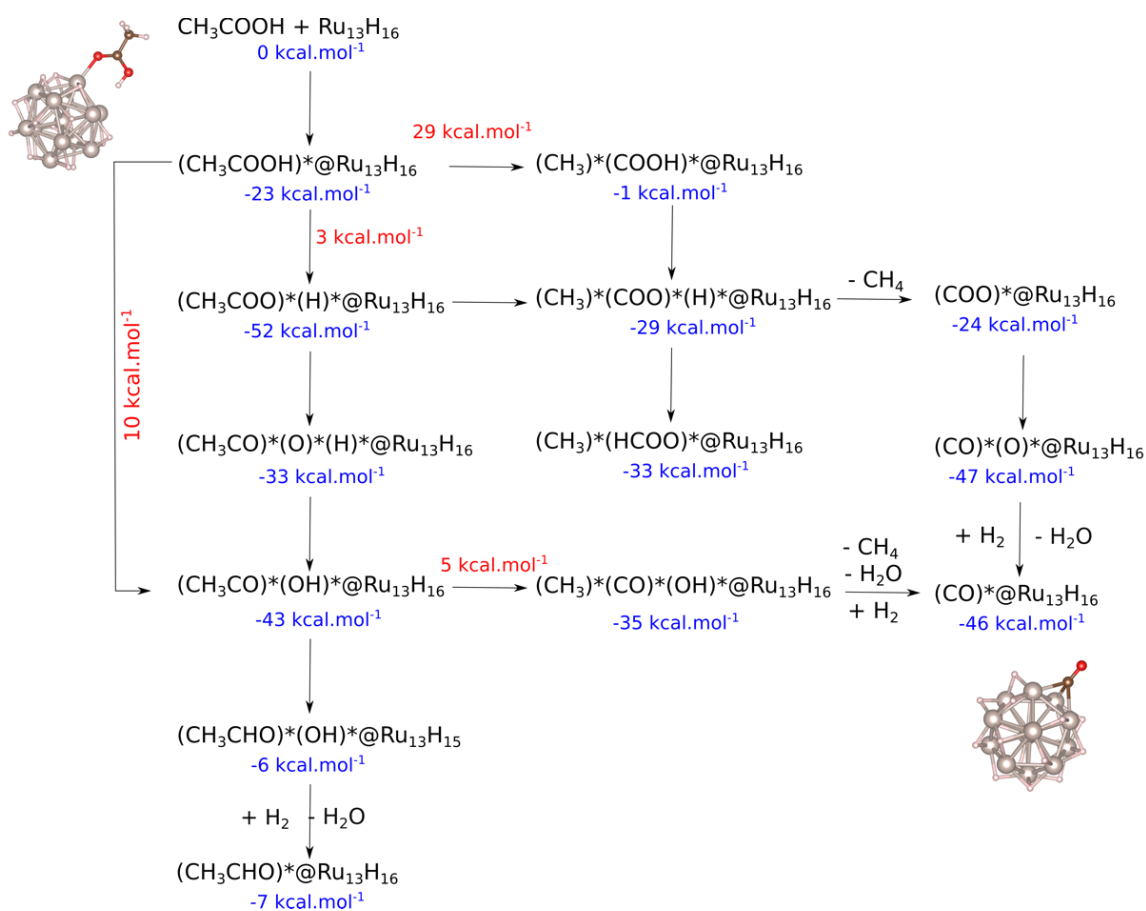
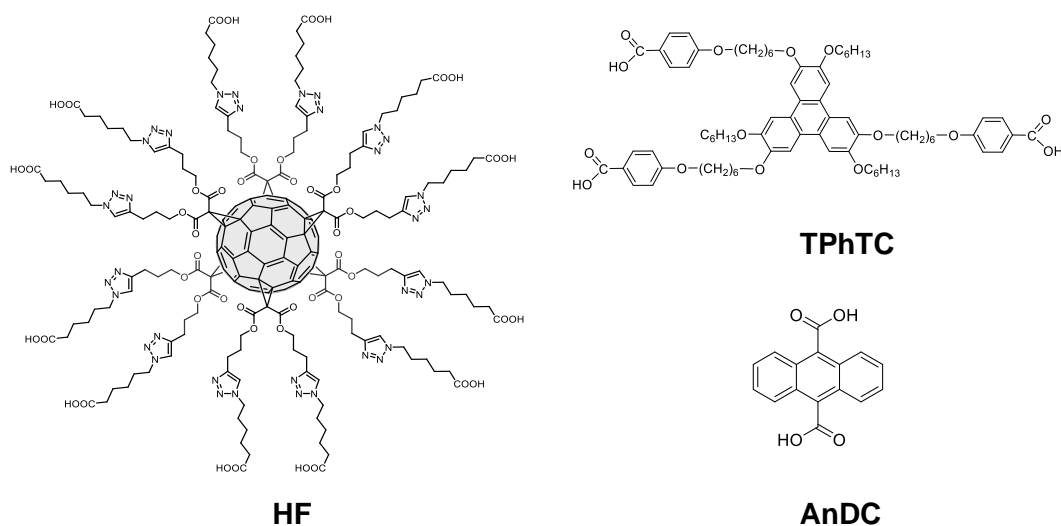


Figure 5.6 Investigation DFT du mécanisme de la réaction de décarbonylation d'acides carboxyliques par un cluster de ruthénium. Les valeurs bleues correspondent aux différences énergétiques totales par rapport à l'état initial, alors que les rouges indiquent la hauteur de la barrière énergétique.

5.4 Auto-assemblages 3D et 2D de nanoparticules de Ru produits à partir des ligands multitopiques

Dans le troisième chapitre, plusieurs molécules terminées par des groupes carboxyliques, comme le triphénylène tri-carboxylique (**TPhTC**) fourni par le professeur Silverio Coco (Liquid Crystal and New Materials Group de l'Université de Valladolid), et un adduit de fullerène C_{60} contenant douze groupements carboxyliques (**HF**) synthétisé dans le laboratoire du Prof. Nazario Martin à Madrid (Espagne). Avec l'anthracène dicarboxylique (**AnDC**), les trois types de composés (Schéma 5.2) ont été utilisés pour produire des assemblages de NP de Ru en suivant la même méthode organométallique que celle décrite dans la partie précédente : le précurseur $[Ru(COD)(COT)]$ étant décomposé sous H_2 en présence de ligands.



Scheme 5.2 Structures moléculaires des ligands **HF**, **TPhTC** et **AnDC**.

Dans des travaux précédents de l'équipe, un fullerène contenant douze groupes carboxyliques nommé $C_{66}(COOH)_{12}$ avait été utilisé afin de produire des auto-assemblages de NP de Ru. Ici, l'hexa-fullerène comportant de longues chaînes alkyles terminées par des groupes acides carboxylique (**HF**) est utilisé, conduisant à des assemblages en trois dimensions avec un diamètre de NP de Ru moyen de $2,2 \pm 1,8$ nm et une distance inter-particules plus longue de 3,3 nm (spectres SAXS sur la Figure 5.7) que la valeur de 2,85 nm obtenu pour $Ru@C_{66}(COOH)_{12}$. La présence de groupes carboxylates bidentés en surface des NP de Ru et celle du fullerène fonctionnalisé (cage C_{60} , triazole, carbone quaternaire et alkyle) ont été mis

en évidence par IR et RMN du solide.

Grâce à la forme plane de la molécule de cristal liquide, **TPhTC**, un assemblage de NP de Ru bidimensionnel a été produit avec une structure *hcp* bien cristallisée des NP de Ru, des diamètres de NP homogènes et une distance interparticulaire contrôlée.

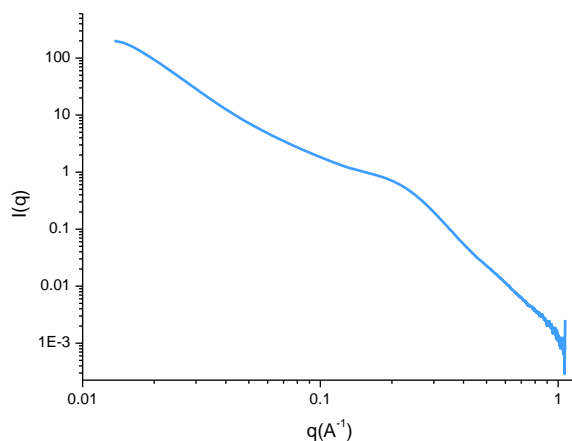


Figure 5.7 Analyse SAXS de **Ru@HF**.

La structure est obtenue avec une large gamme de rapport Ru/L (4/1, 6/1, 20/1, 40/1, 70/1 à 120/1), la taille des NP augmentant d'environ 1,3 nm à 2,8 nm avec le rapport Ru/L. En particulier, des atomes de Ru isolés ont pu être détectés dans les assemblages aux faibles rapports Ru/L (20/1) (Figure 5.8g). Les distances interplanaires et les relations angulaires mesurées par analyse de transformée de Fourier rapide bidimensionnelle (2D-FFT) pour les NP produites sont cohérentes avec la présence de Ru *hcp*.

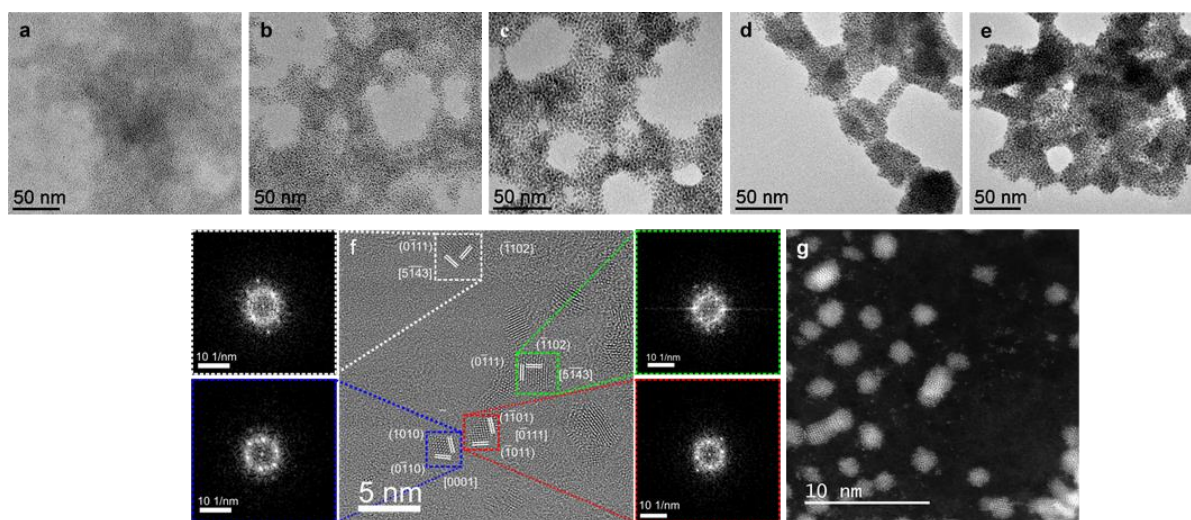


Figure 5.8 Images MET de **Ru@TPhTC** avec un rapport Ru/L de a) 4/1 (barre d'échelle = 50 nm); b) 20/1 (barre d'échelle = 50 nm); c) 40/1 (barre d'échelle = 50 nm); d) 70/1 (barre d'échelle = 50 nm); et

e) 120/1 (barre d'échelle = 50 nm); Images HR-MET de **Ru@TPhTC** avec un rapport Ru/L de f) 6/1 (barre d'échelle = 5 nm) avec analyse par transformée de Fourier rapide bidimensionnelle (2D-FFT) et g) images STEM-HAADF de Ru/L 20/1 (barre d'échelle = 10 nm).

La distance interparticulaire confirmée par SAXS et tomographie électronique (Figure 5.9) est plus longue que celles obtenues dans les assemblages produits à partir des ligands polymantanes en raison du cœur aromatique plus volumineux du ligand **TPhTC** et de la longue chaîne ramifiée attachée. La distance de centre de NP à centre de NP est de 3,5 nm, 3,1 nm et 2,9 nm, pour les échantillons 70/1, 40/1 et 20/1, respectivement. **TPhTC** conduit à un assemblage 2D des NP avec une épaisseur de l'assemblage de 3 à 8 nm et une extension de plus de 200 nm, tel que vérifié par l'analyse AFM.

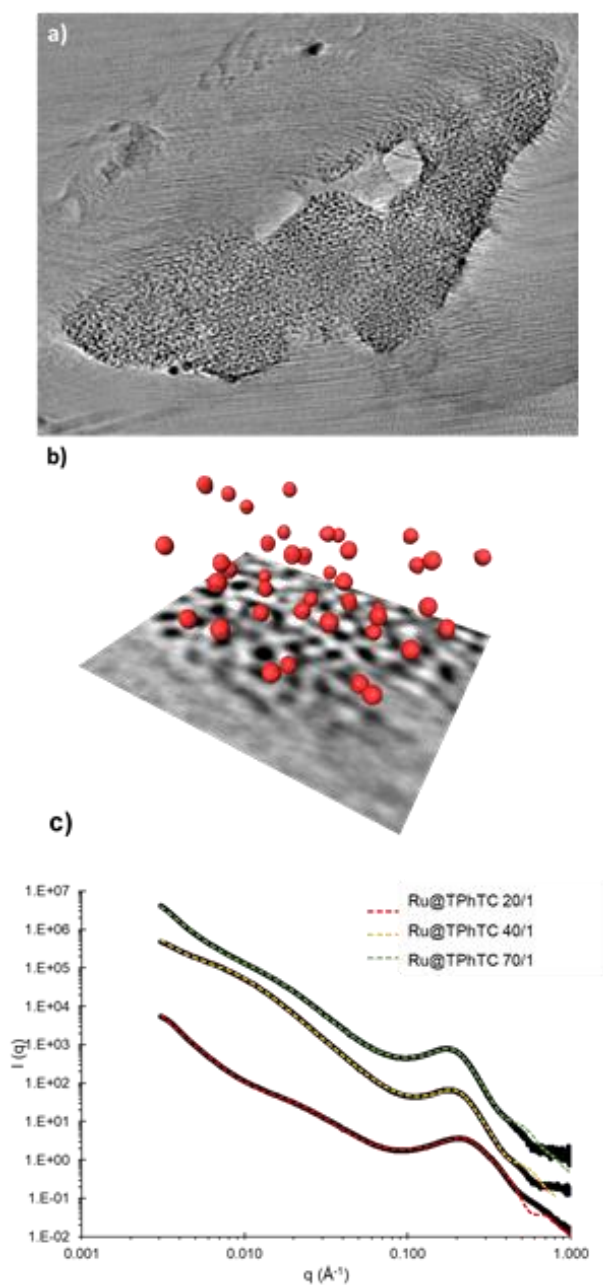


Figure 5.9 a) Tomogramme de l'ensemble de NP de Ru produit à partir de **TPhTC** en utilisant un rapport 40/1 Ru/L; b) reconstruction manuelle de certaines NP de Ru à partir du tomogramme correspondant; et c) analyse SAXS de **Ru @ TPhTC** avec le rapport Ru/L de 20/1, 40/1 et 70/1.

L'analyse par IR et RMN du solide (Figure 5.10) de la chimie de coordination de surface montre l'existence de groupes carboxylates bidentés de surface et l'intégrité de la molécule de ligand dans le matériau, c'est-à-dire les nœuds du groupe aromatique et la fonction éther (Schéma 5.2). De plus, du CO adsorbé est également mis en évidence par les spectres IR, à 1930 cm^{-1} , valeur inférieure à celles obtenues dans le cas des ligands polymantanes carboxyliques ($1940\text{-}1960\text{ cm}^{-1}$). La stabilité thermique entre **Ru@TPhTC** (40/1 et 4/1) et le ligand **TPhTC** a été comparée par TPD/MS. Les résultats montrent que **Ru@TPhTC** 40/1 est moins stable que **Ru@TPhTC** 4/1 et le ligand, ceci pouvant s'expliquer par une décomposition de l'assemblage catalysée par la présence du ruthénium lui-même.

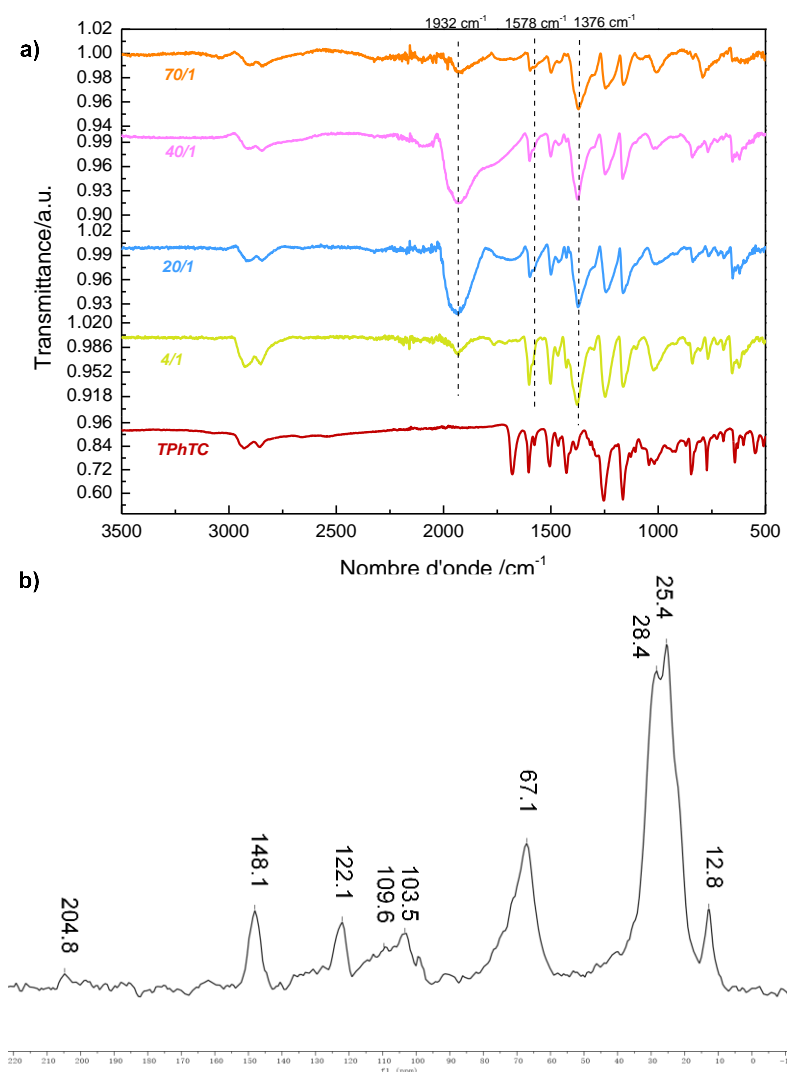


Figure 5.10 a) Spectres ATR-IR de **TPhTC** et **Ru@TPhTC** avec un rapport Ru/L de 4/1 à 70/1 (de bas en haut); et b) spectre ^{13}C CP-MAS-RMN à l'état solide de **Ru@TPhTC** avec un rapport Ru/L de 40/1.

Un autre ligand planaire pouvant conduire à des auto-assemblages 2D, l'acide anthracène dicarboxylique, a également été utilisé. Dans ce cas, néanmoins, la taille des NP de Ru obtenues n'est pas homogène, ceci pouvant résulter de l'hydrogénation partielle du cycle aromatique du ligand pendant la synthèse comme montré dans les spectres carbone en RMN du solide. Les informations principales sur la structure des assemblages de NP de Ru obtenues avec les trois ligands étudiés dans ce chapitre sont résumées dans le Tableau 5.3.

Tableau 5.3 Distribution de taille moyenne, distances interparticulaires et teneur en ruthénium des réseaux de NP de Ru synthétisés à partir des ligands **HF**, **TPhTC** et **AnDC**.

Assemblages	Ru/L (molaire)	Taille NP (nm) ^{a)}	Taille NP (nm) ^{b)}	Distance inter-particules (nm) ^{c)}
Ru@HF	120/1	2,2 ± 1,8	2,3	3,3
	3/1	-	1,3-1,4	-
	15/1	1,3 ± 0,5	1,8	3,11
Ru@TPhTC	30/1	1,7 ± 0,8	2,1	3,56
	60/1	1,9 ± 0,7	2,2	3,68
	90/1	2,4 ± 1,2	2,7-2,8	-
Ru@AnDC	20/1	2,0 ± 0,6, 2,6 ± 0,7	3,0	-

^{a)} Par TEM; ^{b)} Par WAXS; ^{c)} Par SAXS.

5.5 Applications catalytiques des assemblages covalents de NP de Ru

Dans le dernier chapitre de la thèse, les assemblages de NP de Ru nouvellement créés sont appliqués à trois réactions de catalyse différentes : une bromation impliquant une activation C-H, l'hydrogénation de la quinoléine et l'hydrogénation du phénylacétylène. Il est démontré que les assemblages covalents de type carboxylate, même s'ils présentent une bonne activité catalytique, sont détruits pour former des NP de Ru isolées à la fois dans les réactions de

bromation et d'hydrogénation de la quinoléine (Schéma 5.3). Ceci peut être attribué aux conditions de réaction assez dures, mais aussi à la présence de base de type amine, provenant soit du substrat (quinoléine) soit ajoutée dans le milieu réactionnel.

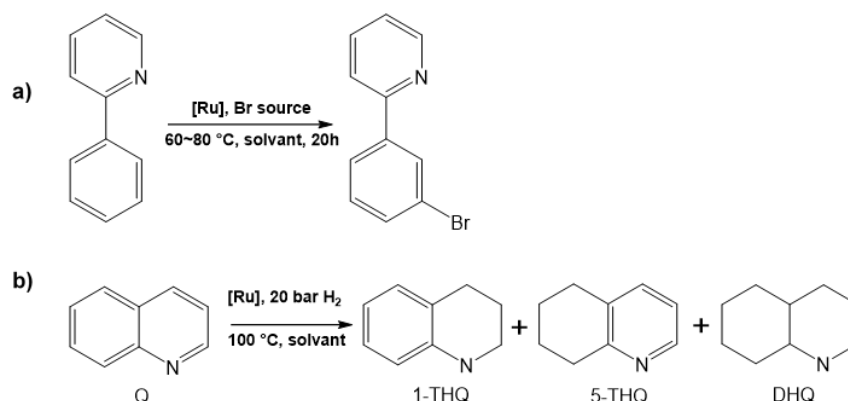


Schéma 5.3 a) Réaction de bromation ; et b) d'hydrogénation de la quinoléine

Dans l'hydrogénation du phénylacétylène qui nécessite des conditions plus douces sans présence de base, les assemblages gardent leur intégrité et présentent une bonne sélectivité pour le styrène, autour de 60~70%. Une distribution représentative des produits d'hydrogénation dans le temps est présentée sur la Figure 5.11 pour le catalyseur **Ru@2** (Ru/ligand = 10). Le groupe alcyne est tout d'abord hydrogéné pour donner de l'éthylbenzène avec une sélectivité allant jusqu'à 95% à de faibles taux de conversion, puis l'hydrogénation complète en éthylcyclohexane peut être accomplie à des temps de réaction prolongés.

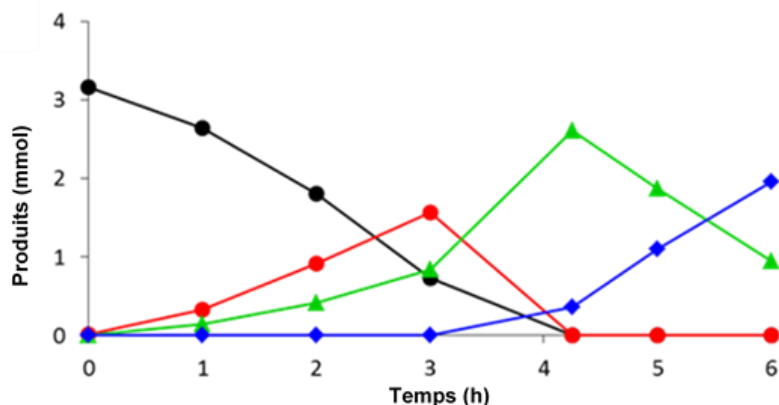
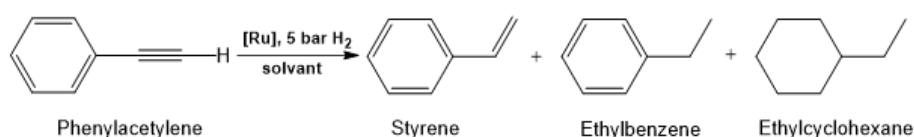


Figure 5.11 Hydrogénation du phénylacétylène et distribution des produits de réaction (carrés noirs =

phénylacétylène; cercles rouges = styrène; triangles verts = éthylbenzène; et losanges bleus = éthylcyclohexane) pour **Ru@2** (Ru/ligand = 10).

Le Tableau 5.4 répertorie les performances catalytiques représentatives de ces séries d'assemblages de NP de Ru et de NP de Ru isolées. Les NP isolées présentent une activité plus élevée que les assemblages de NP. Les assemblages coordonnés aux amines surpassent les assemblages carboxylates en activité, mais entraînent une plus faible sélectivité. De plus, les ligands les plus volumineux, qui conduisent aux plus grandes distances interparticulaires nuisent à l'activité catalytique.

Tableau 5.4 Hydrogénation du phénylacétylène catalysée par des catalyseurs au Ru.^{a)}

Entrée	Catalyseurs	Heure (h)	Conv. (%)	S _{20%} (%)	S _{60%} (%)	TOF (h ⁻¹) ^{b)}	TOF (h ⁻¹) ^{d)}
1	Ru@1 - 10/1	3	73,1	64,5	61,5	57,3	112,9
2	Ru@2 - 10/1	3	71,6	66,7	63,6	52,0	64,9
3	Ru@4 - 10/1	5	62,1	71,3	65,4	28,0	18,9
4	Ru@5 - 10/1	2	72,7	64,3	59,6	79,0	99,2
5	Ru@6 - 10/1	2	65,9	62,5	58,9	68,4	101,4
6	Ru@7 - 10/1	3	66,8	60,5	56,3	48,5	66,6
7	Ru@8 - 10/1	3	72,6	65,2	64,9	60,3	74,9
8	Ru@TPhTC - 30/1	5	64,0	57,5	53,5	27,0	15,6
9	Ru@TPhTC - 30/1 ^{c)}	4	53,8	67,6	65,2	25,4	2,6
10	Ru@HF - 120/1	3	86,1	59,5	51,2	64,1	70,2
11	Ru@AnDC - 20/1	3	75,2	62,4	59,5	58,5	66,9 ^{e)}

^{a)} Conditions de réaction: 0,02 mmol Ru, 412 mg (4,00 mmol) de phénylacétylène, 71 mg (0,50 mmol) de décane (étalon interne), température ambiante, 5 bar H₂, 25 mL MeOH; ^{b)} TOF en mol_{PAconverted}.mol_{Ru}⁻¹.h⁻¹ calculé à l'instant indiqué dans la colonne 3; ^{c)} sous 3 bar de H₂; ^{d)} TOF calculé en fonction de la teneur en Ru de surface à 1 h; ^{e)} Le diamètre est de 1,8 nm.

Une étude des relations structures/performances catalytiques a montré que pour ces assemblages qui présentent des tailles de particules similaires, les paramètres qui gouvernent l'activité et la sélectivité sont la distance interparticulaire et la densité électronique sur les NP de Ru. Nous avons ainsi démontré que pour les assemblages produits à partir des ligands polymantanes, les NP de Ru riches en électrons sont plus actives et moins sélectives que celles

qui sont déficientes en électrons. Nous avons également mis en évidence qu'une distance interparticulaire plus longue entrave l'activité mais profite à la sélectivité de la réaction (Figure 5.12).

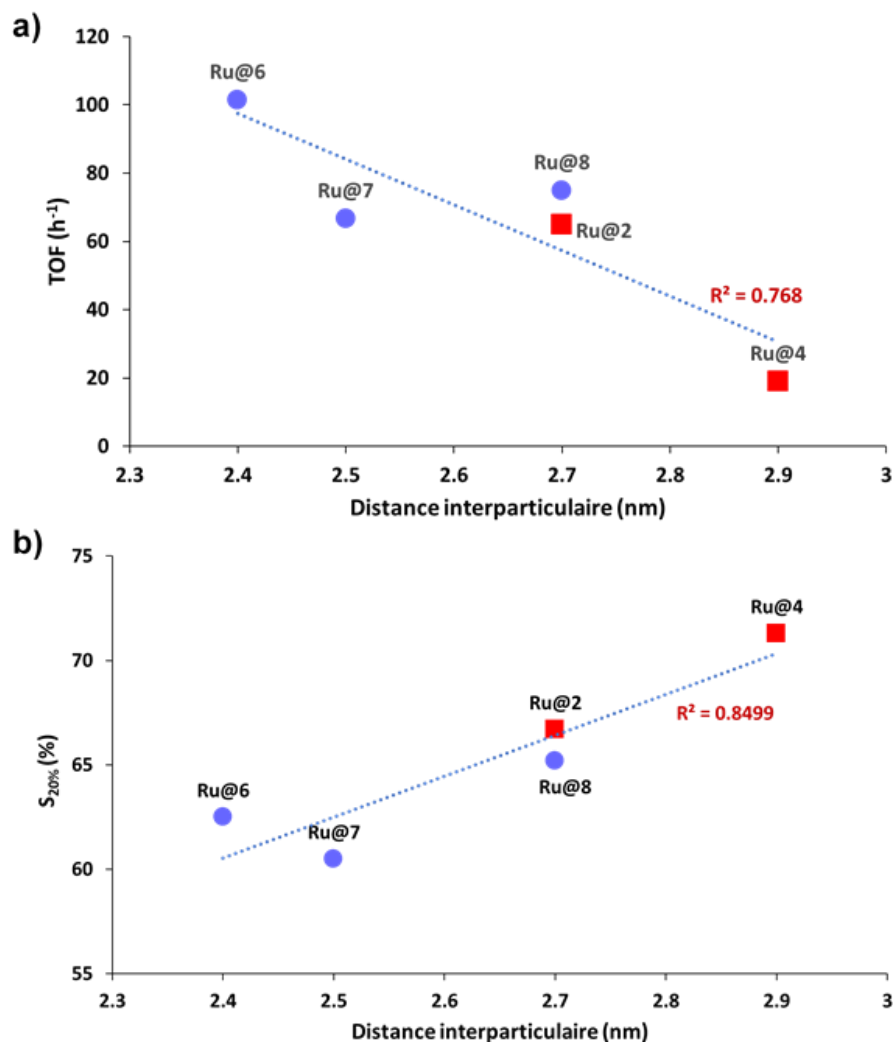


Figure 5.12 a) Activité en fonction de la distance interparticulaire (sphères bleues pour les ligands amines et carrés rouges pour les ligands acides), le rapport Ru/ligand dans ces catalyseurs est de 10/1; b) sélectivité du styrène à une conversion de 20% en fonction de la distance interparticulaire (ligands amines sphères bleues et ligands acides carrés rouges). Le rapport Ru/ligand dans ces catalyseurs est de 10/1.

Considérant que cinq ligands carboxyliques fonctionnalisés différents ont été utilisés dans l'hydrogénation du phénylacétylène, nous avons cherché des corrélations possibles entre la sélectivité et l'activité et les propriétés électroniques ou la distance interparticulaire: les NP de Ru déficientes en électrons présentent une sélectivité plus élevée (Figure 5.13). L'activité des

catalyseurs est influencée de manière synergique par la distance interparticulaire ainsi que la densité électronique à la surface des NP de Ru.

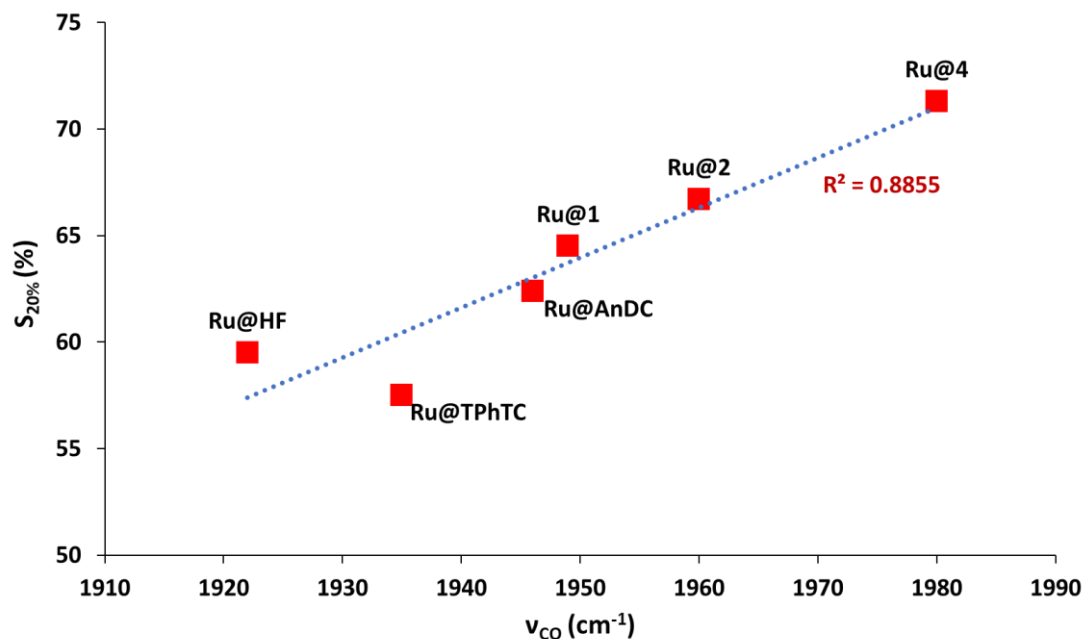


Figure 5.13 Sélectivité du styrène à une conversion de 20% en fonction de la fréquence ν_{CO} du CO adsorbé sur les catalyseurs avec un ligand carboxylique. Les rapports Ru/L sont respectivement de 120, 40, 20, 10, 10, 10 pour **HF**, **TPhTC**, **AnDC**, **4**, **2** et **1**.

Cependant, en dépit de la stabilité observée lors de la réaction, nous avons démontré que la structure des assemblages carboxylates se détériorait en partie lors de recyclages successifs des catalyseurs, montrant des NP isolées hors des assemblages (Figure 5.14). Nous avons exploré la possibilité d'appliquer un traitement thermique aux assemblages dans le but de créer une interface Ru-ligand de type carbène qui serait plus robuste. Bien que les premiers essais soient encourageants, des travaux supplémentaires seraient nécessaires pour valider cette approche.

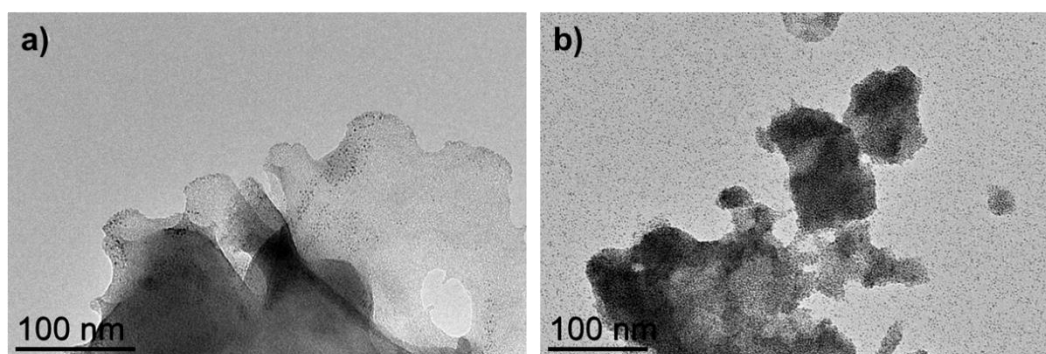


Figure 5.14 Images MET du catalyseur **Ru@2** après a) le 3^{ème} recyclage et b) le 4^{ème} recyclage.

5.6 Perspectives à ces travaux de thèse

Des perspectives pour la poursuite de ce travail et des perspectives inspirées pour de futures recherches sont suggérées ci-dessous :

La possibilité de produire des assemblages covalents 2D ou 3D de nanoparticules métalliques par une méthode simple pouvant être appliquée à grande échelle a été validée. Nous avons démontré que le choix du ligand influence fortement : la dimensionnalité de la structure, la distance interparticulaire et la densité électronique sur le métal. Dans certains cas, un effet du ligand sur la taille des particules a été noté. Compte tenu du grand nombre de ligands disponibles ainsi que du choix du métal, les possibilités d'assemblage ne sont limitées que par l'imagination et bien sûr l'application. En particulier, il serait intéressant : a) d'utiliser des ligands portant des groupes fonctionnels de différents types, afin d'obtenir une modulation plus importante des caractéristiques clés des assemblages; et b) d'étendre l'étude à d'autres applications telles que l'électrocatalyse ou les capteurs de gaz, pour lesquels des charges élevées de métaux sont souvent recherchées.

Les corrélations trouvées entre l'activité/sélectivité catalytique et l'arrangement des NP et les effets électroniques fournissent des indices pour une conception plus fine du catalyseur au niveau moléculaire. La caractérisation détaillée des assemblages permet de mieux comprendre les catalyseurs hétérogènes, qui sont toujours difficiles à caractériser finement de nos jours, comme pour les catalyseurs supportés sur carbone. Nos travaux ouvrent des perspectives intéressantes pour la conception rationnelle de catalyseurs hétérogènes et offrent des catalyseurs modèles intéressants pour mieux comprendre les catalyseurs supportés sur carbone.

Le principal problème que notre travail a soulevé est la stabilité des assemblages dans des conditions catalytiques. La principale raison du choix des ligands acides carboxyliques ou aminés pour stabiliser les assemblages vient du fait qu'il est bien connu pour les catalyseurs supportés sur des matériaux carbonés que la présence de fonctions de surface de type acide ou amine permet une meilleure dispersion de la phase active, et assure une bonne stabilité. Nos travaux démontrent que la présence de ces groupes, permet en effet un bon contrôle sur la taille des NP, mais n'est pas suffisante pour stabiliser fortement les NP, du moins dans le cas du ruthénium. Une contribution Ru-C à la liaison métal/support finale est en fait nécessaire pour stabiliser les NP sur les matériaux carbonés.²² Sur la base de nos résultats, une perspective intéressante sera d'utiliser d'autres types de ligand montrant une affinité plus élevée pour un métal comme le ruthénium comme des diphosphines ou des di-carbènes, ou des ligands portant

des fonctionnalités différentes comme phosphine + carboxylates.

La découverte de la décarbonylation d'acide carboxylique se produisant dans des conditions douces dans la procédure de synthèse mérite d'être exploitée pour une application en catalyse. Nos travaux suggèrent également que la désorption du CO du métal devrait être problématique pour rendre cette réaction catalytique dans des conditions douces. Cependant, étant donné que le Ru est actif pour l'oxydation préférentielle du CO dans des environnements riches en hydrogène,²³ il pourrait être intéressant d'effectuer cette réaction toujours dans des conditions douces mais en présence de petites quantités d'oxygène

5.7 Références

1. Robertson, A., The Early History of Catalysis. *Platinum Met. Rev.* **1975**, *19*, 64-69.
2. Hagen, J., *Industrial Catalysis: A Practical Approach*. John Wiley & Sons: **2015**.
3. Derouane, E. G., Catalysis in the 21st Century, Lessons from the Past, Challenges for the Future. *Cattech* **2001**, *5*, 214-225.
4. Furdala, K. L.; Tilley, T. D., Design and Synthesis of Heterogeneous Catalysts: the Thermolytic Molecular Precursor Approach. *J. Catal.* **2003**, *216*, 265-275.
5. Zhang, Y.; Yang, X.; Zhou, H.-C., Synthesis of MOFs for Heterogeneous Catalysis via Linker Design. *Polyhedron* **2018**, *154*, 189-201.
6. Dufaud, V.; Davis, M. E., Design of Heterogeneous Catalysts via Multiple Active Site Positioning in Organic-inorganic Hybrid Materials. *J. Am. Chem. Soc.* **2003**, *125* (31), 9403-9413.
7. Vojvodic, A.; Nørskov, J. K., New Design Paradigm for Heterogeneous Catalysts. *Natl. Sci. Rev.* **2015**, *2*, 140-143.
8. Greeley, J., Theoretical Heterogeneous Catalysis: Scaling Relationships and Computational Catalyst Design. *Annu. Rev. Chem. Biomol. Eng.* **2016**, *7*, 605-635.
9. Hutchings, G. J., Heterogeneous Catalysts-Discovery and Design. *J. Mater. Chem.* **2009**, *19*, 1222-1235.
10. Gao, C.; Wang, J.; Xu, H.; Xiong, Y., Coordination Chemistry in the Design of Heterogeneous Photocatalysts. *Chem. Soc. Rev.* **2017**, *46*, 2799-2823.
11. Sun, L. B.; Liu, X. Q.; Zhou, H. C., Design and Fabrication of Mesoporous Heterogeneous Basic Catalysts. *Chem. Soc. Rev.* **2015**, *44*, 5092-5147.
12. Yan, N.; Yuan, Y.; Dyson, P. J., Nanometallic Chemistry: Deciphering Nanoparticle Catalysis from the Perspective of Organometallic Chemistry and Homogeneous Catalysis. *Dalton Trans* **2013**, *42*, 13294-13304.
13. Jiang, Y.; Gao, Q., Heterogeneous Hydrogenation Catalyses over Recyclable Pd(0) Nanoparticle Catalysts Stabilized by PAMAM-SBA-15 Organic-Inorganic Hybrid Composites. *J. Am. Chem. Soc.* **2006**, *128*, 716-717.
14. Losch, P.; Huang, W.; Goodman, E. D.; Wrasman, C. J.; Holm, A.; Riscoe, A. R.; Schwalbe, J. A.; Cargnello, M., Colloidal Nanocrystals for Heterogeneous Catalysis. *Nano. Today* **2019**, *24*, 15-47.
15. Luechinger, N. A.; Loher, S.; Athanassiou, E. K.; Grass, R. N.; Stark, W. J., Highly Sensitive Optical Detection of Humidity on Polymer/Metal Nanoparticle Hybrid Films. *Langmuir* **2007**, *23* (6), 3473-3477.
16. Teddy, J.; Falqui, A.; Corrias, A.; Carta, D.; Lecante, P.; Gerber, I.; Serp, P., Influence of Particles Alloying on the Performances of Pt-Ru/CNT Catalysts for Selective Hydrogenation. *J. Catal.* **2011**, *278*, 59-70.
17. Karakulina, A.; Gopakumar, A.; Akcok, I.; Roulier, B. L.; LaGrange, T.; Katsyuba, S. A.; Das, S.;

- Dyson, P. J., A Rhodium Nanoparticle-Lewis Acidic Ionic Liquid Catalyst for the Chemoselective Reduction of Heteroarenes. *Angew. Chem. Int. Ed. Engl.* **2016**, *55*, 292-296.
18. Scholten, J. D.; Leal, B. C.; Dupont, J., Transition Metal Nanoparticle Catalysis in Ionic Liquids. *ACS Catal.* **2012**, *2*, 184-200.
19. Antolini, E., Structural Parameters of Supported Fuel Cell Catalysts: The Effect of Particle Size, Inter-particle Distance and Metal Loading on Catalytic Activity and Fuel Cell Performance. *Appl. Catal. B* **2016**, *181*, 298-313.
20. Prieto, G.; Zečević, J.; Friedrich, H.; de Jong, K. P.; de Jongh, P. E., Towards Stable Catalysts by Controlling Collective Properties of Supported Metal Nanoparticles. *Nat. Mater.* **2013**, *12*, 34-39.
21. Mistry, H.; Behafarid, F.; Reske, R.; Varela, A. S.; Strasser, P.; Roldan Cuenya, B., Tuning Catalytic Selectivity at the Mesoscale via Interparticle Interactions. *ACS Catal.* **2016**, *6*, 1075-1080.
22. Machado, B. F.; Oubenali, M.; Rosa Axet, M.; Trang Nguyen, T.; Tunckol, M.; Girleanu, M.; Ersen, O.; Gerber, I. C.; Serp, P., Understanding the Surface Chemistry of Carbon Nanotubes: Toward a Rational Design of Ru Nanocatalysts. *J. Catal.* **2014**, *309*, 185-198.
23. Nilekar, A. U.; Alayoglu, S.; Eichhorn, B.; Mavrikakis, M., Preferential Co Oxidation in Hydrogen: Reactivity of Core-Shell Nanoparticles. *J. Am. Chem. Soc.* **2010**, *132*, 7418-7428.